Numerical methods for the evaluation of the structural response of ship appendices

Bakica, Andro

Doctoral thesis / Disertacija

2022

Degree Grantor / Ustanova koja je dodijelila akademski / stručni stupanj: **University of Zagreb, Faculty of Mechanical Engineering and Naval Architecture / Sveučilište u Zagrebu, Fakultet strojarstva i brodogradnje**

Permanent link / Trajna poveznica: https://urn.nsk.hr/urn:nbn:hr:235:347969

Rights / Prava: In copyright/Zaštićeno autorskim pravom.

Download date / Datum preuzimanja: **2024-04-27**

University of Zagreb

Faculty of Mechanical Engineering and Naval Architecture

Andro Bakica

NUMERICAL METHOD FOR THE EVALUATION OF THE STRUCTURAL RESPONSE OF SHIP APPENDICES

DOCTORAL DISSERTATION

Zagreb, 2022

University of Zagreb

Faculty of Mechanical Engineering and Naval Architecture

Andro Bakica

NUMERICAL METHOD FOR THE EVALUATION OF THE STRUCTURAL RESPONSE OF SHIP APPENDICES

DOCTORAL DISSERTATION

Supervisor:
Associate Professor Nikola Vladimir, PhD

Zagreb, 2022

University of Zagreb

Fakultet strojarstva i brodogradnje

Andro Bakica

NUMERIČKA METODA ZA ANALIZU ODZIVA KONSTRUKCIJE BRODSKIH PRIVJESAKA

DOKTORSKI RAD

Mentor:
Izv. prof. dr. sc. Nikola Vladimir

Zagreb, 2022.

Acknowledgements

I am thankful to my supervisor Nikola Vladimir for giving me with the opportunity to work on the advanced subjects in the field of naval architecture with one of the leading shipyards in the industry. Without his enormous dedication and time, especially in the beginning of the PhD, this work would never reach the necessary maturity. The experiences and knowledge obtained throughout this study will always remain invaluable.

I am grateful to Šime Malenica for his continuous guidance in the theoretical background related to hydro-structural issues as well as for his clear and understandable way of communication related to the complex physical problems. His advices and commitment had a substantial impact on the thesis quality. Also, I am thankful for the time spent in the Bureau Veritas Research Department and colleagues (Sopheak Seng, Charaf Ouled-Housseine and Guillaume De-Hauteclocque) who have helped me significantly in the course of my PhD.

I wish to express my gratitude to the colleagues at the 8th CFD floor group, especially Inno Gatin, who was always there when the simulation problems occurred, ready to help and discuss the issue. My thanks also go to Marin Palaversa for the never-ending discussions regarding code implementation along with other scientific and engineering issues.

Abstract

Numerical framework for the assessment of hydrodynamic loads and structural responses of ship appendages is developed in this work. The ship entire life cycle is considered, and the expected long-term maximum loads are evaluated emphasizing the statistical wave environment and appropriate loading parameters. Different existing numerical models are employed, and hydro-structure interaction models are developed and verified. The study can be generally divided into two parts: definition of the relevant load cases for the ship appendage and development of the applicable hydro-structural model capturing the necessary physical phenomena relevant for accurate structural response calculation. First part relates to the input for the numerical simulation model, while the second part provides the structural stresses essential for the appendage design. Both steps combined make the basis for the direct approach in the design of ship structures.

The numerical method proposed in this work is applied on the design of Pre-Swirl Stator (PSS) ship appendage. PSS is an Energy Saving Device (ESD) which aims to reduce the amount of the rotational kinetic energy in the propeller slipstream, thus resulting in lower power delivered to the propeller shaft and decreasing the on-board total fuel consumption. Although majority of the current research is dedicated to the performance and efficiency gains of ESDs, this study is primarily related to the structural issues exhibited by such appendages. Due to the position of the PSS in the ship stern wake near the propeller, the obvious and foremost load case on PSS is related to the propeller rotation. For these simulations to reach a satisfying level of accuracy, Computational Fluid Dynamics (CFD) solvers are necessary because the inclusion of viscosity, turbulence and non-linearity is mandatory. However, propeller induced loads cover only one segment of the PSS life cycle i.e., when the ship operates in calm-water. On the contrary, design life wave loads are much harder to approximate, and their quantification requires stochastic methods to reach a representative load-case for the variety of sea-states the ship may encounter. Usually, the sea-states are represented through multiple design conditions or the so-called Equivalent Design Waves (EDWs) corresponding to different levels of probability and this methodology is developed and used in the current work for the case of PSS. In order to analyse a vast number of possible sea-states and directions, a linear potential flow code in frequency domain is deemed sufficient given its incomparable CPU efficiency.

For non-linear simulations on defined EDWs, two hydro-structural models are developed in the scope of the study: quasi-static and dynamic (or so-called hydroelastic). The former presumes the independence of the fluid force on the structural nodal displacements and the problem deduces to the pressure interpolation from fluid to structural sharing interface. The latter requires solution of the structural dynamics inside the fluid domain and subsequent influence of nodal displacement on the fluid field is taken into account. The structure is modelled with a well-established Finite Element Method (FEM) which follows a need for the FEM-CFD interaction model. The quasi-static model is implemented as the projection method and the dynamic model is realized with the modal superposition which greatly adds to the efficiency of the coupling.

The developments in this study are performed mainly on the interface between the CFD and FEM computational tools for which OpenFOAM and NASTRAN software is applied, respectively. The linear potential solution is obtained by means of Bureau Veritas software HydroStar.

Keywords

Numerical simulation, CFD-FEM, fluid-structure interaction, quasi-static response, hydroelastic response, Pre-Swirl Stator, Equivalent Design Wave, long-term wave statistics.

Prošireni sažetak

Modeliranje i proračun hidrodinamičkih opterećenja i naprezanja relevantnih za projektiranje plutajućih konstrukcija se aktivno istražuju posljednjih nekoliko desetljeća. Sukladno unaprjeđenju računalnih mogućnosti i numeričkih modela, u brodograđevnoj praksi su se razvila dva temeljna smjera projektiranja: metoda utemeljena na pravilima i direktni proračuni opterećenja i odziva. Metoda utemeljena na pravilima se sastoji od skupa formula koje proizlaze iz iskustveno definiranih parametara na temelju mjerenja na brodovima u naravi ili modelskih ispitivanja. Ovakav princip projektiranja imao je ključnu ulogu u dimenzioniranju brodova i plutajućih konstrukcija dugi niz godina. Praksa pokazuje da konstrukcije projektirane isključivo prema pravilima imaju izrazito visoku granicu sigurnosti, dok primjena direktnih proračuna nudi mogućnost da se ona smanji na ekonomski poželjniju razinu, a da se pri tome bitnije ne ugrožava sigurnost broda i posade. Napredak je naročito potpomognut razvitkom suvremenih numeričkih modela i dostupnosti računalnih alata koji se kontinuirano nadograđuju.

Pri određivanju potrebne razine točnosti, a posljedično i prihvatljive razine složenosti direktnog proračuna, postoje dvije ključne nepoznanice koje zahtijevaju pažnju: definicija opterećenja i izbor odgovarajućeg načina međudjelovanja modela konstrukcije i fluida. Definicija opterećenja podrazumijeva znanje o okolišnim uvjetima tijekom životnog vijeka konstrukcije. Za plutajuće objekte, okolišni uvjeti uobičajeno znače proučavanje morskih valova. S obzirom na široki raspon valnih visina i duljina te vjerojatnosti njihova pojavljivanja, stohastičke metode su neizbježne za evaluaciju nailaznih valova i stanja mora tijekom predviđenog životnog vijeka konstrukcije. Opis stanja mora kao valnih spektara pojednostavljuje širu statističku analizu. Ovisno o konstrukciji ili položaju strukturnog elementa, mogući su dodatni slučajevi opterećenja (npr. utjecaj brodskog vijka). Nakon što su definirani relevantni slučajevi opterećenja, bilo u mirnoj vodi ili na valovima, potreban je izbor prikladnog matematičkog modela međudjelovanja konstrukcije i fluida.

U slučaju brodskih privjesaka, oba rješavača su isključivo ovisna o tipu samog brodskog privjeska. Vezano za model konstrukcije, Metoda konačnih elemenata (*eng. Finite Element Method,* FEM) je gotovo isključivo korištena u brodograđevnoj industriji s velikom bazom verificiranih i validiranih rezultata. Što se tiče hidrodinamičkog modela, ako je dio konstrukcije pozicioniran blizu ravnine brodskog vijka, kao što je slučaj kod uređaja za uštedu energije (*eng. Energy Saving*

Device, ESD), gdje su nelinearnosti, viskoznost i turbulencija izraženi, računalna dinamika fluida (*eng. Computational Fluid Dynamics,* CFD) je nužna za postizanje zadovoljavajuće razine točnosti. Štoviše, visok red točnosti ostvaren računalnom dinamikom fluida dolazi uz korištenje vrlo velikih računalnih resursa. Iz perspektive direktnih proračuna, ovakav tip proračuna bio bi nemoguć uzimajući u obzir doprinos svih stanja mora. Iz spomenutog razloga, potrebna je učinkovitija metoda kako bi numerički proračun postao izvediv u realnom vremenu. U navedenu svrhu, statistička analiza stanja mora je provedena na jednostavnijem hidrodinamičkom modelu koristeći linearne potencijalne matematičke modele diskretizirane pomoću metode panela (*eng. Boundary Element Method,* BEM). BEM metoda izračunava rješenje u frekvencijskoj domeni kao prijenosne funkcije (*eng. Response Amplitude Operator,* RAO). Pomoću rješenja nižeg reda točnosti, kritični slučajevi opterećenja su identificirani i nadalje analizirani u simulacijama višeg reda točnosti koristeći proračunate projektne valove (*eng. Equivalent Design Wave,* EDW) za pojedine razine vjerojatnosti. Ovakav pristup uvelike smanjuje potreban broj nelinearnih simulacija i trenutno predstavlja jedini mogući pristup uzimajući u obzir granice računalnih resursa. Čak i kada su nelinearne simulacije svedene na minimum, provedba jedne simulacije međudjelovanja fluida i konstrukcije spregom CFD-FEM rezultira značajnim poteškoćama tijekom proračuna.

Izbor prikladnog načina međudjelovanja je temeljen na samoj prirodi odziva konstrukcije koji je uobičajeno podijeljen na dvije kategorije: statički i dinamički. U literaturi postoji određeni nesporazum vezano za navedenu podjelu koji je vezan za činjenicu da su i statički i dinamički odziv izazvan od vremenski ovisnih okolišnih opterećenja. Međutim, temeljna razlika između statičkog i dinamičkog odziva konstrukcije je u tome što statički odziv ne uzima u obzir gibanje konstrukcije. Važno je spomenuti da su različite varijante statičkog i dinamičkog odziva često upotrebljavane, a glase kvazi-statički i kvazi-dinamički, gdje se riječ „kvazi" odnosi na opterećenje konstrukcije koje je neovisno o njenom odzivu. U isto vrijeme, termini jednosmjerna i dvosmjerna sprega su korišteni i razlika između ova dva pristupa je često nejasna. Statički ili kvazi-statički se često uzima kao jednosmjerna sprega, dok su dinamički ili kvazi-dinamički klasificirani kao dvosmjerna sprega. Ovakva podjela nije ispravna i odvajanje termina je vezano za ovisnost odziva konstrukcije i njenog opterećenja te u jednosmjernoj sprezi navedena ovisnost ne postoji, dok je u dvosmjernoj ovisnost uzeta u obzir. I statički i dinamički pristup mogu pripadati jednosmjernoj ili dvosmjernoj sprezi ovisno o pretpostavkama s obzirom na linearnost odziva konstrukcije tj. male

ili velike deformacije. Konačno, ovisno o periodu opterećenja i prirodnom periodu konstrukcije, u brodograđevnoj praksi upotrebljavaju se ili kvazi-statički ili dinamički tj. hidroelastični pristup.

Metode

U ovom radu razvijena je numerička metoda za direktni proračun pri projektiranju brodskih privjesaka. Metoda je ilustrirana na slučaju uređaja za uštedu energije naziva pred-vrtložni stator (*eng. Pre-Swirl Stator,* PSS) koji je pozicioniran ispred ravnine brodskog vijka. Cilj ovog uređaja je smanjenje rotacijskih gubitaka uvođenjem dodatne rotacijske komponente brzine na ulaznu ravninu brodskog vijka. U svrhu modeliranja strujanja u blizini PSS-a, moderne računalne metode su korištene te su razvijeni različiti FEM-CFD modeli za simuliranje međudjelovanja fluida i konstrukcije. CFD simulacije su validirane i verificirane s eksperimentalnim podacima u slučaju polja sustrujanja i pokusa slobodne vožnje. Jednostavniji idealizirani modeli propulzije su prikazani i uspoređeni s eksperimentom ovisno o dostupnosti podataka. Odziv konstrukcije pred-vrtložnog statora je istražen u mirnoj vodi koristeći CFD simulacije slobodne vožnje s direktnim modeliranjem rotacije brodskog vijka. U svrhu procjene vijeka trajanja konstrukcije PSS-a, jedan od ciljeva rada je razvoj postupka određivanja projektnog vala što obuhvaća definiranje dominantnog parametra opterećenja te određivanje prikladnog pristupa modeliranja međudjelovanja konstrukcije i fluida. Nadalje, CFD-FEM sprega je implementirana za kvazi-statičku i hidroelastičnu analizu. Rad je podijeljen na šest članaka od kojih svaki predstavlja određeni doprinos za konačnu definiciju numeričke metode za analizu odziva brodskih privjesaka. Istraživanja temeljem kojih je nastao ovaj doktorski rad vezana su za Uspostavni istraživački projekt „Zeleni modularni putnički brod za Mediteran" (UIP-2017-05-1253), koji je financirala Hrvatska zaklada za znanost.

Validacija i verifikacija hidrodinamičkih alata je prvi korak detaljnije analize odziva konstrukcije pri CFD-FEM sprezi. U prvom radu prikazana je usporedba rezultata otpora broda i polja sustrujanja s eksperimentalnim rezultatima. Detalji strujanja su uspoređeni s PIV mjerenjima u blizini brodskog vijka. Također, korišten je i verificiran jednostavniji model propulzije idealiziranog diska s dobrim slaganjima s eksperimentom. U ovom radu prikazane su temeljne

postavke CFD simulacija i matematičkog modela pomoću kojih je točnost proračuna zadovoljavajuća. Rezultati su prikazani na dva različita modela broda.

Nadalje, vezano za strukturni model PSS-a, u drugom radu je provedena dinamička analiza konstrukcije koristeći FEM alat te su prirodni periodi konstrukcije uspoređeni s očekivanim vanjskim periodom opterećenja. Omjeri ovih perioda su temelj pri određivanju prikladnog pristupa modeliranja međudjelovanja fluida i konstrukcije. Važno je naglasiti kako u slučaju plutajućih objekata, relevantna frekvencija konstrukcije je mokra frekvencija zbog utjecaja dodane mase. Dva različita software-a su korištena za proračun dodane mase tj. mokre frekvencije te su dobivena dobra podudaranja. Vanjska opterećenja koja su uzeta u obzir su vibracije uzrokovane vrtloženjem fluida te vibracije uzrokovane radom brodskog vijka. U radu je zaključeno kako ne postoji mogućnost rezonancije s prirodnim periodom konstrukcije.

Za potrebe CFD-FEM sprege, kvazi-statički pristup je razvijen u trećem radu gdje je temeljni problem interpolacija hidrodinamičkog tlaka s mreže fluida na mrežu konstrukcije preko 2D dijeljenje površine. Metoda koja je validirana i prezentirana u ovome radu temelji se na metodi projekcije integracijskih točaka konstrukcije na mrežu fluida. Pažljiva i detaljna interpolacijska metoda razvijena u radu omogućava očitavanje vrijednosti tlaka u projiciranim točkama s visokom točnošću, ali u isto vrijeme zadržavajući maksimalne vrijednosti dobivene u hidrodinamičkom rješavaču. Validacija metode provedena je na dva fundamentalno različita slučaja s zadovoljavajućim rezultatima.

U četvrtom radu provedena je analiza odziva konstrukcije pred-vrtložnog statora na mirnoj vodi te je analiziran utjecaj modela strujanja na odziv na valovima. Tri modela strujanja su analizirana: bez brodskog vijka, s idealiziranim diskom i s brodskim vijkom. Na mirnoj vodi je zaključeno kako idealizirani disk dostatno modelira aksijalna opterećenja na konstrukciju. Kako je za potrebe zamora materijala potrebna amplituda uzrokovana rotacijom krila vijka, modeliranje vijka je obvezno. Međutim, na valovima, utjecaj propulzije je zanemariv na naprezanja u konstrukciji gdje gibanje broda ima ključnu ulogu. Zaključeno je kako u simulacijama na valovima, modeliranje i utjecaj brodskog vijka nisu potrebni.

Iako je u prijašnjom analizom pokazano kako svi navedeni slučajevi opterećenja spadaju u područje kvazi-statičke sprege, za potrebe detaljne analize, u petom radu je razvijen hidroelastični model kako bi se dinamički utjecaji na odziv direktno kvantificirali. Model je verificiran na pred-

vrtložnom statoru i jednostavnim narinutim impulsnim ili konstantnim opterećenjima. U realističnim uvjetima opterećenja na mirnoj vodi s brodskog vijka, izračunati su umjereni hidroelastični učinci na konstrukciju koji zbog kompleksnosti provođenja ovakvih simulacija mogu biti zanemareni. U slučaju valnih opterećenja, dinamički i kvazi-statički odziv je jednak zbog velike razlike valnog perioda i prirodnog perioda konstrukcije.

Posljednji rad objedinjuje sve zaključke iz prijašnjih članaka te prikazuje cjelovitu numeričku metodu za analizu odziva konstrukcije brodskog privjeska pred-vrtložnog statora. Definiran je dominantni parametar opterećenja te su rezultati uspoređeni s linearnim potencijalnim rješenjem čime se opravdava vjerodostojnost kompletne metode. Iz statističke analize dobiveni su projektni valovi za različite razine vjerojatnosti te su provedeni nelinearni proračuni CFD-FEM sprege na tim valovima. Iz amplituda naprezanja procijenjen je životni vijek konstrukcije koji u slučaju pred-vrtložnog statora zadovoljava projektni standard od 25 godina.

Cilj i hipoteza

Glavni je cilj ovog rada je razvoj numeričke metode za analizu odziva konstrukcije brodskih privjesaka i razvoj programske podrške za spregu hidrodinamičkog i konstrukcijskog rješavača. Primjena na brodske privjese zahtjeva sljedeće: definiciju parametra opterećenja, metodu procjene maksimalnih opterećenja pomoću matematičkih modela nižeg reda točnosti i nelinearnih simulacija odabranih projektnih valova iz kritičnih slučajeva statističke analize. Također, potrebno je razviti matematički model koji će dovesti do veće razine točnosti između hidrodinamičkog i konstrukcijskog modela. Navedeno podrazumijeva razvijanje sveobuhvatnog modela međudjelovanja konstrukcije i fluida za sve slučajeve opterećenja.

Hipoteza istraživanja je da je moguće razviti numeričku metodu za analizu odziva konstrukcije brodskih privjesaka koja uključuje maksimalna valna opterećenja kojima je brod izložen tijekom svog životnog ciklusa, stoga definicija i verifikacija koraka u numeričkoj metodi koristeći različite matematičke modele može prikazati maksimalna opterećenja ispravno uzeta u obzir. Nadalje, u drugom dijelu, hipoteza je da je moguće razviti matematički model za spregu računalne dinamike fluida i metode konačnih elemenata primjenjiv na brodske privjeske. Uspješna primjena i validacija razvijenog modela međudjelovanja fluida i konstrukcije na pred-vrtložnom statoru dokazuje navedenu hipotezu.

Znanstveni doprinos

Jedan od doprinosa ovog rada vezan je uz definiciju numeričke metode za analizu odziva konstrukcije brodskih privjesaka preko detaljne analize nailaznih stanja mora tijekom životnog vijeka konstrukcije. Na primjeru pred-vrtložnog statora je prikazana primjena razvijene metode kroz definiciju dominantnog parametra opterećenja i metode za određivanje maksimalnih vrijednosti na kojima su utemeljeni projektni valovi. Drugi dio je vezan za međudjelovanje fluida i konstrukcije koristeći CFD i FEM numeričke modele gdje je prikazana sveobuhvatna analiza odgovarajućih pristupa te su implementirani i verificirani kvazi-statički i hidroelastični pristup.

Ova dva djela zajedno tvore temelj za evaluaciju strukturnog integriteta brodskih privjesaka što je u ovom slučaju prikazano na primjeru uređaja za uštedu energije. U ovom radu, opisana je efikasna metoda s detaljnim pojašnjenjima za svaki korak pri analizi odziva konstrukcije na mirnoj vodi i na valovima.

Ključne riječi

Numerički model, Računalna dinamika fluida, Metoda konačnih elemenata, Sprega konstrukcije i fluida, Kvazi-statični odziv, Hidroelastični odziv, Pred-vrtložni stator, Projektni val.

Abbreviations

CFD	Computational Fluid Dynamics
FEM	Finite Element Method
EDW	Equivalent Design Wave
PSS	Pre-Swirl Stator
FV	Finite Volume
DLP	Dominant Loading Parameter
GFM	Ghost Fluid Method
BEM	Boundary Element Method
DAF	Dynamic Amplification Factor

List of Figures

Contents

1 Introduction

Modelling and estimation of hydrodynamic loads and stresses necessary for the design of floating structures has been an active area of research for decades. Over the years and following the improvements of computational power and numerical models, the ship design practices have formed two fundamental courses: rule-based and direct approach design. The rule-based design is composed as a set of formulas originating from the variety of experience-based and empirically deduced parameters from measurements on full-scale ships in service or model experiments. This type of design principles has been the leading route in the design of ships and floating structures for a long time. Despite the quite high safety margin of vessels based on such regulations, the growing need for a lighter and optimized structural design has greatly enhanced the maturity of the direct approach in recent years. This progress is especially aided by the state-of-the-art numerical models and accessibility to the steadily and continuously advancing computer hardware.

When contemplating the necessary complexity in the direct calculation approach there are two key unknowns which need addressing: definition of the load cases and choice of hydro-structural coupling regime. Each of the two objectives have a fundamentally different way of modelling and quantification. Definition of the load cases presumes the knowledge of the structure surrounding during its design life. For floating objects, this usually equates to studying of the wave environment. Given the enormous amount of the probable wave directions and wavelengths, stochastic methods are essential for the evaluation of the encountered sea-states in the estimated floating structure design life. Description of the sea-states as wave spectrums aids to the simplicity of the broader statistical analysis [1]. Depending on the structure or position of the structural element, additional necessary load cases may vary (e.g. propeller excitation). After the load cases are defined whether in calm-water or in waves, the selection of proper hydro-structural coupling regime and the choice of the mathematical models for each side of the interaction is required.

In case of ship appendages, both solvers are highly dependent on the type of the ship appendage analysed. Regarding the structural model, the Finite Element Method (FEM) is almost exclusively used in the shipbuilding industry with a very large validated and verified amount of test cases. When computing the fluid loads, if the structural segment is located near the propeller

plane, such as Energy Saving Devices (ESDs), where the non-linearity, viscosity and turbulence is high, Computational Fluid Dynamics (CFD) needs to be employed for the satisfying level of accuracy. Nevertheless, the high order solution obtained by CFD comes at an expensive CPU cost and time which cannot be overlooked. From a direct approach design perspective, this type of calculations would be impossible concerning all the contributing sea-states. For this reason, a more efficient approach is compulsory for the numerical simulation method to become practical. This is achieved by developing the sea-state statistical analysis using the simpler fluid models i.e. linear potential flow discretised with Boundary Element Method (BEM) which allows the solution to be exported in the frequency domain as the Response Amplitude Operators (RAOs). Through lower order solutions, critical cases can be identified and they lead to the definition of Equivalent Design Waves (EDWs) per each probability level. This drastically reduces the number of high-fidelity simulations and seems to be the only sensible way to do it given the current computational power limitations. Even as the non-linear simulations are reduced to a minimum, the single hydro-structure or CFD-FEM coupling represents a significant numerical modelling issue.

Choice of the suitable hydro-structural model is governed by the nature of the structural response which is usually divided into two main categories: static and dynamic. There is sometimes a certain misunderstanding observed in the literature regarding this separation. The misunderstanding occurs mainly because both the static and the dynamic structural responses are induced by the time varying (i.e. dynamic) environmental loading. However, the fundamental difference in between the static and dynamic structural response lies in the fact that the static response does not account for the structural dynamics (vibrations) while the dynamic response does. It is also worth mentioning that the different variants of the static and dynamic responses are sometimes introduced and are called quasi-static and quasi-dynamic, where the wording "quasi" is related to the structural loading which is considered to be independent of the structural response (in "quasi -***" approach). At the same time, from the numerical modelling point of view, very often the denomination one-way or two-way coupling procedure are used and the clear separation in between the two procedures is also sometimes confusing. Indeed, quite often, the static (or quasi static) approach for the evaluation of the structural responses is classified as the one-way coupling approach and the dynamic (or quasi dynamic) is classified as the two-way coupling approach. This is however not true, and the separation should be related to the fact that for one-way coupling approach the loading does not depends on the response while for two way coupling approach it

does. This means in particular that both the static and the dynamic responses can belong to either one or two-way coupling procedures, depending on the assumptions made regarding the linearity of the structural behaviour (small or large deformations). Overall, depending on the excitation and the structural natural period, either the quasi-static or dynamic (hydroelastic) approach is applied for floating structures.

In this work, the numerical simulation framework for direct approach design of the ship appendage is presented. The approach is illustrated on the case of the ESD placed in front of the propeller called the Pre-Swirl Stator (PSS). This device aims to recover the rotational losses by introducing an additional rotative velocity component on the propeller blades inflow. For this cause, state-of-the-art computational tools are used and hydro-structural CFD-FEM models are developed. CFD computations for the wake field and self-propulsion are thoroughly verified and validated with the experimental results. Simpler idealised disk approaches are presented and the self-propulsion results are compared to experiment where available. PSS structural response is investigated in calm-water with the propeller loads evaluated directly through CFD self-propulsion simulation including the propeller rotation. Regarding the direct design approach in the light of the PSS design life, the aim of the work is focused on the definition of EDW design method applicable to the PSS design. This assumes definition of the relevant Dominant Loading Parameter (DLP) for the PSS and setup of the appropriate simulation condition for the hydro-structure analysis. Furthermore, the CFD-FEM interaction is implemented for quasi-static and dynamic analysis. Quasi-static implementation is based on the projection method and the thorough verification and validation is given. Dynamic approach is based on the modal superposition method and applied to the PSS with necessary verification. Comparison with the quasi-static approach is presented complying with the theoretical background. This thesis has been funded by the Croatian Science Foundation under the project Green Modular Passenger Vessel for Mediterranean (GRiMM), (Project No. UIP-2017-05-1253).

1.1 Previous and related studies

Numerical simulations involving high level of accuracy still pose a challenging task for the evaluation of the structural response especially when the interaction of two fundamentally different mathematical models is necessary. In-depth understanding of both models and their capabilities is

a prerequisite for the accurate and efficient implementation of their intercommunication. Numerical CFD simulations solving Reynolds Averaged Navier Stokes (RANS) equations have remarkably matured in the recent years with the accuracy, reliability and accessibility incrementally improving each year.

1.1.1 Hydrodynamic CFD simulations

Foundation of the CFD hydrodynamic validation lies in the openly available experimental results [2]–[4] and most of the new numerical models usually are tuned according to the model basin data. In the CFD framework, governing equations (continuity and momentum) discretisation is most frequently performed by the FV method. As far as CFD Workshop 2010 [5], only one-fifth of the participants presented their results based on finite difference discretisation. Part of this reasoning is due to the ease of implementation and geometrical discretisation of various shapes. Although FV discretisation is second order accurate [6], for engineering purposes this is satisfactory.

For naval application, the free-surface handling features an important subject in the CFD ship hydrodynamics. Jump conditions on the interface impose a serious numerical limitation which requires treatment to reduce the smearing of the physically sharp profile. Common method for the interface modelling is the Volume-of-Fluid (VOF) [7] where the scalar field obtains the value of 0 in air and 1 in water. To supress the smearing of the VOF model a compressive term is introduced [8]. However, this model still needed additional improvement which is introduced through Ghost Fluid Method (GFM) [9]–[11]. Vukčević et al. [12] presented a VOF implementation and GFM specifically for ship hydrodynamics. Slightly different approach to sharp interface called the geometric VOF is presented in [13] which alleviates the mass conservation issues. Other methods of interface capturing besides VOF, include the Level Set (LS) method [14] based on signed distance function or Phase Field (PF) [15] which uses a hyperbolic tangent function. These methods have also been successfully applied to ship hydrodynamics in [16], [17] following the theoretical background in [18]. It is worth mentioning that all the CFD software has some type of free-surface treatment to preserve the sharp profile when solving the ship hydrodynamic problems.

Numerous authors contributed to the validation of the CFD code in ship resistance and wake field study [19], [20]. Ozdemir et al. [16] obtained sufficiently correct results with the k-ε turbulence model [22], but showed a necessity to use a second order discretisation on advection

for improved wake results. Also, two equation turbulence model is preferred [23] with very good agreement using the *k-ω* SST model [24] at the propeller vicinity [25], [26]. However, quality of the wake field solution is only a prerequisite for the correct self-propulsion simulations.

Due to the high CPU cost and complexity of the direct propeller simulations, often a simplified or less expensive model is sought to circumvent the full CFD propeller rotation. Jasak et al. [27] computed the thrust parameters with the actuator disk model placed on the mesh faces at the propeller plane. This model introduces the pressure and velocity jump conditions on those faces and is much easier to implement than the volumetric source in a body force model [28]. Trodlborg et al. [29] presented an improvement of the usual volumetric actuator disk model in order to remove the numerical instabilities. Multi Reference Frame (MRF) is another version of the steady state propeller solution which requires the propeller geometry but does not include the rotation. Wu et al. [30] simulated the underwater vehicle during manoeuvring using MRF with good agreement. Novel approach for solving the non-linear periodic flows inside CFD is by Harmonic Balance (HB) method [31] where the variable decomposition is performed using the Fourier series. If the rotation of the propeller is mandatory for the simulation, RANS-BEM coupling offers a decent CPU advantage capturing most of the unsteady forces phenomena when compared to full RANS propeller rotation. Hally et al. [32] presented a RANS-BEM coupling where the blade blockage effect is introduced as a mass source term in the governing equations. Rijpkema et al. [33] presented a body force interpolation from BEM propeller solution where the effective wake is computed in an iterative manner. Krasilnikov [34] imported the BEM propeller forces to the actuator disk region inside the CFD domain. This approach is justified since the majority of the propeller flow is governed by the pressure forces on the blades.

On the contrary, if the direct propeller simulation in CFD is compulsory, there are two widespread types of modelling and both require the addition of the rotative mesh region inside the surrounding hull mesh. First type is the sliding mesh technique where the rotative and surrounding mesh have a strictly geometrically binding interface. Mesh faces at this connecting interface do not need to conform exactly, yet the averaging of the flow variables is performed through careful spatial consideration. General Grid Interface (GGI) implementation and algorithm is described in detail by Beaudoin and Jasak [35]. Regarding the application of sliding mesh to ship propeller flows, numerous authors validated and verified the method reliability. Yilmaz et al. [36]

successfully applied the sliding mesh technique for the study of propeller cavitation. Nouroozi and Zeraatgar [37] employed the sliding mesh for the surface piercing propeller. Yao et al. [38] studied the propeller parameters and forces in oblique flow with the sliding mesh with good results. Although the sliding mesh approach is quite robust, there are certain deficiencies of the model. In some cases, the placement of the rotative region is not easy to establish due to rudder location, ship stern shape or ship appendages near the propeller. As an alternative, the overset mesh approach offers a much wider range of flexibility without any limitations on the body motion, mesh deformation or region intersection issues. The method is based on two or more mutually intersecting mesh regions on which boundary cells are computed. It is on these boundary cells where the interpolation of flow variables is performed. Over the years, the method has matured and is often more preferred than the sliding mesh due to ease of the simulation setup. Shen et al. [39] computed accurate results in self-propulsion and manoeuvring simulation with the overset mesh. Also on manoeuvring, Mofidi and Carrica [40] managed to obtain sufficiently correct results compared to experiment. Other works related to application of overset can be found in [41]–[43].

This work utilizes the GFM based approach for the sharp interface resolution between the two immiscible fluids. Propeller simulations are performed with the sliding mesh technique and with the simple actuator disk implementation also comparing the results of the two approaches on the PSS structural response.

1.1.2 Energy saving devices

Simulation of ESDs has come to prominence due to the environmental concerns on the greenhouse gas emissions which initiated the new IMO regulations concerning ship efficiency. The ESDs are divided into three section according to the classification in [44] as shown in Figure 1. Their proximity to the propeller, complex flow field of operation under the influence of ship motions, wake field and blade rotation requires, for forces and loads to be accurately predicted, the highest order of numerical accuracy which can be achieved only with CFD.
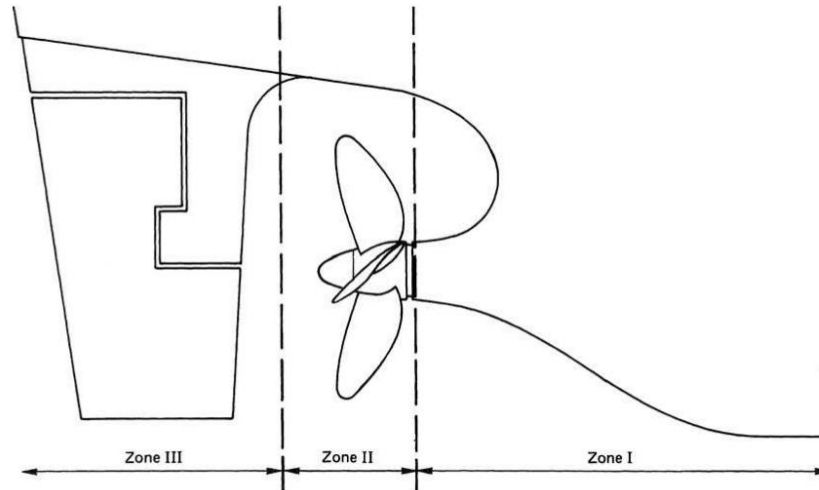
Figure 1 – ESD classification by position [44]

There is a large number of published works related to the CFD and ESDs. In Zone I, the devices aim to alter the flow in the manner to reduce the axial or rotational kinetic losses in the propeller slipstream. One of the first ESDs is dedicated to the reduction of axial losses and is designed as a duct modifying the inflow velocity for the propeller plane. Duct has been thoroughly tested and verified using CFD [45]–[47] and also compared well with the experimental data [48]. In the case of rotational losses in the flow, the PSS appendage can reduce the magnitude of transversal velocities in the propeller wake, thus contributing directly to the propeller efficiency. Furcas and Gaggero [49] developed a genetic algorithm on RANS-BEM coupling until optimal design is found, and performed full RANS simulation with the estimated savings ranging above 5%. Koushan et al. [50] validated a PSS design made by CFD with model basin data and reported sufficiently accurate results with the k-ω SST model. However, more often in the literature, a combination of duct and PSS device is present, such as a commercially available device in [51]. Kim et al. [52] developed a PSS and PSS with duct appendage using CFD with reported savings in the region of 3% to 6%. Dang et al. [53] presented the experimental results for the duct and PSS, finding the latter much less sensitive to scale effects with the "smart ship model" mimicking the full-scale wake. Investigation is further extended in [54] where the authors state that the local forces on ESD alone are internal forces of the propulsion systems and that the shape should not be optimized with the ESD alone as it is often found in the literature, but for the interaction with both the propeller and hull.

In Zone II, the devices are placed either near the propeller plane and the classification also includes the unconventional modifications at the propeller geometry. The goal is to mainly minimize the rotational losses, the appearance of cavitation or wing tip vortices. Regarding non-standard propeller design, mostly under development are the Contracted and Loaded Tip (CLT) propellers, where the end plate is formed as a part of the geometry substantially lowering the loads on the tip, and Contra-Rotating Propellers (CRPs). Very detailed work for CLT propellers can be found in [55], [56] with scale effects assessed in [57], while the CRP CFD investigation is given in [58]. Also, the Propeller Boss Cap Fins (PBCF) are deemed reliable for 1-2% of savings in delivered power [59], [60]. For the ESDs in Zone III, the unconventional rudder designs are rapidly developed, Z-twisted rudder [61], X-twisted rudder [62], rudder bulb and fin [63], wavy-rudder [64] or twin rudder system [65], and there has been moderate progress with the design of turbines extracting the rotational flow in the slipstream [66], [67].

Following the references in the ESD design, it can be outlined that the CFD as a numerical tool has played a vital role in the evolution, improvement and usability of modern thrust augmented devices. Usually, a simpler flow model is employed for the design, but the inevitable trial and error of such designs, as well as additional fine tuning, is made possible in the reasonable amount of time only by CFD results. However, the structural problems know for some of the ESDs such as PSS have been rarely investigated and their structural integrity is not accomplished with certainty. This gap in the literature and in the scientific community initiated a joint research project Green Retrofitting through Improved Propulsion (GRIP) [68] where the sea-trials have been performed, optimized PSS shape is tested and the structural dynamics are studied through evaluation of the natural structural frequencies and excitation frequencies. Furthermore, Paboeuf and Cassez [69] in the scope of the same project developed a design procedure for the approximation of the wave loads for the ship design life and included the dynamic analysis of the structure compared to Vortex Induced Vibration (VIV) and propeller excitation. Lee et al. [70] first studied a 2-D section of the PSS in regular and irregular motion concluding the regular motion is sufficient to capture the peak velocity since the vertical velocity is higher. The authors further elaborated on the method based on the neural network trained on CFD results to reduce the costly viscous simulations. To further generalize the method, Ju et al. [71] proposed a regression method to consider variable PSS shape, ship speed and direction producing a simplified formula for the early levels of PSS design. Report on PSS loads in waves is done by Wang et al. [72] where BEM loads were estimated as higher,

thus yielding a more conservative structural stress solution. In the similar manner, Tsou et al. [73] estimated fatigue of the PSS, but without any EDW procedure for the wave load cases.

In the mentioned PSS structural studies [68]–[73], the transfer of fluid loadings to the structural mesh is either performed in a simplified manner or it remains unclear how the hydro-structural interaction is considered. This part is crucial for the assessment of the PSS structural response because the equal amount of lift (vertical) force on the PSS can have a different pressure distribution, hence producing a significantly different structural response. For this reason, the current work is dedicated to the determination of the appropriate hydro-structural regime as well as careful and detailed description of how the loading is transferred.

1.1.3 Hydro-structural coupling

As previously mentioned in Sec. 1, either the quasi-static or the dynamic response are relevant for the floating structures. The quasi-static response assumes the independence of the forcing term on the structural motion and the stiffness matrix is assumed constant throughout the computation without any time dependency between the structural solutions. The dynamic approach considers the influence of the structural motion on the fluid load with the vibrations (structural inertia) included. The two approaches are usually referred to as the one-way or two-way coupling in the literature, despite these terms giving limited information regarding the hydro-structural model.

Modern developments in the field of hydro-structural coupling followed by the improvements in the numerical models, lead to the coupling of the fluid 3-D BEM and structural 3-D FEM models [74], [75]. The progress is initiated by the hydroelasticity effects in ultra large container ships and further developments included sophisticated structural 1-D beam models suitable for the preliminary design computations [76]–[78]. Recently, the predominant direction in the hydro-structural field of research is the CFD-FEM coupling as the CFD computational framework for naval hydrodynamics has increasingly gained reliability with the invaluable fully non-linear fluid solution. However, irrelevant of the mathematical complexity of the numerical models, all the coupling tools are still theoretically divided into quasi-static and dynamic approaches depending on the excitation and structural natural frequency.

In the quasi-static coupling approach, the structural and hydrodynamical solvers can be run independently of each other when the excitation period is much higher than the natural structural period. The fluid solution can simply be exported to the structural model and selected time-steps can be imported to the structural solver for a set of linear static analysis. The main problem is deduced to the consistent transfer of the pressure loads between the partially overlapping meshes, fluid and structural wetted elements. The quality of the transfer is reliant on the interpolation method. Radial Basis Function (RBF) is often employed due to its ease of implementation and robustness [79], [80]. For greatest accuracy, the method requires the global RBF matrix construction and the process is repeated for each change of the field values. This can lead to costly matrix construction and updates on a large full matrix which can carry a considerable CPU expense. To alleviate these problems, a projection method is developed. Malenica and Tuitman [81] implemented a geometrical algorithm between the FEM and BEM mesh by projecting panel centres, proving the algorithm to be very robust and stable. Instead of projecting the panel points, Ji et al. [82] projected the entire FEM panel on the hydrodynamical mesh calculating the resulting pressure as the contribution from each element which overlaps with the projected FEM panel. If there are differences between the total forces and moments between meshes, the optimizing algorithm removes it artificially. Wang et al. [83] proposed an improvement to the standard projection algorithm when the fluid mesh is significantly finer than the structural mesh. De Boer [84] gave a broad range of mathematical formulations together with the detailed tests of the results depending on the mesh densities and error examination with regard to the method used. Piro and Maki [85] presented a projection algorithm where the structural integration points are projected. Fluid pressure at the structural point is computed as the average of the nearest element fluid centres which inevitably leads to the lowering of the possible pressure peak value. Use of structural integration points as projection points is also found in [86]–[88] where the consistent load transfer is a prerequisite for the dynamic coupling computation.

In case when the excitation and natural structural frequencies are close, the dynamic or hydroelastic approach is necessary. The standard form of CFD-FEM coupling procedure adopts the intercommunication between the solvers as obligatory. First, the structural mode shapes are computed and stored in the FEM framework. Second, the fluid flow solution is initiated where the iteration between the solvers is necessary at every time-step. FEM modal solution enables fast structural computations with the nodal displacements exported to the CFD which affect the fluid

pressure loads. This process is repeated until the solution on the CFD-FEM interface converges. Pernod et al. [89] studied the CFD-FEM coupling for flexible hydrofoil with good correlation between numerical and experimental results as well as Huang et al. [90], who accurately computed the wet frequencies on the hydrofoil with CFD-FEM. Application has also been successful on the ship structures as shown in [91] where comparison with experiment also yielded sufficient results. El Moctar et al. [92] examined the vibrations and forces on ship section depending on the different definition of the irregular wave with the experiment and suggested trends of a vertical mid-ship moment well captured. Overall, slamming and whipping are commonly investigated with the CFD-FEM framework [93], [94]. For the flexible barge experiment, Lakshmynarayanana and Temarel [95] also successfully employed the intercommunicating FEM-CFD framework per time-step. Iterative FEM-CFD approach is justified when the non-linear structural response is considered, but when the linear structural response is sought, the structural mode shapes can be imposed directly in the hydrodynamical framework, thus removing the CPU expensive need for the solver mutual communication during the fluid simulation. Tuitman et al. [96] used a time-domain BEM computation with non-linear rigid body motions coupled with the mode shapes extracted from the structural mesh with good comparison of numerical data and measurements. Regarding CFD-FEM and using generalized modes, Seng et al. [23] validated the CFD flow solution using modal projection method with the experimental data for the flexible barge. The mode shapes are interpolated using radial basis functions on the hydrodynamical mesh and the dynamic equation is solved inside the CFD framework. This approach depends upon the structural model only in the pre-processing stage for dry mode-shape computation.

The current study implements both types of the hydro-structural coupling regimes relevant for floating and submerged structures, quasi-static and dynamic. Quasi-static approach follows the projection method implementation in the CFD-FEM framework with the consistent pressure transfer and detailed description of the procedure. Same type of interpolation is used when developing the modal superposition based dynamic approach in the step of transferring the pre-computed structural mode shapes (vector of nodal displacements) to the fluid mesh. Dynamic model is implemented inside the CFD framework, thus achieving high CPU efficiency.

1.1.4 Equivalent Design Wave approach

The main difficulty when developing the method for structural design of ships and ship appendices is related to the fact that the whole ship design life (25 years) needs to be considered. When assessing the structural integrity of any floating object, whose excitation is governed by the waves, the wave loads are described through stochastic procedures. Since any statistical approach requires a vast number of data points, these are always computed with fast and efficient linear potential theory compared to costly CFD calculations. Jensen [97] defined the procedure and set the foundation for the stochastic method. The procedure is illustrated on the Vertical Bending Moment (VBM) as the indicator variable (or otherwise called the DLP) for the design of ship hull structures. The aim is to define a representative EDW based on the maximizing of the indicator in order to reduce the CFD calculations to a single or multiple wave simulation depending on the number of necessary probability levels. Additionally, Jensen [98] presented a first order reliability method on the prediction of the ship roll motions with a simplified hydrodynamic model. Application to flexible ships is proposed in [99].

Mathematical description of the EDW strongly affects the long-term stress distribution and is studied as a separate subject. Hauteclocque et al. [100] presented a broad study of different EDWs and their mutual comparison. Authors suggest that Response Conditioned Wave (RCW) should be used whenever it is possible since it includes more real-life physics than a regular wave. Furthermore, Hauteclocque et al. [101] studied the non-linearity effects in the VBM and concluded that the spreading effect on the results is less than 6% with the suggestion of utilizing irregular wave whenever possible. In both studies, the authors employed a BEM linear potential fluid solver which makes it straightforward to enable the accurate RCW profile. To clarify, the RCW includes the parameters of the selected sea-state and is composed of various wave frequencies. By definition, it requires an exact wave profile on the ship hull when interacting with the incoming irregular wave. Although linear potential methods make this profile matching feasible, the employment of non-linear fluid models such as CFD for the RCW is far from easy. Quentin et al. [102] compared different EDWs and concluded that the difference in the results between regular wave and RCW is not significant, however, the authors suggest using the RCW since the computational expense is similar for both models, but the RCW comprises of the sea-state wave parameters. This negligible CPU cost is true only for the linear BEM potential flow. To investigate the behaviour of different EDW using CFD, Gatin et al. [16] calculated the loading exerted on the

break water of a container ship. Relative elevation on the ship fore is set as DLP and due to its linearity, the statistical analysis can be performed in the frequency domain which significantly eases the computation. This is actually the standard in direct approach design for the development of the ship design life evaluation of wave loads. Providing a full CFD solution for the ship life cycle is not possible given the enormous CPU expense for the computations. Simpler potential linear models are employed to analyse a vast amount of possible sea-state data and ship directions to estimate the critical conditions on which non-linear simulations are performed. This is the only practical way to reach realistic wave load and structural response.

Another important aspect for the evaluation of the EDW is the modelling of the wave environment, especially in the non-linear CFD domain. Vukčević et al. [103] validated and verified the two-phase flow with the GFM sharp interface treatment coupled method with the water wave mathematical methods. For higher order wave models, work in [104] presented a high order spectral method inside the CFD framework with the two-phase fluid. With respect to ship motions, wave loads and added resistance, the CFD wave models have been extensively validated and verified in the literature. Carrica et al. [105] presented a good agreement with the experimental data for ship in head waves with similar work in [106]. Added resistance and motions are studied in [107], [108] while seakeeping analysis can be found in [109]–[111]. Overall, the CFD framework is shown to be reliable and accurate for the analysis of the important ship parameters in waves.

In this work, an EDW approach is developed for the application to the ship appendage of PSS with the relevant DLP maximized. The ship design life is considered and appropriate wave load cases are deduced from the simpler potential flow analysis. Since the irregular RCW design wave is far from maturity for CFD analysis a regular design wave is employed. Wave simulations are safely performed in the CFD fluid domain given the large amount of validated and verified results concerning ship motions in waves.

1.2 Objective and hypotheses of the research

The primary objective of this research is to develop a numerical procedure for the structural evaluation of ship appendices and the computational tool for the coupling of hydrodynamic and structural solvers. The application to ship appendage requires following: the definition of the

relevant DLP for the observed structure, method to maximize these loads in the lower-order mathematical model leading to EDWs and performing higher order simulations on the defined EDWs from the critical conditions highlighted by the statistical analysis. Also, it is required to develop a mathematical model which will lead to a more accurate balancing between the structural and hydrodynamic model. This suggests the development of the clear and comprehensive hydro-structural model covering the possible load cases with the accurate and robust implementation.

Hypotheses of the research are that it is possible to develop a numerical method for ship appendices which includes maximum wave loads to which the ship is exposed during the entire life cycle, hence a definition and verification of the steps in the numerical method using different mathematical models can show the maximized loads correctly considered. Additionally, for the second part, the research states that it is possible to develop a mathematical model for the coupling of computational fluid dynamics and finite element method which is applicable to ship appendices. The development, validation and implementation of the hydro-structural model to the PSS structure can show the interaction regime as successfully utilized.

1.3 Scientific contribution

The presented work contributes to two separate research fields. First is the definition of the numerical method for the evaluation of the structural response of ship appendices. This is elaborated through detailed life cycle analysis of the possible sea-state encounters which is illustrated on the ship appendage of PSS. The definition of the DLP and the process for finding the maximum probable values underlying the EDW determination is included in the method description. Second part is related to the hydro-structural coupling of the CFD and FEM numerical models where a comprehensive evaluation of the appropriate FEM-CFD regime is given and both approaches, quasi-static and dynamic, are implemented and verified.

These two parts together constitute the basis for the evaluation of the ship appendage structural integrity which in this case is an ESD appendage of PSS. The efficient and straightforward framework is described in this work with details given for each step of the structural analysis, whether in calm-water or in waves.

2 Discussion

The key findings of this thesis are presented briefly in the following section step by step. The current work comprises of multiple journal articles which together form the necessary framework for the accomplishment of the thesis objectives. Contribution of each article is elaborated and their relevance for the realization of the research aim is highlighted. The importance of each article is given as follows:

1. Validation and verification of utilized CFD framework for the ship wake flow and self-propulsion simulations (ARTICLE 1).
2. Vibration analysis of pre-swirl stator (ARTICLE 2).
3. Development of the quasi-static hydro-structural CFD-FEM model for quasi-static coupling (ARTICLE 3).
4. Propulsion model effect on the pre-swirl stator structural response (ARTICLE 4).
5. Development and application of the dynamic hydro-structural CFD-FEM model (ARTICLE 5)
6. Pre-swirl stator structural integrity evaluation considering the ship design life (ARTICLE 6).

2.1 Validation and verification of the CFD framework

Validation and verification of the hydrodynamic code is the first milestone in the detailed analysis of ship structural issues for the CFD-FEM coupling. ARTICLE 1 presents the thorough comparison of ship resistance and wake field results with the experimental values. Detailed flow patterns are examined near the propeller and compared to PIV measurements. Two ship hull forms are investigated and the simplified propeller model accuracy is assessed. The practices outlined in this work are used in the subsequent articles developed in this thesis wherever ship hydrodynamic simulations are needed.

The simulations employed a second order accurate scheme with the GFM method for the resolution of the sharp interface. Turbulence model used in the study is the k-ω SST model. Simulated wave field compared well with the measured values as shown in Figure 2 where the EFD represents the experimental results. More importantly when evaluating the flow near the

propeller i.e. where the PSS is located, the comparison of the velocities at the propeller plane with the experimental values is a good indicator if the simulation of the propeller and ESDs is performed correctly. Velocity vector components at the propeller plane are presented in Figure 3. Overall, when comparing the wake field results the average error equals 2.52%, while the resistance error is below 3% for all meshes. Wake results slightly improve when full second order discretisation on the velocity gradients is used.
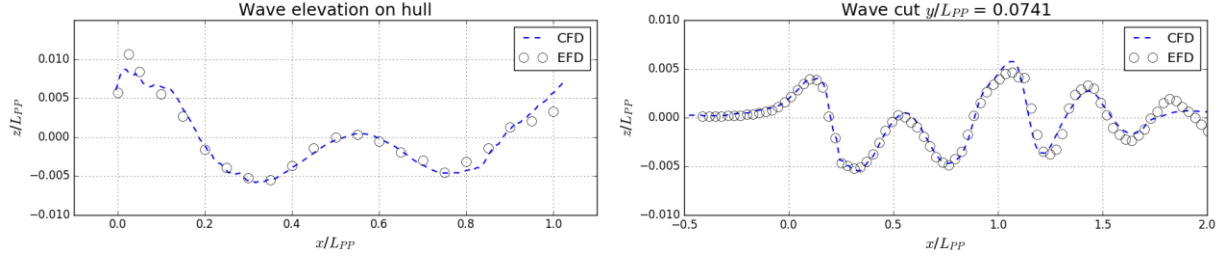

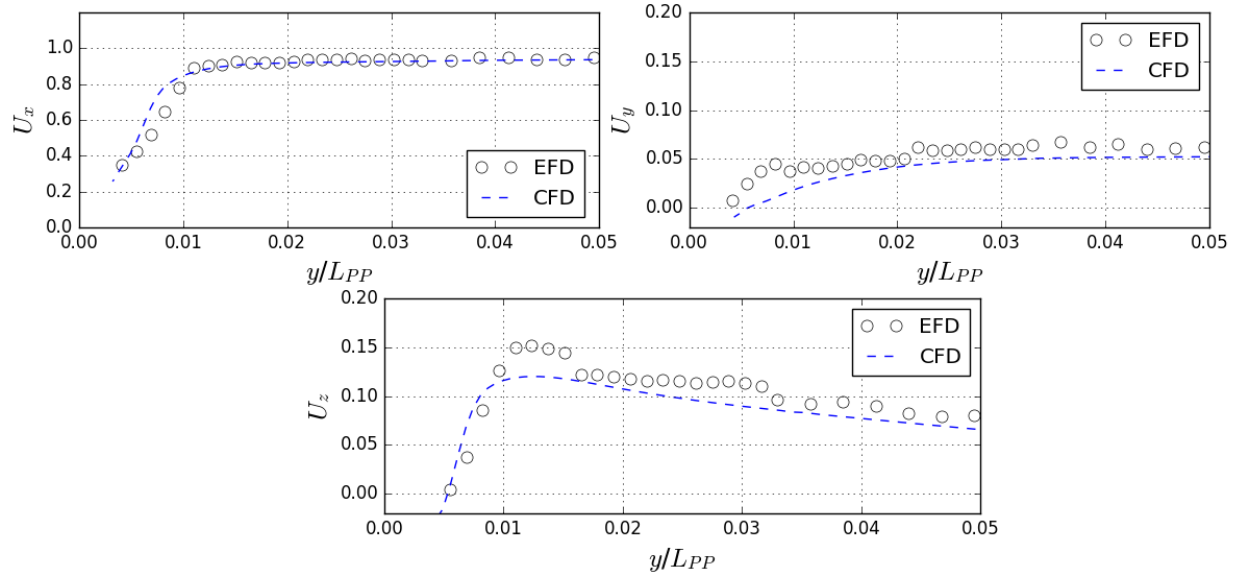*Figure 2 – Comparison of wave field with experiment (ARTICLE 1)*

Figure 3 - Probed velocity at propeller plane (ARTICLE 1)

Implementation of the actuator disk model is further compared to the experimental results. For this simplified propulsion model, the main goal is to analyse the accuracy of the flow upstream of the propeller. This is quantified by the thrust deduction parameter which represents the increase in the ship drag when the propeller is operational compared to the bare hull resistance. This parameter is important since the PSS location is upstream of the propeller plane and correct

estimation would serve as the verification of the flow accuracy near the ESD. Also, here Proportional-Integral (PI) controller is employed to achieve the experimentally set difference between the model scale resistance and propeller thrust. The convergence of the results is shown in Figure 4 where the PI controller regulating the thrust can clearly be observed. Error in drag coefficient is below 1% with the thrust deduction error equal to 0.56%.
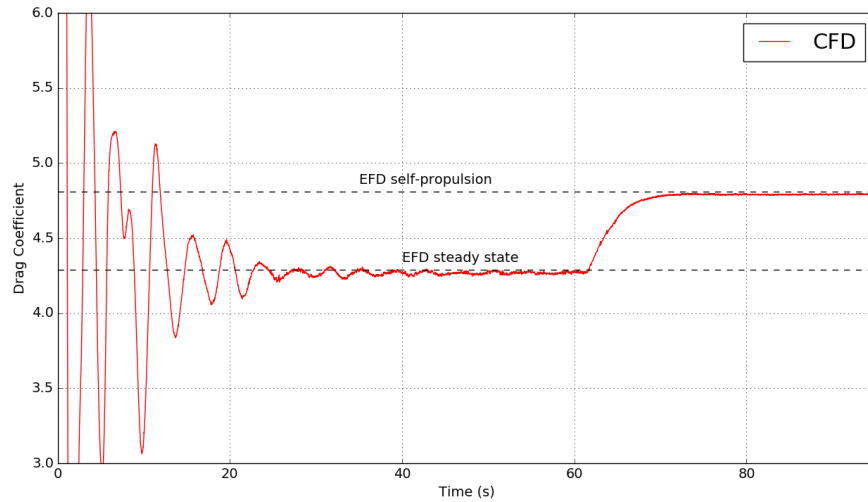

Figure 4 - Drag convergence with and without propulsion (ARTICLE 1)

Overall, the CFD framework employed in this thesis has shown consistency with the experimental values and verified the accuracy of the simplified propulsion model when evaluating the propeller suction effect on the hull stern. This is important since the fully direct propeller simulations require a significantly larger amount of CPU time to converge meaning that when possible, the propeller model can be replaced by the actuator disk, but only if the observed problem allows such simplifications.

2.2 Dynamic structural analysis

Prerequisite for the hydro-structural interaction simulations is the evaluation of the structural vibrational characteristics. ARTICLE 2 presents the dynamic analysis required for the comparison of the structural natural frequencies and the expected excitation frequencies. Ratio of these frequencies govern the choice of the necessary hydro-structural regime as shown in Figure 5. However, it should be stresses that in the case of ship or any fully submerged structures, the relevant parameters for comparison is the wet frequency due to the effect of the added mass. For

this reason, the computed mode shapes in the structural model are usually abbreviated as dry mode shapes if the effect of the surrounding fluid is not considered.
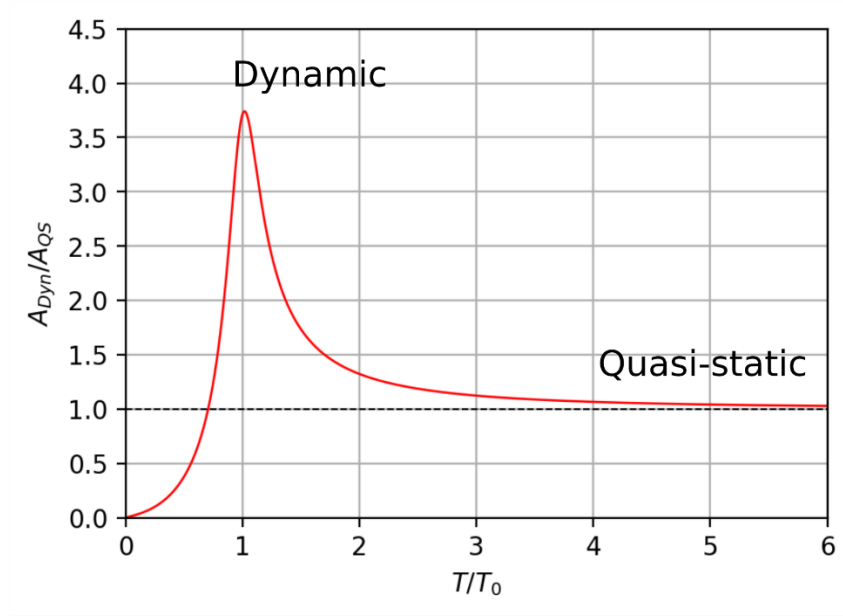

Figure 5 – Hydro-structural regime depending on T_0 (structural natural frequency) and T (excitation frequency) (ARTICLE 5)

The structural model is shown in Figure 6 with the abbreviation of each fin in the PSS. Computation of the dry mode shapes is performed in *NASTRAN*. Wet frequencies are computed using the *MFLUID* option in *NASTRAN*. Additionally, the dry mode shapes are exported to the Bureau Veritas *Homer* software to compare with the already obtained FEM results. An artificial FEM model is created to be able to perform the computations in *Homer*. Wet frequencies compared well between the two numerical tools with consistent difference across all modes.

Regarding the external excitation, the propeller and VIV induced forces are considered. Propeller excitations are computed analytically from known propeller revolutions per minute and the VIV frequency is calculated approximately using analytical formulas, but also with the CFD simulations. Flow at the PSS is shown in Figure 7. Propeller excitation for 1st and 2nd harmonic are below the resonance range with the ratios of T/T_0 being 4 and 2, respectively. Regarding the VIV frequency, the analytical and the CFD computed period is even higher than the propeller excitation period. However, the CFD results should be regarded with care, since two-equation turbulence model is used which cannot accurately predict the higher frequency VIVs.

Overall, the results presented in this paper provided consistent correlation between two different numerical tools when estimating the structural wet frequency. The results suggest the quasi-static approach for the PSS to be sufficient in terms of calm-water expected hydrodynamic loads. Only the propeller 2nd harmonic could induce dynamic amplification, but still being away from the resonance point, only a moderate increase is expected.
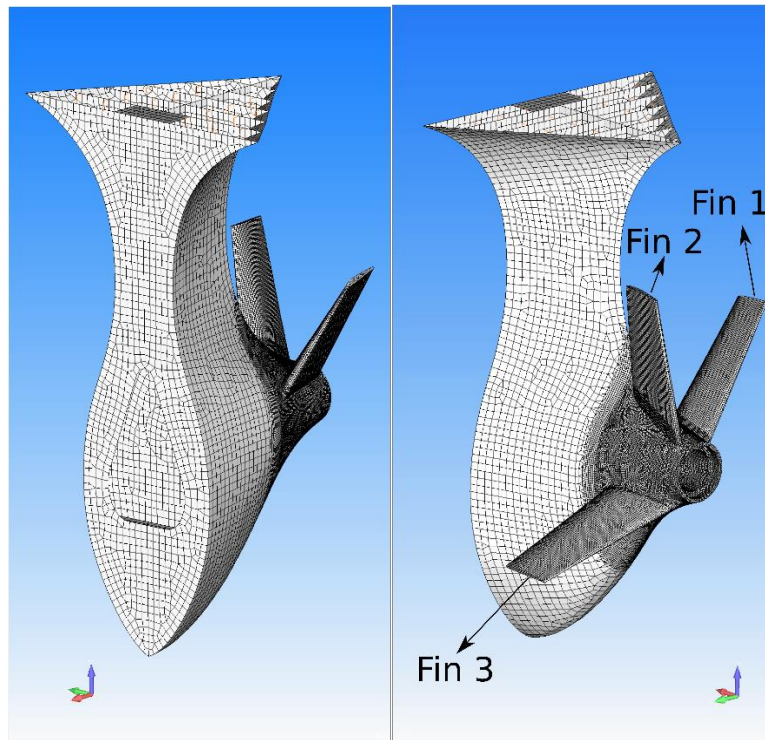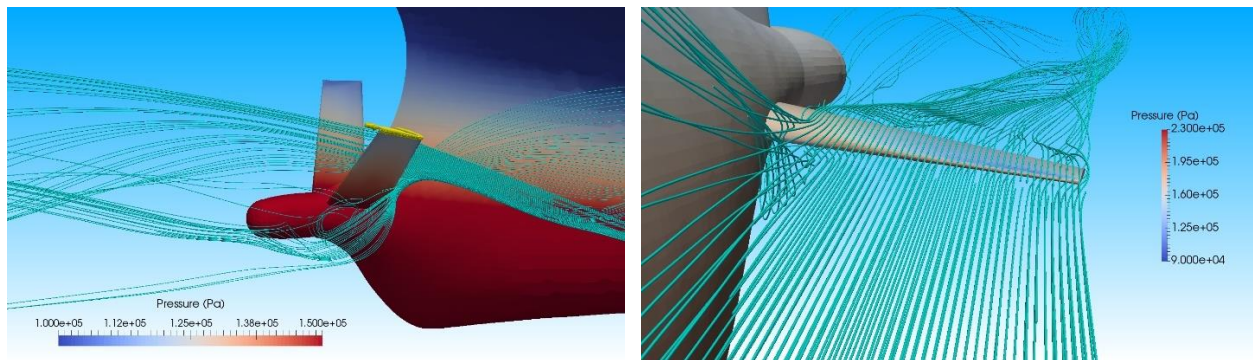

Figure 6 – Structural model (ARTICLE 4)

Figure 7 – Streamlines in the vicinity of PSS fin (ARTICLE 2)

2.3 Hydro-structure coupling – quasi-static approach

Following with the ARTICLE 3, the development of the field transfer between the fluid and structural mesh sharing interfaces is obviously needed to achieve a consistent quasi-static model. The emphasis of the paper is on the implementation of a robust and accurate pressure transfer from the CFD hydrodynamic mesh to the FEM structural mesh. The approach is validated and verified on two fundamentally different cases with varying mesh size. The method is not only applicable to ship structures but can easily be used in any type of quasi-static fluid-structure interaction problems.

Pressure transfer is based on the projection method where the structural integration points, or otherwise called Gauss points, are projected to the fluid mesh. This assumes a strict definition of the structure and hydrodynamic interfaces as an input to the interpolation process. Careful consideration of the CFD internal solution system, allows the minimization of pressure peaks diffusion in the fluid solution. This is performed by triangulation around the boundary face centres in the CFD interface mesh as shown in Figure 8. The pressure value is obtained by interpolating between the averaged values in the CFD points and the exact CFD value at the face centre. When the pressure value is obtained at the structural integration points, the loads per structural element are directly converted to the nodal force values and the loading file is exported to the desired FEM software. Since there is no mutual interaction of the CFD and FEM solvers, the fluid solution can be computed prior to the coupling and the selected time-steps and loading files can be calculated in the post-processing stage. The scheme of the method is shown in Figure 9 where G_i^h represents the projected Gauss point on the fluid mesh and N are the shape function coefficients for calculating interpolated pressure p.
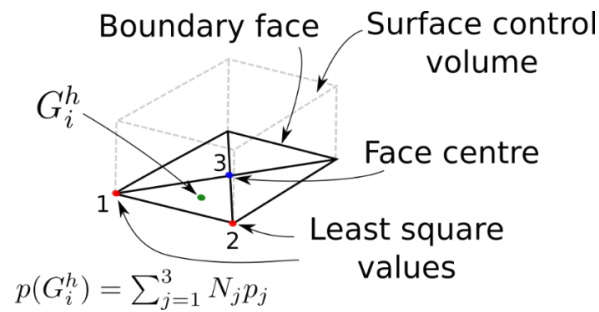

Figure 8 – Triangulation of the fluid surface mesh and computation of the interpolated value at projected structure integration point (ARTICLE 3)

The method is validated on two fundamentally different cases. Smooth pressure distribution case (cylinder in short and long wavelength) and chaotic pressure case (green water on ship breakwater structure). For both cases the results obtained are consistent and sufficiently accurate when comparing force and moments differences on the CFD and FEM mesh. The method is also compared to the simpler method without the interpolation of the pressure values which assumes the pressure is taken directly from the CFD wetted element.
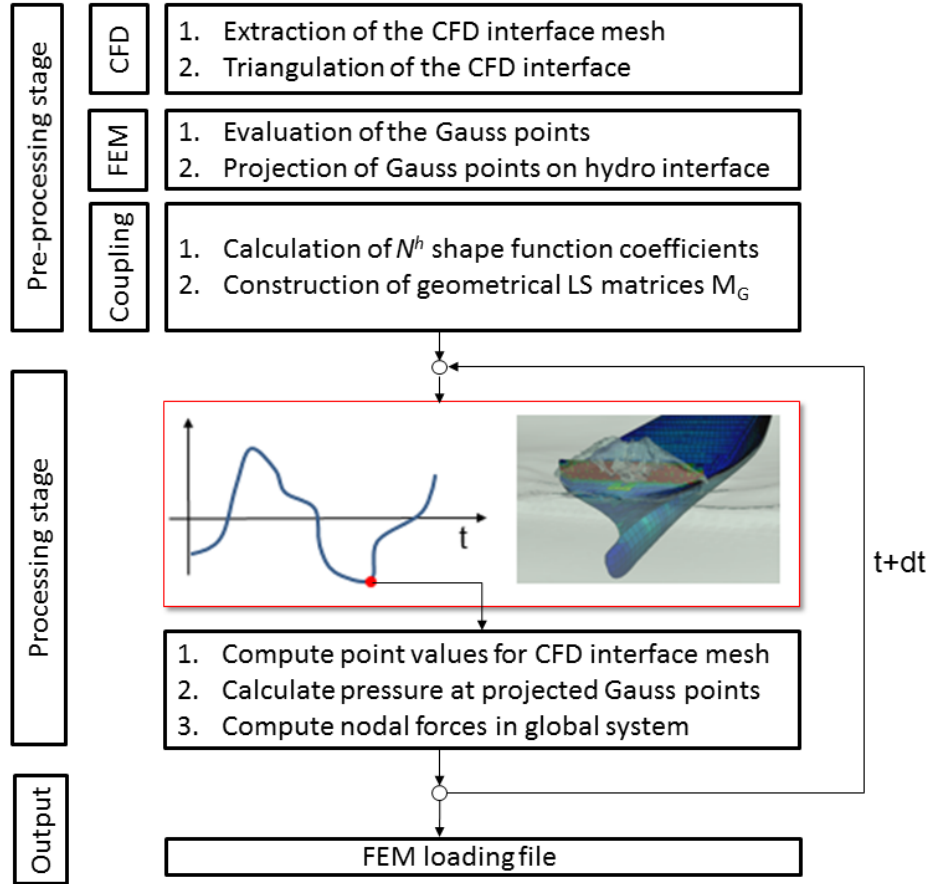

Figure 9 – Scheme of the quasi-static coupling procedure (ARTICLE 3)

The cylinder case errors for force and moment with the highest order of interpolation considered (3rd order), which equates to 9 Gauss points per quadrilateral structural element, are below 3% for longer wavelength (λ_1) even when the FEM mesh is made quite coarse compared to the fluid mesh. On the shorter wavelength (λ_2), for medium and fine mesh the error is lower than 2%. Most importantly, the trend of the proposed method shows consistency with the increase in the FEM mesh density as shown in Figure 10. On the other hand, the green water case exhibited similar results with error also lower than 2% for all cases. The container ship results depending on

the interpolation order have shown similar consistency and reliability when correlating with the simpler method. The results are shown in Figure 11. As can be seen, irrelevant of the FEM mesh, the interpolation process maintains the equal amount of forces and moment error below 1%. Overall, the method has shown accurate results for different mesh sizes and a significant improvement is presented opposed to the simple method without pressure interpolation on the fluid face where the projection occurred.

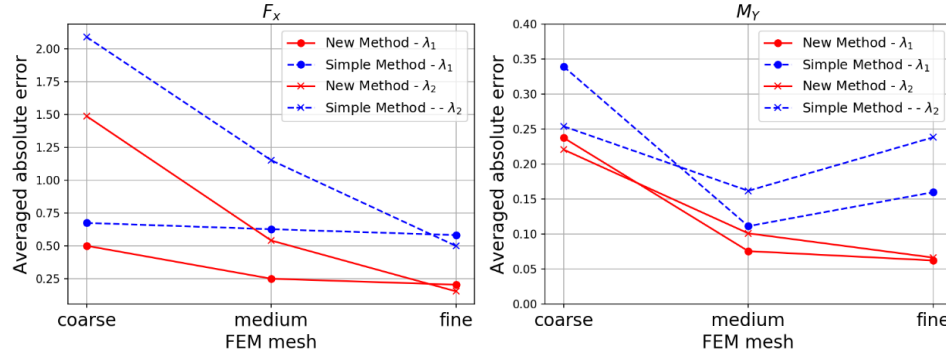*Figure 10 – Averaged absolute error for F_X (left) and M_Y (right) using 3rd order of interpolation (ARTICLE 3)*
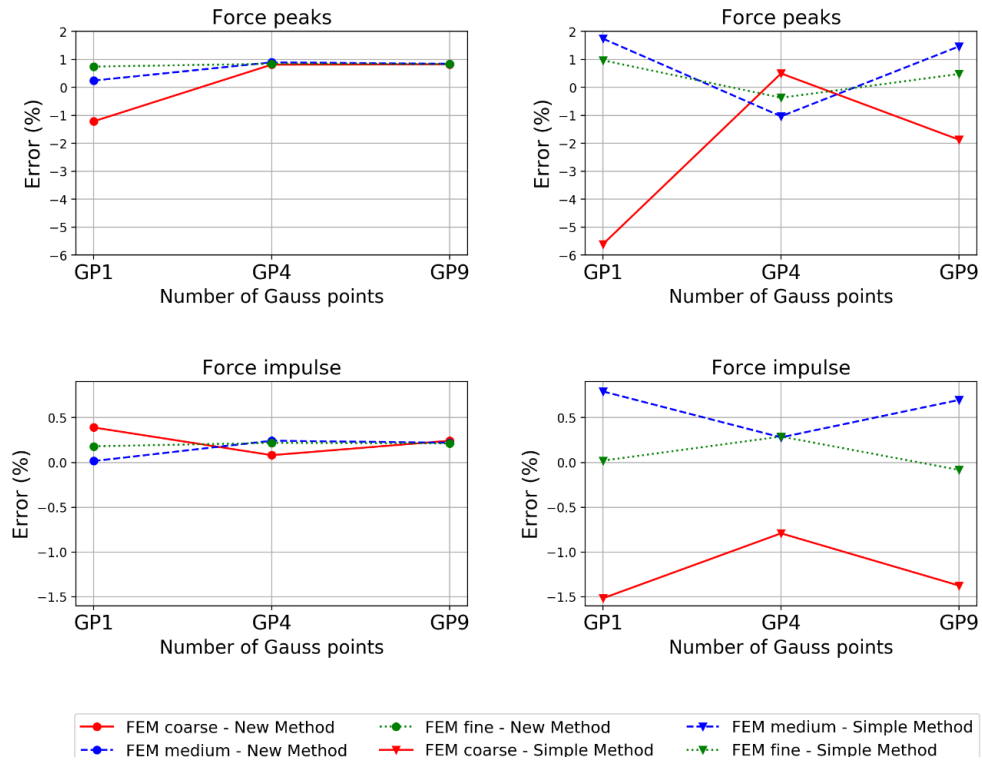

Figure 11 – Error in the force peaks and force impulse compared to CFD solution. New method (left), Simple method (right) (ARTICLE 3)

2.4 Propeller modelling impact on the PSS structural stresses

ARTICLE 4 investigates the propeller modelling influence on the PSS hydrodynamical loads and structural responses in calm-water and waves. Three different numerical models are considered: without propeller, with propeller and with the simplified actuator disk model. Main goal is to clarify the mandatory amount of complexity for the correct evaluation of structural responses. Calm-water results are computed to assess the impact of the direct propeller modelling on the PSS structural responses and to evaluate the quality of the pressure loads with the simplified propeller model. On the contrary, wave simulations serve as the guideline for the forthcoming broader wave simulations study to clarify which type of flow model is necessary to capture the nature of the fluid loads during ship motions.

In the calm-water study, besides the structural response evaluation, the PSS efficiency is studied by performing the simulations with and without the PSS. Direct propeller simulations are employed with the rotative GGI region introduced inside the surrounding ship mesh. The computational mesh is shown in Figure 12. The simulation with the PSS produces higher torque loads on the propeller blades, but effectively reduces the rotation rate needed to realize the same amount of thrust for the ship design speed. The consequence is the lowering of the ship delivered power to the shaft which is reduced by 4.7%, thus proving the PSS design to be beneficial.
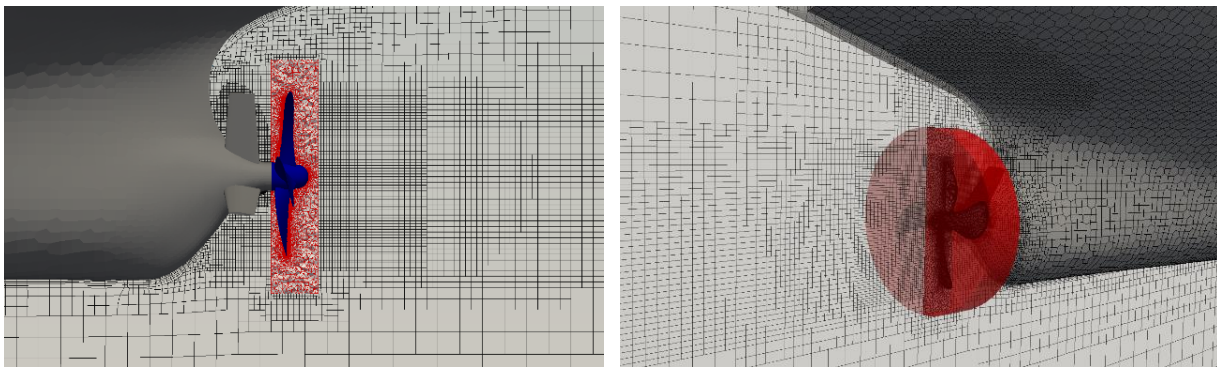
Figure 12 – Propeller mesh with GGI region highlighted in red (ARTICLE 4)

Regarding the comparison of three different flow models, the calm-water numerical fluid loads on the Fin 3 are shown in Figure 13. The drag force mean value is quite well captured with the simplified propeller model. Nonetheless, the lift coefficient has significant differences when the propeller geometry is neglected. Actuator disk model offers partial improvement compared to

the case without any propulsion, but the mean force value is still significantly lower. As expected, the direct propeller model is mandatory in calm-water calculations since there is no other physical way of capturing the loading amplitude relevant for fatigue computations, but the extreme response is captured well with the actuator disk model. When assessing the structural response, in all three fins, there is no danger of reaching the yielding strength with the maximum stress values being around 50 MPa as seen in Figure 14. The stress amplitudes correlate to a design life well above the 25 years limit.
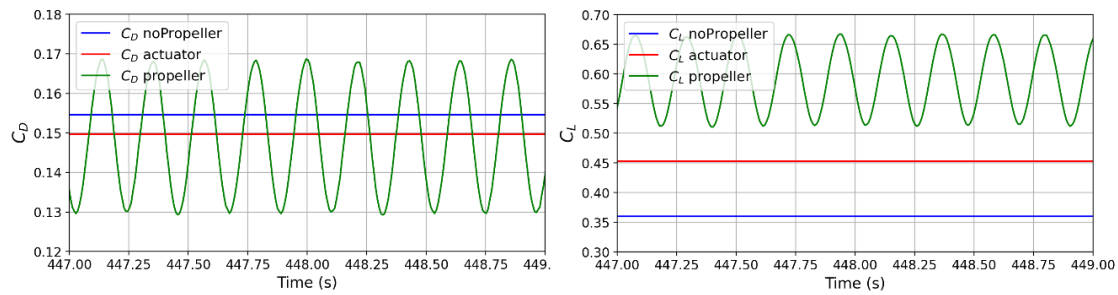

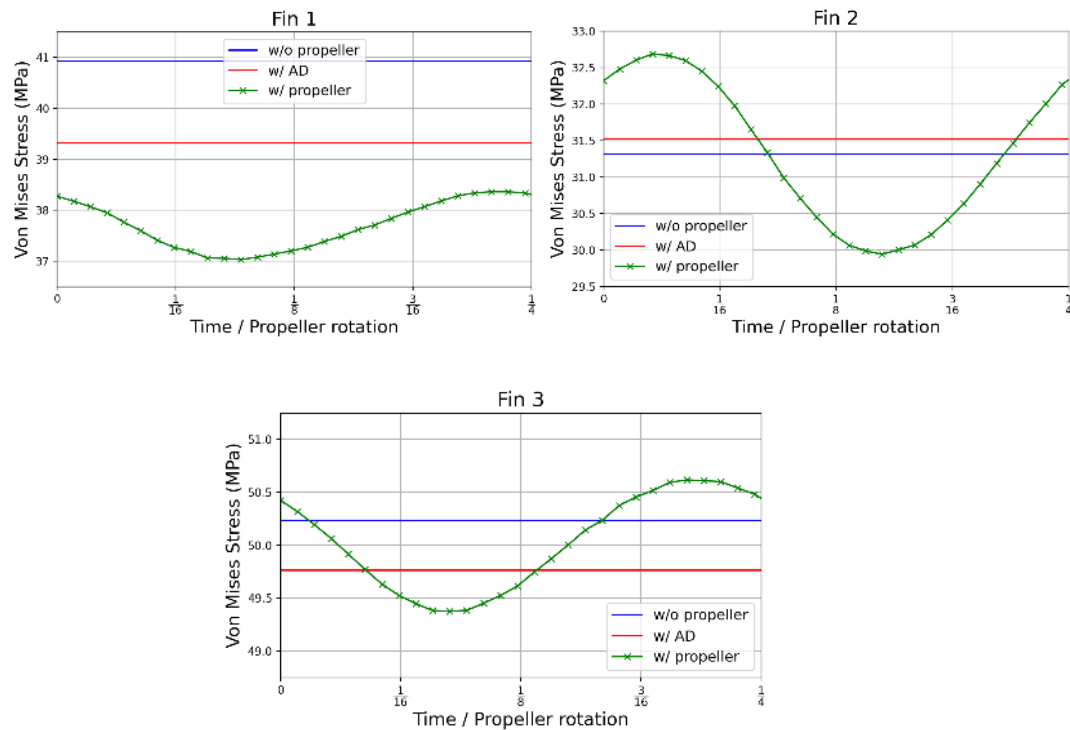*Figure 13 – Drag and lift coefficient signal for Fin 3 (ARTICLE 4)*

Figure 14 – VMS distribution in calm-water for the maximum loaded element (ARTICLE 4)

Continuing with the wave simulation where ship motions have a large influence on the stress range, same set of flow models is analysed. Force coefficient analysis shows much smaller difference between the cases on Fin 3, hence implying the reduced influence of the flow model on the pressure distribution. In this case the ship motion has a leading influence on the stress range even more than the propeller rotation. From the results as shown in Figure 15, it can be concluded that in the waves simulation the simplest model without any propulsion is sufficient to accurately capture the amplitude exhibited by waves.
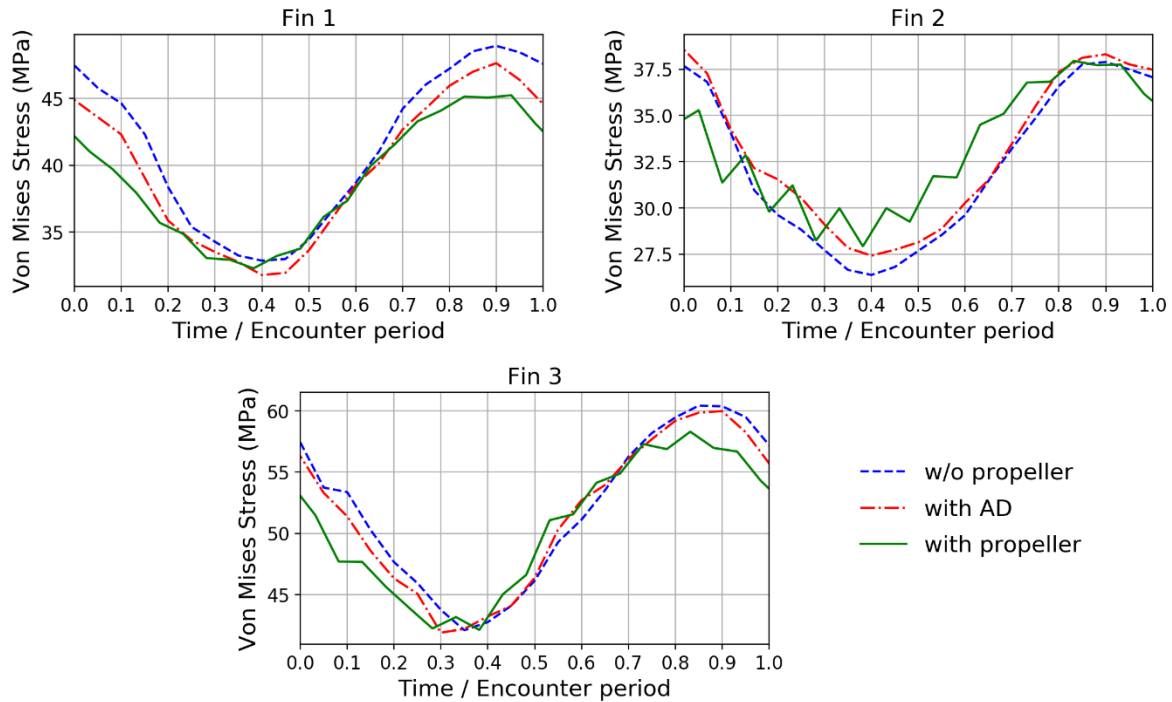
Figure 15 – VMS distribution in an encounter period for the maximum response element per fin.
(ARTICLE 4)

2.5 Hydro-structural coupling – Dynamic approach

ARTICLE 5 presents the hydroelastic model for CFD-FEM coupling. The model is implemented in an efficient manner using the modal superposition method. This requires the structural model to compute the mode-shapes in the pre-processing stage and enables the hydro-structural interaction to be solved strictly inside the CFD framework. Although the investigations in ARTICLE 2 clarified the quasi-static regime as relevant for waves and propeller, the dynamic

hydro-structure model is developed to verify the amount of the hydroelastic effects and providing a framework for the inclusion of the structural dynamics whenever needed.

Model is based on dry mode shapes computed in the FEM solver. Assessment of computed dry frequencies clearly suggests that only the 1st mode (16.79 Hz) is relevant for any kind of structural response comparison since the 2nd dry mode frequency (97.73 Hz) is well above any reasonable ratio, compared to excitation frequencies, to exhibit dynamic amplification. The ratio of the dynamic and static amplitude is usually denoted as Dynamic Amplification Factor (DAF) and this parameter is critical in the region close to $T/T_0=1$, where T stands for excitation period and T_0 stands for structural natural period. Dynamic equation for the flexible body is implemented in the so-called modal projection method where the external forces and loads are projected to the selected number of mode-shapes. Mode shapes on the hydrodynamical mesh are obtained by using the same interpolation method presented in ARTICLE 3 and reversing the meshes i.e. the field values are interpolated from the structural mesh to the fluid mesh. Upon constructing the dynamic equation, the structural nodal displacements are directly available in the CFD domain, thus removing the expensive time-step iteration between CFD and FEM solution. Mode shape interpolation is shown in Figure 16.
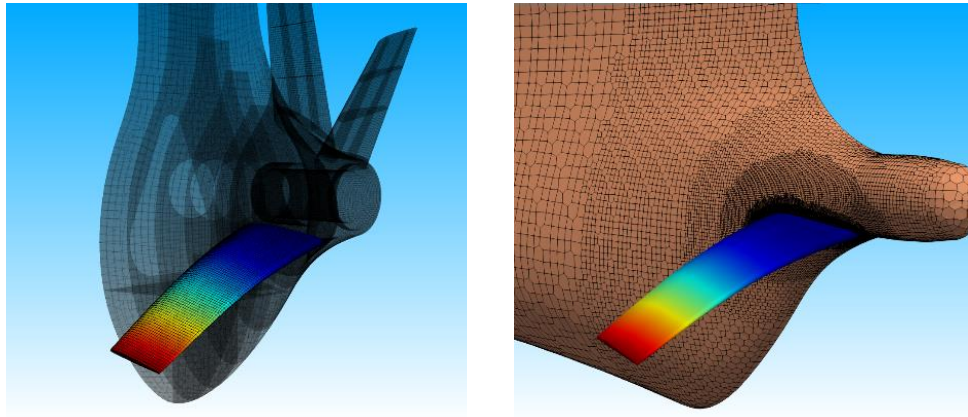
Figure 16 – FEM mode shape for PSS fin (left), interpolated mode shape in CFD (right)
(ARTICLE 5)

The hydroelastic model is tested on two verification cases with artificially imposed force and with fluid velocity set to zero. First case is the impulse force which initiates the fin vibrational response, thus enabling the calculation of the wet frequency response and amplitude depending on the time-step and time-derivative scheme. The wet frequency compares almost exactly with the

26

MFLUID wet frequency computed in *NASTRAN*. The response amplitude is tested with first and second order time-derivative schemes and reliable results are obtained with lowering of the time-step. Guidelines deduced from this case are further employed in the second verification case where the artificial periodic force is introduced to study the DAF on the fin structure. The computed DAF is consistent with the theoretical background of the vibrational system. The DAF curve is shown in Figure 17 with the highlighted expected propeller excitation frequencies and wave loads.

Figure 17 –DAF from CFD and close-up for $T/T_0 < 2$ ratio (ARTICLE 5)

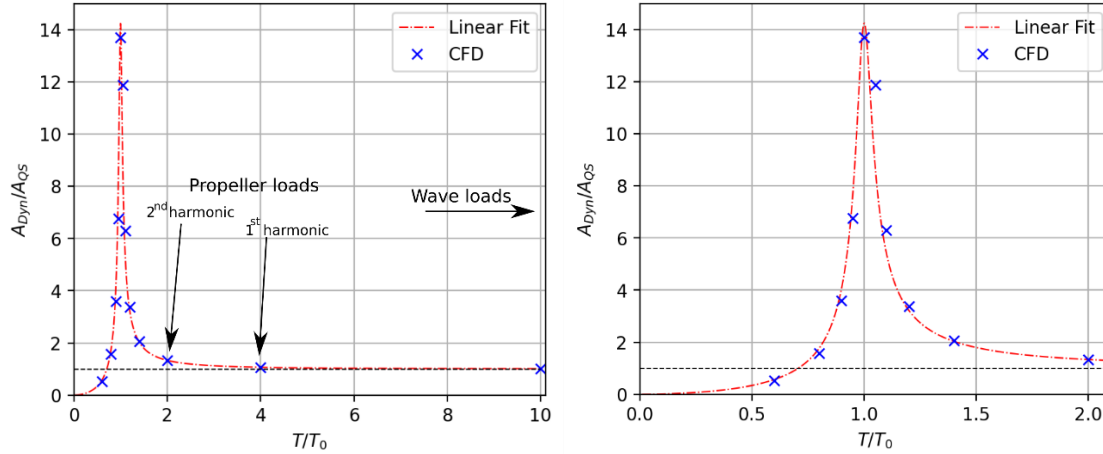After verifying the results on the two simple cases and using the obtained guidances for the dynamic hydro-structure simulations, two realistic ship load cases are setup, the calm-water self-propulsion simulation and the ship motions in waves. Self-propulsion simulations are performed similar as in the ARTICLE 4 with the imposing of the flexible appendage on the PSS fin. Interestingly, moderate hydroelastic effects are found and the DAF is equal to 1.197 for the 1st mode. However, when considering the contribution of the 1st mode on the overall stress response, the dynamic effect is negligible. For the element with the maximum stress range, the amplification accounts to only a 6.32% increase of the VMS. The results are shown in Figure 18. Obviously, this minor increase does not significantly affect the fatigue life estimation. For the wave case, an arbitrary head wave is selected as it allows the use of symmetry plane. After convergence of ship motions and the flow field, the fin modal response is compared to the static modal response. The results are almost exactly equal which is expected since the wave period is inside the quasi-static range when comparing to the structural natural period. The modal responses are shown in Figure

19. Further investigations into the stress distributions in this case are not needed since the dynamic and static responses are equivalent.
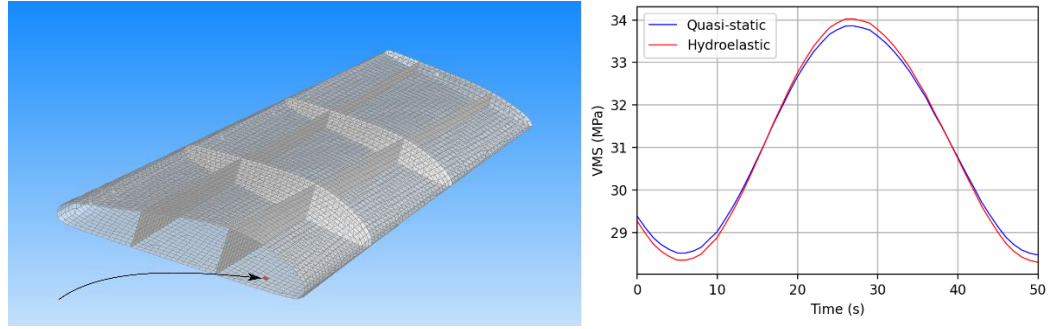
Figure 18 –VMS for propeller load cycle (right) on the element with highest stress range (left) (ARTICLE 5)

Following the results presented in this article, the propeller and wave simulations can be prepared in a quasi-static manner and still contain the required amount of accuracy in terms of hydrodynamical loads and stress ranges. The dynamic model implementation and comparison to static results has further proved the assumptions of employing the quasi-static as reasonable and correct. All this, together with the previous articles, had laid foundations for the setup of the PSS wave simulations while considering the wave environment encountered during its design life.

Figure 19 –Modal response for the wave simulation (ARTICLE 5)

2.6 Pre-swirl stator structural integrity evaluation

ARTICLE 6 synthesis the entire thesis and studies presented in the previous articles. The scheme of the final numerical method for PSS integrity evaluation is shown in Figure 20. The

28

method is proposed for the evaluation of the PSS structural response in waves based on the DLP defined as the simplified lift force model. Hybrid linear potential and CFD wave statistical analysis is performed to reach the critical conditions for the computation of the extreme response and fatigue. The structural responses are obtained from non-linear computations in waves in a quasi-static manner as justified in the previous articles.
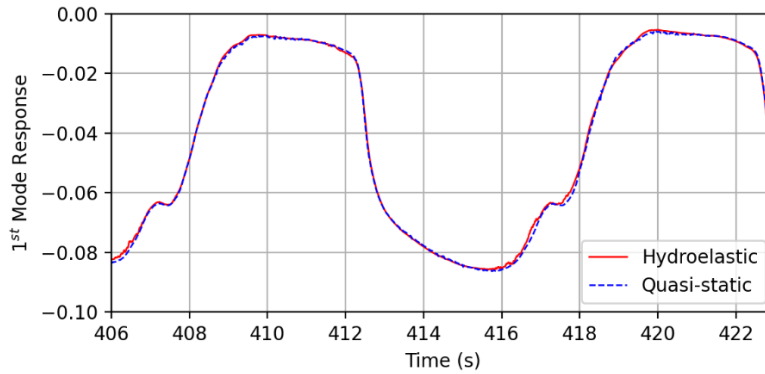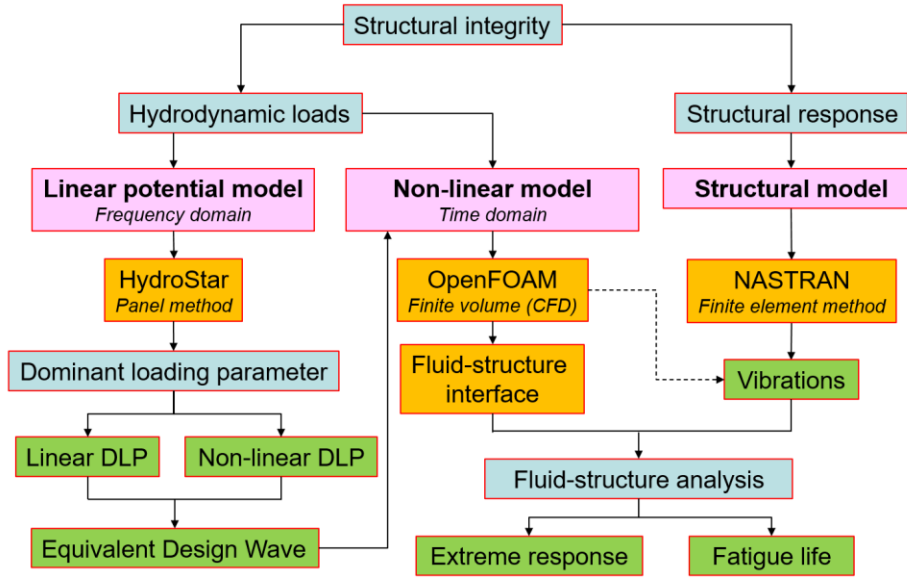

Figure 20 –Numerical method for PSS structural integrity evaluation (ARTICLE 6)

In the modern approach to direct design of floating structures, the methodology is based on the two-step model. First part is dedicated to the analysis of the wave statistics with the low order flow model (linear potential) and in the second part, the identified critical conditions are utilized in the higher-order numerical model to assess the realistic structural stresses.

Statistical analysis of the wave environment in this work is performed by the Bureau Veritas software HydroStar with the solution obtained in the frequency domain (RAO). However, before applying the linear solver, the DLP for the PSS structure needs to be identified. A simplified lift force value is taken as relevant. Unfortunately, the lift force DLP depending on the lift velocity is not linear, meaning that the regular spectral methods are not applicable, but the resolvent of each sea-state to the time domain is needed. This significantly complicates the process of the large number of sea-state evaluation. The hybrid lift velocity model is based on the addition of calm-water CFD velocity and the perturbed velocity from HydroStar. Prior to the development of each contributing sea-state to time domain, a dependency of angle of attack and PSS fin 2D section is

29

established through CFD simulations for various angles expected to cover the range encountered by the PSS during its life cycle. Each step of the method is transparently verified. The statistical parameters of the lift force time-domain signal is done by up-crossing analysis and the distribution fit is made on the empirical data. The analytical definition enables the use of standard methods for assessing the critical conditions and defining the EDWs. Process leading to the EDWs is schematically shown in Figure 21.
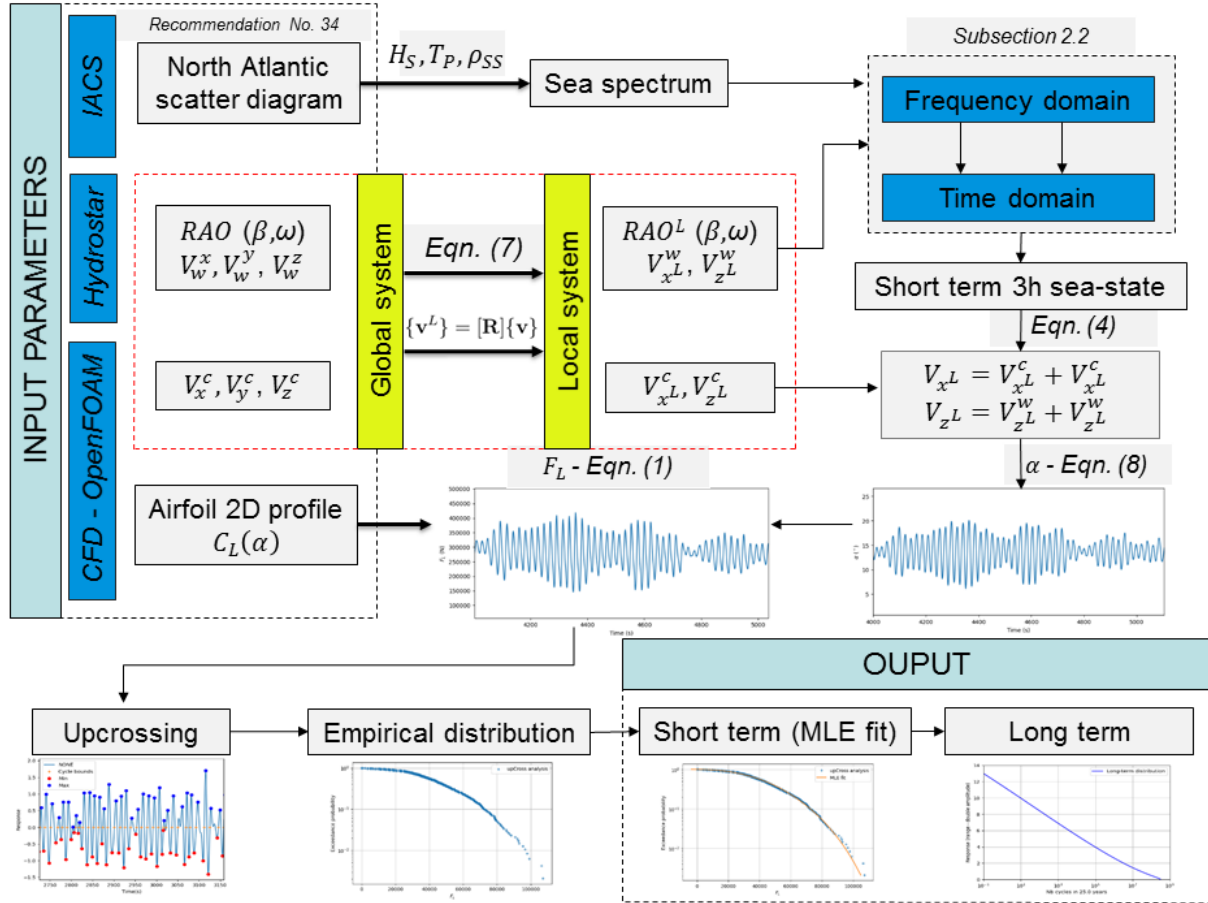
Figure 21 –Schematic illustration of the procedure for obtaining the short-term distribution for each H_S, T_P and heading (β) (ARTICLE 6)

Defined EDWs are made of a single wave frequency (regular wave) and without the propeller as justified in ARTICLE 4. Pressure field from the CFD simulations per each probability level are exported to the FEM model as nodal forces and a set of linear static analysis is run. The VMS distribution is analysed over the entire fin until the FEM element most liable to fatigue damage is found. This element and its VMS distribution are shown in Figure 22. The stress ranges

obtained for each probability level allow for the evaluation of the fatigue life and for the observed element this is far above the 25 years design life limit for both fitting methods.

Lastly, the methodology presented here can be easily extended to any type of ship appendage with only the DLP parameter being adjusted accordingly. Since the current DLP is non-linear, the presented framework can also serve as the guideline when such instances occur. For the observed appendage design, the PSS structural integrity in waves is ensured.

Figure 22 – Highlighted element with highest long-term fatigue damage and stress signal at different probabilities (ARTICLE 6)

3 Conclusion

3.1 Concluding remarks of doctoral thesis

Process of realistic hydrodynamic loads and corresponding structural response predictions on the floating structures enters multiple research fields and depending on a different level of accuracy demanded, can be a tedious task to perform correctly. Considering all the possible load cases the ship may encounter, some type of deduction is necessary to make a high-fidelity hydrodynamic CFD model usable.
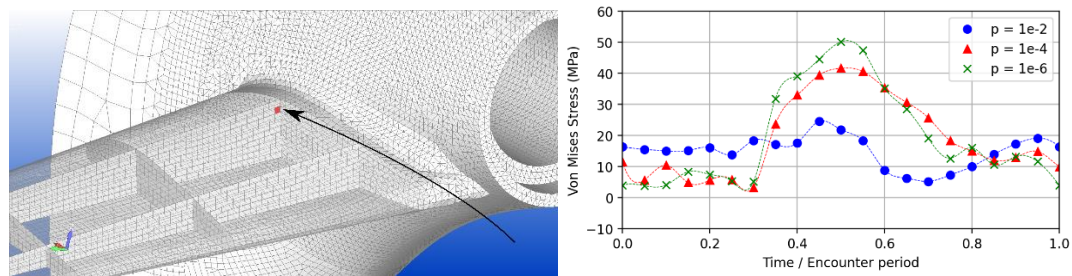
This thesis presented a direct design approach for the structural integrity evaluation of ship appendage. Different numerical methods available for ship hydrodynamics are employed and structural design method is explained in detail considering the expected external load excitations on the case of PSS. Computationally lighter linear potential flow model is employed for the wave statistical analysis while the expensive CFD simulations are run on the selected number of design cases. Prior to conducting the study, an in-house CFD code developed in the foam-extend version of OpenFOAM is thoroughly validated and verified on the flow conditions relevant for the study of aforementioned ESD. The results have shown good agreement with the experimental data and the setup for future ship simulations is deduced guaranteeing the accuracy of the fluid solution in both local and global scale.

Upon verifying the CFD code, dynamic analysis of the structure is conducted. This step is important since the appropriate hydro-structure regime should be selected and the structural design should avoid the resonance phenomena with the external excitation. For this reason, the PSS dry modes are evaluated and corresponding wet frequencies are computed using two different numerical models. Both models yielded similar results for the wet frequency. Structural wet frequency is compared to the propeller and VIV excitations. The results suggest circumvention of the resonance and show the structure to be very stiff with only the first mode at reasonably low frequency to exhibit any type of dynamic amplification. Although the results imply the use of quasi-static approach suitable for the PSS hydro-structure issue, in this work both models are developed, quasi-static and dynamic, to exactly quantify the hydroelastic effects.

Hydro-structure coupling models are independently developed. Quasi-static model is developed on the CFD-FEM numerical models where the consistent pressure transfer is validated and verified on different mesh sizes between fluid and structural model. Superior accuracy is proven through comparison with the simpler method which excludes the careful interpolation method implemented in the current study. Two cases are studied: smooth pressure distribution case and chaotic wave impact. For both conditions the interpolation process has shown reliability and consistency. Hydroelastic hydro-structure model is developed following the modal superposition method with dry mode-shapes pre-computed in the structural model and interpolated on the fluid mesh, hence enabling highly efficient hydroelastic coupling procedure.

The propeller loadings are evaluated in calm-water with the propeller operational and three different flow models are assessed: without the propeller, with actuator disk and with the propeller. In the calm-water, propeller modelling is mandatory to capture the stress range required by the fatigue analysis, but in waves, the propeller influence is negligible on the stress range induced by the ship motions. This enables the wave simulations to be run without the propeller which besides bringing less computational expense, also makes the potential and CFD fluid numerical setups consistent. Comparison of static and the dynamic modal response in waves is deemed equal, thus showing quasi-static approach appropriate for the wave simulation. On the other hand, the dynamic effects on the structural response in propeller load cases are evident, but their contribution to the overall stress response is negligible.

Following the obtained guidelines and performed simulations, the methodology for the PSS ship appendage is further defined. The dominant loading parameter is set as the lift force based on the hybrid CFD and linear potential flow components. The critical cases are deduced from the analysis and simulated in the non-linear CFD environment. The results compared well with the long-term expectations. The extreme response stresses are well below the steel yielding strength. The PSS fatigue life is obtained from stress ranges at different probability levels and is above the necessary 25 years.

3.2 Guidelines for future research

For future work and with respect to the PSS, a more detailed analysis of the flow induced vibrations should be studied. There are different phenomena related to the VIV which could exhibit

high frequency vortices in relation to the structural natural frequencies. However, this requires the investigation into more complex turbulence models and their detailed evaluation which was out of the scope in this work.

In general, the developed methodology can be applied to different ship appendages and structural issues. It is only required to properly define the DLP depending on the structure and position of the appendage even giving the guidelines when the DLP is non-linear. Most importantly, hydro-structure tools, specifically CFD-FEM coupling developed within this study can be used in a broad range of applications beyond the shipping industry. The interpolation of the pressure is easily applied to any type of hydro-structural problem when the hydrodynamic loads are mandatory to compute by CFD and high amount of accuracy is needed. Also, the methodology to include the structural dynamics in the structural stresses can be used on any type of structure where there are considerable vibrations. In terms of hydrodynamic vibrational problems, the tools developed are easily applied to common research subjects such as slamming, whipping and springing. Application to flexible propellers or even on the structures beyond the shipping industry such as wind turbines would be straightforward. Another important subject is the effect of structural damping in resonance conditions which by employing the developed models can be tested and applied for more complex hydrodynamical load case. Since the CFD offers a fully non-linear solution, a theoretical hydroelastic models developed from the linear potential flow theory can be employed for verification perhaps shedding more light on the subject.

Overall, the study conducted here and the numerical tools developed offer a wide range of application cases. This enables the future research to go in a broad direction in terms of floating structure design and vibrational issues in general.

Bibliography

[1]   J. M. J. Journeé and W. W. Massie, *Offshore Hydromechanics*. Delft University of Technology, Cambridge University Press, 2001.

[2]   W. J. Kim, S. H. Van, and D. H. Kim, "Measurement of flows around modern commercial ship models," *Exp. Fluids*, vol. 31, no. 5, pp. 567–578, 2001, doi: 10.1007/s003480100332.

[3]   S. H. Van, W. J. Kim, H. S. Yoon, Y. Y. Lee, and I. R. Park, "Flow measurement around a model ship with propeller and rudder," *Exp. Fluids*, pp. 533–545, 2006, doi: 10.1007/s00348-005-0093-6.

[4]   A. Olivieri, F. Pistani, A. Avanaini, F. Stern, and R. Penna, *Towing Tank Experiments of Resistance, Sinkage and Trim, Boundary Layer, Wake and Free Surface Flow Around a Naval Combatant INSEAN 2340 Model*, no. IIHR Report No. 421, 56 pp. The university of Iowa: Iowa Institute of Hydraulic Research, 2001.

[5]   L. Larsson, F. Stern, and M. Visonneau, *Numerical Ship Hydrodynamics: An assessment of the Gothenburg 2010 workshop*. Springer, 2013.

[6]   H. Jasak, "Error Analysis and Estimation for the Finite Volume Method with Applications to Fluid Flows," Imperial College of Science, Technology & Medicine, London, 1996.

[7]   O. Ubbink and R. I. Issa, "A method for capturing sharp fluid interfaces on arbitrary meshes," *J. Comput. Phys.*, vol. 153, pp. 26–50, 1999.

[8]   H. Rusche, "Computational Fluid Dynamics of Dispersed Two - Phase Flows at High Phase Fractions," Imperial College of Science, Technology & Medicine, London, 2002.

[9]   J. Huang, P. M. Carrica, and F. Stern, "Coupled ghost fluid/two--phase level set method for curvilinear body--fitted grids," *Int. J. Numer. Meth. Fluids*, vol. 44, pp. 867–897, 2007, doi: 10.1002/fld.1499.

[10]   O. Desjardins, V. Moureau, and H. Pitsch, "An accurate conservative level set/ghost fluid method for simulating turbulent atomization," *J. Comput. Phys.*, vol. 227, no. 18, pp. 8395–8416, 2008.

[11]   B. Lalanne, L. R. Villegas, S. Tanguy, and F. Risso, "On the computation of viscous terms for incompressible two-phase flows with Level Set/Ghost Fluid Method," *J. Comput. Phys.*, vol. 301, pp. 289–307, 2015.

[12]   V. Vukčević, H. Jasak, and I. Gatin, "Implementation of the Ghost Fluid Method for free surface flows in polyhedral Finite Volume framework," *Comput. Fluids*, vol. 153, pp. 1–19, 2017.

[13] J. Roenby, H. Bredmose, and H. Jasak, "A computational method for sharp interface advection," *Open Sci.*, vol. 3, no. 11, 2016, doi: 10.1098/rsos.160405.

[14] M. Sussman, P. Smereka, and S. Osher, "A Level Set Approach for Computing Solutions to Incompressible Two-Phase Flow," *J. Comput. Phys.*, vol. 114, pp. 146–159, 1994.

[15] R. Folch, J. Casademunt, and A. Hernández--Machado, "Phase--field model for Hele--Shaw flows with arbitrary viscosity contrast. I. Theoretical approach," *Phys. Rev. E*, vol. 60, p. 1724, 1999.

[16] V. Vukčević, H. Jasak, and Š. Malenica, "Decomposition model for naval hydrodynamic applications, Part I: Computational method," *Ocean Eng.*, vol. 121, pp. 37–46, 2016, doi: 10.1016/j.oceaneng.2016.05.022.

[17] V. Vukčević, H. Jasak, and S. Malenica, "Decomposition model for naval hydrodynamic applications, Part II: Verification and validation," *Ocean Eng.*, vol. 121, pp. 76–88, 2016, doi: 10.1016/j.oceaneng.2016.05.021.

[18] Y. Sun and C. Beckermann, "Sharp interface tracking using the phase-field equation," *J. Comput. Phys.*, vol. 220, pp. 626–653, 2007.

[19] S. Enger, M. Perić, and R. Perić, "Simulation of Flow Around KCS-Hull," in *Gothenburg 2010: A Workshop on CFD in Ship Hydrodynamics*, 2010.

[20] J. Banks, A. B. Phillips, P. W. Bull, and S. R. Turnock, "RANS simulations of the multiphase flow around the KCS hullform," in *Gothenburg 2010: A Workshop on CFD in Ship Hydrodynamics Gothenburg*, 2010.

[21] Y. H. Ozdemir, T. Cosgun, A. Dogrul, and B. Barlas, "A numerical application to predict the resistance and wave pattern of KRISO Container Ship," *Brodogradnja/Shipbuilding*, vol. 67, no. 2, pp. 47–65, 2016.

[22] W. P. Jones and B. E. Launder, "The Prediction of Laminarization with a Two-Equation Model of Turbulence," *Int. J. Heat Mass Transf.*, vol. 15, pp. 301–314, 1972.

[23] B. Starke, J. Windt, and H. C. Raven, "Validation of viscous flow and wake field predictions for ships at full scale," no. September, pp. 17–22, 2006.

[24] F. R. Menter, "Two-Equation Eddy-Viscosity Turbulence Models for Engineering Applications," *AIAA J.*, vol. 32, no. 8, pp. 1598–1605, 1994.

[25] C. yu Guo, T. cheng Wu, Q. Zhang, and J. Gong, "Numerical simulation and experimental research on wake field of ships under off-design conditions," *China Ocean Eng.*, vol. 30, no. 5, pp. 821–834, 2016, doi: 10.1007/s13344-016-0053-3.

[26] M. Heydari and H. Sadat-Hosseini, "Analysis of propeller wake field and vortical structures

using k−ω SST Method," *Ocean Eng.*, vol. 204, no. March, 2020, doi: 10.1016/j.oceaneng.2020.107247.

[27] H. Jasak, V. Vukčević, I. Gatin, and I. Lalović, "CFD validation and grid sensitivity studies of full scale ship self propulsion," *Int. J. Nav. Archit. Ocean Eng.*, vol. 11, no. 1, pp. 33–43, 2019, doi: 10.1016/j.ijnaoe.2017.12.004.

[28] P. Rattanasiri, P. A. Wilson, and A. B. Phillips, "Numerical investigation of a pair of self-propelled AUVs operating in tandem," *Ocean Eng.*, vol. 100, pp. 126–137, 2015, doi: 10.1016/j.oceaneng.2015.04.031.

[29] N. Troldborg, N. N. Sørensen, P. E. Réthoré, and M. P. van der Laan, "A consistent method for finite volume discretization of body forces on collocated grids applied to flow through an actuator disk," *Comput. Fluids*, vol. 119, pp. 197–203, 2015, doi: 10.1016/j.compfluid.2015.06.028.

[30] X. Wu, Y. Wang, C. Huang, Z. Hu, and R. Yi, "An effective CFD approach for marine-vehicle maneuvering simulation based on the hybrid reference frames method," *Ocean Eng.*, vol. 109, pp. 83–92, 2015, doi: 10.1016/j.oceaneng.2015.08.057.

[31] G. Cvijetić, I. Gatin, V. Vukčević, and H. Jasak, "Harmonic Balance developments in OpenFOAM," *Comput. Fluids*, vol. 172, pp. 632–643, 2018, doi: 10.1016/j.compfluid.2018.02.023.

[32] D. Hally, "Propeller Analysis Using RANS/BEM Coupling Accounting for Blade Blockage," *4th Int. Symp. Mar. Propulsors*, no. June, pp. 297–304, 2015.

[33] D. Rijpkema, B. Starke, and J. Bosschers, "Numerical simulation of propeller-hull interaction and determination of the effective wake field using a hybrid RANS-BEM approach," *3rd Int. Symp. Mar. Propulsors*, no. May, pp. 421–429, 2013.

[34] V. I. Krasilnikov, "Self-Propulsion RANS Computations with a Single-Screw Container Ship," in *Third International Symposium on Marine Propulsors smp' 13, Launceston, Tasmania, Australia*.

[35] M. Beaudoin and H. Jasak, "Development of a Generalized Grid Interface for Turbomachinery simulations with OpenFOAM," in *Open Source CFD International Conference*, 2008, pp. 1–11.

[36] N. Yilmaz, M. Atlar, and M. Khorasanchi, "An improved Mesh Adaption and Refinement approach to Cavitation Simulation (MARCS) of propellers," *Ocean Eng.*, vol. 171, no. October 2018, pp. 139–150, 2019, doi: 10.1016/j.oceaneng.2018.11.001.

[37] H. Nouroozi and H. Zeraatgar, "A reliable simulation for hydrodynamic performance prediction of surface-piercing propellers using URANS method," *Appl. Ocean Res.*, vol. 92,

no. August, p. 101939, 2019, doi: 10.1016/j.apor.2019.101939.

[38] J. Yao, "Investigation on hydrodynamic performance of a marine propeller in oblique flow by RANS computations," *Int. J. Nav. Archit. Ocean Eng.*, vol. 7, no. 1, pp. 56–69, 2015, doi: 10.1515/ijnaoe-2015-0005.

[39] Z. Shen, D. Wan, and P. M. Carrica, "Dynamic overset grids in OpenFOAM with application to KCS self--propulsion and maneuvering," *Ocean Eng.*, vol. 108, pp. 287–306, 2015, doi: 10.1016/j.oceaneng.2015.07.035.

[40] A. Mofidi and P. M. Carrica, "Simulations of zigzag maneuvers for a container ship with direct moving rudder and propeller," *Comput. Fluids*, vol. 96, pp. 191–203, 2014.

[41] O. F. Sukas, O. K. Kinaci, F. Cakici, and M. K. Gokce, "Hydrodynamic assessment of planing hulls using overset grids," *Appl. Ocean Res.*, vol. 65, pp. 35–46, 2017, doi: 10.1016/j.apor.2017.03.015.

[42] J. Wang, L. Zou, and D. Wan, "Numerical simulations of zigzag maneuver of free running ship in waves by RANS-Overset grid method," *Ocean Eng.*, vol. 162, no. February, pp. 55–79, 2018, doi: 10.1016/j.oceaneng.2018.05.021.

[43] D. Kim, S. Song, and T. Tezdogan, "Free running CFD simulations to investigate ship manoeuvrability in waves," *Ocean Eng.*, vol. 236, no. June, p. 109567, 2021, doi: 10.1016/j.oceaneng.2021.109567.

[44] J. Carlton, *Marine Propellers and Propulsion*, 3rd ed. 2012.

[45] F. Çelik and M. Güner, "Energy saving device of stator for marine propellers," *Ocean Eng.*, vol. 34, no. 5–6, pp. 850–855, 2007, doi: 10.1016/j.oceaneng.2006.03.016.

[46] H. J. Shin, J. S. Lee, K. H. Lee, M. R. Han, E. B. Hur, and S. C. Shin, "Numerical and experimental investigation of conventional and un-conventional preswirl duct for VLCC," *Int. J. Nav. Archit. Ocean Eng.*, vol. 5, no. 3, pp. 414–430, 2013, doi: 10.3744/JNAOE.2013.5.3.414.

[47] N. Abbas, N. Kornev, I. Shevchuk, and P. Anschau, "CFD prediction of unsteady forces on marine propellers caused by the wake nonuniformity and nonstationarity," *Ocean Eng.*, vol. 104, pp. 659–672, 2015, doi: 10.1016/j.oceaneng.2015.06.007.

[48] M. K. Gokce, O. K. Kinaci, and A. D. Alkan, "Self-propulsion estimations for a bulk carrier," *Ships Offshore Struct.*, vol. 14, no. 7, pp. 656–663, 2019, doi: 10.1080/17445302.2018.1544108.

[49] F. Furcas and S. Gaggero, "Pre-swirl stators design using a coupled BEM-RANSE approach," *Ocean Eng.*, vol. 222, no. January, p. 108579, 2021, doi: 10.1016/j.oceaneng.2021.108579.

[50] K. Koushan, V. Krasilnikov, M. Nataletti, L. Sileo, and S. Spence, "Experimental and numerical study of pre-swirl stators PSS," *J. Mar. Sci. Eng.*, vol. 8, no. 1, 2020, doi: 10.3390/JMSE8010047.

[51] F. Mewis and T. Guiard, "Mewis Duct ® – New Developments , Solutions and Conclusions," *Second Int. Symp. Mar. Propulsors*, no. June, pp. 1–8, 2011.

[52] J. H. Kim, J. E. Choi, B. J. Choi, S. H. Chung, and H. W. Seo, "Development of Energy-Saving devices for a full Slow-Speed ship through improving propulsion performance," *Int. J. Nav. Archit. Ocean Eng.*, vol. 7, no. 2, pp. 390–398, 2015, doi: 10.1515/ijnaoe-2015-0027.

[53] J. Dang, H. Chen, D. Guoxiang, A. Van Der Ploeg, R. Hallmann, and F. Mauro, "An Exploratory Study on the Working Principles of Energy Saving Devices (ESDs)," *Symp. Green Sh. Technol.*, no. October, 2011.

[54] J. Dang, G. Dong, and H. Chen, "An Exploratory Study on the Working Principles of Energy Saving Devices (ESDs): PIV, CFD Investigations and ESD Design Guidelines," in *International Conference on Ocean, Offshore and Arctic Engineering*, 2012, p. 25, doi: 10.1115/OMAE2012-83053.

[55] S. Gaggero, J. Gonzalez-Adalid, and M. Perez Sobrino, "Design of contracted and tip loaded propellers by using boundary element methods and optimization algorithms," *Appl. Ocean Res.*, vol. 55, pp. 102–129, 2016, doi: 10.1016/j.apor.2015.12.004.

[56] S. Gaggero, J. Gonzalez-Adalid, and M. P. Sobrino, "Design and analysis of a new generation of CLT propellers," *Appl. Ocean Res.*, vol. 59, pp. 424–450, 2016, doi: 10.1016/j.apor.2016.06.014.

[57] A. Sánchez-Caja, J. González-Adalid, M. Pérez-Sobrino, and T. Sipilä, "Scale effects on tip loaded propeller performance using a RANSE solver," *Ocean Eng.*, vol. 88, no. 2006, pp. 607–617, 2014, doi: 10.1016/j.oceaneng.2014.04.029.

[58] K. J. Paik *et al.*, "Investigation on the Wake Evolution of Contra-Rotating Propeller using RANS Computation and SPIV Measurement," *Int. J. Nav. Archit. Ocean Eng.*, vol. 7, no. 3, pp. 595–609, 2015, doi: 10.1515/ijnaoe-2015-0042.

[59] K. Mizzi, Y. K. Demirel, C. Banks, O. Turan, P. Kaklis, and M. Atlar, "Design optimisation of Propeller Boss Cap Fins for enhanced propeller performance," *Appl. Ocean Res.*, vol. 62, pp. 210–222, 2017, doi: 10.1016/j.apor.2016.12.006.

[60] S. S. Lim, T. W. Kim, D. M. Lee, C. G. Kang, and S. Y. Kim, "Parametric study of propeller boss cap fins for container ships," *Int. J. Nav. Archit. Ocean Eng.*, vol. 6, no. 2, pp. 187–205, 2014, doi: 10.2478/IJNAOE-2013-0172.

[61] J. H. Kim, J. E. Choi, B. J. Choi, and S. H. Chung, "Twisted rudder for reducing fuel-oil consumption," *Int. J. Nav. Archit. Ocean Eng.*, vol. 6, no. 3, pp. 715–722, 2014, doi: 10.2478/IJNAOE-2013-0207.

[62] K. Ahn, G. H. Choi, D. I. Son, and K. P. Rhee, "Hydrodynamic characteristics of X-Twisted rudder for large container carriers," *Int. J. Nav. Archit. Ocean Eng.*, vol. 4, no. 3, pp. 322–334, 2012, doi: 10.3744/JNAOE.2012.4.3.322.

[63] S. Hai-Long, E. O. Obwogi, and S. Yu-Min, "Scale effects for rudder bulb and rudder thrust fin on propulsive efficiency based on computational fluid dynamics," *Ocean Eng.*, vol. 117, pp. 199–209, 2016, doi: 10.1016/j.oceaneng.2016.03.046.

[64] Y. J. Shin, M. C. Kim, J. H. Lee, and M. S. Song, "A numerical and experimental study on the performance of a twisted rudder with wavy configuration," *Int. J. Nav. Archit. Ocean Eng.*, pp. 1–12, 2018, doi: 10.1016/j.ijnaoe.2018.02.014.

[65] N. Sasaki, M. Atlar, and S. Kuribayashi, "Advantages of twin rudder system with asymmetric wing section aside a propeller: The new hull form with twin rudders utilizing duct effects," *J. Mar. Sci. Technol.*, vol. 21, no. 2, pp. 297–308, 2016, doi: 10.1007/s00773-015-0352-z.

[66] K. J. Lee, J. H. Bae, H. T. Kim, and T. Hoshino, "A performance study on the energy recovering turbine behind a marine propeller," *Ocean Eng.*, vol. 91, pp. 152–158, 2014, doi: 10.1016/j.oceaneng.2014.09.004.

[67] L. X. Hou, C. H. Wang, A. K. Hu, and F. L. Han, "Wake-adapted design of fixed guide vane type energy saving device for marine propeller," *Ocean Eng.*, vol. 110, pp. 11–17, 2015, doi: 10.1016/j.oceaneng.2015.09.036.

[68] H. J. Prins *et al.*, "Green Retrofitting through Optimisation of Hull-propulsion Interaction - GRIP," *Transp. Res. Procedia*, vol. 14, pp. 1591–1600, 2016, doi: 10.1016/j.trpro.2016.05.124.

[69] S. Paboeuf and A. Cassez, "ESD structural issue - UPstream device," *Int. Shipbuild. Prog.*, vol. 63, no. 3–4, pp. 291–314, 2017, doi: 10.3233/ISP-170135.

[70] D. B. Lee, B. S. Jang, and H. J. Kim, "Development of procedure for structural safety assessment of energy saving device subjected to nonlinear hydrodynamic load," *Ocean Eng.*, vol. 116, pp. 165–183, 2016, doi: 10.1016/j.oceaneng.2016.02.038.

[71] H. B. Ju, B. S. Jang, D. B. Lee, H. J. Kim, and C. K. Park, "A simplified structural safety assessment of a fin-typed energy saving devices subjected to nonlinear hydrodynamic load," *Ocean Eng.*, vol. 149, no. June 2017, pp. 245–259, 2018, doi: 10.1016/j.oceaneng.2017.12.022.

[72]   P. W. Wang, P. K. Liao, C. Y. Hsin, Y. Quéméner, and C. W. Lin, "Ship motions contribution to the fatigue life of a pre-swirl stator," in *Proceedings of PRADS2016*, 2016.

[73]   W. H. Tsou, P. C. Guan, W. H. Chang, and C. J. Chen, "Structural Design and Strength Estimation of Energy Saving Y-FIN by Using Finite Element Method," *Proc. 14th Int. Symp. PRADS 2019*, vol. 2, pp. 209–231, 2019, doi: 10.1007/978-981-15-4672-3_13.

[74]   Š. Malenica, E. Stumpf, F. X. Sireta, and X. B. Chen, "Consistent hydro-structure interface for evaluation of global structural responses in linear seakeeping," *Proc. Int. Conf. Offshore Mech. Arct. Eng. - OMAE*, vol. 6, no. 1, pp. 61–68, 2008, doi: 10.1115/OMAE2008-57077.

[75]   S. Malenica *et al.*, "HOMER - Integrated hydro-structure interactions tool for naval and off-shore applications," *RINA, R. Inst. Nav. Archit. - Int. Conf. Comput. Appl. Shipbuild. 2013, ICCAS 2013*, vol. 3, pp. 209–221, 2013.

[76]   I. Senjanović, Š. Malenica, and S. Tomašević, "Hydroelasticity of large container ships," *Mar. Struct.*, vol. 22, no. 2, pp. 287–314, 2009, doi: 10.1016/j.marstruc.2008.04.002.

[77]   I. Senjanović, S. Tomašević, and N. Vladimir, "An advanced theory of thin-walled girders with application to ship vibrations," *Mar. Struct.*, vol. 22, no. 3, pp. 387–437, 2009, doi: 10.1016/j.marstruc.2009.03.004.

[78]   I. Senjanović, N. Vladimir, M. Tomić, N. Hadžić, and Š. Malenica, "Global hydroelastic analysis of ultra large container ships by improved beam structural model," *Int. J. Nav. Archit. Ocean Eng.*, vol. 6, no. 4, pp. 1041–1063, 2014, doi: 10.2478/IJNAOE-2013-0230.

[79]   W. Dou, L. Zhang, G. Chen, and W. Zhu, "A combined radial basis function based interpolation method for fluid-structure interaction problems and its application on high-speed trains," *Adv. Eng. Softw.*, vol. 131, no. January, pp. 143–152, 2019, doi: 10.1016/j.advengsoft.2018.12.006.

[80]   D. Thomas *et al.*, "CUPyDO - An integrated Python environment for coupled fluid-structure simulations," *Adv. Eng. Softw.*, vol. 128, no. April 2018, pp. 69–85, 2019, doi: 10.1016/j.advengsoft.2018.05.007.

[81]   Š. Malenica and J. T. Tuitman, "3DFEM – 3DBEM model for springing and whipping analyses of ships," in *RINA Conf. on Design and Operation of Container Vessels.*, 2008.

[82]   J. Ji *et al.*, "Load mapping for seamless interface between hydrodynamics and structural analyses," *Adv. Eng. Softw.*, vol. 71, pp. 9–18, 2014, doi: 10.1016/j.advengsoft.2014.01.015.

[83]   T. Wang, R. Wüchner, and S. Sicklinger, "Assessment and improvement of mapping algorithms for non-matching meshes and geometries in computational FSI," *Comput. Mech.*, vol. 57, no. 5, pp. 793–816, 2016, doi: 10.1007/s00466-016-1262-6.

[84]   A. de Boer, "Computational fluid-structure interaction," TU Delft, 2008.

[85]   D. J. Piro and K. J. Maki, "Hydroelastic analysis of bodies that enter and exit water," *J. Fluids Struct.*, vol. 37, pp. 134–150, 2013, doi: 10.1016/j.jfluidstructs.2012.09.006.

[86]   N. Maman and C. Farhat, "Matching fluid and structure meshes for aeroelastic computations: A parallel approach," *Comput. Struct.*, vol. 54, no. 4, pp. 779–785, 1995, doi: 10.1016/0045-7949(94)00359-B.

[87]   C. Farhat, M. Lesoinne, and P. LeTallec, "Load and motion transfer algorithms for fluid/structure interaction problems with non-matching discrete interfaces: Momentum and energy conservation, optimal discretization and application to aeroelasticity," *Comput. Methods Appl. Mech. Eng.*, vol. 157, no. 1–2, pp. 95–114, 1998, doi: 10.1016/S0045-7825(97)00216-8.

[88]   K. J. Paik and P. M. Carrica, "Fluid-structure interaction for an elastic structure interacting with free surface in a rolling tank," *Ocean Eng.*, vol. 84, pp. 201–212, 2014, doi: 10.1016/j.oceaneng.2014.04.016.

[89]   L. Pernod, A. Ducoin, H. Le Sourne, J. A. Astolfi, and P. Casari, "Experimental and numerical investigation of the fluid-structure interaction on a flexible composite hydrofoil under viscous flows," *Ocean Eng.*, vol. 194, no. November, 2019, doi: 10.1016/j.oceaneng.2019.106647.

[90]   Z. Huang, Y. Xiong, and Y. Xu, "The simulation of deformation and vibration characteristics of a flexible hydrofoil based on static and transient FSI," *Ocean Eng.*, vol. 182, no. January, pp. 61–74, 2019, doi: 10.1016/j.oceaneng.2019.04.028.

[91]   K. J. Paik, P. M. Carrica, D. Lee, and K. Maki, "Strongly coupled fluid-structure interaction method for structural loads on surface ships," *Ocean Eng.*, vol. 36, no. 17–18, pp. 1346–1357, 2009, doi: 10.1016/j.oceaneng.2009.08.018.

[92]   O. el Moctar, J. Ley, J. Oberhagemann, and T. Schellin, "Nonlinear computational methods for hydroelastic effects of ships in extreme seas," *Ocean Eng.*, vol. 130, pp. 659–673, 2017, doi: 10.1016/j.oceaneng.2016.11.037.

[93]   T. Takami, S. Matsui, M. Oka, and K. Iijima, "A numerical simulation method for predicting global and local hydroelastic response of a ship based on CFD and FEA coupling," *Mar. Struct.*, vol. 59, no. August 2017, pp. 368–386, 2018, doi: 10.1016/j.marstruc.2018.02.009.

[94]   H. Xie, F. Liu, H. Tang, and X. Liu, "Numerical study on the dynamic response of a truncated ship-hull structure under asymmetrical slamming," *Mar. Struct.*, vol. 72, no. November 2018, p. 102767, 2020, doi: 10.1016/j.marstruc.2020.102767.

[95] P. A. Lakshmynarayanana and P. Temarel, "Application of CFD and FEA coupling to predict dynamic behaviour of a flexible barge in regular head waves," *Mar. Struct.*, vol. 65, no. May 2018, pp. 308–325, 2019, doi: 10.1016/j.marstruc.2019.02.006.

[96] J. T. Tuitman, Š. Malenica, and R. Van't Veer, "Generalized modes in time-domain seakeeping calculations," *Trans. - Soc. Nav. Archit. Mar. Eng.*, vol. 120, no. 4, pp. 228–246, 2013, doi: 10.5957/JOSR.56.4.100034.

[97] J. J. Jensen, "Stochastic procedures for extreme wave load predictions - Wave bending moment in ships," *Mar. Struct.*, vol. 22, no. 2, pp. 194–208, 2009, doi: 10.1016/j.marstruc.2008.08.001.

[98] J. J. Jensen, "Efficient estimation of extreme non-linear roll motions using the first-order reliability method (FORM)," *J. Mar. Sci. Technol.*, vol. 12, no. 4, pp. 191–202, 2007, doi: 10.1007/s00773-007-0243-z.

[99] J. J. Jensen, I. M. V. Andersen, and S. Seng, "Stochastic procedures for extreme wave induced responses in flexible ships," *Int. J. Nav. Archit. Ocean Eng.*, vol. 6, no. 4, pp. 1148–1159, 2014, doi: 10.2478/IJNAOE-2013-0236.

[100] G. De Hauteclocque, Q. Derbanne, and A. El-Gharbaoui, "Comparison of different equivalent design waves with spectral analysis," in *Proceedings of the International Conference on Offshore Mechanics and Arctic Engineering - OMAE*, 2012, vol. 1, pp. 353–361, doi: 10.1115/OMAE2012-83405.

[101] G. de Hauteclocque, Q. Derbanne, and T. Mienahou, "Non-linearity of extreme vertical bending moment - Comparison of design wave approaches and short term approaches," in *Proceedings of 32nd International Conference on Offshore Mechanics and Arctic Engineering*, 2013, pp. 1–9.

[102] Q. Derbanne, "Omae2012-8 Comparison of Design Wave Approach and Short Term Approach," *Omae*, no. 1979, pp. 1–10, 2012.

[103] V. Vukčević, "Numerical modelling of coupled potential and viscous flow for marine applications," Faculty of Mechanical Engineering and Naval Architecture, University of Zagreb, 2016.

[104] I. Gatin, V. Vukčević, and H. Jasak, "A framework for efficient irregular wave simulations using Higher Order Spectral method coupled with viscous two phase model," *J. Ocean Eng. Sci.*, vol. 2, pp. 253–267, 2017, doi: 10.1016/j.joes.2017.09.003.

[105] P. M. Carrica, H. Fu, and F. Stern, "Computations of self-propulsion free to sink and trim and of motions in head waves of the KRISO Container Ship (KCS) model," *Appl. Ocean Res.*, vol. 33, pp. 309–320, 2011.

[106] J. F. Otzen, C. D. Simonsen, and F. Stern, "RANS Simulation and Validation of Added Resistance and Motions of the KCS in Regular Head Waves," in *Proceedings of the Tokyo 2015: A Workshop on CFD in Ship Hydrodynamics*, 2015, vol. 3, pp. 273–278.

[107] M.-G. Seo, K.-K. Yang, D.-M. Park, and Y. Kim, "Numerical analysis of added resistance on ships in short waves," *Ocean Eng.*, vol. 87, pp. 97–110, 2014.

[108] H. Sadat-Hosseini, P.-C. Wu, P. M. Carrica, H. Kim, Y. Toda, and F. Stern, "CFD verification and validation of added resistance and motions of KVLCC2 with fixed and free surge in short and long head waves," *Ocean Eng.*, vol. 59, pp. 240–273, 2013.

[109] G. P. Filip and K. J. Maki, "Seakeeping Analysis of the KCS Vessel in Regular Waves," in *Proceedings of the Tokyo 2015: A Workshop on CFD in Ship Hydrodynamics*, 2015, vol. 3, pp. 419–424.

[110] T. Castiglione, F. Stern, S. Bova, and M. Kandasamy, "Numerical investigation of the seakeeping behavior of a catamaran advancing in regular head waves," *Ocean Eng.*, vol. 38, pp. 1806–1822, 2011, doi: 10.1016/j.oceaneng.2011.09.003.

[111] B. J. Guo, S. Steen, and G. B. Deng, "Seakeeping prediction of KVLCC2 in head waves with RANS," *Appl. Ocean Res.*, vol. 35, pp. 56–67, 2012.

Curiculum Vitae

Andro Bakica, born in Split, Croatia on 15th December 1992, has finished mathematical and natural sciences high school in Split. He has finished his undergraduate studies at the Faculty of Electrical Engineering, Mechanical Engineering and Naval Architecture, University of Split in 2015. and obtained his master's degree at the Faculty of Engineering, University of Rijeka with an award for excellence throughout the graduate programme in 2017. He defended his master thesis in the field of ship hydrodynamics with the use of Computational Fluid Dynamics (CFD) in OpenFOAM. Upon graduating he started an internship at the Bureau Veritas Research Department, Paris, France in the period of six months. Since October 2018 he works as a research assistant at the Chair of Marine Engineering, Faculty of Mechanical Engineering and Naval Architecture, University of Zagreb. He has published five articles in international peer-reviewed journals and participated at number of specialized conferences. His research interests include the following: ship hydrodynamics, hydro-structure interactions, ship design, numerical procedures, etc.

Summary of articles

1. **A. Bakica**, I. Gatin, V. Vukčević, H. Jasak, N. Vladimir: Accurate assessment of ship-propulsion characteristics using CFD, *Ocean Engineering*, Vol. 175, 2019.

2. N. Vladimir, **A. Bakica**, Š. Malenica, H.I. Im, I. Senjanović, D.S. Cho Numerical method for the vibration analysis of pre-swirl stator, *Ships and Offshore Structures*, 2021.

3. **A. Bakica**, Š. Malenica, N. Vladimir: Hydro-structure coupling of CFD and FEM – Quasi-static approach, *Ocean Engineering*, Vol. 217, 2020.

4. **A. Bakica**, N. Vladimir, H. Jasak, E. S. Kim: Numerical simulations of hydrodynamic loads and structural responses of a Pre-Swirl Stator, *International Journal of Naval Architecture and Ocean Engineering*, Vol. 13, 2021.

5. **A. Bakica**, Š. Malenica, N. Vladimir, I. Senjanović: Hydroelastic analysis of Pre-Swirl Stator, *Marine Structures*, Vol. 85, 2022.

6. **A. Bakica**, N. Vladimir, Š. Malenica, H.I. Im: Numerical Procedure for Pre-Swirl Stator Structural Integrity Evaluation, *Ocean engineering*, Vol. 258, 2022.

ARTICLE 1

Preprint of the published journal article.

Accurate assessment of ship-propulsion characteristics using CFD

Andro Bakica[a], Inno Gatin[a], Vuko Vukčević[a], Hrvoje Jasak[a,b,*], Nikola Vladimir[a]

[a]*University of Zagreb, Faculty of Mechanical Engineering and Naval Architecture, Ivana Lučića 5, Zagreb, Croatia*
[b]*Wikki Ltd, 459 Southbank House, SE1 7SJ, London, United Kingdom*

Abstract

In this paper RANS based CFD calm-water resistance and propulsion simulations of two benchmark cases (container ship KCS and bulk carrier JBC) are presented. Two-phase flow is handled using the Volume-of-Fluid method, while the discontinuities at the free surface are resolved using the Ghost Fluid Method. Propeller is modeled using an idealized pressure-jump actuator disk model, allowing large time step size suitable for naval hydrodynamics with the preservation of accuracy and CPU time efficiency. Computations are performed with the Naval Hydro Pack developed in FV framework of foam-extend, a community driven fork of OpenFOAM. Model scale KCS resistance and wave pattern is evaluated with a detailed analysis of the bare hull wake field following ITTC recommendations. Self propulsion simulation is carried out for the JBC case comparing the global features of the flow with the experiment.

Keywords: ship hydrodynamics, NavalHydro, foam–extend, wake field, actuator-disk, self-propulsion

---

[*]Corresponding author.
Email addresses: `andro.bakica@fsb.hr` (Andro Bakica), `inno.gatin@fsb.hr` (Inno Gatin), `vuko.vukcevic@fsb.hr` (Vuko Vukčević), `h.jasak@wikki.co.uk` (Hrvoje Jasak), `hrvoje.jasak@fsb.hr` (Hrvoje Jasak), `nikola.vladimir@fsb.hr` (Nikola Vladimir)

1. Introduction

For the last few decades computer technology has been exponentially evolving in an unrestrained manner bringing massive Central Processing Unit (CPU) power for acceptable price to the regular high-end users. Computational Fluid Dynamics (CFD) is greatly dependent on CPU power since the basis in solving a fluid flow of any kind is found in a non-linear Navier-Stokes (NS) equations with extensions, such as two phase-free surface flow. These require high computational effort to acquire a satisfactory solution.

According to Larsson et al. [1], on the Gothenburg 2010 Workshop approximately 80% of the participants used FV discretisation, while the rest relied on FD discretisation. Although the FV methods are only second-order accurate (see Jasak [2]) simplicity of the method in developing complex geometries and straightforward implementation of complex mathematical models is deemed invaluable since, in most engineering applications, second order accuracy is found sufficient.

In order to validate the FV based CFD a set of benchmark cases is experimentally tested and data is made publicly available (e.g. Kim et al. [3], Van et al. [4], Olivieri et al. [5]) which, together with workshop gatherings in Gothenburg (Larsson et al. [1]) or Tokyo (Hino [6], Larsson et al. [7]), ensure an improvement of numerical tools.

Wide range of publications is available on the topic of the analysis of the Korea Research Institute for Ships and Ocean Engineering (KRISO) Container Ship case. Experimental data for KRISO Container Ship (KCS) is openly available at [8] for a different number of cases ranging from simple towing tank tests in calm water or head seas to wake and flow field study (Kim et al. [3]) and self propulsion (Hino [6]).

Starke et al. [9] used a FD type solver PARNASSOS for Reynolds Averaged Navier Stokes (RANS) equations and obtained accurate results when comparing computed and experimental wave elevation. Interesting observation is made comparing viscous and non-linear potential flow solver on a stern wave system where a clear overestimation of wave height in potential flow can be seen due to neglecting the diffusion term in the NS equations. Also, in the study, it is obvious that two equation turbulence model produces much better results for the wake field analysis then a simpler one equation model. Ozdemir et al. [10] employed a commercial code STAR CCM+ and obtained satisfactory results for resistance and wave elevation using k-ϵ turbulence model (Jones and Launder [11]). However, results for the wake field

are fairly diffused, most probably due to the first order discretisation that was used for advection.

Enger et al. [12] carried out a detail investigation with Star CCM+ using different turbulence models where the best results were obtained for k-ϵ model with a y^+ value ranging from 40 to 60. Geometrical properties of the boundary layer were set with three parameters: overall thickness (20 mm), expansion rate (1.5) and number of layers (6). Through the given parameters the resulting first layer height is 0.9 mm. Test was made by lowering the number of layers to four, but keeping the overall thickness and expansion rate the same. Discrepancy in results was evident on the coarsest mesh, increasing the error by 1.6%.

In Guo et al. [13] an experiment on KCS hull is made by measuring the wake field using Particle Image Velocimetry (PIV) and comparing the results with Kim et al. [3], where a pitot tube, stereoscopic camera and other equipment is used. Sufficient agreement was found between the data. Obtained results are then compared with the computed result from STAR CCM+ using the k-ω Shear Stress Transport (SST) model (Menter [14]) where good agreement was found between the wake fields, but no quantitative data comparison was given beside the visual inspection. A somewhat different approach is seen in Banks et al. [15] using an ANSYS CFX RANS flow solver on a structured grid. Results were compared for the k-ω SST model and the baseline model. Similar results are produced by both models for resistance and wave elevation. Further on, for a self propulsion simulation using body force model, it is concluded that in order to achieve accurate computation of propulsion forces a greater level of detail is needed in the propeller inflow region. Wave elevation is correctly captured in almost every study and depends mostly on mesh grid density in the vertical direction near the free surface (also advised in ITTC [16]).

Regarding self-propulsion cases, modeling the propeller behind the hull in sliding mesh technique (Yang et al. [17]) or using dynamic overset grids (Caricca et al. [18], Shen et al. [19]) are obviously one of the first choices. However, problem is in dealing with different time scales of the flow around the hull and the propeller. In order to simulate physically correct interaction between the propeller and the hull, simulation time-step must be adjusted to the propeller rotation which drastically increases computational time. Max time-step size in such cases corresponds to the 2-3 degrees of rotation of the propeller. If for model scale propeller rotation equals to 7-8 rps, global and local time scale can differ from $\mathcal{O}(10)$ to $\mathcal{O}(10^3)$ depending on the solver. At

3

the same time, another problem lies in creating a good quality mesh topology in such cases.

Another approach is to model the flow around the hull and the propeller inflow as two separate problems, where a different solver can be used for each part of the simulation. As for the coupling procedure, Badoe et al. [20] coupled blade element theory and the momentum theory (BEMt) with RANS calculations in OpenFOAM. Coupling procedure is made by converting local thrust and torque into momentum sources which are added into the equations until convergence is reached. Effective wake field is defined by total wake field and then subtracting the propeller induced velocities calculated from the BEMt code. On the other hand, Hally [21], proposed a Boundary Element Method (BEM) and RANS coupling, also implemented in Open-FOAM. In order to account for the blade blockage a mass source term is added in the pressure and the momentum equation, where the effect of blade blockage is estimated at about 1% on the resulting thrust force.

Another example of RANS/BEM coupling is presented in Rijpkema et al. [22]. Computed nominal wake in RANS calculations without the propeller in action is used as an input for BEM computation. Pressure loading distribution on propeller is then interpolated as a body force field in RANS simulation and scaled to provide equal thrust, if necessary. Total wake field is computed with RANS and the propeller induced velocities are subtracted to obtain the effective wake field. The process is repeated until there is no change in thrust and effective wake velocities in the coupling. This approach is very similar to one used in Krasilnikov [23], where a panel method is used to solve the pressure distribution on propeller blades followed by the implementation of calculated forces in the actuator disk region in RANS simulation. The process is repeated until the imbalance between propeller thrust and hull resistance becomes smaller than desired tolerance.

The present paper will introduce a different way of modeling the actuator disk forces as a momentum jump condition for the normal and tangential component at the location of the propeller mid-plane which is applied only on the adjacent mesh faces which significantly simplifies the numerical implementation and simulation setup. Only the mean features of the flow are considered, where instead of using external algorithms (Badoe et al. [20], Rijpkema et al. [22], Krasilnikov, [23]), the entire computation is being done inside a single CFD simulation. In order to avoid the complex coupling procedure, completely different approach will be considered for self-propulsion case by applying the correction on the inflow velocity based on the momen-

4

tum transfer in the vicinity of the actuator disk which will be described in the Sec. 2.3 and by using the Proportional-Integral (PI) controller to achieve the desired thrust. Only the most important characteristics of the self-propulsion condition will be evaluated in order to achieve high CPU efficiency, thus ignoring the local flow features near the propeller.

The current study is divided into three sections. The first section is dedicated to mathematical equations and numerical discretisation with a short description of meshing procedure. The second section describes the KCS case setup from the Gotenburg 2010 Workshop for resistance (Case 2.2a) on a coarse mesh with wave elevation and wake field (Case 2.1) evaluated on a more refined mesh in order to compute a more accurate result. The third section is dedicated to Japanese Bulk Carrier (JBC) resistance (Case 1.1a) and self-propulsion (Case 1.5a) from the Tokyo 2015 Workshop with only the global aspects of the flow being evaluated on a coarse mesh.

KCS case is chosen for the wake field analysis due to invaluable data quality with proven high degree of accuracy. However, for the KCS there was no equal experimental setup for the resistance and self-propulsion test without the rudder to properly evaluate the thrust deduction coefficient. For the stated reason, JBC is chosen for the self-propulsion test leaving an opportunity to demonstrate the solver consistency and accuracy on different hull forms and Froude numbers.

Regarding resistance and wake field on the KCS case, similar geometrical properties of the boundary layer mesh are used as in [12], but the effect of the overall layer thickness on the solution is observed. In all of the previously mentioned studies, if wake field was investigated, results were found sufficiently accurate using k-ω SST model with second order discretisation schemes. Some authors (Krasilnikov [23], Enger et al. [12]) report that most precise results can be obtained with Reynolds Stress Model (RSM), but at the cost of larger computation expense and decrease of simulation stability. For the current analysis, k-ω SST model is weighted as the best choice.

Solver used for the study is `navalFoam` and it is a part of an in-house code library Naval Hydro Pack developed in the `foam-extend` environment. It is a community driven fork of OpenFOAM software for Computational Continuum Mechanics using FV discretisation in an arbitrary polyhedral framework(see Weller et al. [24]).

2. Mathematical and Numerical Model

This section contains the governing equations for the resistance and self-propulsion flow cases. Detailed mathematical background is given for the two-phase incompressible flow followed by the actuator disk (AD) model implemented (Šeb [25]) in the Naval Hydro Pack. Interface capturing is accomplished using the Volume-of-Fluid (VOF) method (Ubbink et al. [26]) while for the handling of the free surface discontinuities, the Ghost Fluid Method (GFM) (Huang et al. [27], Desjardin et al. [28], Lalanne [29]) is used. To account for the turbulence in the flow, k-ω SST (Menter [14]) model with standard wall functions is used, where only the calculation of the main variables is given. Discretisation methods and coupling procedure for pressure and velocity are briefly mentioned. For the rigid body motion and flow-motion coupling the reader is referred to Gatin el al.[30], for details.

2.1. Governing Equations

Mathematical model is based on the following assumptions which are justified for large scale flows in naval hydrodynamics: surface tension is considered negligible and tangential stress balance is taken into account assuming continuous effective viscosity and velocity gradient. However, the dynamic pressure jump due to the density jump and continuity of the velocity field (kinematic boundary condition) is obtained without simplifications.

Since both fluids are considered incompressible with constant density and continuous velocity field, the continuity equation reads:

$$\nabla_{\bullet}\mathbf{u} = 0. \tag{1}$$

The momentum equation or the Navier-Stokes equation for the incompressible two-phase flow with the previously defined assumptions taken into account is defined as:

$$\frac{\partial \mathbf{u}}{\partial t} + \nabla_{\bullet}(\mathbf{uu}) - \nabla_{\bullet}(\nu_e \nabla \mathbf{u}) = -\frac{1}{\rho(\mathbf{x})}\nabla p + \mathbf{g}, \quad \mathbf{x} \in \Omega_a \cup \Omega_w \cup \Gamma_{wa}, \tag{2}$$

where Ω_w and Ω_a stand for water phase and air phase, respectively. Γ_{wa} denotes the free surface, $\mathbf{x}$ is the position vector, ∇p is the pressure gradient, $\mathbf{g}$ is gravitational acceleration and ν_e is the effective kinematic viscosity.

Using the decomposition of the pressure term on dynamic and static component(Rusche [31]):

$$p = p_d + \rho \mathbf{gx}, \tag{3}$$

6

where p_d is the dynamic pressure, yields a different formulation of the combined two-phase flow in the gravitational field:

$$\frac{\partial \mathbf{u}}{\partial t} + \nabla\bullet(\mathbf{uu}) - \nabla\bullet(\nu_e \nabla \mathbf{u}) = -\frac{1}{\rho(\mathbf{x})}\nabla p_d. \tag{4}$$

Terms from left to right are: transient, convection, diffusion and dynamic pressure gradient term. Free surface Γ_{wa} is labeled separately due to usage of GFM (Huang et al. [27]). GFM handling of the free surface in mathematical formulation is defined in the following equations:

- discontinuity of the density field

$$[\rho] = \rho_a - \rho_w, \quad \mathbf{x} \in \Gamma_{wa}, \tag{5}$$

- continuity of pressure

$$[p] = 0, \quad \mathbf{x} \in \Gamma_{wa}, \tag{6}$$

- pressure gradient jump condition due to kinematic boundary condition (continuity of the velocity field at the free surface)

$$[\frac{\nabla p}{\rho}] = 0, \quad \mathbf{x} \in \Gamma_{wa}, \tag{7}$$

where [.] is a jump condition operator as used in Huang et al. [27], while ρ_a and ρ_w are the air and water densities, respectively.

For interface capturing (VOF) method is used (Ubbink et al. [26]) which is based on an indicator function α that takes the value of 0 or 1 inside the air phase or water phase, respectively. Transport equation for α reads:

$$\frac{\partial \alpha}{\partial t} + \nabla\bullet(\mathbf{u}\alpha) + \nabla\bullet\mathbf{u}_r\alpha(1-\alpha) = 0, \tag{8}$$

where the terms are (from left to right) unsteady, convective and compressive term. Compressive term (see Rusche [31] for details) prevents excessive smearing of the interface while the implementation in the current work will be described in more detail in Sec. 2.2. $\mathbf{u}_r$ stands for compressive velocity which is only used in the vicinity of the free surface due to the multiplier $\alpha(1-\alpha)$.

Effective viscosity is assumed continuous across the interface approximating the tangential stress balance:

$$\nu_e = \alpha\nu_{e,w} + (1-\alpha)\nu_{e,a}, \tag{9}$$

7

where $\nu_{e,w}$ and $\nu_{e,a}$ are effective kinematic viscosities for water and air, respectively. It is important to notice that smearing of the interface due to usage of GFM does not affect the density field:

$$\rho(\mathbf{x}) = \begin{cases} \rho_w & \text{if } \alpha(\mathbf{x}) \geq 0.5 \\ \rho_a & \text{if } \alpha(\mathbf{x}) < 0.5 \end{cases}, \tag{10}$$

A brief description of the used turbulent model is needed to be able to solve the given Reynolds Averaged Navier Stokes (RANS) equations. $k - \omega$ SST model is fully described in Menter [14], so here only the procedure to specify the far-field boundary condition for the variables of turbulent kinetic energy k and specific dissipation rate ω will be presented. Value of k is defined as:

$$k = \frac{3}{2}(UI)^2, \tag{11}$$

where U is the free stream velocity and I is the assumed turbulence intensity. Used values for turbulent intensity of KCS case is 3% and 2% for JBC simulation. Specific dissipation rate is obtained following Eça and Hoekstra, [32]:

$$\omega = 10\frac{U}{L_{PP}}, \tag{12}$$

where L_{PP} is ship length between perpendiculars.

Next step is to properly discretise given equations so that the numerical solution adheres to the solution of the proposed partial differential equations. For full text concerning two-phase incompressible flow coupled with GFM and VOF see Vukčević et al. [33] and Vukčević [34].

2.2. Numerical Model

Discretisation schemes used in this study will be briefly mentioned in this section. For details about FV discretisation of any arbitrary polyhedral Control Volume reader is referred to Jasak [2]. Temporal derivative is discretised using first order accurate Euler implicit scheme, since quasi steady-state solution is sought. Convective term is discretised using the Gauss theorem, while for the interpolation from cell center to face center linear upwind-biased interpolation is used. Explicit correction, in order to achieve a second order accurate solution, is made with the gradient extrapolation from an upwind cell. All gradients are discretised using least square fit (see Jasak and Weller

[35]) with or without limiters to accomplish a second order accurate solution despite of mesh skewness. Diffusion term is discretised using the Gauss theorem with linear interpolation using the over relaxed approach for the non-orthogonal correction [2].

Following Vukčević [33] a segregated pressure-velocity coupling is accomplished and interface-corrected schemes are used in the vicinity of the free surface to account for the discontinuous jumps (Eqn. (5), Eqn. (6) and Eqn. (7)). To mark the interface faces, compact polyhedral computational stencil is used. Reader can refer to Vukčević [33] for more details regarding interface-corrected approach.

In α transport Eqn. (8) Euler implicit scheme is used for temporal derivative, convective term is discretised using the Gauss theorem with Van Leer's Total Variation Diminishing scheme (Van Leer, [36]) with deferred correction (Ferziger and Perić [37]) that ensures scalar field boundedness between zero and one. The compressive term is discretised using the Gauss theorem yielding compressive fluxes which are dependent on the compressive velocity $\mathbf{u}_r$, which is defined in Jasak et al. [38] as:

$$\mathbf{u}_r = c_\alpha \mathbf{n}_\Gamma \frac{CFL_{ref}|\mathbf{d}_f|}{\Delta t}, \tag{13}$$

where c_α denotes a compression constant with default value of one, $\mathbf{n}_\Gamma$ is a unit vector normal to the free surface, CFL_{ref} is a reference compression Courant Friefrichs Levy number, $\mathbf{d}_f$ is the distance between neighboring control volumes and Δt is the time step. Interpolation scheme in the compressive term is specially designed to be upwind if the interface is sharp, while switching to central differences with appropriate weighting factors if the interface smearing becomes too large. For full details regarding the α equation see Rusche [31] and for the implementation details see Jasak et al. [38].

Solving large sparse matrices produced by a FV mesh is achieved using a Krylov Subspace method with Conjugate Gradient (CG) method and a Cholesky preconditioner for a symmetric pressure equation, while for asymmetrical matrices (three components of velocity, indicator function and turbulence variables) Biconjugate Gradient Stabilized Method (BiCGStab) is used [39].

Pressure, velocity and free surface capturing are coupled with a combination of SIMPLE (Patankar and Spalding, [40]) and PISO algorithm where a PISO pressure-velocity loop is nested inside an outer SIMPLE loop updating

9

the pressure multiple times per one momentum-equation update [41]. Due to prior experience with the solver, two outer (SIMPLE) and two inner (PISO) loops are deemed sufficient for a steady state solution. For a complete description of the solution algorithm the reader is referred to Vukčević [33].

To avoid wave reflection from the boundaries of the domain, relaxation zones are set up following the procedure from [42].

2.3. Actuator Disk

Actuator disk model following the Goldstein optimum distribution ([43]) will be explained in this section (for full details on the implementation of the theory in OpenFOAM see Šeb [25]). A mathematical model for an ideal propeller (infinitely thin disc) is based on the modeling of only the two most important aspects of a functional propeller: the torque and thrust forces. Regarding ship propulsion, torque - Q and thrust - T are usually given in dimensionless form with respect to the advance coefficient J which is defined as:

$$J = \frac{V_A}{nD}, \tag{14}$$

where V_A is the advance speed, n is the propeller rotation rate and D is the propeller diameter. Values of $T(J)$ and $Q(J)$ are obtained from the open water test curve and used to determine pressure and tangential velocity jump for thrust and torque, respectively. Since the advance speed V_A in an experimental set-up is equal to carriage speed for given thrust, in order to properly compute the inflow velocity on the propeller plane, correction of the axial velocity is needed. From the actuator disk theory propeller thrust can be calculated as the mass flux at the propeller plane and the difference in flow velocities (Jasak et al. [38]):

$$T = \rho_w A_D V_D (V_2 - V_1), \tag{15}$$

where A_D is the actuator disk surface, V_D is the axial speed at the propeller plane while V_1 and V_2 are velocities in front and behind the propeller, respectively. Note that the velocity V_D, following the actuator disk theory, can be defined as:

$$V_D = 0.5(V_2 + V_1). \tag{16}$$

If V_2 is expressed as the unknown and linked with the Eqn. (15), the inflow velocity $V_1 = V_A$ can then be computed, after rearranging the terms,

as:
$$V_A = V_{D,CFD} - \frac{T}{2\rho_w A_D V_{D,CFD}}, \tag{17}$$

where the second term on the r.h.s. accounts for the velocity correction due to the propeller suction on the inflow side while $V_{D,CFD}$ is the averaged velocity in the propeller axis direction gathered from the AD faces in the computational domain.

Non-linearity of the Eqn. (17) for the advance speed, since T is a function of J, is easily solved inside of a single time-step in a segregated solution algorithm for pressure-velocity coupling. Pressure jump is calculated as [38]:

$$\Delta p = \frac{105}{8\pi} \frac{T(J)}{(R_P - R_H)(3R_H + 4R_P)} f_T(r), \tag{18}$$

where R_H is the hub radius, R_P is the propeller radius and $f_T(r)$ is defined as [38]:

$$f_T(r) = r^* \sqrt{1 - r^*}, \tag{19}$$

where r^* is the normalized disc radius defined as:

$$r^* = \frac{r' - r'_h}{1 - r'_h}, \tag{20}$$

where $r'_h = R_H/R_P$ and $r' = r/R_P$. The tangential velocity jump that models the swirl caused by the propeller in action is calculated using following expression [38]:

$$\Delta u_t = \frac{105}{8\pi} \frac{Q(J)}{u_x(R_P - R_H)(3R_H + 4R_P)} f_Q(r), \tag{21}$$

where u_x is the axial speed at the propeller plane and $f_Q(r)$ is defined as [38]:

$$f_Q(r) = \frac{r^* \sqrt{1 - r^*}}{r^*(1 - r^*) + r'_h}, \tag{22}$$

Note that Δu_t is imposed tangentially at the propeller plane, in the circumferential direction.

FV framework makes it suitable to easily collect the set of faces on which computed pressure and velocity jumps are imposed. Four parameters are needed to define the AD model: location of the propeller plane, direction of

11

the propeller thrust, propeller and hub radius. Using the given parameters AD faces are collected and imposed with a special type of boundary condition. Reader should be aware that such boundary faces are in fact internal faces of the mesh coinciding with the position of the propeller mid-plane. If there are no faces present at the exact propeller mid-plane location, the imposed boundary condition will be forced upon the next set of closest mesh internal faces. It is obvious that the quality and the density of the mesh in the given region has a significant role in the definition of the AD. However, when performing self-propulsion simulation mesh is expected to be thoroughly refined in the stern region so the location of the propeller mid-plane is easily satisfied to an acceptable tolerance.

Regarding the numerical implementation, imposing a jump conditions on the chosen set of faces is straightforward and much more simplified compared to the volumetric source terms in the body force model which are added to the right hand side of the momentum equation. In the following text the procedure of prescribing the pressure jump is described.

During the outer SIMPLE and inner PISO loop, boundary conditions are updated several times in order to ensure the conservation of quantities in the domain. In the time instance of each boundary condition update, pressure jump calculated in Eqn. (18) is added to the current value of the pressure field on the chosen AD faces. Due to the iterative type of solution algorithm, both the pressure field and the pressure jump converge to a certain value. Although, if it happens that the required thrust and computed thrust are not equal, pressure jump is simply scaled to account for the difference. Same procedure is applied on the velocity in the circumferential direction. Also, it should be noted that the AD boundary condition requires as an input a propeller open water test data to compute the thrust and torque during the simulation.

Coupling between the body motion and the AD is fully resolved by recalculating the thrust direction axis and AD faces position after each mesh motion update.

3. KCS Resistance and Flow Field Study

One of the most studied and validated cases in modern naval hydrodynamics CFD is the KCS case, featured in both Gothenburg ([1]) and Tokyo Workshops ([6], [7]). A wide range of numerical results are validated against the experimental data as shown in the introduction, with good overall agree-

ment.

Simulations around the KCS hull are divided into two sections. The first section is dedicated to drag coefficient calculation by varying the boundary layer thickness in order to study the effect of the near-wall layer mesh resolution on drag data and to approximate the optimal boundary layer for the further wake field analysis. The goal is to find the smallest possible boundary layer thickness while preserving the accuracy of the results in order to have a good quality mesh in the propeller region where high boundary layer thickness produces skewed and non-orthogonal cells thus disrupting the downstream solution.

The study is performed on a coarse mesh to save CPU time. Suitable boundary layer is then chosen and the mesh is refined for the second simulation, where the entire flow field is evaluated, giving special attention to detailed wake field analysis. The grid uncertainty is not evaluated in this study.

The mesh for all cases spans $2L_{PP}$ from amidship section to the inlet, $2.5L_{PP}$ to the outlet and $2L_{PP}$ to side boundaries. Only half of the ship is being simulated since the flow problem is symmetric. The mesh height from the free surface to the top boundary is $1L_{PP}$, while the bottom boundary is set at $1.5L_{PP}$ below the free surface.

3.1. Steady Resistance - Case 2.2a (Gothenburg 2010)
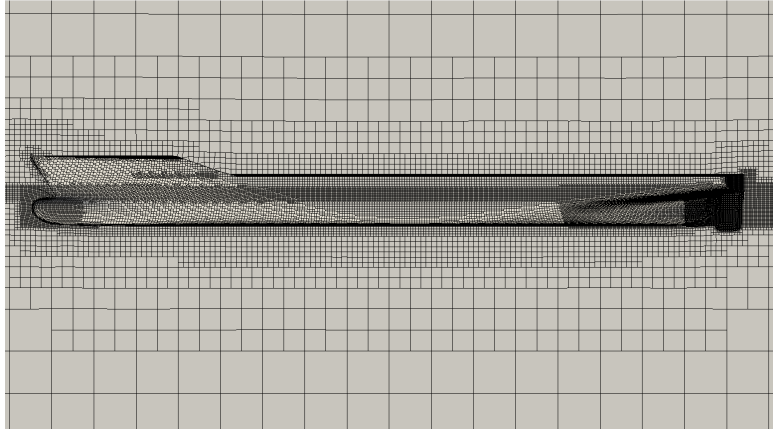
Fig. 1: KCS - coarse mesh with rudder.

13

For this case, rudder is added to hull geometry in order to match the experimental conditions (see Fig. 1). Fluid properties are set up to correspond the towing tank ([8]) Reynolds and Froude number of 1.4×10^7 and 0.26, respectively. Ship particulars are given in Table 1. Boundary layer disretisation is varied in thickness (10 mm, 15 mm, 20 mm) and number of layers (5 or 6) where the initial boundary layer parameters are taken from [12]. Consequently, by changing the boundary layer mesh, dimensionless distance y^+ on the hull is being altered, but it retains a suitable value for all meshes, ranging from 40 to 80. Generated grid consists of roughly 0.640×10^6 cells for each mesh, where most of the cells are hexahedrons with a maximum non-orthogonality of $70°$, skewness of 4 and only 10 cells in the z direction near the free surface.

Table 1: KCS model particulars.

Length between perpendiculars	$L_{PP}(m)$	7.2785
Maximum beam of waterline	$B_{WL}(m)$	1.0190
Depth	$D(m)$	0.6013
Draft	$d(m)$	0.3418
Wetted surface area w/o rudder	$S_{w/orudder}(m^2)$	9.438
Wetted surface area of rudder	$S_{w/rudder}(m^2)$	0.115
Block coefficient	C_B	0.6505
Model Speed	$U(m/s)$	2.19699
Reynolds number	Rn	1.4×10^7
Froude number	Fr	0.26
Propeller diameter	D_P	0.25
Hub ratio		0.18
Propeller center, long. location (from FP)	x/L_{PP}	0.983
Propeller center, vert. location (below WL)	$-z/L_{PP}$	0.02913

Besides the residuals reaching a satisfactory tolerance and the continuity of mass and volume preserved in the whole domain, force acting on the hull is used a convergence criterion. Fig. 2 shows convergence of the force acting on the hull after being converted into the dimensionless drag coefficient for a mesh with six layers and 20 mm layer thickness. The drag coefficient is decomposed into viscous and pressure components with the viscous component compared to the ITTC 1957 correlation line:

$$C_F = \frac{0.075}{(\log Re - 2)^2}. \tag{23}$$

Slight overshoot of the viscous component is considered adequate due to the

hull coefficient impact on the viscous part of a few percent. Results for all grids are presented in Table 2. Experimental friction coefficient C_F in the Table 2 is computed from Eqn. (23).
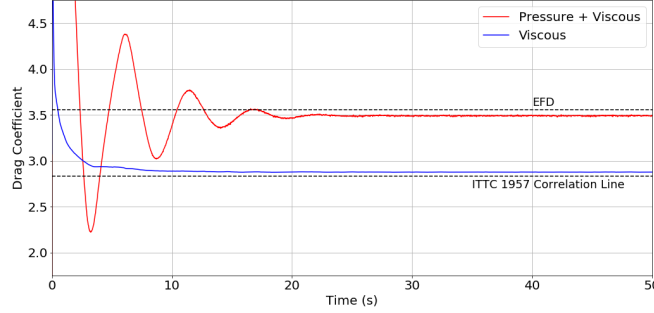

Fig. 2: Convergence of drag coefficient for mesh with 6 layers and 0.20m thickness.

The solution is in reasonable agreement with experimental results, while the computed error becomes significant when lowering the boundary layer thickness to a value of $10\,\mathrm{mm}$, most probably due to the boundary layer being too thin to properly evaluate the flow near the hull and resolve the velocity gradient. Evaluating the computed results, a five layer mesh with a $15\,\mathrm{mm}$ thickness and 1.4 expansion rate is regarded as sufficient for wake field analysis in the next section.

Table 2: KCS Resistance results with varying boundary layer.

Boundary layer parameters				$C_T \times 10^{-3}$	Error(%)	$C_F \times 10^{-3}$	Error(%)
Thickness	Layer	Expansion	First layer height				
$20\,\mathrm{mm}$	6	1.5	$0.9\,\mathrm{mm}$	3.508	1.38%	2.898	-2.33%
$20\,\mathrm{mm}$	5	1.5	$1.5\,\mathrm{mm}$	3.492	1.83%	2.899	-2.37%
$15\,\mathrm{mm}$	6	1.4	$0.9\,\mathrm{mm}$	3.493	1.81%	2.877	-1.60%
$15\,\mathrm{mm}$	5	1.4	$1.4\,\mathrm{mm}$	3.476	2.28%	2.881	-1.66%
$10\,\mathrm{mm}$	5	1.35	$0.9\,\mathrm{mm}$	3.398	4.47%	2.797	1.25%
Experiment				3.557		2.832	

3.2. Flow Field Study - Case 2.1 (Gothenburg 2010)

Based on the above, the mesh for the flow field analysis is refined to approximately 2×10^6 cells, also with mostly hexahedron cells and 16 cells
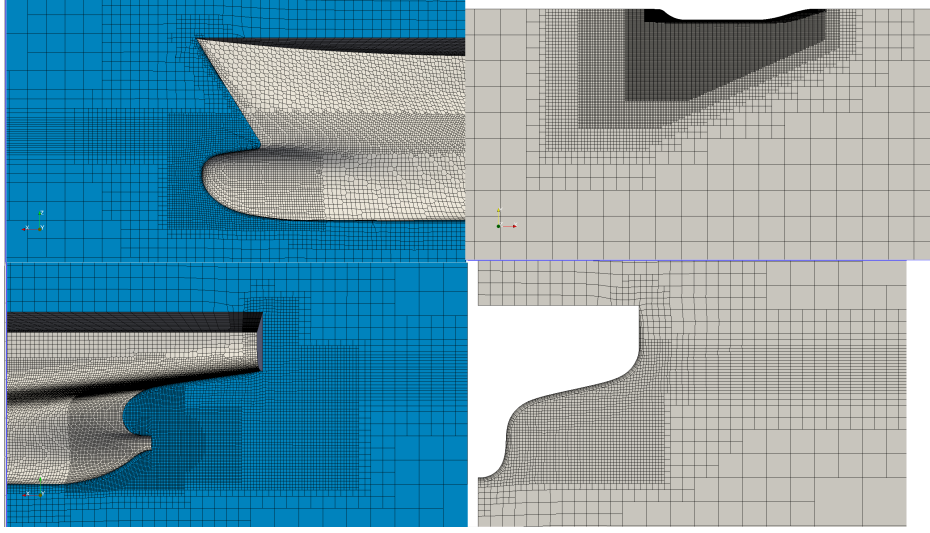
Fig. 3: KCS - Final mesh geometry.

in the vertical z direction near the free surface, Fig. 3. Also, the rudder is removed from the mesh to match the experimental condition [8]. The jump in the drag force time signal at around 45 seconds is visible in Fig. 4 due to switching off the limiters on the gradient schemes, yielding a second order accurate solution. Limiters are used in the beginning in order to stabilize the simulation. Another measure of convergence shown in Fig. 4 is the wetted surface area that stabilizes, proving sharp and stable resolution of the interface on the hull.
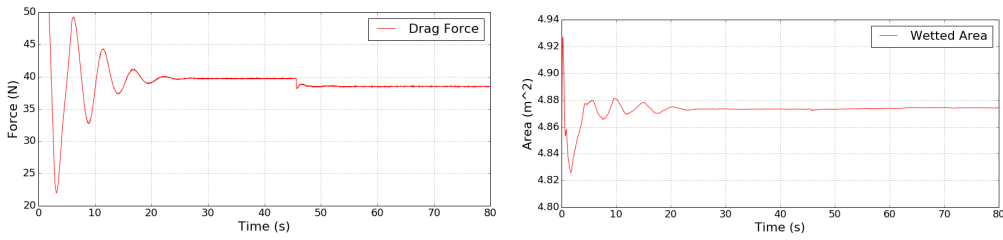
Fig. 4: Convergence of drag force(left) and wetted area(right) for fine mesh in the KCS case.

16
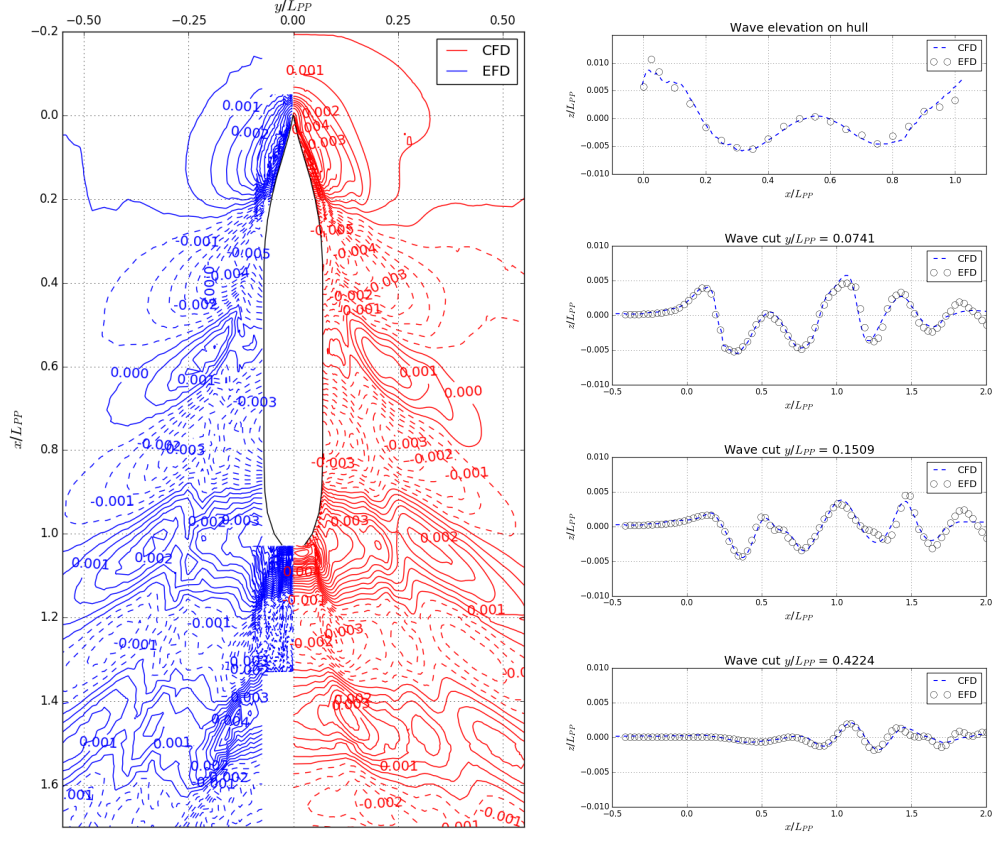
Fig. 5: Wave elevation comparison.

Fig. 5 shows the wave elevation compared with the experiment where accurate correlation between the data is observed. Surprisingly, even the bow crest is well captured together with a complex stern wave field caused by the immersed transom. Small diffusion in the results is most probably due to mesh coarsening in the given area. The graph is obtained using a contour plot for $\alpha = 0.5$.

Apart from the wave field, free surface elevation on the hull is reported together with three longitudinal cuts on the y plane. Results are also compared in Fig. 5. Correlation with the experiment is found to be satisfactory. Loss of accuracy in the results after $L_{PP} = 1.5$ is mostly due to mesh coarsening, which is also the cause of slightly inaccurate comparison on the $y/L_{PP} = 0.4224$ cut.
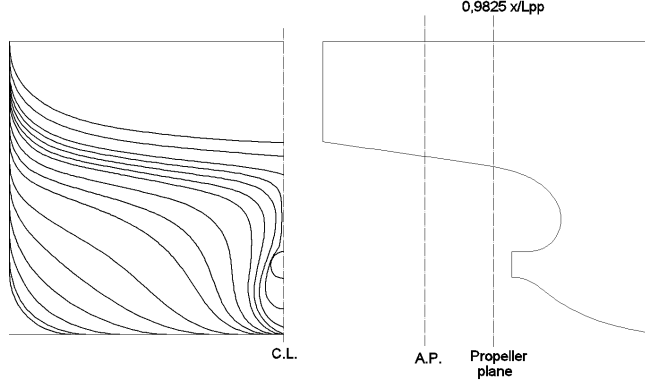
Fig. 6: Hull sections on the stern of the KCS case.

Regarding the wake field study, a detailed analysis is performed following the ITTC, Practical Guidelines for RANS Calculation of Nominal Wake Fields [44]. Data is examined in order to evaluate the flow pattern in the propeller location. In Fig. 6, hull sections and the propeller plane are shown for a more clear visual correlation between the hull shape and the wake fraction contours.Wake fraction contours are presented in Fig. 7, where the intermediate solution with gradient limiters is also shown.
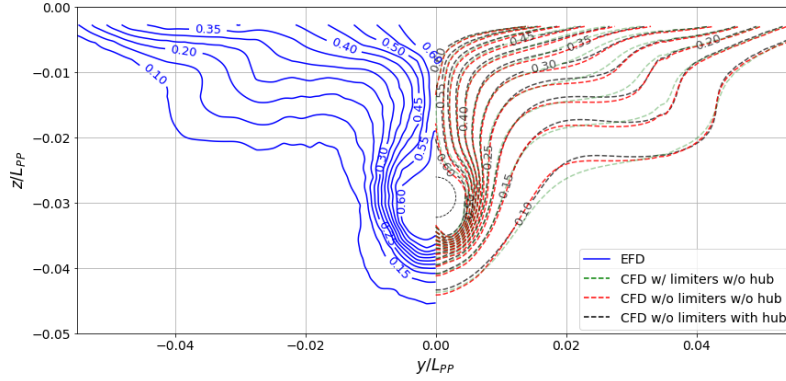
Fig. 7: Wake fraction contours at the propeller plane.

Nonetheless, it is clear that the flow is adequately captured with the gradient clipping, hence it should always be weighted if the limiters should be

18

removed, since the removal can introduce a high amount of instability in the simulation in the regions of insufficient mesh resolution and in the areas of low mesh quality.

From the contour plot in Fig. 7, overestimation of the so-called hook-like shaped vortices is observed, as well as that the vortex center is moved vertically comparing to the experiment. Due to a fine stern shape, bilge vortices are not clearly identified because fuller stern frame-lines usually generate stronger vortices (as noted in Van et al. [45]). However, according to Kim et al. [3], in the experimental setup a dummy hub was used to prevent the abrupt change in the flow after stern boss. To match the setup more correctly, a hub was placed inside of the computational mesh and the results are shown in Fig. 7. Vortex center is moved downwards, but the intensity of the hook-shape vortex remains overestimated.
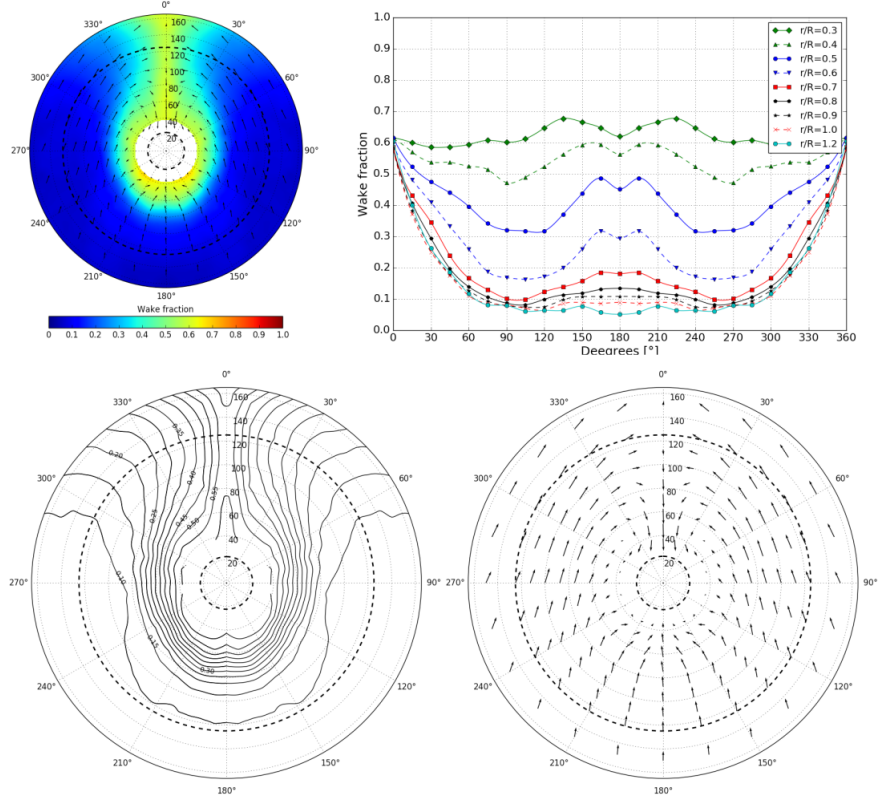
Fig. 8: EFD - wake field on the propeller plane.
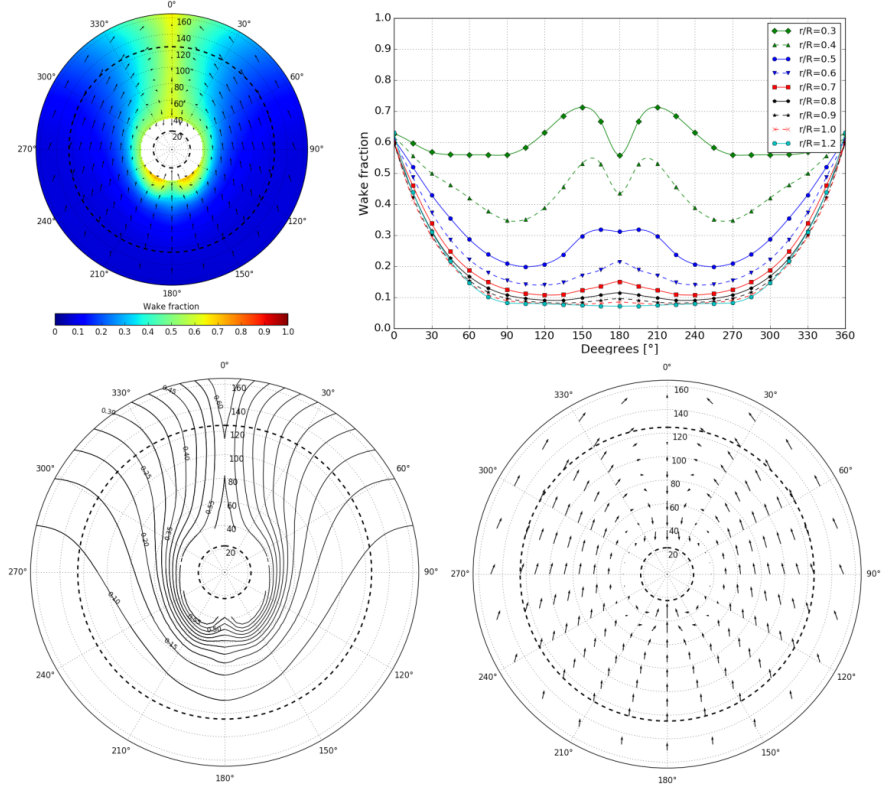
Fig. 9: CFD - wake field on the propeller plane.

For further analysis, data is extrapolated for the experimental values near the center of the propeller plane in order to get a fully resolved plot of wake fraction contours. The values near the center were out of the calibration range due to high vorticity in the experiment [3]. Experimental and numerical results are shown in Fig. 8 and Fig. 9, with the propeller hub and the tip of the propeller plotted as dashed circles. Radius dimensions are in millimeters, while transverse velocities are drawn every 15° degrees in the circumferential direction from the smallest radius of $r/R = 0.3$ to $r/R = 1.2$ according to ITTC [44], where R is the propeller radius. Numerical values with the dummy hub were used for comparison in order to be more consistent with the experimental setup.

To make a more detailed investigation of the flow field, each referenced radii is compared to experimental values. Circumferential mean wake comparison at each propeller radius is shown in Fig. 10. The error is clearly
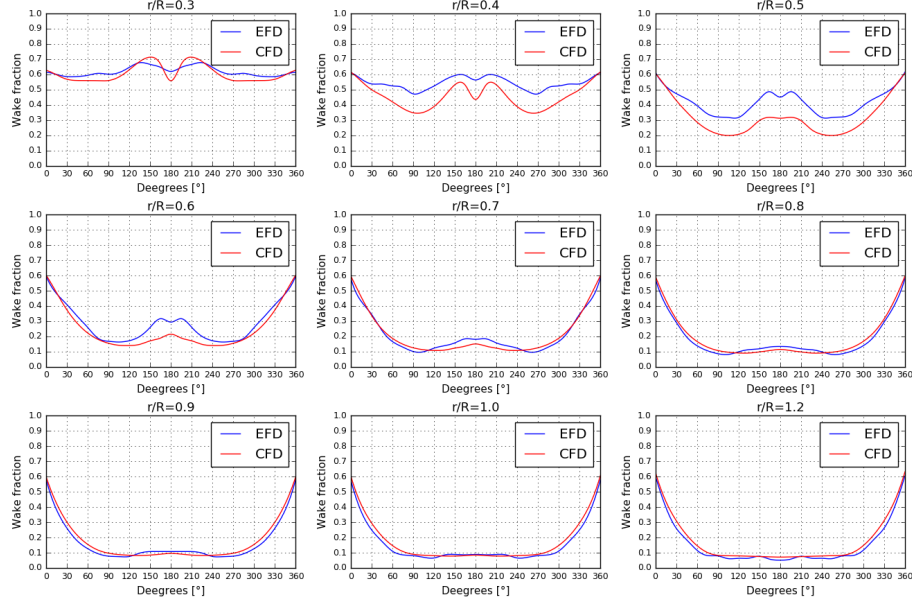
Fig. 10: Comparison of circumferential wake.

higher closer to the center of the propeller and the reason is due to a more complex flow near the propeller hub. To further analyze the results, a mean wake fraction of every reference radii is also presented in Table 3. Errors are below 6% for the range of $r/R =$ between 0.6 to 1.2, while for the r/R lower than 0.5 the error remains within 20%.

To achieve a more clear view of the comparison, a radial wake distribution shall be plotted together with the experimental results, Fig. 11. By integrating the circumferential wakes following the procedure from ITTC [46] a nominal wake can be computed for a propeller plane from 30% to 100% of propeller diameter. The comparison of nominal wake is also shown in Table 3 with differences in the inflow velocities on the propeller plane below 3%. The nominal wake in both cases should be somewhat larger because the flow from the hub to $r/R = 0.3$ is ignored.

In the experiment, axial velocities along a vertical cut on the propeller plane were measured with a probe that was set-up along a z-coordinate just below the center of propeller. Values are compared in Fig. 12. where good agreement is observed. Large scale aspects of the flow are computed correctly while the small scale flow disturbances are not captured.

To conlude, acceptable results have been computed at the propeller

21

Table 3: Comparison of radial wake distribution.

	EFD	CFD	Error (%)
r/R	$1 - w_{EFD}$	$1 - w_{CFD}$	
0.3	0.38	0.394	-3.68%
0.4	0.457	0.546	-19.47%
0.5	0.586	0.687	-17.24%
0.6	0.717	0.759	-5.86%
0.7	0.791	0.795	-0.51%
0.8	0.823	0.816	0.85%
0.9	0.841	0.828	1.55%
1.0	0.851	0.833	2.12%
1.2	0.852	0.832	2.35%
Nominal wake (from 0.3 to 1.0 r/R)			
	$1 - w_{n_{EFD}}$	$1 - w_{n_{CFD}}$	
	0.753	0.772	2.52%
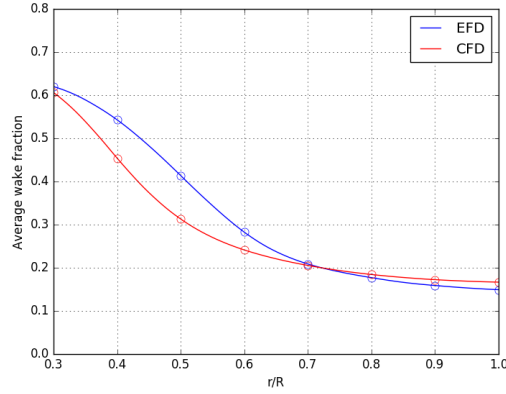
Fig. 11: Radial wake distribution.

plane using a $k - \omega$ SST model for model scale. However, it should be clear that the amount of turbulence present in model scale is not equivalent to full scale, hence in full scale the wake field is less dependent on the turbulence model.

4. JBC - Resistance and Self-Propulsion

In the this section, AD is implemented inside of the computational mesh for JBC hull to evaluate bare hull resistance and capture the global features of the flow in self-propulsion condition. Propeller open water test data are provided in [47] as an input for the AD . The main dimensions of the JBC
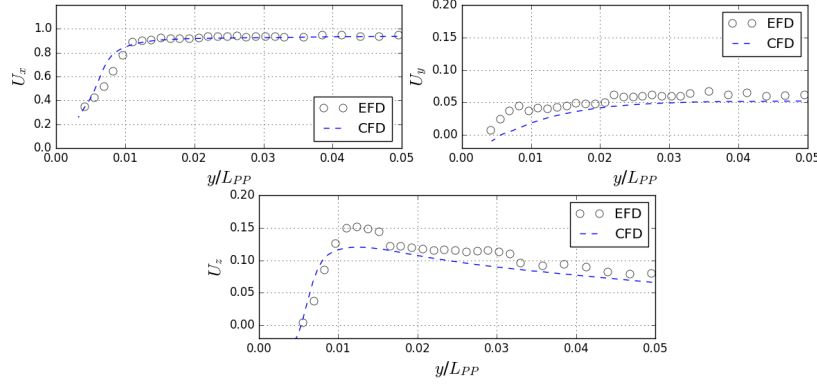
Fig. 12: Velocity components comparison at $z/L_{PP} = 0.0302$.

hull are presented in Table 4. No coupling is made with an external (BEM or BEMt) solver. Instead, the flow is resolved inside the FV mesh using the AD model with local flow phenomena (such as blade blockage etc.) being neglected.

Table 4: JBC model particulars.

Length between perpendiculars	$L_{PP}(m)$	7.000
Maximum beam of waterline	$B_{WL}(m)$	1.125
Depth	$D(m)$	0.625
Draft	$d(m)$	0.4125
Wetted surface area w/o ESD	$S_{w/oESD}(m^2)$	12.223
Block coefficient	C_B	0.858
Metacentric height	$GM(m)$	0.133
Moment of Inertia	K_{xx}/B	0.4
Moment of Inertia	$K_{yy}/L_{PP}, K_{zz}/L_{PP}$	0.25
Model Speed	$U(m/s)$	1.197
Reynolds number	Rn	7.46×10^6
Froude number	Fr	0.142
Propeller diameter	D_P	0.203
Hub ratio		0.18
Propeller center, long. location (from FP)	x/L_{PP}	0.985714
Propeller center, vert. location (below WL)	$-z/L_{PP}$	-0.04042
Vertical center of gravity (from keel)	$KG(m)$	0.3323
LCB(% L_{PP}), fwd+		2.5475

To properly evaluate the asymmetry in the propeller flow due to the tangential velocity jump related to torque force modeling, full domain is simulated. Mesh with 1.012×10^6 cells is used. Note that the mesh models the

whole ship instead of half, thus this resolution corresponds to approximately 0.5×10^6 cells in half of the domain. The hull shape extracted from the mesh with the AD present is shown in Fig. 13. The mesh is generated in the manner as in the KCS case. The AD is implemented inside of the FV mesh in the last step, after the entire mesh is completed. Similar approach as in Sec. 3.1 is applied to approximate the optimum boundary layer thickness which resulted in a four boundary layers with expansion rate of 1.2 and a overall layer thickness of 12 mm, yielding an average y^+ value of 40 to 60 on the hull. Mesh metrics are similar as in the KCS case.

Instead of performing two separate simulations for steady resistance and self-propulsion, a single simulation is performed where the AD is being turned on when the drag force for the bare hull converges, thus saving CPU time. Convergence of the drag force is shown in Fig. 14.
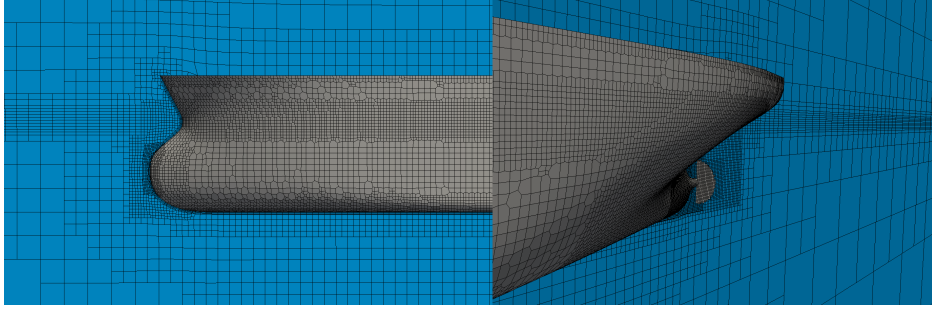
Fig. 13: JBC bow (left) and stern mesh with actuator disk (right).
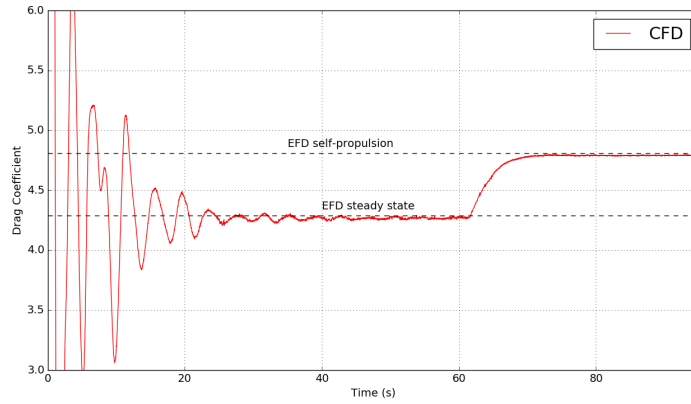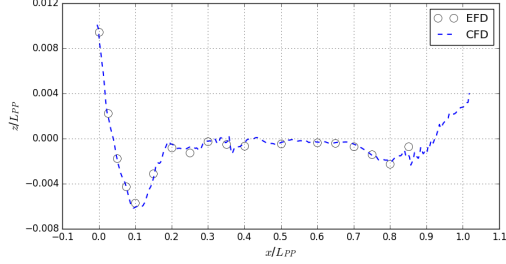

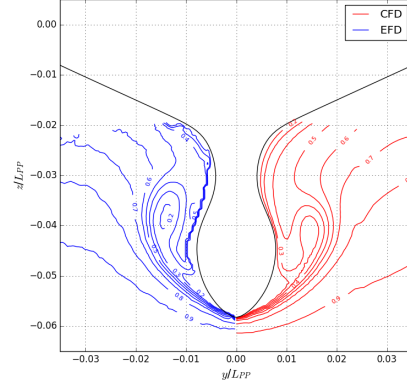Fig. 14: Force convergence on JBC hull.

24

Fig. 15: Wave elevation on hull.

Fig. 16: U_X at $x/L_{PP} = 0.9625$.

4.1. Bare hull

First, bare hull results are evaluated where the resistance is measured with the AD turned off. Wave elevation comparison along the hull is shown in Fig. 15, where good agreement between experimental ([47]) and numerical results is observed. In Fig. 16 and Fig. 17 contours of axial velocities are plotted on plane $x/L_{PP} = 0.9625$ where the bilge vortices start to form, and on a plane $x/L_{PP} = 0.9843$ just before the propeller plane with hub and propeller radius indicated by dashed lines. Main features of the flow are accurately captured with certain amount of diffusion present in numerical results. Intensity of bilge vortices is underestimated, with the inflow axial velocities on plane $x/L_{PP} = 0.9843$ obviously exhibiting similar behavior as in the experiment with certain asymmetry present in the flow. Nonetheless, good overall agreement is obtained.
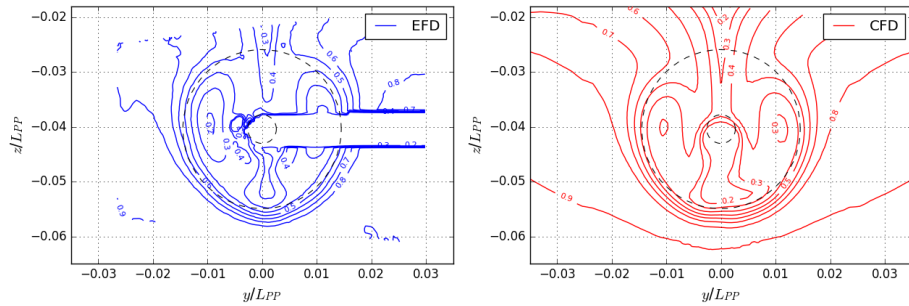

Fig. 17: Axial velocities $x/L_{PP} = 0.9843$, dashed lines hub and propeller tip.

4.2. Self propulsion

After 60 seconds of the simulation AD is turned on, measuring the computed resistance for self-propulsion condition. Initial rotation rate on AD is set to zero in order to avoid sudden jumps in the flow that may cause instabilities in the simulation. Average mean velocity on the propeller plane is calculated from the simulation, while the effective wake field is established using an inflow velocity corrected approach described in Sec. 2.3. Results from the experiment and the simulation are used to compute the experimental and numerical thrust deduction t coefficient to investigate the influence of the suction of the propeller on the hull stern pressure distribution. Thrust deduction is calculated as:

$$t = \frac{R_{t,SP} - R_t}{R_{t,SP}}, \tag{24}$$

where $R_{t,SP}$ and R_t are the resistance force at self-propulsion and towing tank condition, respectively. Propeller rotation rate is varied depending on the following coefficient (notation used as in [23]):

$$\Delta = R_{t,SP} - SFC - T, \tag{25}$$

where SFC is the skin friction correction equal to $18.2N$ from the experimental setup, $R_{t,SP}$ is the resistance force on the hull and T is the computed thrust on the AD. PI controller is used to control the propeller rotation rate, while the intention is to keep the force imbalance Δ minimum as possible. Due to the unsteady nature of the flow behind the hull and varying resistance force in each time step Δ is able to converge on a minimum value of about 1% of the resistance force with a rotation rate of $7.4\,\text{RPS}$ opposed to the experimental $7.8\,\text{RPS}$.

Mean axial velocity is integrated from $0.4R$ to propeller tip due to a loss of data near the hub in the experiment. For the same reason, only the left side of the axial velocities in the EFD data is used for calculation. Lower rotation rate in the CFD simulation is expected due to the lower mean axial velocity on the propeller plane of 0.445 compared to the 0.452 in the experimental setup. Since thrust is modeled in terms of advance coefficient J (Eqn. (14)) any decrease in the inflow velocity must be accounted by the decrease in n to compute the same thrust.

In Fig. 18 contour plot at $x/L_{PP} = 0.9625$ cut shows increased axial velocities compared with Fig. 16 where AD is not working. Results show the

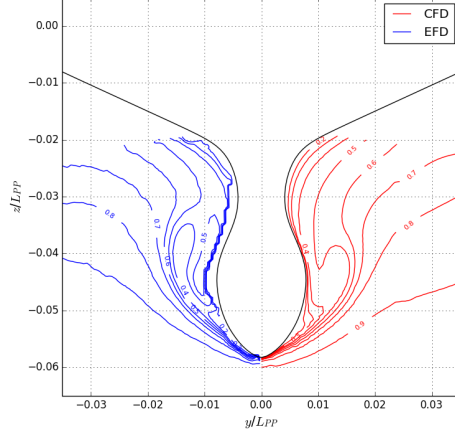comparable amount of numerical smearing as in the bare hull simulation.

Fig. 18: U_x at $x/L_{PP} = 0.9625$ with AD working.

Complete results for bare hull resistance and self-propulsion simulation are presented in Table 5. Experimental C_F is computed using Eqn. (23). Resistance coefficient for both resistance and self-propulsion simulation is in a good agreement with the experiment with relative error smaller than 1% for both cases. Propeller suction on the hull stern is properly modeled which can be seen as the small relative error of the thrust deduction coefficient of 0.56%. High relative error of sinkage and trim are due to small absolute values, which are below one cell height resolution in the current mesh. Notable error in computation of thrust and torque coefficients is present and overestimated for about 8%, while the error is linked to the inflow velocities on the propeller plane being inaccurately computed as seen in Fig. 17.

Table 5: JBC Results.

	w/o AD				with AD			
	$C_T \times 10^3$	$C_F \times 10^3$	Sinkage $(\%L_{PP})$	Trim $(\%L_{PP})$	$C_{SP} \times 10^3$	K_T	K_Q	t
CFD	4.270	3.073	-0.092	-0.197	4.797	0.235	0.0299	0.1091
EFD	4.289	3.159	-0.086	-0.18	4.811	0.217	0.0279	0.1085
Error (%)	-0.44	2.71	6.97	9.44	-0.29	8.3	7.16	0.56

27

Results for the entire JBC simulation are found to be satisfactory. Use of a PI controller and inflow velocity momentum correction proved to be reliable for simplification of the self-propulsion condition with an idealized thin disc. In the given setup, AD activation is implemented as a run time modifiable variable allowing the user to modify activation time while the simulation is running.

Regarding CPU efficiency, a straightforward comparison can be made with the real propeller simulation. Time step used for the current simulation is equal to 1×10^{-2} s. As stated in the introduction in a real propeller simulation a maximum allowable time step is constrained by the approximately 2 degrees of propeller rotation. In the current case, propeller rotation rate equals to 7.8 RPS which can be easily used to derive the maximum time step value of approximately 7×10^{-4} s. Compared to the current simulation the CPU time would be increased by more than ten times at the least. Also, for the real propeller simulation the grid density and size would have to be significantly increased in the stern region to properly evaluate the complex propeller flow and geometry, all of which additionally increase the CPU time.

5. Conclusion

Numerical approach in the FV framework of Naval Hydro has proved accurate for evaluation of resistance and the flow field around the ship. Ghost Fluid Method handling of interface discontinuities has produced a very high resolution of the free surface position together with the Volume-of-Fluid conservative treatment of the two-phase flow preserving both mass and volume inside of the domain. For both of the simulated hull geometries with different Froude numbers, CFD code has demonstrated consistency and reliability.

Regarding the wake field study, detailed qualitative investigation of the KCS wake field has shown good agreement with the experimental results using $k - \omega$ SST model, yielding a total mean inflow velocity difference of only 2.52%. Closer to the propeller hub complexity and turbulence of the flow increases with the relative error being under 20%. For r/R ratio above 0.6 correlation between the data is very accurate. Since the flow in the propeller region is demanding to capture even experimentally, numerical results are found satisfactory.

Resistance on both ships (KCS and JBC) has shown good correlation between the numerical and experimental results. Both resistance tests are done on the coarse mesh, with the relative error on JBC case under 1% and for

the KCS case around 1-2.5% depending on the mesh boundary layer. Self-propulsion condition for JBC using an actuator disk computed with sufficient accuracy added amount of resistance to the hull due to suction from the propeller, yielding a thrust deduction coefficient relative error of 0.56%. Such formulation can be used in early steps of the hull design process to improve propeller and hull interaction at low CPU cost.

For future work, a more thorough investigation with multiple mesh refinements and inclusion of local flow effects should be considered for use in the later stages of the ship and propeller design.

Acknowledgement

References

[1] L. Larsson, F. Stern, M. Visonneau, Numerical Ship Hydrodynamics: An assessment of the Gothenburg 2010 workshop, Springer, 2013. `doi: 10.1007/978-94-007-7189-5`.

[2] H. Jasak, Error Analysis and Estimation for the Finite Volume Method with Applications to Fluid Flows, Ph.D. thesis, Imperial College of Science, Technology & Medicine, London (1996).

[3] W. J. Kim, S. H. Van, D. H. Kim, Measurement of flows around modern commercial ship models, Experiments in Fluids 31 (5) (2001) 567–578. `doi:10.1007/s003480100332`.

[4] S. H. Van, W. J. Kim, G. T. Yim, K. D. H., C. J. Lee, Experimental Investigation of the Flow Characteristics Around Practical Hull Forms, in: Proceedings of the 3rd Osaka Colloguium on Advanced CFD Applications to Ship Flow and Hull Form Design, 1998.

[5] A. Olivieri, F. Pistani, A. Avanaini, F. Stern, R. Penna, Towing Tank Experiments of Resistance, Sinkage and Trim, Boundary Layer, Wake and Free Surface Flow Around a Naval Combatant INSEAN 2340 Model, no. IIHR Report No. 421, 56 pp, Iowa Institute of Hydraulic Research, The university of Iowa, 2001.

[6] T. Hino, Proceedings of CFD Workshop Tokyo 2005, NMRI report, 2005.

[7] Tokyo 2015: A Workshop on CFD in Ship Hydrodynamics, in: L. Larsson, F. Stern, M. Visonneau, N. Hirata, T. Hino, J. Kim (Eds.), Tokyo 2015: A Workshop on CFD in Ship Hydrodynamics, Vol. 3, NMRI (National Maritime Research Institute), Tokyo, Japan, 2015.

[8] Chalmers University of Technology, Gothenburg 2010: A Workshop on CFD in Ship Hydrodynamics, \url{http://www.insean.cnr.it/sites/default/files/gothenburg2010/index.html} (2010).

[9] B. Starke, J. Windt, H. C. Raven, Validation of viscous flow and wake field predictions for ships at full scale (September) (2006) 17–22.

[10] Y. H. Ozdemir, T. Cosgun, A. Dogrul, B. Barlas, A numerical application to predict the resistance and wave pattern of KRISO Container Ship, Brodogradnja/Shipbuilding 67 (2) (2016) 47–65.
URL `http://dx.doi.org/10.21278/brd67204`

[11] W. Jones, B. E. Launder, The Prediction of Laminarization with a Two-Equation Model of Turbulence, International Journal of Heat and Mass Transfer 15 (1972) 301–314.

[12] S. Enger, M. Peric, R. Perić, Simulation of Flow Around KCS-Hull, in: Gothenburg 2010: A Workshop on CFD in Ship Hydrodynamics, Gothenburg, Sweden, 2010.
URL `http://www.cd-adapco.com/sites/default/files/conference{_}proceeding/pdf/CDadapcoPaper.pdf`

[13] C. yu Guo, T. cheng Wu, Q. Zhang, J. Gong, Numerical simulation and experimental research on wake field of ships under off-design conditions, China Ocean Engineering 30 (5) (2016) 821–834. `doi: 10.1007/s13344-016-0053-3`.

[14] F. R. Menter, Two-Equation Eddy-Viscosity Turbulence Models for Engineering Applications, AIAA J. 32 (8) (1994) 1598–1605.

[15] J. Banks, A. Phillips, P. Bull, S. Turnock, RANS simulations of the multiphase flow around the KCS hullform, in: Gothenburg 2010: A Workshop on CFD in Ship Hydrodynamics Gothenburg, 2010.

[16] ITTC, Recommended Procedures and Guidelines: Practical Guidelines for Ship CFD, 26th International Towing Tank Conference (2011) 1–18.

[17] C. Yang, H. D. Lu, R. Löhner, On the simulation of highly nonlinear wave-breakwater interactions, Journal of Hydrodynamics 22 (5 SUPPL. 1) (2010) 932–938. `doi:10.1016/S1001-6058(10)60055-8`. URL `http://dx.doi.org/10.1016/S1001-6058(10)60055-8`

[18] P. M. Carrica, A. Mofidi, E. Martin, Progress Toward Dircet CFD simulation of Manoeuvres in Waves, in: Proceedings of the MARINE 2015 Conference, 2015, pp. 327–338.

[19] Z. Shen, D. Wan, P. M. Carrica, Dynamic overset grids in OpenFOAM with application to KCS self–propulsion and maneuvering, Ocean Eng. 108 (2015) 287–306. `doi:10.1016/j.oceaneng.2015.07.035`.

[20] C. Badoe, A. Phillips, S. R. Turnock, Ship wake field analysis using a coupled BEMt-RANS approach, in: NuTTS '14: 17th Numerical Towing Tank Symposium, Marstrand, Sweden, Chalmers University of Technology, 6pp, 2014.

[21] D. Hally, Propeller Analysis Using RANS/BEM Coupling Accounting for Blade Blockage, 4th International Symposium on Marine Propulsors (smp'15) (June) (2015) 297–304.

[22] D. Rijpkema, B. Starke, J. Bosschers, Numerical simulation of propeller-hull interaction and determination of the effective wake field using a hybrid RANS-BEM approach, 3rd International Symposium on Marine Propulsors (May) (2013) 421–429.

[23] V. I. Krasilnikov, Self-Propulsion RANS Computations with a Single-Screw Container Ship, in: Third International Symposium on Marine Propulsors smp' 13, Launceston, Tasmania, Australia.

[24] H. G. Weller, G. Tabor, H. Jasak, C. Fureby, A tensorial approach to computational continuum mechanics using object oriented techniques, Computers in Physics 12 (1998) 620–631.

[25] B. Šeb, Master thesis, Faculty of Mechanical Engineering and Naval Architecture, University of Zagreb, Croatia, Numerical characterisation of a ship propeller (2017).

[26] O. Ubbink, R. I. Issa, A method for capturing sharp fluid interfaces on arbitrary meshes, J. Comput. Phys. 153 (1999) 26–50.

[27] J. Huang, P. M. Carrica, F. Stern, Coupled ghost fluid/two–phase level set method for curvilinear body–fitted grids, Int. J. Numer. Meth. Fluids 44 (2007) 867–897. doi:10.1002/fld.1499.

[28] O. Desjardins, V. Moureau, H. Pitsch, An accurate conservative level set/ghost fluid method for simulating turbulent atomization, J. Comput. Phys. 227 (18) (2008) 8395–8416.

[29] B. Lalanne, L. R. Villegas, S. Tanguy, F. Risso, On the computation of viscous terms for incompressible two-phase flows with Level Set/Ghost Fluid Method, J. Comput. Phys. 301 (2015) 289–307.

[30] I. Gatin, V. Vukčević, H. Jasak, H. Rusche, Enhanced coupling of solid body motion and fluid flow in finite volume framework, Ocean Engineering 143 (December 2016) (2017) 295–304. doi:10.1016/j.oceaneng.2017.08.009.

[31] H. Rusche, Computational Fluid Dynamics of Dispersed Two-Phase Flows at High Phase Fractions, Ph.D. thesis, Imperial College of Science, Technology & Medicine, London (2002). doi:10.1145/1806799.1806850.
URL http://portal.acm.org/citation.cfm?doid=1806799.1806850

[32] L. Eça, M. Hoekstra, The numerical friction line, J Mar Sci Technol (2008) 328–345doi:10.1007/s00773-008-0018-1.

[33] V. Vukčević, H. Jasak, I. Gatin, Implementation of the Ghost Fluid Method for free surface flows in polyhedral Finite Volume framework , Computers & Fluids 153 (2017) 1–19.

[34] V. Vukčević, Numerical modelling of coupled potential and viscous flow for marine applications, Ph.D. thesis, Faculty of Mechanical Engineering and Naval Architecture, University of Zagreb (2016).

[35] H. Jasak, H. G. Weller, Application of the finite volume method and unstructured meshes to linear elasticity, Int. J. Numer. Methods Eng. 48 (2000) 267–287.

[36] B. van Leer, Towards the Ultimate Conservative Difference Scheme. {IV}. {A} New Approach to Numerical Convection, J. Comput. Phys. 23 (1977) 276–299.

[37] J. H. Ferziger, M. Peric, Computational Methods for Fluid Dynamics, Springer, 1996.

[38] H. Jasak, V. Vukčević, I. Gatin, I. Lalović, CFD Validation and Grid Sensitivity Studies of Full Scale Ship Self Propulsion, International Journal of Naval Architecture and Marine Engineering In Press.

[39] H. A. van der Vorst, Bi-CGStab: a fast and smoothly converging variant of Bi-CG for the solution of nonsymmetric linear systems, SIAM J. Sci. Comput. 13 (1992) 631–644.

[40] S. V. Patankar, D. B. Spalding, A calculation procedure for heat, mass and momentum transfer in three-dimensional parabolic flows, Int. J. Heat Mass Transf. 15 (1972) 1787–1806.

[41] R. I. Issa, Solution of the implicitly discretised fluid flow equations by operator-splitting, J. Comput. Phys. 62 (1986) 40–65.

[42] H. Jasak, V. Vukčević, I. Gatin, Numerical Simulation of Wave Loads on Static Offshore Structures, in: CFD for Wind and Tidal Offshore Turbines, Springer Tracts in Mechanical Engineering, 2015, pp. 95–105.

[43] S. Goldstein, On the Vortex Theory of Screw Propellers, Proceedings of the Royal Society of London. Series A, Containing Papers of a Mathematical and Physical Character 123 (792) (1929) 440–465.

[44] ITTC, Recommended Procedures and Guidelines - Practical guidelines for RANS calculation of nominal wakes. 7.5-03-03-02 (Revision 00) (2014) 9.

[45] S. H. Van, W. J. Kim, H. S. Yoon, Y. Y. Lee, I. R. Park, Flow measurement around a model ship with propeller and rudder, Experiments in Fluids (2006) 533–545`doi:10.1007/s00348-005-0093-6`.

[46] ITTC, Recommended Procedures and Guidelines - Nominal wake measurement by a 5-Hole pitot tube. 7.5-02-03-02.4 (Revision 01) (2011) 11.

[47] Tokyo 2015: A Workshop on CFD in Ship Hydrodynamics (2015). URL http://www.t2015.nmri.go.jp/

ARTICLE 2

Preprint of the published journal article.

ARTICLE TEMPLATE

Numerical method for the vibration analysis of pre-swirl stator

Nikola Vladimir[a*], Andro Bakica[a], Šime Malenica[b], Hongil Im[c], Ivo Senjanović[a],
Dae-Seung Cho[d]

[a]Faculty of Mechanical Engineering and Naval Architecture, University of Zagreb, Ivana
Lučića 5, Zagreb, Croatia;
[b]Bureau Veritas, Le Triangle de l'Arche 8, Cours du Triangle CS 50101, 92937 Paris La
Defense Cedex, France;
[c]Hyundai Heavy Industries Co. Ltd., 1000, Bangeojinsunhwan-doro, Dong-gu, Ulsan, 44032,
Korea;
[d]Pusan National University, Department of Naval 63 beon-gil 2, Busandaehak-ro,
Geumjeong-gu, Busan, 46239, Korea

ABSTRACT

Marine transportation is continuously oriented to the reduction of fuel consumption
and nowadays this is even more pronounced due to stringent rules and regulations
leading to the reduced ship environmental footprint. For this purpose, there are dif-
ferent technical solutions and operational strategies at disposal. Typical technical
solution that reduces ship total power needs (particularly for the propulsion) is the
Energy Saving Device (ESD), i.e. special hydrodynamically designed appendage in-
stalled on the ship aft body. There are different types of ESDs such as ducts, flow
control fins (FCFs), pre swirl stators (PSSs), propeller boss cap fins, Costa bulbs,
rudder fins, etc., and their design procedures differ from each one to another. If PSS
is considered, from a structural point of view, beside its yielding and buckling capac-
ities relevant dynamic properties should be ensured in order to reduce fatigue risks
and probable damage accumulation. Proper design from the vibration viewpoint
includes natural vibration analysis of PSS fins and comparisons with relevant load-

---

*Corresponding author. CONTACT N. Vladimir, Email: nikola.vladimir@fsb.hr

ings in order to avoid frequency overlapping, i.e. resonant behaviour. In this work the procedure is illustrated on the pre-swirl stator of a tanker. Several approaches to determine PSS fin natural frequencies were examined ranging from approximate procedures to sophisticated FEM approaches combined with different options to account for the effect of added mass. The obtained responses are compared with Vortex Induced Vibration (VIV) frequencies and propeller blade frequencies. Special attention is paid to VIV frequency determination where approximate expressions are validated against computational fluid dynamics (CFD) approach.

1. Introduction

Strict requirements for environmental protection and the reduction of harmful gas emissions, as well as oscillating oil prices, are some of the challenges that the shipbuilding industry and waterway transport are facing today. In accordance with the Marine Environment Protection Committee (MEPC) of the International Maritime Organization (IMO) resolution has been adopted and a new chapter on ship energy efficiency has been added and according to it, ships engaged in the international shipping should have an International Energy Efficiency Certificate (IEEC) (IMO, 2011). In spite of different issues with the smooth implementation of the above regulations and its fundamental shortcomings, as discussed in Ančić et al. (2018a), Vladimir et al. (2018) and Ančić et al. (2018b), there is permanent aim of ship-owners to reduce operative costs by fuel savings and consequently to reduce ship environmental footprint. In order to comply with IEEC requirements, there are different technical and operational measures at disposal. In general, technical measures are: measures related to the propulsion system, vessel design and vessel equipment, exhaust after treatment, engine internal measures, use of alternative fuels, while the set of operational measures is comprised of: measures related to speed reduction, smart steaming, journey planning, on board information systems, optimal maintenance, etc.

Since the ship propulsion is generally the largest energy consumer on-board,

2

energy savings at this point significantly reduce ship fuel consumption and consequently both costs and emissions during the ship operation. For the above-mentioned purposes, the Energy Saving Devices (ESDs), i.e. special hydrodynamic appendages installed on the ship aft body and affecting the inflow or outflow of the propeller, are the promising option (Bakica et al., 2020b). ESDs are classified by their relative position to the propeller plane and based on this one can distinguish their working principles. There are different types of ESDs as for instance ducts (Mewis and Guiard, 2011), flow control fins (FCFs) (Huang and Lin, 2019; Song et al., 2019), pre swirl stators (PSSs) (Sakamoto et al., 2019; Shin et al., 2019), propeller boss cap fins (Mizzi et al., 2017), rudder bulb-turbine (Wang et al., 2020), Costa bulbs, rudder fins, etc., or even some hybrid solutions (like for instance WAFon-D presented by Kim et al. (2015)) and their design procedures differ from each one to another. Irrespective on the ESD type, the designer should ensure its hydrodynamic performance (by shape optimization), structural integrity (both from viewpoint of extreme response and fatigue) as well as appropriate dynamic properties (to ensure that its natural frequencies are far from the excitation frequency range to avoid excessive structural vibration that might lead to damage). Literature survey indicates that most of the references in this field deal with different types of circular ducts and pre-swirl stators with their hydrodynamic performance of main interest. Regardless of such recent research interest, the accurate estimation of its gains is still relatively unknown (Bakica et al., 2020b). Although some model tests indicated promising results at model scale, sea trials showed doubtful contributions of ESDs to propulsion efficiency (Prins et al., 2016). Recognizing that only viscous flow computations can provide acceptable accuracy in ESD performance prediction, Computational Fluid Dynamics (CFD) is widely used approach (Mizzi et al., 2017; Shin et al., 2019). Bearing in mind the fact that assessing ESD performance by means of CFD requires modelling of hull-propeller-ESD interaction (Mofidi and Carrica, 2014; Shen et al., 2015) leading to high computational costs, different propeller modelling principles are developed, ranging from relatively complex ones (Wu et al., 2015) to simpler idealised disk approaches (Bakica et al., 2019; Gokce et al., 2019). It should be mentioned that use of simplified propeller models with the ESDs still has to be investigated both from

3

the viewpoint of efficiency prediction and evaluation of loads acting on ESD structure (Bakica et al., 2020a).

Although ESDs are an increasingly investigated subject for the last decade, to the best author's knowledge, their structural aspects still remain a rarely addressed issue. The reason for this might be in a fact that ESD structure is not reviewed or standardized by classification societies, but only its attachment to the hull, as reported by Paboeuf and Cassez (2017). This is partially due to complexities involved when estimating the ESD hydrodynamic loads and the inability to model the structural response through simplified analytical formulas. Lee et al. (2016) approximated the non-linear loadings on PSS through trained neural network on a CFD results, while Ju et al. (2018) presented a structural safety assessment formula for fin-typed energy saving devices subjected to non-linear hydrodynamic load as well as simplified method predicting the extreme loading and fatigue damage based on that formula. The accuracy is claimed to be lower than CFD calculations but due to its simplicity it is useful at least for quick comparative assessments in the early design stage. Matsui et al. (2018) conducted numerical simulations of a duct structural response subjected to the impact of an ice block by means of a commercial software package LS-DYNA, which is relevant for ship operation in ice-covered waters. Several years ago, an integral approach to the design of ESD considering all above aspects (hydrodynamic, structural, vibration) is investigated in a collaborative project GRIP (Paboeuf and Cassez, 2017; Prins et al., 2016). Within the project, Paboeuf and Cassez (2017) proposed a numerical approach to evaluate the structural strength of an ESD for which the design waves producing the maximum bending of the fins are determined by potential flow based seakeeping analyses, and the corresponding loads exerted on the ESD are obtained by CFD simulations for previously determined design waves. In Paboeuf and Cassez (2017) the so-called Ship Motions Methodology (SMM) is presented, which enables to determine loads on ESDs with the through statistical analysis with the linear potential flow models. Wang et al. (2016) evaluated the fatigue life of a 5-fin PSS fitted ahead of the propeller of an 80,000 DWT bulk carrier. The fatigue loads were exerted on the fins by the stern wake and the ship motions, neglecting the propeller induced effects. A Boundary Element Method (BEM) pressure

distribution is used to load the finite element (FE) model and to extract the hot spot stress at the fin connection. Tsou et al. (2019) analysed structural strength of PSS by means of FE commercial code LS DYNA. In that paper some FE modelling aspects like mesh density influence and shell and solid element coupling are discussed. It is important to mention that in all above references, loadings and responses of ESD structure are considered in a quasi-static manner, thus not evaluating or describing the approach when the structural dynamics become important.

Regarding the PSS vibration analysis, which is a main subject of this work, to the author's knowledge there is only a reference of Paboeuf and Cassez (2017) addressing the structural dynamic problem. In that work, natural vibration analysis is performed by analytical formulas and FE method (by means of commercial code NASTRAN), while the effect of added mass is calculated by approximate formulas. Comparisons of natural frequencies against propeller-blade frequency and approximately determined VIV frequency are performed. This paper aims to shed more light on a vibrational problems of PSS, where the research gap regarding the validity of the currently applied procedures is investigated. Dry natural vibration analysis is performed with both the analytical approach and with the FEM model. Additionally, wet natural frequency i.e. effect of added mass is estimated with the analytical formula from Paboeuf and Cassez (2017) and also by using modern numerical methods. Two approaches are utilized: MFLUID option in NASTRAN and Homer software (Malenica et al., 2013) combining NASTRAN and potential flow code HYDROSTAR (Bureau Veritas, 2016). Although it may seem exaggerated to use two different mathematical models for the estimation of wet natural modes their mutual comparison offers an increased reliability of the computed results and serves for validation purposes of both software. Furthermore, the VIV frequencies are calculated by approximate expressions and compared with the CFD simulations. Two types of CFD simulations are performed, first without the propeller, and second with the simplified Actuator Disk (AD) propeller model (Bakica et al., 2019) for simulation CPU efficiency. It is investigated how the change in the velocity near the PSS due to AD effects alters the resulting force oscillation on the PSS.

This paper is divided into four sections. Second section contains the theoretical

Table 1. Ship particulars.

Length between perpendiculars	L_{PP} (m)	320.0
Breadth	B (m)	58.0
Depth	D (m)	30.0
Draft	T (m)	20.8
Displacement	Δ (m^3)	312622
Design speed	U (kn)	16.5
Block coefficient	C_B	0.81
Vertical centre of gravity	KG (m)	18.6
Moment of Inertia	K_{xx}/B	0.4
Moment of Inertia	K_{yy}/L_{PP}, K_{zz}/L_{PP}	0.25

background of the underlying tools and methods. Third section features the computed results and discussion. At last, in the fourth section the relevant conclusions are drawn and suitability of each step in the procedure is discussed.

2. Analysis procedure

2.1. General

To illustrate the dynamic analysis procedure a PSS of an oil tanker with main particulars shown in Table 1 is considered.

The considered ship is equipped with 3-fin PSS shown in Figure 1. Vibration analysis can be performed at different levels of complexity and accuracy. Natural frequencies can be determined in a simplified manner by analytical formulas for cantilever plates or by the finite element method (Paboeuf and Cassez, 2017). In both approaches added mass effect that reduces fin natural frequency should be taken into account.

2.2. Simplified calculations of PSS fins natural response

According to Paboeuf and Cassez (2017) PSS fin frequencies can be approximated by rectangular plates frequencies with one (shorter) edge clamped. In this case there is
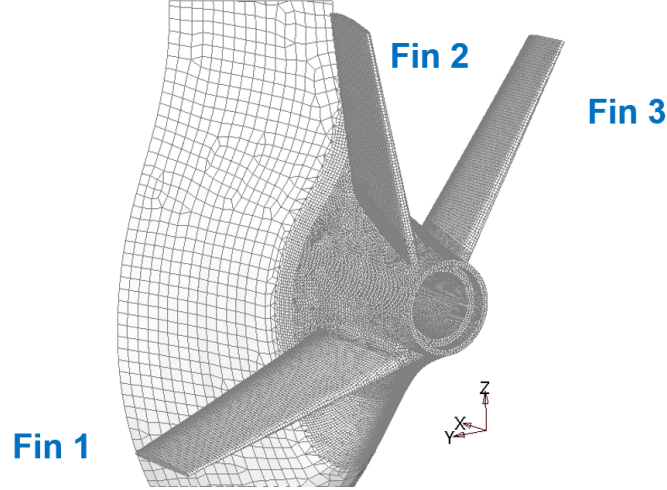
Figure 1. 3D FEM model of a pre-swirl stator.

analytical formula for calculation of natural frequencies (in Hz):

$$f_i = \frac{\lambda_{ij}^2}{2\pi a^2} \left(\frac{Eh^3}{12\gamma(1-\nu^2)} \right)^{1/2} \qquad \text{for } i = 1, 2, ... \text{for } j = 1, 2, ... \tag{1}$$

where λ represents dimensionless parameter which is a function of boundary conditions and ratio of plate edges (a/b),E is Young modulus, h is plate thickness while γ and ν represent mass per unit area and Poissons ratio, respectively. In this analysis, values of boundary parameters are directly adopted from Paboeuf and Cassez (2017) and yield $\lambda_{11}^2 = 3.46$ and $\lambda_{12}^2 = 17.99$. Also, a and b denote plate length and width, respectively.

Effect of added mass is approximately expressed as (Paboeuf and Cassez, 2017):

$$\frac{(f_i)_{wet}}{(f_j)_{dry}} = \frac{1}{\sqrt{1 + \frac{A_P}{M_P}}} \tag{2}$$

where A_P is added mass and M_P is plate (fin) mass.

According to Paboeuf and Cassez (2017) and Blevins (1979) added mass is predicted using Equation 2 as $2/\pi$ times the volume enclosed by rotating the plate about the longer symmetric axis:

$$2A_P = \left(\frac{2}{\pi} \right) \frac{\pi}{4} b^2 a\rho \tag{3}$$

7
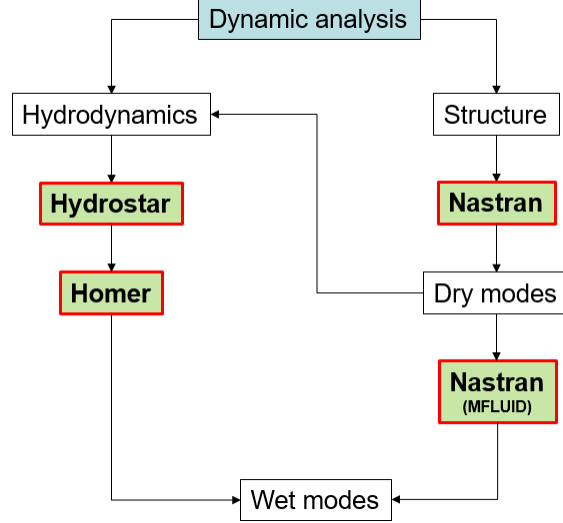
Figure 2. Dynamic analysis procedures by FEM.

where ρ is the surrounding fluid density.

2.3. FE analysis of PSS fins natural response

Dynamic analysis procedures of PSS fins are illustrated in Figure 2, where the above mentioned options to use Homer or NASTRAN are distinguished. For dry natural vibration analysis there are two basic approaches. The first includes modelling of the aft structure with all fins of PSS and constraining the model at some frame of the ship aft body. Another way is to model only one fin with appropriate boundary conditions (mostly clamped at fin connection at the root). It is reasonable to assume that single-fin approach should give slightly higher natural frequencies, as a consequence of boundary conditions. Homer requires special finite element model of PSS structure connected to ship outer shell, as shown in the next section. When it comes to the added mass calculation, it can be done directly within NASTRAN or by means of HYDROSTAR within the Homer framework. It is important to understand that in both cases, the identical structural model is used and the dry modes are calculated in the same manner (dry natural modes in Homer are also calculated by means of NASTRAN).

Before explaining the differences between these two approaches when calculating

the wet modes, first the definition for the dry modes is necessary. For the general vibration problem, the equation reduces to the well-known eigenvalue problem:

$$\{-\omega^2 \cdot [\mathbf{M}] + [\mathbf{K}]\} \cdot \{\xi\} = 0 \tag{4}$$

where ξ is the modal amplitude, $[\mathbf{M}]$ is the mass matrix and $[\mathbf{K}]$ is the stiffness matrix. For the dry modes calculation the mass matrix equals the body mass $[m]$ while the stiffness matrix equals the structural stiffness matrix $[\mathbf{K}^{st}]$. As previously stated, this part is computed using the FEM model in NASTRAN for both Homer and MFLUID option.

When calculating the wet modes the key concept is in the effect of the added mass of surrounding fluid which, in general, reduces the calculated dry natural frequencies. In that case the $[\mathbf{M}]$ in Equation 4 reads:

$$[\mathbf{M}] = [m] + [\mathbf{A}] \tag{5}$$

where $[\mathbf{A}]$ is the added mass. This is precisely what MFLUID option calculates using the Virtual Fluid Mass (VFM) method. It is important to mention here that the method uses BEM to solve the potential flow problem around the immersed body where each finite element on the wetted surface is represented as a source of constant strength. For full details of the method the reader is referred to SIEMENS (2014). After obtaining the added mass by VFM, the computation of the wet frequencies is straightforward.

On the other hand, Homer employs a HYDROSTAR software for the potential flow where also BEM method is used to solve the inviscid and irrotational flow around the floating body. This requires the development of the entire ship model in order for the mesh to function properly in the HYDROSTAR framework which slightly increases the setup complexity. Since the HYDROSTAR solution exists only on a newly created mesh, some type of interpolation must be performed back to the FEM mesh. To completely reduce the interpolation error, Homer always uses the FEM mesh as the integration mesh by re-calculating the Green function at the necessary FEM

points (see Malenica et al., 2013, for details). Given the involved difficulties, it seems unreasonable to follow this approach, since the added mass is readily available in the MFLUID option directly in NASTRAN and any differences in the added mass can occur only due to numerical or interpolation issues since both softwares are solving the same mathematical problem. However, there is a subtle difference contained in the stiffness matrix from Equation 4. When computing the wet modes, Homer includes the hydrostatic stiffness which consists of the gravity part and the restoring part, finally yielding:

$$[\mathbf{K}] = [\mathbf{K}]^{st} + [\mathbf{C}] \tag{6}$$

where $[\mathbf{C}]$ is the overall hydrostatic stifness. For full details regarding the Homer software, reader is referred to Malenica et al. (2013).

2.4. Propeller blade frequency

Propeller blade frequency is dependent on the blade number and propeller rotation speed. It is calculated according to following equation:

$$f_{propeller} = \frac{RPM \cdot n}{60} H \tag{7}$$

where RPM denotes number of revolutions per minute, n is number of propeller blades, while H denotes number of harmonic.

2.5. Vortex induced vibrations

VIV is an unsteady oscillating flow phenomenon induced by the interaction of body and the external flow which causes larger vortices to detach from the body surface in an periodic manner. It can cause severe structural vibrations especially when resonance happens. Structural response can be reduced by increasing the structural

damping or by breaking down the wake pattern by addition of spoilers, thus affecting the VIV frequency overlap with the natural modes. All told, it is important to estimate VIV frequencies beforehand for any structure susceptible to such resonance behaviour. The simplest approach for estimating the VIV frequencies is the use of empirical formulas. Although their lack in accuracy is evident, the practicality of approach makes them frequently used in the industry. Other approach, recently frequently investigated and much more accurate is by using CFD simulations. This type of investigation requires a significantly larger amount of work and knowledge to be applied properly. It should be noted that in this work, CFD simulations are performed without a grid refinement study and with only one type of turbulence model, hence the results presented are strictly for the entire procedure illustration purpose and their detailed investigation is beyond the scope of this paper.

2.5.1. Empirical formula

The frequency f_{VIV}, (in Hz), can be expressed by the following formula:

$$f_{viv} = \frac{S_t \cdot V}{d} \tag{8}$$

where S_t is Strouhal number, V is fluid velocity and d is length of the profiles chord.

The Strouhal number depends on Reynolds number defined by:

$$Re = \frac{\rho \cdot V \cdot L}{\mu} \tag{9}$$

where ρ is fluid density, μ is dynamic viscosity and L is profile length.

Relationship between Strouhal number and Reynolds number is available in the literature for different profiles. However, for the NACA profile there is no general rule relating the geometrical characteristics of the profile to the VIV frequency. According to Blevins (2001) for a slender body, the expected VIV frequency is related to the width of the profile which would correspond to the trailing edge width for NACA profiles. In this case, Strouhal number is reported as almost fixed around

0.2 irrelevant of the Reynolds number. However, it is important to note that most of the work related to this subject is usually performed for low Reynolds number flows (see also Yarusevych and Boutilier, 2011). On the other hand, when the angle of attack is considered the trailing edge does not govern the separation of the flow since the detachment usually already occurs somewhere in the middle of the profile and it may even occur already at the leading edge depending on the severity of the angle (for example, see Ragab et al., 2018). In the current case for higher Reynolds number and larger angle of attack, none of the analytical methods is deemed as sufficiently accurate to use, especially bearing in mind the non-uniformity of the flow near the PSS. In order to have at least some type of referent value with respect to the numerically computed VIV frequency, the approach suggested by Paboeuf and Cassez (2017) is used. The main idea is to consider the fin cross-section as the circular one for rough approximation purposes (Achenbach and Heinecke, 1981; Lienhard, 1966).

2.5.2. VIV analysis by CFD

Simulations are performed in the Finite Volume (FV) framework of OpenFOAM which is an actively developed open-source CFD library using a NavalHydro Pack developed in the foam-extend environment (Vukčević, 2016). The flow solution is fully non-linear to second-order accuracy. Since the vortex separation is a highly transient phenomena, PISO loop is employed inside a SIMPLE loop to couple the pressure and the velocity field.

Mathematical model is based on the incompressible two-phase flow for which the momentum equation yields:

$$\frac{\partial \mathbf{u}}{\partial t} + \nabla_\bullet(\mathbf{u}\mathbf{u}) - \nabla_\bullet(\nu\nabla\mathbf{u}) = -\frac{1}{\rho(\mathbf{x})}\nabla p_d + \nabla_\bullet\mathbf{R}, \tag{10}$$

where $\mathbf{u}$ is the fluid velocity, $\mathbf{x}$ is the position vector, ∇p_d is the gradient of dynamic pressure, $\rho(\mathbf{x})$ is the fluid density for water or air, $\mathbf{R}$ is the Reynolds stress tensor and ν is the kinematic viscosity. Considering the flow conservation, the continuity equation
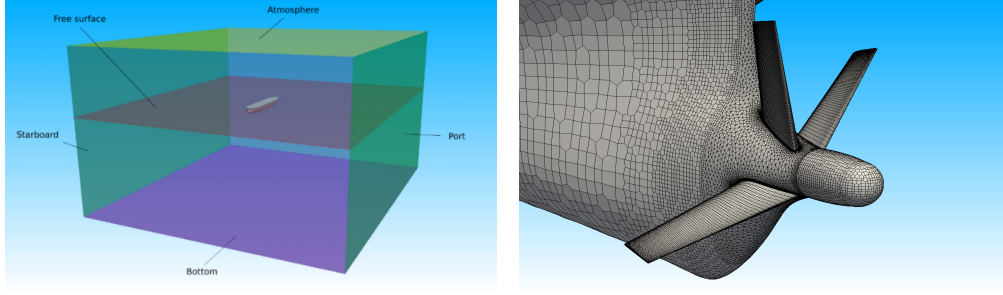
Figure 3. Computational domain (left) and the computational mesh near stator (right).

reads:

$$\nabla \cdot \mathbf{u} = 0. \tag{11}$$

It is important to note that the implemented model (Vukčević, 2016) uses Ghost Fluid Method (GFM) which considers the jump of the density field exactly at the interface between the two fluids, while the viscosity variation is taken approximately, since the tangential stresses are of lower importance for the naval CFD applications.

In order to simulate the flow separation and to estimate the vortex shedding frequency near the PSS, a full ship model is generated. Given a highly non-uniform flow at the ship stern with a strong pressure gradient, such complex model is required to accurately represent the flow separation occurring at the PSS surface. Free surface is also modelled in order to increase the accuracy of the computed wake field. Computational domain is shown in Figure 3 with the snapshot of the mesh near the PSS. Two types of meshes are performed differing in the boundary layer near the PSS surface with the rest of the computational domain equal. First mesh is prepared with the unstructured cut-cell meshing technique with only three boundary layers, while the latter case is meshed with the dedicated body-fitted structured meshing procedure on the PSS surface which insures the smoothness of the geometry and allows a much larger number of boundary layers, which is set to 16 for the current cases, while preserving the mesh quality. First layer height is the same for both meshes and is set to 10 mm.

Vortex separation frequency is estimated by analysing the force signal on the PSS surface when the overall domain solution (free surface, ship motions) converges.
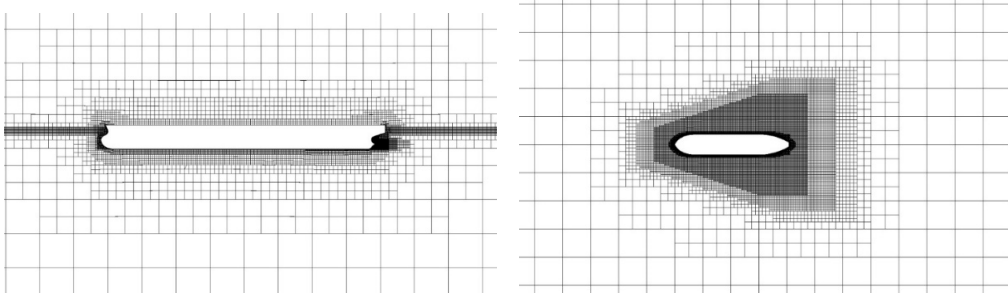
Figure 4. CFD mesh.

The simulation is run only for the calm water case where the inlet speed is set equal as the ship service speed. Propeller is modelled as the simplified pressure jump on the propeller plane using AD (Bakica et al., 2019) for efficiency reasons. It is also worth mentioning that the current implementation of the AD does not require any mesh changes since it is applied directly on the existing mesh faces.

Computational mesh of the surrounding mesh is shown in Figure 4. Simulation is run on mesh size of 3M cells for the unstructured mesh and 3.8M for the body fitted mesh near the PSS. Regarding the turbulence modelling, high frequencies from small vortices are not important in this study since they do not transfer any energy to the structure and the goal here is to avoid resonance with the propeller rotation and structural flexible modes which are of lower order. For stated reason, it is expected from the simpler turbulence models to properly capture the major features of the flow such as the dominant vortex separation frequency which is relevant for structural resonance comparison. $k - \omega \; SST$ turbulence model is used to capture the vortices in the body wake and is employed in all the simulations for its proven quality when capturing the strong pressure gradient effects from flow separation.

3. Numerical results and discussion

Based on the previously described procedure, vibration analysis is performed including comparisons of natural frequencies with the excitation ones. For this assessment two fluid models are applied, i.e. MFLUID option in NASTRAN, Figure 5, and ap-
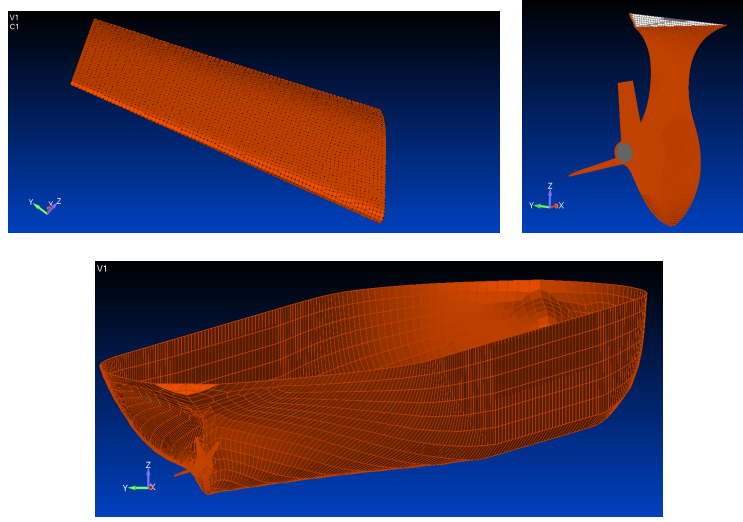
Figure 5. Different models to predict fin wet natural modes in NASTRAN with MFLUID option (single-fin model, complete aft structure model, complete ship model).
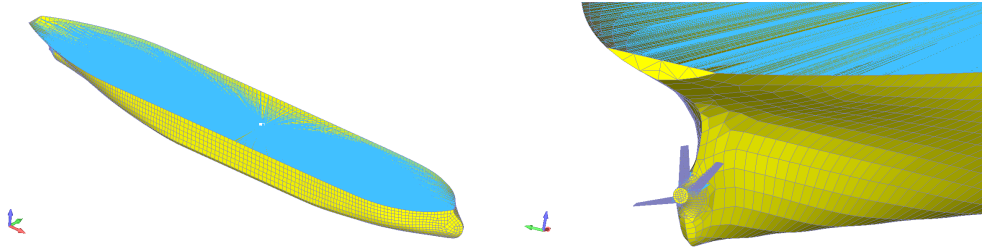

Figure 6. Artificial FE model for computation of wet natural frequencies by means of Homer.

plication of HYDROSTAR software within Homer framework, Figure 6. In the latter case an artificial FE model is developed, where the ship hull form has been kept in its original shape and ship mass properties are modelled by a concentrated mass element and rigidly connected (RBE2 element) to all finite element nodes except those belonging to the PSS. In this way one obtains wet eigenvalues and eigenvectors for 6 rigid body modes and number of flexible modes related to PSS fins. Calculated values are presented in Table 2. Regarding the comparison between NASTRAN and Homer wet modes, consistent difference in the results is observed which can be influenced by both the hydrostatic stiffness or the numerical approach when calculating the added mass.

As can be seen from the above results, there is quite low risk of resonance. For the illustration, mode shapes obtained by single fin approach and complete (artificial)

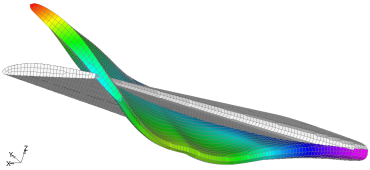**Table 2.** Comparisons of PSS fin frequencies with excitation frequencies (Hz).
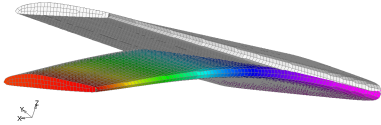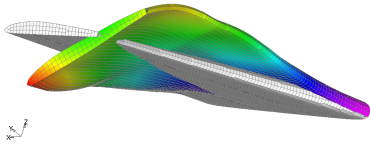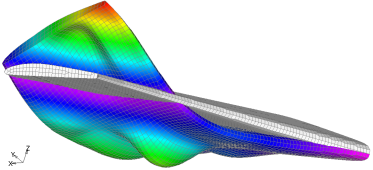
Fin No.	Mode	Dry		Wet		Propeller blade frequency	VIV frequency			Empirical
		Analytical	FEM	NASTRAN	Homer		CFD_u	CFD_s	$CFD_{s,AD}$	
1	1st	26.01	29.2	17.96	18.55	4.27	0.40	0.41,	0.51	
	2nd	98.77	96.73	76.19	77.92	8.53		0.79		
2	1st	34.88	39.21	24.66	25.12	4.27	0.40,	0.41	0.51	1.2
	2nd	134.43	116.10	90.63	92.97	8.53	0.81			
3	1st	29.22	32.60	19.79	20.76	4.27	0.40,	0.41	0.51	
	2nd	120.66	105.79	81.80	83.20	8.53	0.81			

* Subscripts in CFD: u - unstructured, s - structured, AD - actuator disk

FE model for Fin 1 are shown in Table 3.

VIV frequencies shown in Table 2 are calculated by empirical formula and CFD software OpenFOAM, where larger discrepancies occur. Force oscillations for Fin 1 and its pressure distribution for selected time step are shown in Figure 7. Frequencies from the CFD are calculated from the last 25 seconds of simulation time, after the overall simulation domain has converged. Time signal is processed using Fast Fourier Transformation (FFT) with the time-step equal to the CFD simulation time-step and only the dominant frequency is reported. From the results it is obvious that all three fins are induced by the some type of vortex vibration characteristics. Irrelevant of the mesh setup highest amplitudes are consistently obtained on Fin 3. As can be seen from Table 2, Fin 2 and Fin 3 have the same frequency excitation on each mesh. On unstructured mesh, the 2nd harmonic is clear on Fin 3 even by visually observing the Figure 7. This large 2nd harmonic amplitude becomes negligible when performing the analysis on the structured mesh results. On the structured mesh, the 1st harmonic is slightly higher, but the computed signal is almost uniform with only that single dominant frequency present. In the current case, the results are assumed to be more accurate from the structured mesh analysis, since the mesh in the near surface layer is much better in quality. The complete coincidence of the frequencies on Fin 2 and 3 with respect to each mesh case could be due to their mutual interaction. Obviously, the Fin 3 produces most of the vortices energy when observing the amplitude of the force, thus it can be concluded that this excitation actually contributed to the excitation of the Fin 2 force due to vortices interaction in the wake of the PSS. On the other hand, Fin 1 on an unstructured mesh did not produce any meaningful results.

Table 3. Mode shapes and natural frequencies (Hz) of PSS Fin1 obtained by single fin approach, FE analysis.

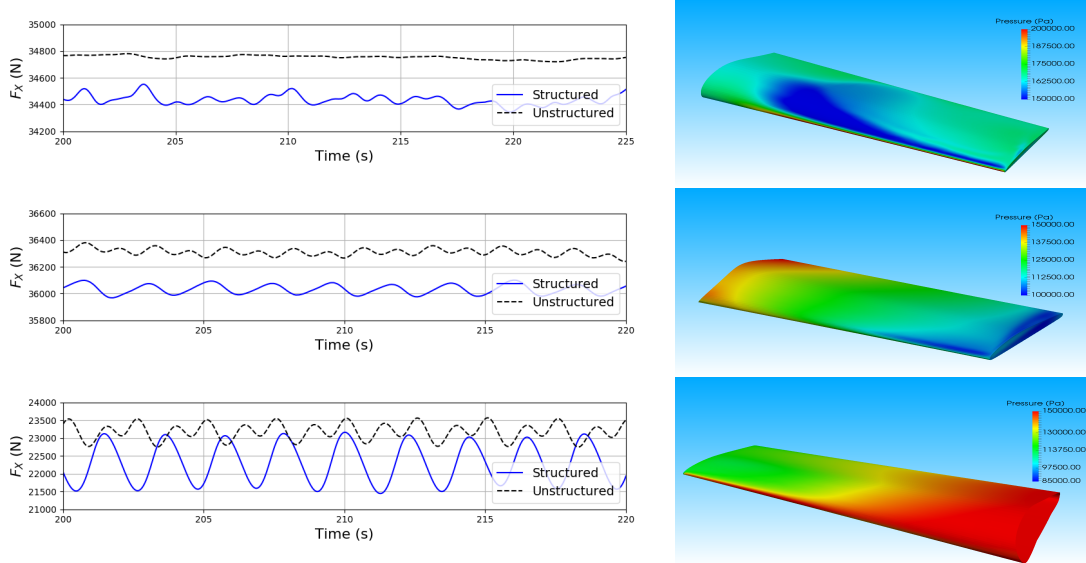| Mode no.	Mode shape	Dry natural frequency	Wet natural frequency
1		29.20	17.96
2		96.73	76.19
3		103.52	80.11
4		142.77	93.12

17

Figure 7. Force signals and pressure distribution on the PSS fins (Fin 1 - top, Fin 2 - middle, Fin 3 - bottom).

Small peak is observed at the $0.4\,\text{Hz}$, but the produced signal contains too much noise and instabilities for the proper evaluation. On an structured mesh, similar frequencies are observed as in the Fin 2 and 3 with a more pronounced 2nd harmonic, but the overall frequencies are slightly lower which could be influenced by the different angle of attack. However, the flow is highly turbulent and unstable so a definite conclusion cannot be drawn from the current results. Furthermore, due to improved simulation stability, on the structured mesh the AD is also included to model the propeller induced velocity on the PSS. The results show a roughly 20% rise in the VIV frequency implying the inclusion of the AD necessary to accurately estimate the resonance risk, especially when the gap between the comparing VIV, propeller or natural frequency is lower. Also, the AD effect completely erases the higher harmonics on all three fins, leaving only single and distinguished peak when analysing the signal in frequency domain. Snapshots of performed CFD simulations are illustrated in Figure 8.

In spite of relatively large discrepancies when estimating the VIV frequencies, both analytical and direct (CFD) approach indicate that there is no resonance risk for the considered structure. Streamlines in the vicinity of PSS fins are illustrated in Figure 9 where a vortex generation in the wake of the PSS can be observed.
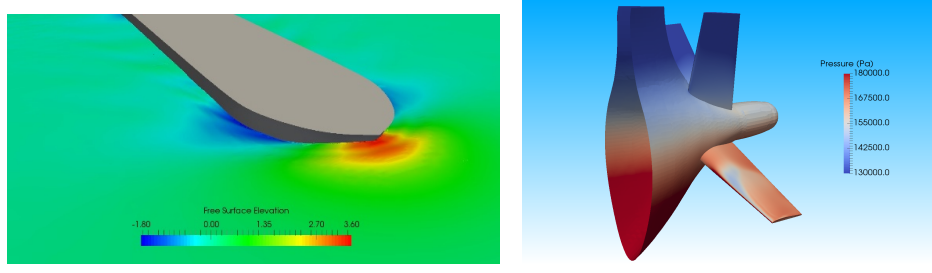
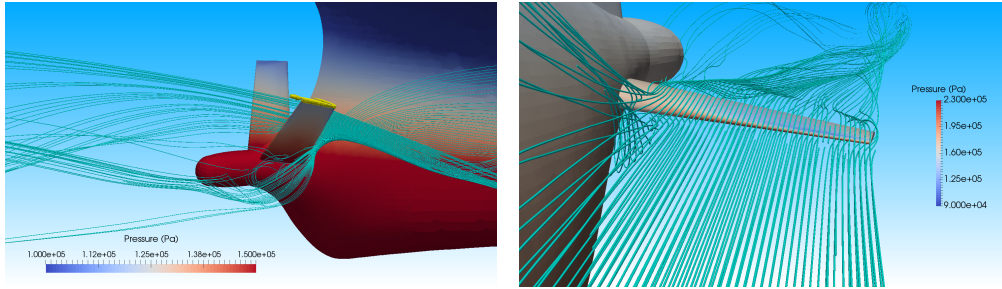**Figure 8.** Snapshots from the CFD simulation.

Figure 9. Streamlines in the vicinity of PSS fins.

4. Conclusion

Efforts to reduce ship fuel consumption and consequently to lower its environmental footprint motivate shipbuilders to develop different types of energy saving devices. For such devices regularly empirical design procedures with unclear levels of accuracy and validity are applied. In order to increase ESDs operational safety, beside hydrodynamic performance assessment, their design should include accurate strength and vibration analyses. In this paper a dynamic analysis of pre-swirl stator type energy saving device is considered. Natural vibration analysis of PSS fins is performed by analytical formulas and by means of commercial software NASTRAN and Homer, utilizing FE method. Natural frequencies are compared against propeller blade excitation frequencies and VIV frequencies. The latter ones are determined by empirical expressions and by the sophisticated CFD computations by means of open source code OpenFOAM. So, the paper original contribution lies in the evaluation of different options to calculate fin natural frequencies and validation of empirical formula to predict VIV frequencies against complex CFD computations. The main findings of this investigation are limited

19

to this PSS case and can be summarized as follows:

- Dry natural vibration analysis performed by analytical formulas leads to the same conclusion as FEM results, i.e. there is no resonance risk for PSS fins. However, the discrepancies between results are rather high indicating that this approach might not be fully reliable, because it depends on how much the fin shape follows the plate-like form.

- Wet natural vibrations can be analysed both by NASTRAN with MFLUID option or by combining NASTRAN with HYDROSTAR within the Homer framework. For this specific application, the former approach seems to be more user friendly since generation of separate hydrodynamic model is not needed.

- CFD results show that empirical formula for VIV frequency results in relatively high scattering of the results. Although it might be good for some specific applications, CFD simulations are highly recommended if a more accurate investigation of VIV phenomenon is needed.

- Propeller modelling (in this case by AD) has a sufficient effect on the estimated CFD VIV frequencies which suggests that the inclusion should be necessary. In this particular case the frequency increase arising from the AD induced velocity field is slightly over 20%.

- If evaluation of structural integrity of the considered PSS structure is needed, quasi-static approach can be reliably used, because overlapping of natural and excitation frequencies both for the lowest bending and twisting modes is avoided.

Future investigation of PSS design procedure should be focused on a deeper insight into the computation of CFD VIV frequencies and the development of reliable methods for the structural integrity evaluation where special attention should be paid to the definition of relevant sea conditions, performing of CFD computations for those conditions, reliable transfer of calculated loadings and finally the structural analysis and comparisons with relevant criteria. It should be also mentioned that design criteria for ship appendices like PSS are not fully mastered today and require more attention.

References

Achenbach, E. and Heinecke, E. (1981). On vortex shedding from smooth and rough cylinders in the range of Reynolds numbers 6103 to 5106. *Journal of Fluid Mechanics*, 109(12):239–251.

Ančić, I., Theotokatos, G., and Vladimir, N. (2018a). Towards improving energy efficiency regulations of bulk carriers. *Ocean Engineering*, 148(November 2017):193–201.

Ančić, I., Vladimir, N., and Cho, D. S. (2018b). Determining environmental pollution from ships using Index of Energy Efficiency and Environmental Eligibility (I4E). *Marine Policy*, 95(June):1–7.

Bakica, A., Gatin, I., Vukčević, V., Jasak, H., and Vladimir, N. (2019). Accurate assessment of ship-propulsion characteristics using CFD. *Ocean Engineering*, 175:149–162.

Bakica, A., Malenica, Š., and Vladimir, N. (2020a). Hydro-structure coupling of CFD and FEM - Quasi-static approach . *Ocean Engineering*, 217.

Bakica, A., Vladimir, N., Gatin, I., and Jasak, H. (2020b). CFD simulation of loadings on circular duct in calm water and waves. *Ships and Offshore Structures*, (In Press).

Blevins, R. D. (1979). *Formulas for natural frequency and mode shape*.

Blevins, R. D. (2001). *Flow-Induced Vibration*. 2nd edition.

Bureau Veritas (2016). *HYDROSTAR for Experts - User Manual*.

Gokce, M. K., Kinaci, O. K., and Alkan, A. D. (2019). Self-propulsion estimations for a bulk carrier. *Ships and Offshore Structures*, 14(7):656–663.

Huang, Y. and Lin, B. (2019). Design and development of the energy saving rudder-bulb-fin combination by using computational fluid dynamics technique. In *Proceedings of PRADS2019*, Yokohama, Japan.

IMO (2011). Resolution MEPC.203(62) Inclusion of regulations on energy efficiency for ships in MARPOL Annex VI. Technical report.

Ju, H. B., Jang, B. S., Lee, D. B., Kim, H. J., and Park, C. K. (2018). A simplified structural safety assessment of a fin-typed energy saving devices subjected to nonlinear hydrodynamic load. *Ocean Engineering*, 149(June 2017):245–259.

Kim, J. H., Choi, J. E., Choi, B. J., Chung, S. H., and Seo, H. W. (2015). Development of Energy-Saving devices for a full Slow-Speed ship through improving propulsion performance. *International Journal of Naval Architecture and Ocean Engineering*, 7(2):390–398.

Lee, D. B., Jang, B. S., and Kim, H. J. (2016). Development of procedure for structural safety assessment of energy saving device subjected to nonlinear hydrodynamic load. *Ocean Engineering*, 116:165–183.

Lienhard, J. (1966). *Synopsis of Lift, Drag and Vortex Frequency Data for Rigid Circular Cylinders*. Washington State University, College of Engineering, Research Division Bulletin 300.

Malenica, S., Derbanne, Q., Sireta, F. X., Bigot, F., Tiphine, E., De-Hauteclocque, G., and Chen, X. B. (2013). HOMER - Integrated hydro-structure interactions tool for naval and off-shore applications. *RINA, Royal Institution of Naval Architects - International Conference on Computer Applications in Shipbuilding 2013, ICCAS 2013*, 3:209–221.

Matsui, S., Uto, S., Yamada, Y., and Watanabe, S. (2018). Numerical study on the structural response of energy-saving device of ice-class vessel due to impact of ice block. *International Journal of Naval Architecture and Ocean Engineering*, 10(3):367–375.

Mewis, F. and Guiard, T. (2011). Mewis Duct ® New Developments , Solutions and Conclusions. *Second international symposium on Marine Propulsors*, (June):1–8.

Mizzi, K., Demirel, Y. K., Banks, C., Turan, O., Kaklis, P., and Atlar, M. (2017). Design optimisation of Propeller Boss Cap Fins for enhanced propeller performance. *Applied Ocean Research*, 62:210–222.

Mofidi, A. and Carrica, P. M. (2014). Simulations of zigzag maneuvers for a container ship with direct moving rudder and propeller. *Computers & Fluids*, 96:191–203.

Paboeuf, S. and Cassez, A. (2017). ESD structural issue - UPstream device. *International Shipbuilding Progress*, 63(3-4):291–314.

Prins, H. J., Flikkema, M. B., Schuiling, B., Xing-Kaeding, Y., Voermans, A. A., Müller, M., Coache, S., Hasselaar, T. W., and Paboeuf, S. (2016). Green Retrofitting through Optimisation of Hull-propulsion Interaction - GRIP. *Transportation Research Procedia*, 14(0):1591–1600.

Ragab, S., Hajj, M. R., Ibrahim, M. M., and Zakaria, M. Y. (2018). A computational study of vortex shedding from a NACA-0012 airfoil at high angles of attack. *International Journal of Aerodynamics*, 6(1):1–17.

Sakamoto, N., Kume, K., Kawanami, Y., Kamiirisa, H., Mokuo, K., and Tamashima, M. (2019). Evaluation of hydrodynamic performance of pre-swirl and post-swirl ESDs for merchant ships by numerical towing tank procedure. *Ocean Engineering*, 178(February):104–133.

Shen, Z., Wan, D., and Carrica, P. M. (2015). Dynamic overset grids in OpenFOAM with application to KCS self–propulsion and maneuvering. *Ocean Eng.*, 108:287–306.

Shin, Y. J., Kim, M. C., Kang, J. G., Kim, H. U., and Rok Shin, I. (2019). Validation of optimally designed stator-propeller system by EFD and CFD. *Brodogradnja*, 70(3):133–151.

SIEMENS (2014). Advanced Dynamic Analysis User's Guide.

Song, K.-w., Guo, C.-y., Wang, C., Sun, C., Li, P., and Zhong, R.-f. (2019). Experimental and numerical study on the scale effect of stern flap on ship resistance and flow field. *Ships and Offshore Structures*, 0(0):1–17.

Tsou, W., Guan, P., Chang, W., and Chen, C. (2019). Structural design and strength estimation of energy saving Y-fin by using finite element method. In *Proceedings of PRADS2019*, Yokohama, Japan.

Vladimir, N., Ančić, I., and Šestan, A. (2018). Effect of ship size on EEDI requirements for large container ships. *Journal of Marine Science and Technology (Japan)*, 23(1):42–51.

Vukčević, V. (2016). *Numerical Modelling of Coupled Potential and Viscous Flow for Marine Applications*. PhD thesis, University of Zagreb.

Wang, C., Guo, C., Wang, C., and Han, F. (2020). A case study on the effect of an energy recovering rudder bulb-turbine device on ship powering characteristics. *Ships and Offshore Structures*, 15(8):878–894.

Wang, P. W., Liao, P. K., Hsin, C. Y., Quéméner, Y., and Lin, C. W. (2016). Ship motions contribution to the fatigue life of a pre-swirl stator. In *Proceedings of PRADS2016*.

Wu, X., Wang, Y., Huang, C., Hu, Z., and Yi, R. (2015). An effective CFD approach for marine-vehicle maneuvering simulation based on the hybrid reference frames method. *Ocean*

Engineering, 109:83–92.

Yarusevych, S. and Boutilier, M. S. (2011). Vortex shedding of an airfoil at low reynolds numbers. *AIAA Journal*, 49(10):2221–2227.

ARTICLE 3

Preprint of the published journal article.

Hydro-structure coupling of CFD and FEM - Quasi-static approach

Andro Bakica[a], Šime Malenica[b], Nikola Vladimir[a,*]

[a]*University of Zagreb, Faculty of Mechanical Engineering and Naval Architecture, Ivana Lučića 5, Zagreb, Croatia*
[b]*Bureau Veritas Marine & Offshore, Departement Recherche, Le Triangle de lArche, 8 Cours du Triangle, Paris La Defense, France*

Abstract

The present article deals with the coupling of hydrodynamic loading, modelled by OpenFOAM Finite Volume (FV) framework for Computational Fluid Dynamics (CFD), and the structural response, modelled by the general 3D Finite Element (FE) approach. The overall methodology and the numerical approaches which are discussed are very general and remain valid for any type of hydro-structure interaction problems, but here the main concern is on marine structures (ships, off-shore platforms...) where the loading is induced by water waves. In the present work, the accent is placed on the linear quasi static structural response which is the problem belonging to the one-way coupling procedures. Particularly, this means that the hydrodynamic and structural simulations can be performed independently of each other. The main technical issue becomes the consistent transfer of the hydrodynamic loads from the hydrodynamic CFD mesh to the structural FE mesh. This paper presents a novel methodology of the load transfer based on the projection method for the specific application to FV hydrodynamic and FE structural coupling. Validation tests are performed on a simple fixed vertical cylinder in presence of waves and on a more practical case of container ship in large waves demonstrating the robustness and accuracy of the method.

Keywords: CFD, FEM, Fluid-Structure Interaction, NASTRAN,

---

*Corresponding author.
Email addresses: `andro.bakica@fsb.hr` (Andro Bakica),
`sime.malenica@bureauveritas.com` (Šime Malenica), `nikola.vladimir@fsb.hr`
(Nikola Vladimir)

1. Introduction

Striving for continuous improvement and weight reduction in marine structures impacts the design philosophy from the initial stage. Conservative classification rules based on the experience are often regarded as too rigorous with respect to the real sea loadings exerted on the structures. In order to reduce the potentially over-dimensioned structural elements while preserving the structural integrity, modern computational tools are increasingly developed for a more realistic sea load calculations.

The first step in the general hydro-structure interaction calculations is the interpolation between partially overlapping meshes of fluid and structure. In recent works, frequently used interpolation method for the field transfer on partially overlapping meshes is the Radial Basis Function (RBF) interpolation due to its robustness (see Dou et al., 2019; Thomas et al., 2019). However, the drawback of the RBF is in the reconstruction of the interpolation matrix at every change of field values and to increase the accuracy of the method, a global interpolation is often performed. All this requires at every time-step to construct and solve a full matrix which can hold huge computational expense in the entire simulation. More efficient alternative to the RBF is the projection method. Ji et al. (2014) proposed a projection of the entire panel to the fluid mesh. In case the structural element projects to multiple fluid elements for each part of the structural element different pressure is assigned. The method results with a difference in the total force and moment on the fluid mesh, which are then artificially removed by an optimizing algorithm. Another type of projection is shown by Piro and Maki (2013). Here the projection is based from structural integration points per finite element i.e. Gauss points. The pressure value is obtained by averaging the values in four closest fluid face centres. Although robust and stable, the averaging of the pressure obviously diffuses the pressure peaks, especially present in slamming effects, hence lowering the structural response. Approach featuring structural integration points is also presented by Paik et al. (2009) and Farhat et al. (1998) where the accent is placed upon the two-way interaction. On the other hand, interesting approach is presented by Martínez-Ferrer et al. (2018) where the entire interaction is solved inside the Finite Volume (FV) framework, thus contributing significantly to the efficiency of the method in parallel.

From a practical point of view, recently there is a significant rise in the application of hydro-structural tools. Most often, solvers employed in the interaction are the Finite Element Method (FEM) for the structural part and the CFD for the fluid solution. Paik and Carrica (2014) employed CFD-FEM coupling and studied the rolling tank motions including the free-surface effects where a good agreement is found with the experimental data. In order to reduce the vortex vibrations, Matin Nikoo et al. (2018) successfully optimized the design using the CFD-FEM interface. Pernod et al. (2019) performed the experimental analysis of the composite hydrofoil and validated the experimental data with the CFD-FEM numerical method. Also, investigating the hydrofoil vibrations, Huang et al. (2019) found similar wet frequencies compared to experimental data. Other applications of hydro-structure coupling can also be found when investigating sloshing effects (Hwang et al., 2016) as well as in offshore structures (Lim and Xiao, 2016). Obvious need for a more accurate structural response with respect to fluid loadings has also influenced a number of industrial software available (see Cole and Neu, 2019; Dhavalikar et al., 2015).

Majority of the above references and some additional recent works (see el Moctar et al., 2017; Takami et al., 2018) feature a two-way coupling procedure with the significance of the work based around the preservation of motions and forces on the interface which mutually interact. In some practical cases, there is no need for the elastic motions to be taken into account and the only major problem becomes how to transfer correctly the fluid surface forces to the structural nodes. Pressure transfer and grid interpolation is frequently referred as a small part of the entire procedure and is not studied in detail due to complexities involved in the communication between the meshes. Additionally, in a two-way coupling physical problems are rather different comparing to the quasi-static approach such as the geometrical change of the mesh topology and the influence of structural deformation on the flow field. For the stated reason, methods employed in a two-way approach can often be too robust when used in a quasi-static manner. The present paper deals with the one-way coupling methods within the linear quasi-static assumptions for the structural response i.e. constant structural stiffness matrix. In this sense, the main technical issue is related to the consistent pressure transfer from the hydrodynamic mesh to the structural mesh as a loading of the FE structural model.

In the present work the fluid solution is based on the FV arbitrary polyhedra framework of OpenFOAM in the community driven branch `foam-extend`.

Coupling with the FEM solver is performed using the method which could be classified as the projection method. The nodal forces are computed from the fluid pressure field on the projection of the structural integration points (Gauss points). For this particular work, it is assumed that the interface structural elements are linear plate elements which are almost exclusively found in the offshore and shipping industry and include finite elements in contact with water. Full theoretical and practical details are given regarding the calculation of nodal forces and the comparison is made with the simpler uniform pressure transfer per element. It is important to stress that the use of different elements would be fairly easy to add since the interaction tool is developed in the objected-oriented environment using C++. Furthermore, the procedure to calculate the pressure at the structural points projected on the fluid mesh is thoroughly described with the highlighted benefits of the rigid body assumption in the quasi-static approach. Pressure is taken without decreasing the possible peak of the loading at a certain fluid cell by careful geometrical consideration. Regarding the differing mesh densities i.e. if the structural model contains few elements at the location of the strong pressure gradients, the number of Gaussian points per element can simply be increased, thus capturing the non-uniformity of the pressure field more accurately.

The paper is divided into four main sections. Second section describes separately the mathematical background of the hydrodynamic and the structural solver with the full implementation details of the coupling interface. Third section features two test cases, force and moment transfer for the fixed cylinder in waves and container ship encountering green-water phenomena for which structural analysis of the breakwater structure is performed. Finally, in the fourth section, conclusions are drawn.

2. Hydro-structure interaction model

For the sake of clarity, the theoretical background of the hydrodynamic and the structural numerical models is presented.

2.1. Hydrodynamic model

Hydrodynamic model is based on the fully non-linear CFD solver using the open-source code OpenFOAM in the FV discretisation. The two-phase

Nomenclature

$()^L$	In FE local coordinate system	G_i^h	i-th Gauss point projection on fluid mesh
α	Indicator function	M_G	Least square geometrical matrix
β	Element rotation vector		
δ	Vector of nodal unknowns	N^w	Interpolation function
ν_e	Effective kinematic viscosity	N_i	Element shape function for node i
ξ, η	FEM element parametric space coordinates		
		p	Total pressure
f^w	Nodal forces vector	p_d	Dynamic pressure
G_i	Element i-th Gauss point	w	Element deflection vector

model for naval applications is solved using a dedicated NavalHydro pack. The governing equations for the incompressible flow are:

- continuity equation

$$\nabla\boldsymbol{\cdot}\mathbf{u} = 0, \tag{1}$$

- momentum equation

$$\frac{\partial \mathbf{u}}{\partial t} + \nabla\boldsymbol{\cdot}(\mathbf{uu}) - \nabla\boldsymbol{\cdot}(\nu\nabla\mathbf{u}) = -\frac{1}{\rho(\mathbf{x})}\nabla p_d + \nabla\boldsymbol{\cdot}\mathbf{R}. \tag{2}$$

where p_d is the dynamic pressure, $\mathbf{x}$ is the spatial vector, $\mathbf{g}$ is gravitational acceleration, $\rho(\mathbf{x})$ is the density dependent on the fluid properties, $\mathbf{R}$ is the Reynolds stress tensor and ν is the kinematic viscosity. As can be seen in the Equation 2, surface tension effects are neglected since they are assumed to be small for the naval hydrodynamic applications.

The two-phase flow formulation is handled with the most conservative indicator function α or the so-called Volume-of-Fluid approach (Ubbink and Issa, 1999):

$$\frac{\partial \alpha}{\partial t} + \nabla\boldsymbol{\cdot}(\mathbf{u}\alpha) + \nabla\boldsymbol{\cdot}\mathbf{u}_r\alpha(1-\alpha) = 0, \tag{3}$$

where the third term is called the compressive term active only in the vicinity of the free-surface i.e. when α is between 0 and 1. Well known problem of the free-surface smearing due to the non-physical density interpolation is handled with the Ghost Fluid Method (GFM). Theoretical details are provided in Huang et al. (2007) with the detailed implementation of the VOF and GFM coupled with the incompressible flow given in Vukčević et al. (2017). It is important to note that with the GFM, the smearing does not influence the density field. Additionally, the tangential stress balance is approximated with the continuous effective viscosity field defined in the following equation:

$$\nu_e = \alpha\nu_{e,w} + (1 - \alpha)\nu_{e,a}, \tag{4}$$

where $\nu_{e,a}$ and $\nu_{e,w}$ are effective kinematic viscosities for air and water, respectively.

In case of fixed cylinder simulations, different method is applied to the two-phase flow formulation since there is no separation of the free surface. Instead of the VOF method, the Level Set (LS) formulation is applied (Sun and Beckermann, 2007) with the Phase Field (PF) defined as the signed distance function which is the shortest Euclidean distance from the free-surface:

$$\phi(\psi) = \tanh(\frac{\psi}{\epsilon\sqrt{2}}), \tag{5}$$

where ψ is the signed distance field and ϵ is the interface smearing parameter. Details of the implementation are provided in Vukčević et al. (2016a) and Vukčević et al. (2016b) with the detailed verification and validation of the method. The waves are defined using a fully non-linear stream function wave theory. To eliminate the wave reflection from the boundaries relaxation zones are placed at the edges of the boundaries following Jasak et al. (2015).

2.2. Structural model

Without loss of generality, a general quadrilateral plate finite element is considered as shown in Figure 1. Description of the element in parametric space eases the evaluation of the different integrals when using the Gauss quadrature integration method. Parametric space can be obtained by mapping the initial physical space using the following shape (mapping) functions:

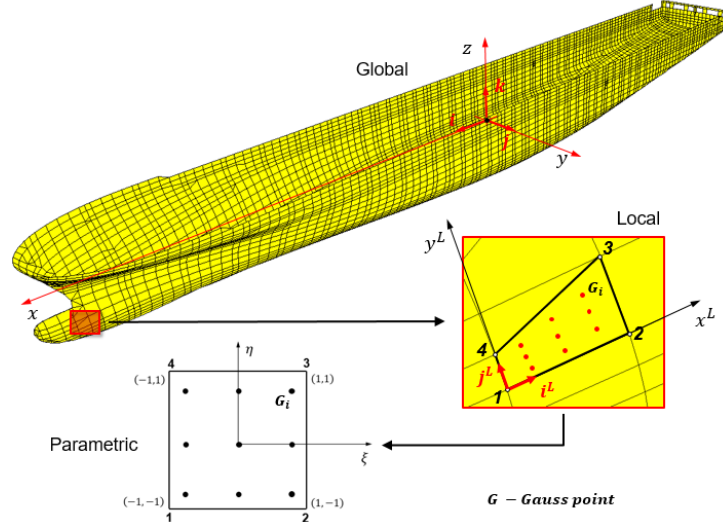$$N_i = \frac{1}{4}(1 + \xi_i\xi)(1 + \eta_i\eta) \tag{6}$$

Figure 1: Quadrilateral plate finite element description in global, local and parametric space.

where ξ_i and η_i are the coordinates of the four nodes in the parametric space. With these notations the local coordinates and local space derivatives can be evaluated using the following expressions:

$$x^L = \sum_{i=1}^{4} N_i(\xi, \eta) x_i^L \qquad y^L = \sum_{i=1}^{4} N_i(\xi, \eta) y_i^L. \tag{7}$$

$$\frac{\partial x^L}{\partial \xi} = \sum_{i=1}^{4} \frac{\partial N_i(\xi, \eta)}{\partial \xi} x_i^L \qquad \frac{\partial y^L}{\partial \xi} = \sum_{i=1}^{4} \frac{\partial N_i(\xi, \eta)}{\partial \xi} y_i^L, \tag{8}$$

$$\frac{\partial x^L}{\partial \eta} = \sum_{i=1}^{4} \frac{\partial N_i(\xi, \eta)}{\partial \eta} x_i^L \qquad \frac{\partial y^L}{\partial \eta} = \sum_{i=1}^{4} \frac{\partial N_i(\xi, \eta)}{\partial \eta} y_i^L, \tag{9}$$

where x_i^L and y_i^L are the nodal coordinates in the local coordinate system specific to each finite element.

Furthermore, the local deformation of the typical plate element is defined by local deflection w^L and two local rotation vectors β_x^L and β_y^L:

$$\beta_x^L = -\frac{\partial w^L}{\partial x^L} \qquad \beta_y^L = -\frac{\partial w^L}{\partial y^L}. \tag{10}$$

7

It follows that there exist three degrees of freedom per node and the vector of the nodal unknowns, in the local coordinate system, become:

$$\{\delta^L\}^T = \{w_1^L | \beta_{x1}^L | \beta_{y1}^L | ... | w_4^L | \beta_{x4}^L | \beta_{y4}^L |\} \tag{11}$$

where the notation "$\{ \ \}^{T}$" is used to denote the transpose operation.

With these notations, the local plate deflection w^L inside the finite element can be formally written in the following form:

$$w^L[x^L(\xi,\eta), y^L(\xi,\eta)] = w^L(\xi,\eta) = \sum_{i=1}^{n} N_i^w(\xi,\eta)\delta_i^L = \{\mathbf{N}^W\}^T\{\delta^L\}, \tag{12}$$

The vector $\{\mathbf{N}^W\}$ in the above equation, is composed of the interpolation functions which are, in principle, independent of the previously defined shape functions N_i. There are many different ways to chose the interpolation functions and usually the polynomial representation is chosen. It is common to write:

$$\{\mathbf{N}^W\}^T = \{N_{11}^w | N_{12}^w | N_{13}^w | ... | N_{41}^w | N_{42}^w | N_{43}^w |\} \tag{13}$$

The well known case of the simple iso-parametric elements is recovered by writing:

$$N_{i1}^w = N_i \qquad , \qquad N_{i2}^w = N_{i3}^w = 0 \tag{14}$$

The simple iso-parametric finite elements are known not to be very precise and usually more sophisticated elements are used. Typical example are the CQUAD elements in Nastran (Siemens, 2014) or the DKQ elements in open source software Code_ASTER (EDF, 2020). The quality and efficiency of the different formulations depends on the choice of those functions. Details of different formulations will not be mentioned here, it is only noted that the representation Equation 13 remains formally valid for all of them. Although this section contains the details regarding the quadrilateral element, the same principles apply to the triangular plate element. The main difference is the number of nodes and the number and position of Gauss points. For the sake of simplicity the detailed expressions are not presented here.

2.2.1. Generalized nodal forces

As already indicated in the introduction, only the pressure induced forces are considered here, so that the virtual work can be written as:

$$W = \iint_{S_L} pw^L dS, \tag{15}$$

8

where p is the external pressure. Within the parametric representation of the finite element surface, equation of the element surface and its differential element can be written as follows:

$$\mathbf{r}^L(\xi, \eta) = x^L(\xi, \eta)\mathbf{i}^L + y^L(\xi, \eta)\mathbf{j}^L \qquad dS = \left\| \frac{\partial \mathbf{r}^L}{\partial \xi} \times \frac{\partial \mathbf{r}^L}{\partial \eta} \right\| d\xi d\eta. \qquad (16)$$

so that the virtual work can be written as:

$$W = \int\limits_{-1}^{1} \int\limits_{-1}^{1} pw^L \left(\frac{\partial x^L}{\partial \xi} \frac{\partial y^L}{\partial \eta} - \frac{\partial y^L}{\partial \xi} \frac{\partial x^L}{\partial \eta} \right) d\xi d\eta. \qquad (17)$$

This can be written in compact form as:

$$W = \{\mathbf{f}^{wL}\}^T \{\delta^L\}, \qquad (18)$$

where:

$$\{\mathbf{f}^{wL}\}^T = \{f_{11}^{wL} | f_{12}^{wL} | f_{13}^{wL} || f_{41}^{wL} | f_{42}^{wL} | f_{43}^{wL}\} \qquad (19)$$

and:

$$f_{ij}^{wL} = \int\limits_{-1}^{1} \int\limits_{-1}^{1} pN_{ij}^{w} \left(\frac{\partial x^L}{\partial \xi} \frac{\partial y^L}{\partial \eta} - \frac{\partial y^L}{\partial \xi} \frac{\partial x^L}{\partial \eta} \right) d\xi d\eta, \qquad (20)$$

where the interpolation functions N_{ij}^{w} are defined by Equation 13.

This is the final expression for the nodal force vector in the local coordinate system. As can be seen, the expression in Equation 20 does not include the viscous shear forces. The viscous shear force contribution would require the consideration of the virtual work in the plane of the element. However, these effects are judged to be negligible for current purposes and are neglected. The main technical issue in the present work is the calculation of nodal forces shown in Equation 20 which are evaluated using the classical Gauss quadrature method. In order to perform such calculations, the pressure needs to be evaluated at the Gauss points for all finite elements. Finally, it is important to stress that the number of Gauss points does affect the computed nodal forces on each finite element. Since the computed hydrodynamic pressure obtained from CFD is fully non-linear, the increase in Gauss points provides a more accurate calculation of the nodal force integral from Equation 20. Of course, this is true only for the cases where there is a discontinuous pressure distribution along the finite element. For a reasonably smooth pressure field, the number of Gauss points per element could be even reduced to 1 without any loss in the integral calculation.

2.2.2. Reference to global coordinate system

For the nodal forces evaluated in the local coordinate system, certain transformations need to be defined in order to compute the global vector field of nodal forces. As known, any vector quantity can be expressed in multiple reference frames preserving its magnitude and direction and the same applies to the nodal force vector. Since the FEM final system of equations is written in the global coordinate system, certain geometrical transformations are necessary. The local coordinate system can be observed in Figure 1 and the definition is expressed as:

$$\mathbf{i}^L = \frac{P_2 - P_1}{\|P_2 P_1\|}, \qquad \mathbf{j}^L = \mathbf{k}^L \times \mathbf{i}^L,$$
$$\mathbf{k}^L = \mathbf{n} = \left(\frac{\partial \mathbf{r}^L}{\partial \xi} \times \frac{\partial \mathbf{r}^L}{\partial \eta} \right) \bigg/ \left\| \frac{\partial \mathbf{r}^L}{\partial \xi} \times \frac{\partial \mathbf{r}^L}{\partial \eta} \right\| d\xi d\eta, \tag{21}$$

where $\mathbf{k}^L$ is the vector oriented in the vertical direction from the element and $\mathbf{i}^L$ is chosen as the tangential vector. With the definition of the local coordinate system the orthogonal transformation matrix Q can be easily evaluated, hence for an arbitrary vector $\mathbf{v}$ it can be written:

$$\{\mathbf{v}\} = [\mathbf{Q}]^T \{\mathbf{v}^L\}, \qquad \{\mathbf{v}^L\} = [\mathbf{Q}]\{\mathbf{v}\}, \tag{22}$$

It is important to note that the definition of the virtual work is independent of the coordinate system meaning:

$$W = \{f^{wL}\}^T \{\delta^L\} = \{f^w\}^T \{\delta\} \tag{23}$$

2.3. FEM-CFD interface

As already indicated the nodal forces follow from the integrals (Equation 20) which are evaluated using the Gauss quadrature rule which requires the values of the hydrodynamic pressure in each Gauss point. Even if the number of Gauss point is very important for the precision of the integration, it is somehow irrelevant in the context of the pressure value interpolation. Indeed, whatever the number of Gauss points, the generic problem reduces to the interpolation of the hydrodynamic pressure from the CFD mesh to one particular Gauss point G_i which position in space is arbitrary. The straight-forward method of evaluating the pressure at Gauss point would be to simply "read" the pressure value at the point spatial location from CFD. Two types inconsistencies can occur with this approach. First, the Gauss point can
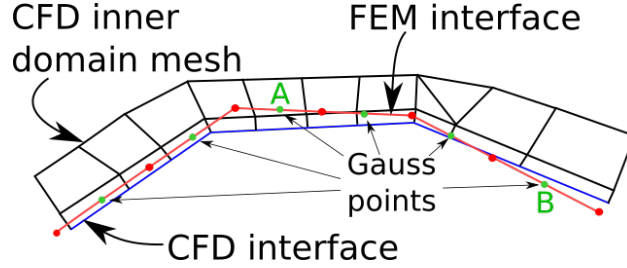
Figure 2: Inconsistencies with the CFD field values at FEM Gauss points. Point A - outside of the first CFD surface layer, Point B - outside of the CFD domain.

be located outside of the CFD domain i.e. where the pressure is undefined, hence making the interpolation invalid. Second, it is possible for the Gauss point to be located in the CFD domain, but outside of the surface layer cells which would significantly reduce the interpolated pressure value especially when assessing impact loads. These two types of inconsistencies are shown in Figure 2.

The present subsection describes the theory and implementation of the method developed within this work. The main difficulty is the preservation of the pressure field smoothness (absence of the discontinuous or step-wise pressure pattern) and the relative balance of total forces on both meshes without any artificial adjustment. The method employed in this study is usually addressed as the consistent interpolation based scheme. The method features a projection based algorithm for the transfer of the field between two non-matching 2D surfaces in 3D space. Algorithms employed are similar to "gluing method" (projection of structural integration points) described by Maman and Farhat (1995) and Farhat et al. (1998) with certain important differences. In further abbreviation structural integration point will be addressed as G_i with its corresponding point on the fluid mesh noted as G_i^h.

2.3.1. Processing of CFD interface mesh

From the CFD point of view in the FV framework, during the calculation of the fluid solution only the face and cell centres of the CFD surface mesh are used in the linear system of equations while solving the discretised form of the Equation 1 and Equation 2. Figure 3 shows the spatial points involved in the discretisation on the boundary surface. Since only the flux between

11

the internal faces is solved in a non-linear loop achieving conservative fluid solution, the key step is how to connect the step-wise profile of the fluid boundary face-centre values to a continuous pressure field. To be more clear on the subject, the interpolation problem is additionally visualised in Figure 4 along a simplified 1D CFD surface where the pressure value is sought for the green point. P_1 value is obtained with no interpolation on the interface surface, while P_2 assumes linear variation between control volumes. Complexity is highly increased for a 3D CFD domain and 2D interface surface, but the problem remains similar. Strictly speaking, any interpolation/extrapolation of the pressure from those discrete values to other points in the domain represents an additional approximation. However, there are different, more or less efficient, ways to perform the interpolation. The quality of this interpolation can be critical for the cases where the gradient of the pressure is important and where the size of the hydrodynamic and the structural meshes is comparable. In practice these situations occur regularly especially in the cases of the hydrodynamic impact where, depending on the local flow conditions, the gradient of the pressure can be huge. In order to reduce the influence of these abrupt changes of the pressure on the structural response the interpolation procedure should be performed very carefully and the smooth distribution needs to be targeted without the reduction of accuracy. The methodology in this study combines two main steps:

- interpolation from face and cell centres to points,

- shape function interpolation inside the fluid boundary face.

The interpolation is carried out using all the adjacent face centres and cell centres for the selected point. The interpolation is performed using the weighted linear least square fit. The details of the least square are given in the Appendix A. All values contributing to the final value at the point are shown in Figure 5. Main advantage of this approach lies in its computational efficiency. Method is purely geometrical, meaning that the distance relation between the points governs the interpolation. The largest part of the procedure lies in the construction of the geometrical matrix abbreviated as M_G for each CFD interface mesh point. In these circumstances, if usual mesh morphing algorithms are considered, for instance the closest point morphing or overset, the geometrical relation near the moving body usually does not change during the entire run-time in the fluid solution, hence leaving the geometrical matrix equal for each point. This advantage is unable to achieve
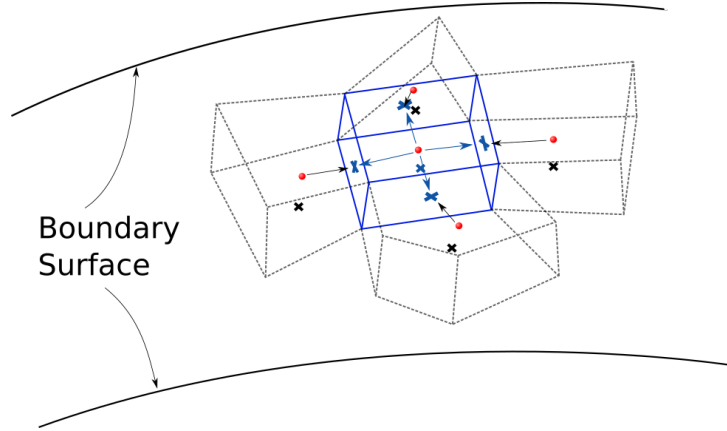
12

Figure 3: Cell centres (red circles) and face centres (crosses) involved in the solution algorithm around the observed control volume (blue).
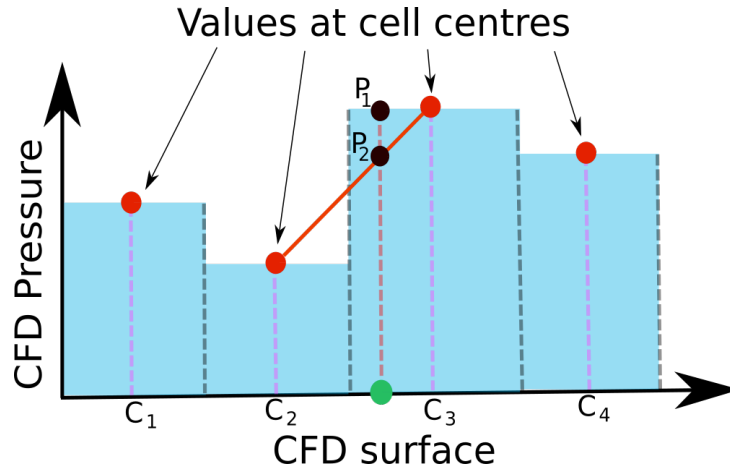

Figure 4: Step-wise pressure profile on the CFD interface mesh.
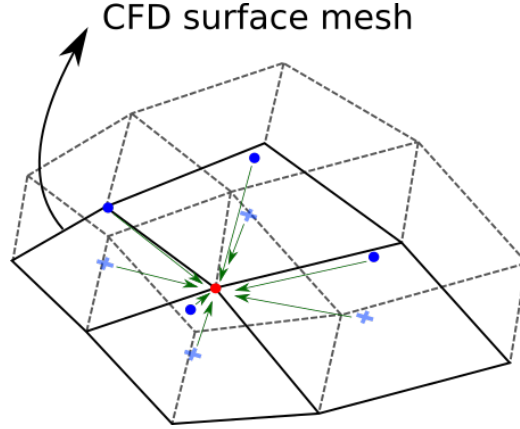
Figure 5: Surrounding cell centres (circles) and face centres (crosses) contributing to the least square volume to point interpolation.

using the usual RBF interpolation which requires the construction of the matrix at every change of surrounding field values. In any case, if the relation between the points has changed i.e. for a deforming body, the geometrical matrix can be simply updated, slightly increasing the computational expense. However, in the scope of quasi-static approach the geometrical matrix should remain equal during the entire pressure transfer process. At the end of this step using the presented interpolation, field values are known both at the nodes and at the centres of the surface elements on the CFD interface mesh.

Due to important practical reasons (additionally explained in the following subsection 2.3.2) the fluid mesh is fully triangulated meaning that, at the end of the step, all the elements of the CFD interface surface contain exactly three nodes. One of the key points is how to properly perform the triangulation, for the later use of the interpolation functions, without loosing any valuable information from the fluid solution. The straightforward method would be to completely skip the triangulation and use directly the shape functions inside each CFD surface face with the values at the points obtained by the least square interpolation. However, this approach would results in a small diffusion of the peak value contained in the face centre, since all the adjacent point values contain smaller or equal values. In order to keep intact the pressure values at the centres of the faces of CFD interface mesh, the triangulation is performed around the face centre. To clarify, it is

14

necessary to assume a regular triangular face on the fluid surface mesh. This triangle is not kept for the triangulation surface, but is subdivided into three triangles around its geometrical centre. Recall that the geometrical centre is equivalent to the face centre which is used in solving of discretised system of equations in CFD. With the proposed method, the value at any point can be obtained by simply using the interpolation function for each triangle. Type of the interpolation functions used should be established according to the order of accuracy of the fluid solver. For that reason, linear approximation of the pressure is selected. With this approach the CFD value at the face centre is preserved with the fully defined variation of the pressure field on the entire CFD interface mesh. Triangulation additionally improves the robustness of the approach without any loss of accuracy in the interpolation process assuming linear field variation inside a CFD control volume. Visual description of the triangulation process and the pressure calculation is shown in Figure 6. Furthermore, similar to FEM, for an arbitrary element belonging to the triangulated fluid surface and given the projected point inside the triangle, it can be written for the pressure:

$$p(G_i^h) = \sum_{j=1}^{3} N_j(G_i^h(x^L, y^L))p_j \tag{24}$$

where $G_i^h(x, y, z)$ is expressed in the local coordinate system as $G_i^h(x^L, y^L)$ in order to determine the shape function coefficient. With respect to the triangulation of the surface, each triangle has two pressure values obtained from the least square interpolation to points and one taken exactly as the value at the face centre in the fluid domain. The shape function coefficients are defined as:

$$N_j^h = 0.5(x_{j+1}^L y_{j+2}^L - x_{j+2}^L y_{j+1}^L + (y_{j+1}^L - y_{j+2}^L)x^L + (x_{j+2}^L - x_{j+1}^L)y^L)/A \tag{25}$$

where A is the area of the triangle, the superscript h in N_j^h denotes the hydro shape function coefficients and the subscript j goes from 1 to 3 since all the elements are triangles. As can be seen from the above expression, the shape function coefficients N_j^h are only dependant on the spatial location of nodes and the projected point. Once again, the rigid body assumption where the elastic motions are considered negligible in the flow solution (quasi-static approach) can be used to gain advantage. Obviously, for a non-deformable
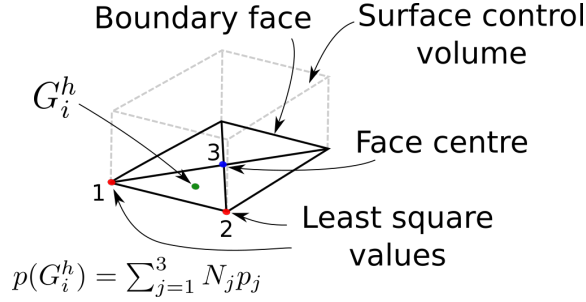
15

Figure 6: Triangulation of the fluid surface mesh and computation of the interpolated value at projected Gauss point.

body, N_j coefficients remain equal throughout the CFD simulation and can simply be stored during the pre-processing stage of the pressure transfer.

2.3.2. Processing of FEM interface mesh

When processing the CFD interface mesh, the hydrodynamic pressure is known at the nodes of all the triangles of the CFD interface surface, hence it is easily calculated at an arbitrary surface location. The distribution of the pressure on each triangle is assumed linear and the same shape functions, as those for the finite elements, are used. In the present case the points where the pressure needs to be interpolated are the projections of the Gauss points of the FE mesh. This means that the dedicated procedure for projection of an arbitrary point in space (Gauss point) onto an arbitrary surface in space discretised by the triangular elements (CFD interface surface) should be established. Due to the continuous rise in the mesh sizes, finding the adjacent closest point on a large meshes can be CPU time consuming. This is where the fact that only triangular elements are involved plays an important practical role. The triangular representation allows the use of highly efficient search algorithms. The algorithm used in the current study is based on a tree data structure called the octree. The algorithm subdivides the searching bounding box into eight sub-boxes (octants) with the process recursively repeating until the boxes with the potentially closest elements are found. At this point the different closest elements can be tested. Since all of the elements are triangles, specialized algorithm for the distance calculation between a point and a triangle in 3D is used to additionally accelerate the mapping procedure. Method is based on the approach from Eberly (1999).
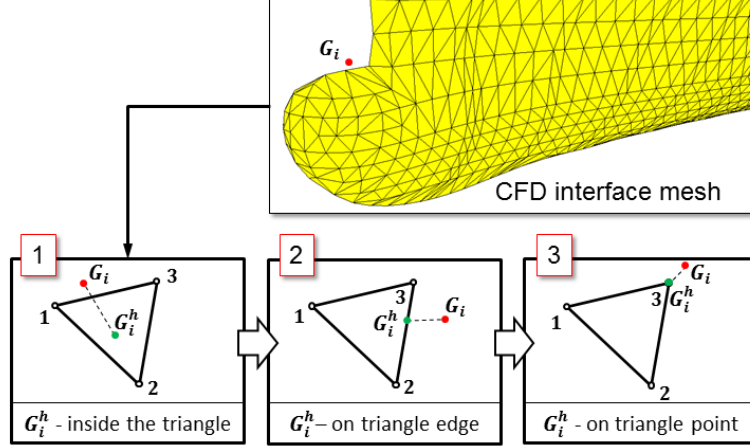
Figure 7: Three possible cases of finding the corresponding Gauss point on CFD interface mesh.

Method handles both the search when the projection is inside the triangle as well as the marginal case when the projection is on the edge or on the point of the element making the overall procedure very robust. Different possibilities for the projected Gauss point are summarized in Figure 7 where three possible cases are identified.

2.3.3. Summary - coupling procedure

After the evaluation of the separate data structures (FEM and CFD) has been defined in the subsections 2.3.1 and 2.3.2, the outline of the coupling will be given here together with the key aspects of the procedure. The above desccribed procedure allows calculating the nodal forces for each FE individually in its local coordinate system. In order to build the final system of equations for the whole structure, it is necessary to transfer the nodal forces from the local to the global coordinate system. This operation is relatively easy and can be done using the explanations in subsection 2.2.2. Finally, it should also be noted that for moving floating structures additional acceleration loading needs to be added but the description of this part of the loading is trivial and requires the knowledge of the global body accelerations of the center of gravity. As previously stated, the entire procedure is currently

made for the application to the linear quasi-static approach. Bearing this assumption in mind, the following procedure can be summarized as follows:

- Pre-processing stage:

  - Triangulation of the CFD surface mesh around the face centres.
  - Projection of the Gauss points only for FEM elements in contact with water onto the fluid surface mesh:

  $$G_{ki} \rightarrow G_{ki}^h, \quad \text{for } k = 1, 2, ..., n_s, \quad \text{for } i = 1, 2, ..., m_k^{gp}, \quad (26)$$

  where n_s is the number of finite elements in the structural model and m_k^{gp} is the number of Gauss points for k-th element.

  - Construction of the weighted linear least square geometrical matrix M_G for each point on the CFD interface mesh.
  - Calculation of shape function coefficients on the triangulated CFD interface mesh N_j^h for every G_{ki}^h with $j = 1, 2, 3$.

- Processing stage:

  - Obtain pressure values for each time step in fluid simulation $t_1, t_2, ..., t_n$.
  - Calculate interpolated values at CFD surface mesh points:

  $$M_{G_i} \cdot b(t, P_i), \quad \text{for } t = t_1, t_2, ..., t_n, \quad \text{for } i = 1, 2, ..., n_h \quad (27)$$

  where n_h denotes the number of points in the CFD interface mesh and b contains the pressure values at cell centres and face centres at a given time-step t. The same cell and face centres were used to construct the M_G in the pre-processing stage.

  - Compute values at the projected points by using previously stored N_j^h looping through all elements and Gauss projected points as in Equation 26 and also for all selected time-steps t:

  $$p(G_{ki}^h, t) = \sum_{j=1}^{3} N_j(G_{ki}^h(x^L, y^L))p_j(t). \quad (28)$$

  - Using calculated pressure values at Gauss points compute the global vector field of nodal forces (transformation from local to global system).
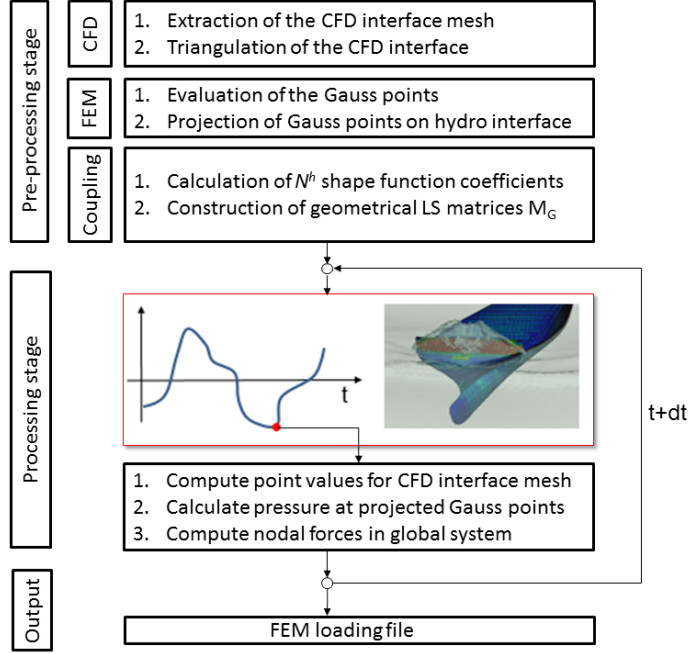
Figure 8: Summary of the overall coupling procedure.

- Post-processing stage:

    - Loading file for the FEM solver (nodal forces, accelerations etc.)

This procedure is very general and due to the object-oriented techniques, it is fairly easy to use it within any FEM software. The interventions are required only in the FEM reader and writer libraries, leaving the core of the interface intact. At the same time it should be noted that the developed tool gives in the comparison of the total forces and moments acting on both meshes which can be used as an initial indicator of how well the pressure transfer was achieved. Additionally, the visualization files of the two interface meshes (hydro and structure), together with corresponding pressure distributions, are produced making the tool easy to use and inspect the possible errors. The overall procedure is shown schematically in Figure 8.

3. Results and discussion

Two test cases are selected to verify and validate the hydro-structure interface. The main idea is to demonstrate the accuracy of the pressure transfer

19

by measuring the forces and moments on CFD mesh and comparing them to the ones acting on the FEM mesh. First case features a fixed vertical circular cylinder exposed to the waves of two different wavelengths. The second test case concerns more complex wave body interactions of the container ship in large waves. The second case is particularly interesting because it leads to the occurrence of the green water phenomena on the ship deck and consequently to large hydrodynamic impact on the structure of the breakwater. For this case both global loads on the whole ship as well as the local loads on breakwater are investigated together with the structural response on the breakwater which is studied in detail with respect to the mesh density. Finally, the proposed method is compared against a more simpler method for all cases. Within this simpler method, the pressure value at the structural Gauss points is taken to be equal to the pressure at the cell centre where the projection occurred, which basically means that the interpolation introduced in section 2.3.1 is not used i.e. for the green point in Figure 4 value P_1 is selected. It is important to note that the projection step is also done for this method because if the FEM Gauss point happens to be located outside of the CFD domain (see point B shown in Figure 2) the entire transfer would be invalid since the pressure for that specific point remains non-existing. This method will be abbreviated as Simple Method while the current method will be abbreviated as New Method in the subsequent graphs of the current section.

3.1. Fixed vertical cylinder in regular waves

In the present study the focus is on the accuracy of the load transfer so the flow solution is not examined in detail and the CFD results are assumed to be converged. It should be noted that this fact does not influence the conclusions about the quality of the pressure transfer because the origin of the CFD solution is somehow irrelevant in the present context. Of course, in the general application cases the convergence of the CFD solution needs to be studied first.

Circular cylinder of 10 m height (h) and of 2 m diameter (d) is fixed to the seabed in the water of 5 m depth. Wave height is chosen as 0.22 m while the wave length λ is set to 2.9 m equalling $\lambda_1 = 1.45 \cdot d$ for the first wave and 1.6 m or $\lambda_2 = 0.8 \cdot d$ for the second. This leads to the wave steepness of $A/\lambda = 0.038$ and $A/\lambda = 0.069$ respectively. CFD domain spans $4 \cdot d$ in front of the cylinder, $4 \cdot d$ on the sides with $10 \cdot d$ behind the cylinder to prevent wave reflection.
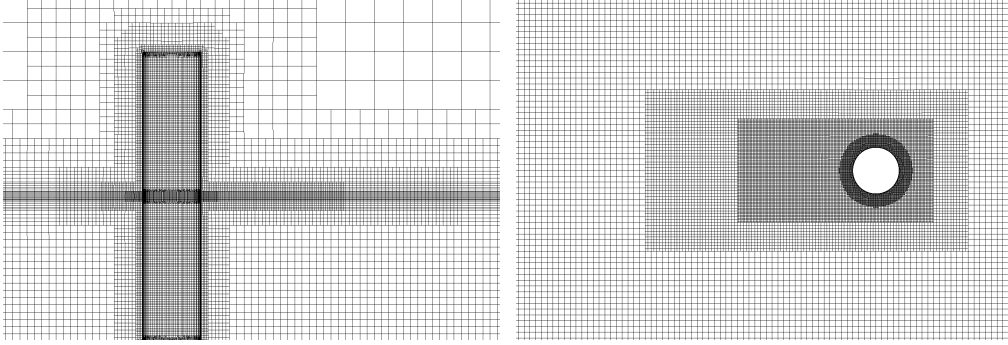
20

Figure 9: Fixed cylinder mesh at $x = 0$ (left) and $z = 0$ (right).

Computational domain is shown in Figure 9. The total number of cells is approximately 10^6 which is deemed enough for the current study. In order to ensure the convergence of the flow more than 10 periods are computed with 400 time-steps per wave period. After convergence is achieved, the pressure is stored for the last period with 40 time-steps per wave period. Snapshot of the computations is shown in Figure 10 for the first wave with the surface elevation and the dynamic pressure contours on the fixed cylinder. At this point CFD calculations are finished and hydro-structure interface can be run.

As already indicated, in this particular case, no structural calculations are performed. The comparison between the forces and moments on fluid and structural meshes is examined only. For that purpose, three different structural FEM meshes are built with 5.404 finite elements for the finest mesh, 2.860 for the medium mesh and 825 elements for the coarse mesh. On the fluid side the resulting CFD mesh at the hydro-structure interface has 18310 faces. Fluid and structural meshes are shown in Figure 11.

Pressure transfer is performed only for the dynamic pressure in this case. The dominant force acting on the cylinder is in the axial direction i.e. aligned with the wave advancing axis, and the relevant moment is around the axis perpendicular to the wave direction in the horizontal plane. In the current simulation abbreviation is F_x for the force and M_y for the moment. Three different numbers of Gauss points per finite element are tested depending on the order of interpolation (1, 4 and 9 for quadrilateral or 1, 3 and 4 for
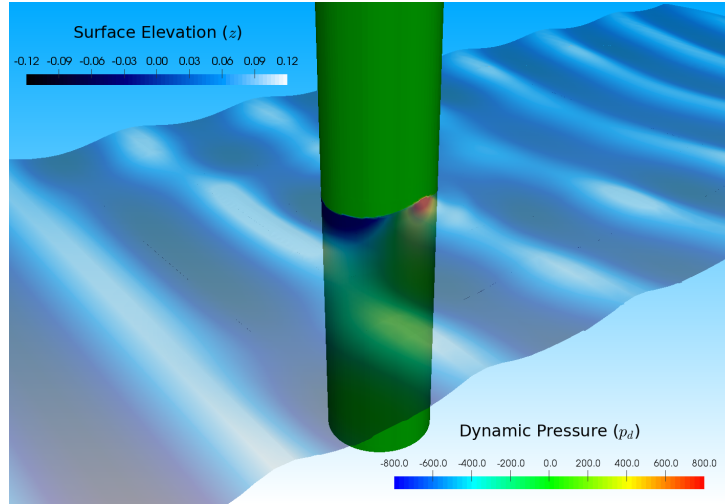
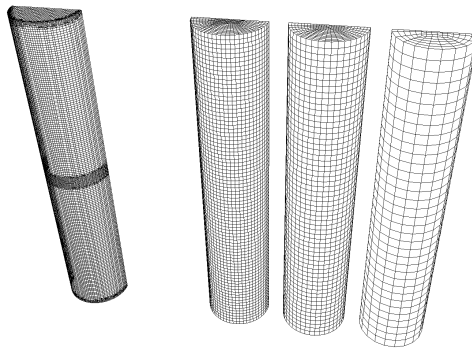Figure 10: Surface elevation and dynamic pressure on cylinder during simulation.

Figure 11: CFD mesh (left) with three FEM meshes (right).

triangular element) and the corresponding approximations are abbreviated with respect to the quadrilateral element as $GP1$ for 1 Gauss point, $GP4$ for 4 Gauss points and $GP9$ for 9 Gauss points. It is also noted that the $GP1$ approximation corresponds to the uniform distribution of the pressure over the element. This means that, in summary 9 types of different comparisons are possible i.e. three different meshes combined with three orders of approximation..

Although force and moment signal in time give a visual impression of the load transfer quality (for example see Figure 12), the difference between the forces is examined more quantitatively with the error defined as the percentage of the force range. This is done in Figure 13, where the distribution of the error for each of the interpolation order and FEM mesh is presented together with the comparison to the Simple Method. It can be seen that for all FEM meshes the simplest $GP1$ approximation shows the worst performance and contains a relatively large error which for the coarsest mesh even rises to 10%. However, the computation of the nodal forces using at least $GP4$ approximation increases the accuracy drastically, particularly for the coarsest FE mesh. Finally, as expected, the $GP9$ approximation additionally improves the accuracy of the model with the error at maximum about 2% meaning that most of the pressure field has been correctly captured and applied to the structural mesh irrelevant to the FEM mesh density. The reason is not only because larger number of Gauss points is included per finite element in the transfer, but also because the nodal forces are calculated using the shape functions relevant to the given element. This basically creates a smooth distribution of the pressure field in the background of the computation which corresponds more accurately to the CFD solution. Obviously, a non-uniform pressure field per element is mandatory. Figure 13 also shows the reduction in the calculated error compared to the Simple Method in all of the orders of interpolation, hence justifying the improved pressure value computation by proper interpolation scheme. In the case of long wave, the average absolute error in the entire wave period for the $GP9$ approximation, and for all meshes, is 0.50%, 0.25% and 0.21% ranging from coarsest to finest FEM by the New Method while for the Simple Method the average error is 0.68%, 0.63% and 0.58%, respectively. For the shorter wavelength, the force transfer features similar pattern of improvement compared to the Simple Method with the overall error increased for all cases with respect to the longer wavelength (see Figure 14). This general increase in the error is attributed to the steeper wave profile, thus creating a stronger pressure gra-
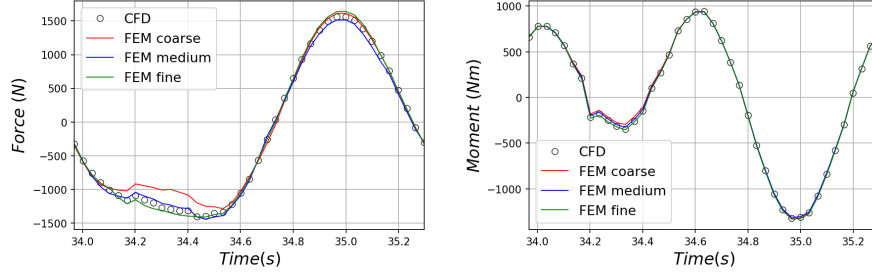
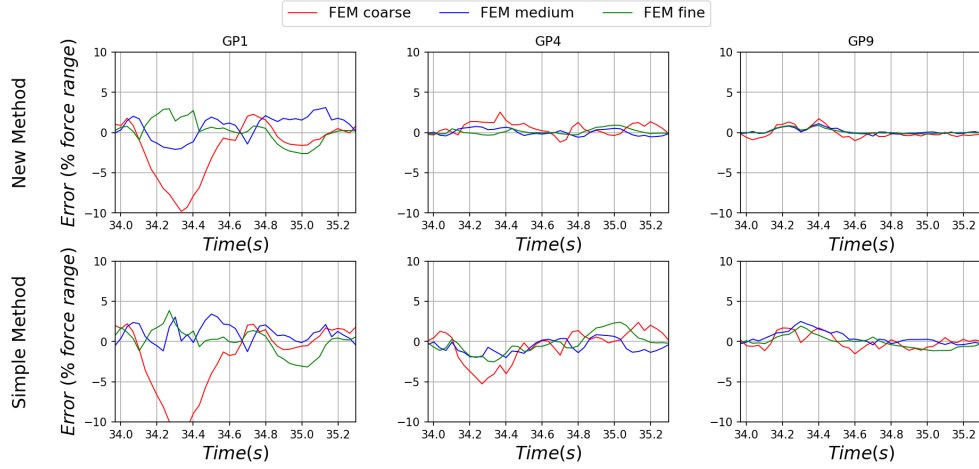Figure 12: Force transfer comparison in time - 1st order of interpolation.

Figure 13: Error in force transfer on cylinder - $\lambda_1 = 1.45 \cdot d$.

dient on the cylinder surface. However, by observing the results, even for the coarsest FEM mesh, the error is kept below 3% with the $GP9$ approximation which is deemed acceptable.

Another important measure of the pressure transfer quality is the bending moment M_y acting on the structure. The results for the moment on the coarsest mesh are shown in Figure 15. It can be seen that the relative error, for this particular case, is lower than for the force transfer with the maximum error rising to about 0.5% for $GP9$ on coarsest mesh. Again, an increase in accuracy is observed when using the direct evaluation of the nodal forces instead of applying the constant pressure ($GP1$). Comparison of the averaged errors for the entire period for both force and moment are given in

24
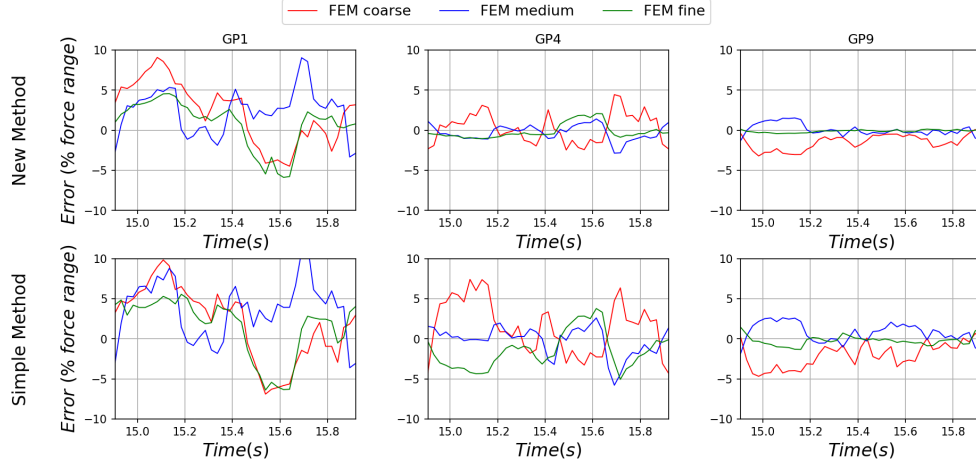
Figure 14: Error in force transfer on cylinder - $\lambda_1 = 0.8 \cdot d$.
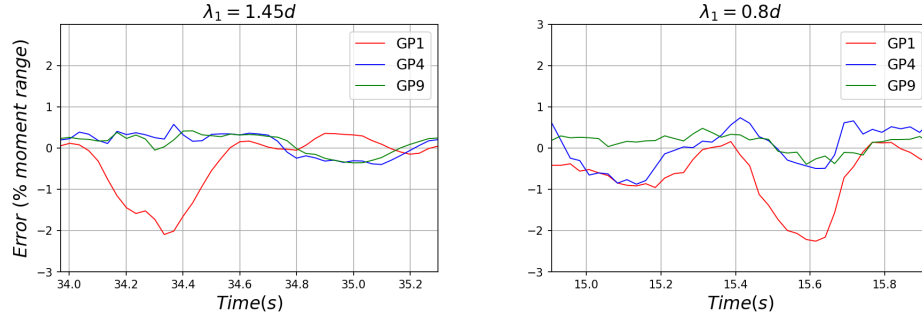
Figure 15: Bending moment transfer on coarse FEM mesh for both waves.

Figure 16 against the Simple Method and for the $GP9$ approximation. From the results, the advantage of applying the proper pressure interpolation is clearly visible.

On this simple example of a vertical cylinder in regular waves, the advantages of the proper interpolation method as well as the more accurate integration scheme (increased number of Gauss points), have been demonstrated, and now in the following section a more complex case of a ship sailing in large waves is presented.
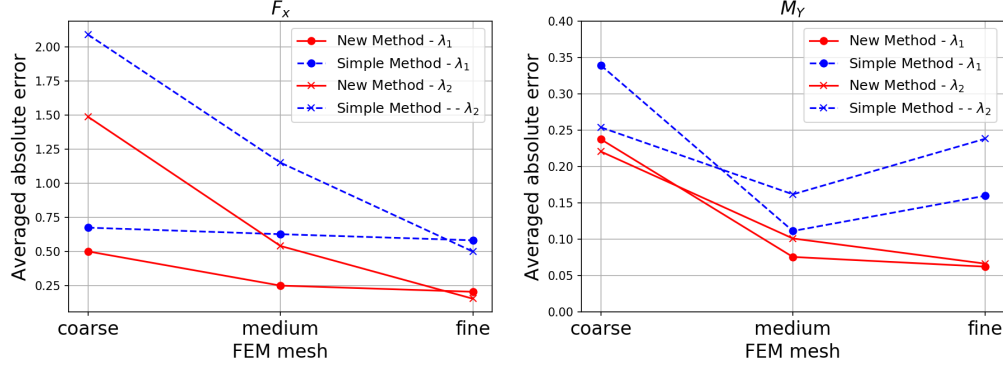
Figure 16: Averaged absolute error for F_X (left) and M_y (right) using 3rd order of interpolation.

Table 1: SkyBench ship particulars and working condition.

Ship particulars			Working condition		
Length over all	L_{OA} [m]	400	Ship speed	U_S [kn]	5.0
Length between perpendiculars	L_{PP} [m]	383	Wave height	H [m]	10.6
Breadth	B [m]	58.6	Wave length	λ [m]	385.0
Depth	H [m]	30.5	Wave incident angle	β [deg]	0.0
Design draught	T_d [m]	14.5			
Design speed	U [kn]	23.0			

3.2. Container ship in large waves

The model of the container ships which was used in the present calculations is the SkyBench Ultra Large Container Ship (Gatin et al., 2019). Ship particulars are given in Table 1 and the wave characteristics are chosen to maximize the green water event on the deck, which lead to the head wave conditions with the wave of amplitude $10.6m$ and the wavelength of $385.0m$. Ship forward speed is set different from the design speed and equals 5 knots according to the expected operating conditions in severe sea-state and classification rules. Full structural model with the extracted wetted surface and side-by-side with the CFD mesh is shown in Figure 17 highlighting the breakwater structure on the deck.
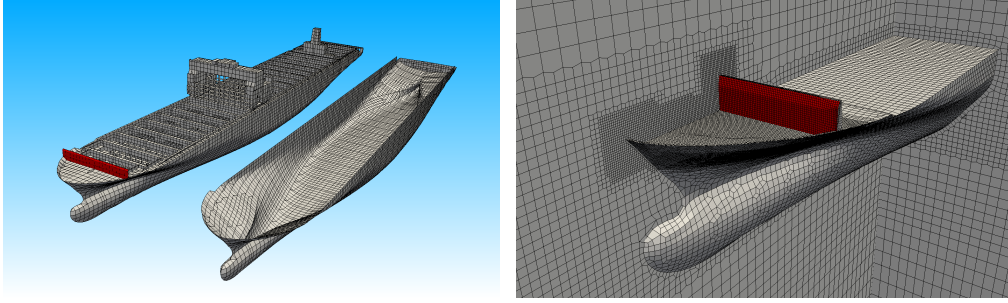
Figure 17: Full FEM model with the extracted wetted hull (left) and CFD mesh (right). Breakwater highlighted in red.

3.2.1. Hydrodynamic solution

CFD simulation is run with a VOF two-phase model and in order to ensure the convergence of the global ship motions, more than 30 wave periods are simulated. After geometrical mapping between the overlapping regions is achieved, the pressure can be transferred to the FEM model. First results are compared for the forces and the moments on the entire ship hull and for one FEM hull mesh only. Time signal and the error are shown in Figure 18. The error for the larger number of structural integration points is decreased below 0.5%, while the $GP1$ with the uniform pressure transfer is again relatively inaccurate as was the case in the fixed cylinder case.

Moving on to the breakwater, three different breakwater FEM meshes have been created with 340, 1027 and 4524 finite elements respectively. The corresponding number of the CFD cell faces at the interface is 2663. As expected, the present case features a violent fluid impact (see in Figure 19 the snapshot from the simulation) on the deck. Three consecutive time-steps around the moment of water impact are shown in Figure 20 for CFD original solution and for the FEM coarse mesh. Only first order of interpolation is shown where the pressure is directly transferred. Visualization of the higher interpolation orders is not feasible since the pressure is directly transformed into nodal forces which cannot be explicitly compared with the CFD surface pressures. Similar to the cylinder case, the error is estimated for the total force F_x on the breakwater and the moment M_y around the breakwater base. The corresponding time signals are shown in Figure 21 from where it is obvi-
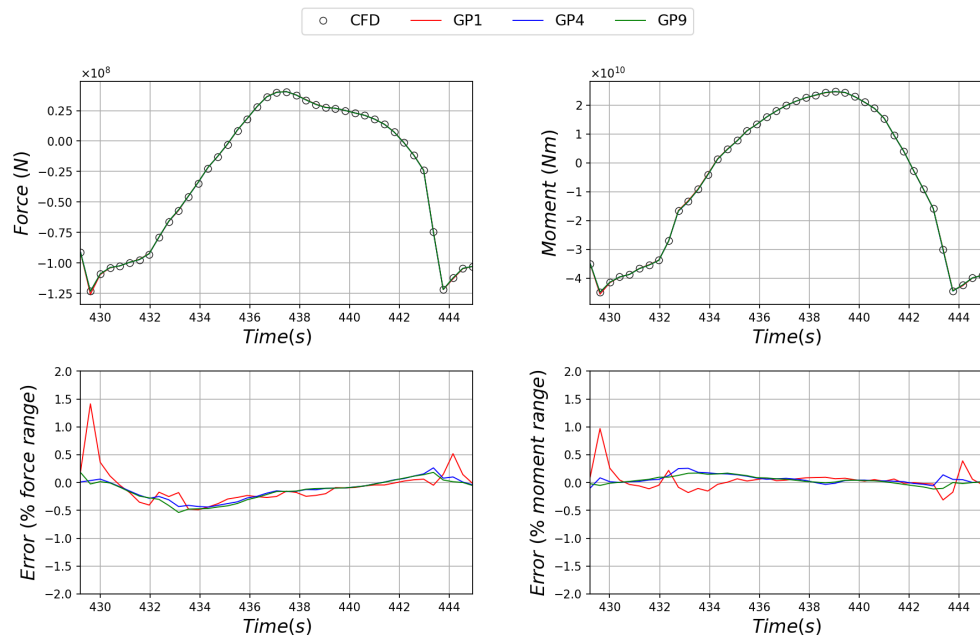
Figure 18: Force (left) and moment (right) transfer for SkyBench in time (1st row) and error (2nd row).
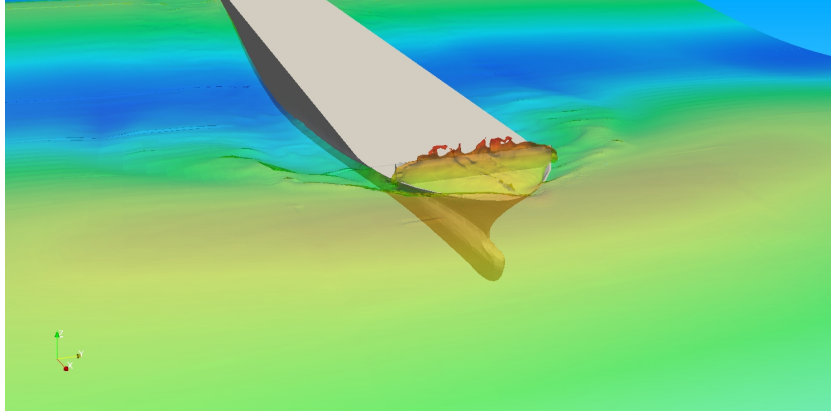
Figure 19: Green water impact on the container ship.

ous the coarsest mesh is capable of only capturing the main impact contours. Different quantities are used for the error estimation in this case, namely the peak values and the corresponding time integrals over the duration of impact which in some sense represent the average error. Main results are summarized in Figure 22 where the comparisons with the Simple Method are also included. The difference between the New Method and the Simple Method is clearly visible for all the FE meshes and for any number of Gauss points ($GP1$, $GP4$ and $GP9$). Indeed, the New Method shows monotonic covergence properties leading to the same result whatever the number of the Gauss points while the Simple Method shows somehow random behaviour even if the error is not very large. This is due to the large pressure gradients which occur during the hydrodynamic impact which can not be properly captured by the Simple Method and the jumps in pressure distribution on Gauss points are likely to occur. This is not the case for the method proposed here, where the pressure interpolation method is used in preprocessing stage and the pressure distribution was made continuous prior to pressure transfer. In addition the increase in the number of Gauss points allows for uniform convergence properties of the calculated integrals (Equation 20) which are needed for the evaluation of the nodal forces. This fact represents the significant advantage of the New Method which allows the uniform convergence properties regardless of the possible discontinuities in the CFD results when hydrodynamic impact occurs.
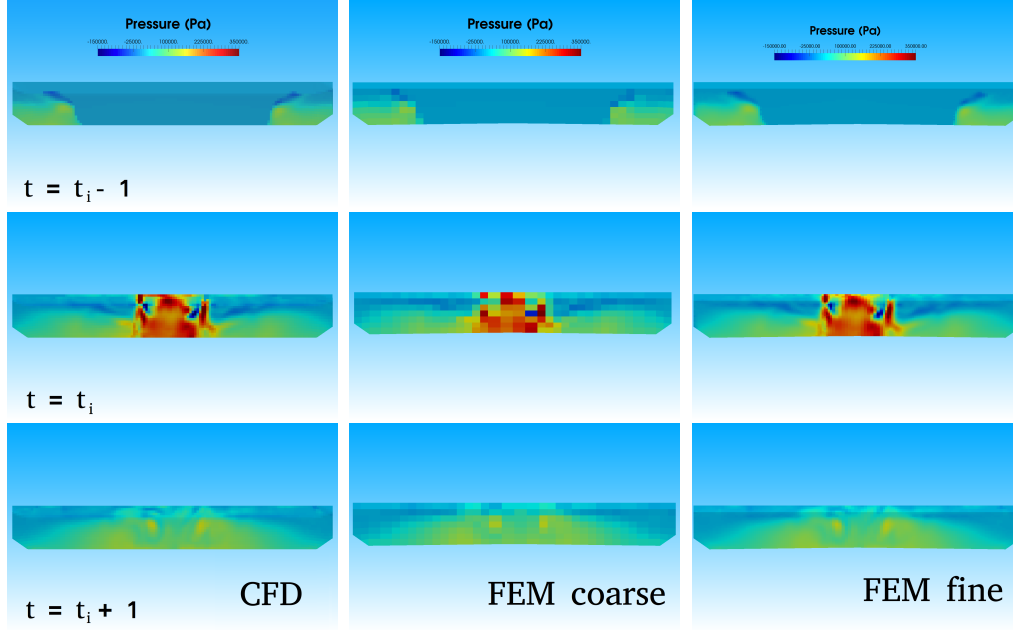
Figure 20: Pressure distribution on the breakwater (t_i at moment of impact). CFD (left) and GP1 interpolation for FEM coarse (center) and FEM fine (right).
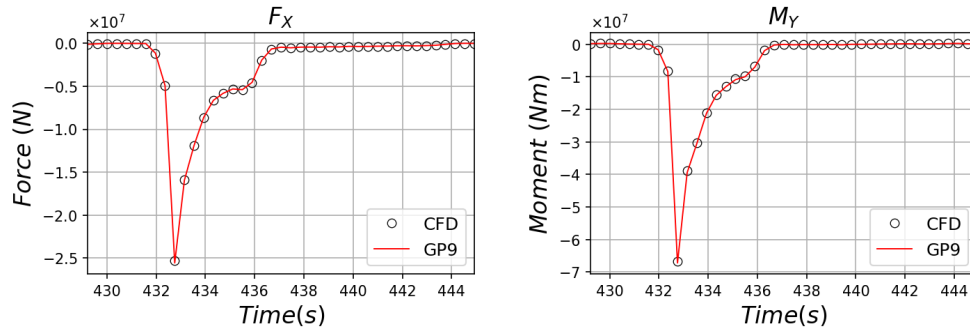

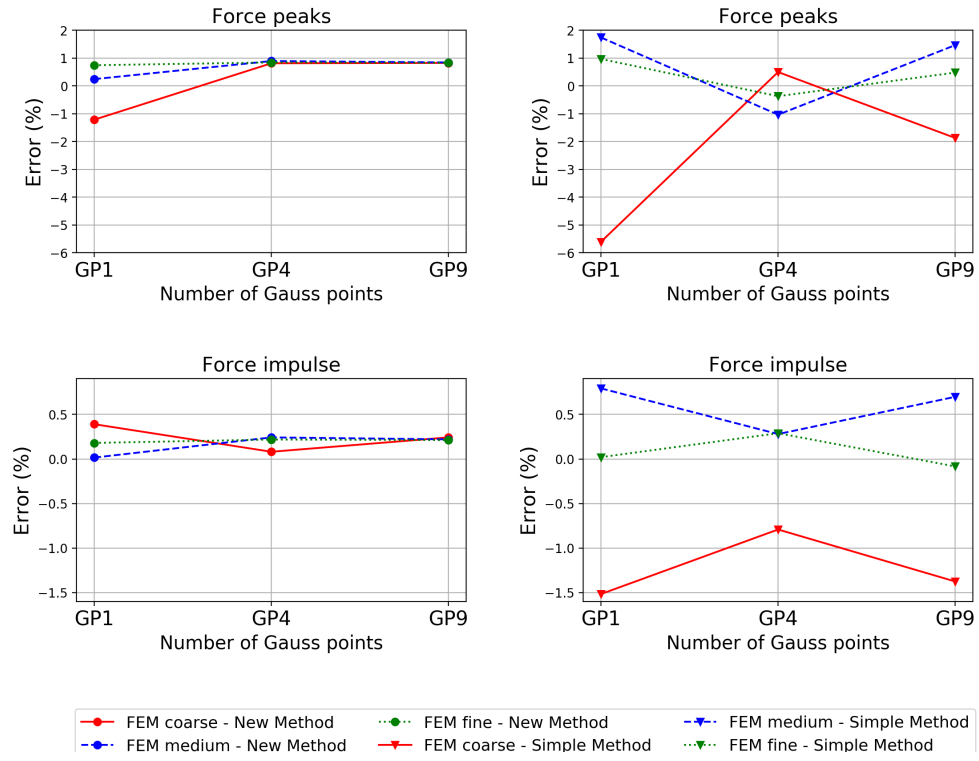Figure 21: Force and moment transfer for the coarse FEM mesh.

Figure 22: Error in the force peaks and force impulse compared to CFD solution. New method (left), Simple method (right).
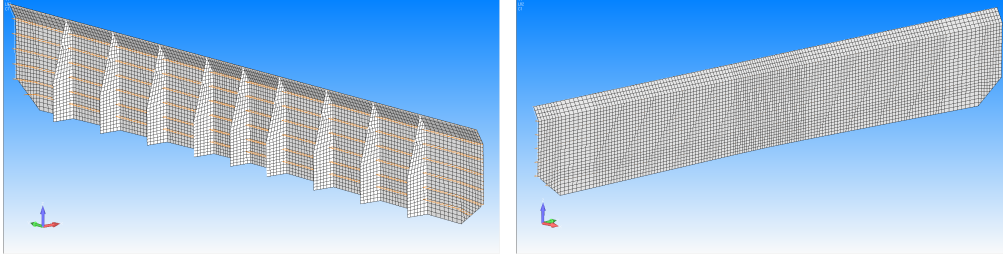
Figure 23: Breakwater FEM structural model with the finest mesh.

3.2.2. Structural response

Structural mesh consists mainly of 2D plate elements, mostly quadrilateral. Breakwater front pane is supported by 2D beam elements and additional vertical plate stiffeners. Fixed constraints are placed at the structure bottom since it is analysed separately from the full ship model. FEM solution is calculated with the commercial FEM software NX NASTRAN within the framework of FEMAP software. Hydrodynamic loads are transferred for the same time-steps as presented in the previous section 3.2.1. Besides the pressure or nodal forces, ship accelerations are also imported to the FEM solver i.e. translational and rotational acceleration. FEM model is kept constant while the global accelerations are rotated to account for the ship motion during transient load. In total 41 load cases were considered in order to cover the encounter period. The FEM model is shown on Figure 23 for the finest mesh.

Structural analysis is performed for all three orders of interpolation ($GP1$, $GP4$ and $GP9$) and for the New Method and Simple Method on all three breakwater FEM meshes differing in grid density. The deformation of two FEM nodes is analysed in more detail. One node is chosen at the middle side of the breakwater (where the impact is highest) and the other node is selected more to the side of a breakwater top structure. These nodes are abbreviated as P_M and P_S for middle and side node, respectively. Node location and corresponding time signal during the impact is presented in Figure 24. Detailed comparison is made only for the instant of the pressure peak. Comparison between all possible cases for the two selected FEM nodes is presented in Figure 25. From the results it can be seen that the New Method shows consistency with relation to the mesh density. For the finest mesh, the order of interpolation almost does not change the resulting
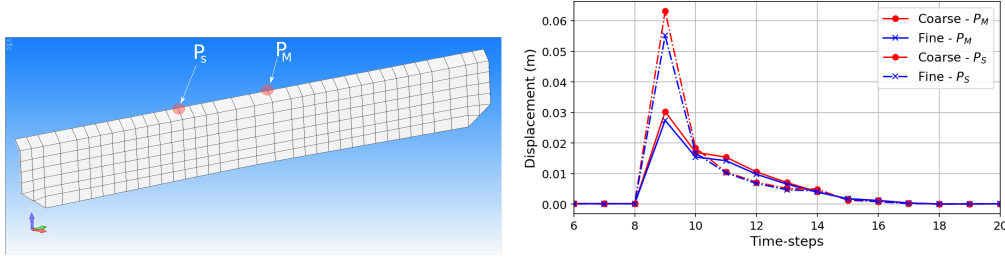
Figure 24: Highlighted selected nodes on the FEM model (left) and displacement time signal for those nodes.

nodal displacement and the improvement is obvious comparing the coarse and medium mesh, while the fine mesh can be regarded to as the reference. The Simple Method performs similar as when comparing the force transfer in section 3.2.1. Solution does not follow consistent improvement with respect to mesh density or interpolation and also for the finest mesh the oscillation dependant on the order is too high. This can be explained by the CFD step-wise pressure pattern since the method depends too much on the location of the Gauss point projection. The New Method simply overcomes this issue by performing the smooth pressure distribution along the CFD interface mesh which makes the method far less influenced by the geometrical differences in the fluid and structural interface surfaces and projection errors. According to the presented results, the pressure interpolation step proves to be important in terms of robustness and consistency of the load mapping method not only for the hydrodynamic pressure transfer, but also for the resulting structural response.

4. Conclusion

In this paper, an efficient numerical procedure for the load transfer from the CFD hydrodynamic model (FV framework) and the general FEM structural solver is described and validated. The method is relevant for any type of the hydro-structure calculations where the structural response is assumed not to influence the hydrodynamic solution. In that respect, the proposed methodology belongs to the class of the one-way coupling methods and is applied here to the evaluation of the linear quasi static structural re-
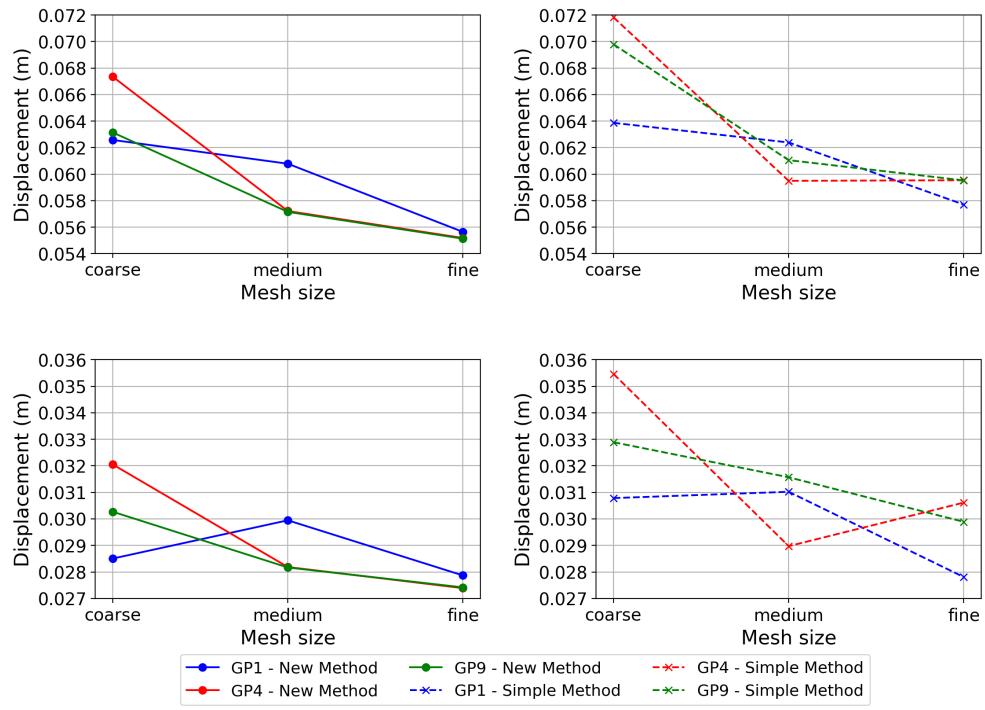
33

Figure 25: Deformation comparison for different cases on selected nodes. P_M first row, P_S second row.

sponse.

Once the interface meshes are properly identified, the proposed approach provides an extremely robust tool able to consistently consider any type of the local load variations which might occur in practice. This is achieved by evaluating the nodal forces outside of the FEM model using very precise numerical integration procedure. This point represents a major difference between the present approach and the more common approaches based on simple pressure transfer using the closest point method. Furthermore, in order not to alter the accuracy of the hydrodynamic solution, the original values of the hydrodynamic pressure are kept within the interpolation procedure using the special triangulation scheme. By doing this no additional numerical error is introduced and the method becomes very stable showing excellent convergence properties.

The superiority of the present method when compared to the simple pressure transfer is demonstrated on two practical examples. The first example considers the water wave diffraction by the circular vertical cylinder where the hydrodynamic loading is relatively smooth in space, and no major issues related to the pressure interpolation occur. Two waves were selected with the difference in wave-length to inspect the influence of the interpolation on a smoother or steeper wave profile. Satisfactory results are found for both waves with the error in the force transfer decreasing with the larger number of Gauss points per element or the number of FEM elements. When comparing to the simpler method, the proposed method performs better in both cylinder wave cases when computing the force transfer error with respect to the hydrodynamic solution. The second example is related to the evaluation of the structural response of the breakwater to the non-uniform impulsive pressure loading induced by the green water event. The proposed approach shows stable and consistent behaviour of the transferred hydrodynamic loads with respect to mesh density and number of Gauss points. Same amount of consistency is observed when assessing the breakwater structural response for the proposed method while the simpler approach shows quite unstable behaviour with the inconsistent convergence properties on both cases.

Even if the work presented here concerns the one way coupling procedure only, an important part of this work is applicable to the two way coupling procedures. Indeed, having clearly defined interfaces between the hydro and structural meshes, together with the corresponding distribution of the physical quantities (e.g. pressure for CFD and displacements for FEM), allows for the consistent exchange of any type of information between the two solvers.

This means in particular that the transfer of the structural deformations from FEM to CFD, which is necessary in the two-way coupling methods, can be done using exactly the same procedure as the one which was used here for the pressure transfer. However, it should be noted that when the dynamic two-way coupling simulations are of concern, and depending on the coupling procedure, it might happen that the CFD interface mesh changes at each time step so that the new coupling needs to be performed at each time step. This will of course lead to the increase of the CPU time but the consistency of the approach will be preserved. The development of the two-way coupling procedure, on the basis of the principles presented here, are left for further studies.

Acknowledgement

Appendix A. Weighted linear least square

By performing the Taylor expansion around the observed point (P_0) i.e. the point for which the interpolation value is sought, the expression is:

$$\phi(\mathbf{r}) = \phi_0 + \mathbf{G} \cdot (\mathbf{r} - \mathbf{r}_0) + \mathcal{O}^2(\mathbf{r}), \tag{A.1}$$

where ϕ_0 is the value of the field at P_0, G is the gradient and $\mathcal{O}^2(\mathbf{r})$ is the neglected part or the order of the error term. The unknowns at this point are ϕ_0 and G. For each neighbour point of P_0 the same expansion can be performed, which can be written in matrix form as:

$$\begin{bmatrix} \phi(\mathbf{r}_1) \\ \phi(\mathbf{r}_2) \\ \vdots \\ \phi(\mathbf{r}_n) \end{bmatrix} = \begin{bmatrix} \phi_0 \\ \phi_0 \\ \vdots \\ \phi_0 \end{bmatrix} + \begin{bmatrix} (\mathbf{r}_1 - \mathbf{r}_0)^\mathsf{T} \\ (\mathbf{r}_2 - \mathbf{r}_0)^\mathsf{T} \\ \vdots \\ (\mathbf{r}_n - \mathbf{r}_0)^\mathsf{T} \end{bmatrix} \mathbf{G} \tag{A.2}$$

where n is the number of neighbouring points used for the interpolation. Final matrix form can then be written as:

$$
\overbrace{\begin{bmatrix} \phi(\mathbf{r}_1) \\ \phi(\mathbf{r}_2) \\ \vdots \\ \phi(\mathbf{r}_n) \end{bmatrix}}^{\mathbf{b}} = \overbrace{\begin{bmatrix} 1 & (\mathbf{r}_1 - \mathbf{r}_0)_x & (\mathbf{r}_1 - \mathbf{r}_0)_y & (\mathbf{r}_1 - \mathbf{r}_0)_z \\ 1 & (\mathbf{r}_2 - \mathbf{r}_0)_x & (\mathbf{r}_2 - \mathbf{r}_0)_y & (\mathbf{r}_2 - \mathbf{r}_0)_z \\ \vdots & \vdots & \vdots & \vdots \\ 1 & (\mathbf{r}_n - \mathbf{r}_0)_x & (\mathbf{r}_n - \mathbf{r}_0)_y & (\mathbf{r}_n - \mathbf{r}_0)_z \end{bmatrix}}^{\mathbf{A}} \overbrace{\begin{bmatrix} \phi_0 \\ G_x \\ G_y \\ G_z \end{bmatrix}}^{\mathbf{x}}
\tag{A.3}
$$

$$
\underbrace{}_{n \times 1} \qquad \underbrace{}_{n \times 4} \qquad \underbrace{}_{4 \times 1}
$$

where the system $\mathbf{A} \cdot \mathbf{x} = \mathbf{b}$ can be recognized. From the vector of unknowns $\mathbf{x}$ the first element represents the field interpolated at point P_0. In order to solve the problem at least 4 points are needed which is satisfied in any CFD mesh. By inverting the matrix of equations and adding the weights, the vector of unknowns and the final form of the weighted linear least square can be expressed as:

$$
\mathbf{x} = [(\mathbf{A}^{\mathsf{T}} \mathbf{W} \mathbf{A})^{-1} \mathbf{A}^{\mathsf{T}} \mathbf{W}] \mathbf{b}
\tag{A.4}
$$

where $\mathbf{W}$ is a diagonal $n \times n$ matrix of weights.

References

Cole, R. E., Neu, W. L., 2019. Validation of a commercial fluid-structure interaction solver with applications to air cushion vehicle flexible seals. Ocean Engineering 189 (June), 106287.
URL https://doi.org/10.1016/j.oceaneng.2019.106287

Dhavalikar, S., Awasare, S., Joga, R., Kar, A. R., 2015. Whipping response analysis by one way fluid structure interaction - A case study. Ocean Engineering 103, 10–20.
URL http://dx.doi.org/10.1016/j.oceaneng.2015.04.048

Dou, W., Zhang, L., Chen, G., Zhu, W., 2019. A combined radial basis function based interpolation method for fluid-structure interaction problems and its application on high-speed trains. Advances in Engineering Software 131 (January), 143–152.

Eberly, D., 1999. Distance between point and triangle in 3D.
URL https://www.geometrictools.com/Documentation/DistancePoint3Triangle3.pdf

EDF, 2020. Finite element Code_ASTER, Analysis of Structures and Thermomechanics for Studies and Research.

el Moctar, O., Ley, J., Oberhagemann, J., Schellin, T., 2017. Nonlinear computational methods for hydroelastic effects of ships in extreme seas. Ocean Engineering 130, 659–673.

Farhat, C., Lesoinne, M., LeTallec, P., 1998. Load and motion transfer algorithms for fluid/structure interaction problems with non-matching discrete interfaces: Momentum and energy conservation, optimal discretization and application to aeroelasticity. Computer Methods in Applied Mechanics and Engineering 157 (1-2), 95–114.

Gatin, I., Vladimir, N., Malenica, Š., Jasak, H., 2019. Green sea loads in irregular waves with Finite Volume method. Ocean Engineering 171, 554–564.

Huang, J., Carrica, P. M., Stern, F., 2007. Coupled ghost fluid/two–phase level set method for curvilinear body–fitted grids. Int. J. Numer. Meth. Fluids 44, 867–897.

Huang, Z., Xiong, Y., Xu, Y., 2019. The simulation of deformation and vibration characteristics of a flexible hydrofoil based on static and transient FSI. Ocean Engineering 182 (January), 61–74.

Hwang, S. C., Park, J. C., Gotoh, H., Khayyer, A., Kang, K. J., 2016. Numerical simulations of sloshing flows with elastic baffles by using a particle-based fluid-structure interaction analysis method. Ocean Engineering 118, 227–241.
URL http://dx.doi.org/10.1016/j.oceaneng.2016.04.006

Jasak, H., Vukčević, V., Gatin, I., 2015. Numerical Simulation of Wave Loads on Static Offshore Structures. In: CFD for Wind and Tidal Offshore Turbines. Springer Tracts in Mechanical Engineering, pp. 95–105.

Ji, J., Kim, K., Seo, M., Kim, T., Park, D., Kim, Y., Ko, K. H., 2014. Load mapping for seamless interface between hydrodynamics and structural analyses. Advances in Engineering Software 71, 9–18.
URL http://dx.doi.org/10.1016/j.advengsoft.2014.01.015

Lim, W. Z., Xiao, R. Y., 2016. Fluid-structure interaction analysis of gravity-based structure (GBS) offshore platform with partitioned coupling method. Ocean Engineering 114, 1–9.
URL http://dx.doi.org/10.1016/j.oceaneng.2015.12.059

Maman, N., Farhat, C., 1995. Matching fluid and structure meshes for aeroelastic computations: A parallel approach. Computers and Structures 54 (4), 779–785.

Martínez-Ferrer, P. J., Qian, L., Ma, Z., Causon, D. M., Mingham, C. G., 2018. An efficient finite-volume method to study the interaction of two-phase fluid flows with elastic structures. Journal of Fluids and Structures 83, 54–71.

Matin Nikoo, H., Bi, K., Hao, H., 2018. Effectiveness of using pipe-in-pipe (PIP) concept to reduce vortex-induced vibrations (VIV): Three-dimensional two-way FSI analysis. Ocean Engineering 148 (August 2017), 263–276.
URL https://doi.org/10.1016/j.oceaneng.2017.11.040

Paik, K. J., Carrica, P. M., 2014. Fluid-structure interaction for an elastic structure interacting with free surface in a rolling tank. Ocean Engineering 84, 201–212.
URL http://dx.doi.org/10.1016/j.oceaneng.2014.04.016

Paik, K. J., Carrica, P. M., Lee, D., Maki, K., 2009. Strongly coupled fluid-structure interaction method for structural loads on surface ships. Ocean Engineering 36 (17-18), 1346–1357.
URL http://dx.doi.org/10.1016/j.oceaneng.2009.08.018

Pernod, L., Ducoin, A., Le Sourne, H., Astolfi, J. A., Casari, P., 2019. Experimental and numerical investigation of the fluid-structure interaction on a flexible composite hydrofoil under viscous flows. Ocean Engineering 194 (November).

Piro, D. J., Maki, K. J., 2013. Hydroelastic analysis of bodies that enter and exit water. Journal of Fluids and Structures 37, 134–150.
URL http://dx.doi.org/10.1016/j.jfluidstructs.2012.09.006

Siemens, 2014. NX NASTRAN User's Guide.

Sun, Y., Beckermann, C., 2007. Sharp interface tracking using the phase-field equation. J. Comput. Phys. 220, 626–653.

Takami, T., Matsui, S., Oka, M., Iijima, K., 2018. A numerical simulation method for predicting global and local hydroelastic response of a ship based on CFD and FEA coupling. Marine Structures 59 (August 2017), 368–386.
URL https://doi.org/10.1016/j.marstruc.2018.02.009

Thomas, D., Cerquaglia, M. L., Boman, R., Economon, T. D., Alonso, J. J., Dimitriadis, G., Terrapon, V. E., 2019. CUPyDO - An integrated Python environment for coupled fluid-structure simulations. Advances in Engineering Software 128 (April 2018), 69–85.
URL https://doi.org/10.1016/j.advengsoft.2018.05.007

Ubbink, O., Issa, R. I., 1999. A method for capturing sharp fluid interfaces on arbitrary meshes. J. Comput. Phys. 153, 26–50.

Vukčević, V., Jasak, H., Gatin, I., 2017. Implementation of the Ghost Fluid Method for free surface flows in polyhedral Finite Volume framework . Computers & Fluids 153, 1–19.

Vukčević, V., Jasak, H., Malenica, Š., 2016a. Decomposition model for naval hydrodynamic applications, Part I: Computational method. Ocean Engineering 121, 37–46.

Vukčević, V., Jasak, H., Malenica, Š., 2016b. Decomposition model for naval hydrodynamic applications, Part II: Verification and validation. Ocean Engineering 121, 76–88.
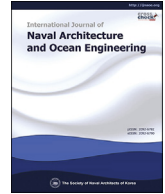
ARTICLE 4

Published journal article.

Numerical simulations of hydrodynamic loads and structural responses of a Pre-Swirl Stator

Andro Bakica [a, *], Nikola Vladimir [a], Hrvoje Jasak [a, b], Eun Soo Kim [c]

[a] Faculty of Mechanical Engineering and Naval Architecture, University of Zagreb, Zagreb, Croatia
[b] Wikki Ltd, London, United Kingdom
[c] Department of Naval Architecture and Ocean Engineering, Pusan National University, Busan, Republic of Korea

ARTICLE INFO

ABSTRACT

This paper investigates the effect of different flow models on the Pre-Swirl-Stator structural response from the perspective of a non-existing unified design procedure. Due to viscous effects near the propeller plane, the hydrodynamic solution is calculated by Computational Fluid Dynamics (CFD). Three different models are analysed: without the propeller, with the actuator disk and with the propeller. The main intention of this paper is to clarify the effects of the propeller model on the structural stresses in calm-water and waves which include the ship motion. CFD simulations are performed by means of OpenFOAM, while the structural response is calculated by means of the Finite Element Method (FEM) solver NAS-TRAN. Calm-water results have shown the inclusion of the propeller necessary from the design perspective, while the wave simulations have shown negligible propeller influence on the resulting stresses arising from the ship motions.

1. Introduction

Tightened rules and regulations for large merchant ships through the imposed requirements on greenhouse gas emissions and ship efficiency are continuously influencing the modern ship design. In these circumstances, hydrodynamic developments have significantly increased in the last decade paired with the huge improvement in computational power accessibility and cost.

Modern approach in ship efficiency improvements is by fitting the so-called Energy Saving Devices (ESDs). ESDs are closely connected with the flow around the propeller in order to improve the overall efficiency of the ship. Such devices can differ in the shape and location on the hull, but their main goal is to reduce the rotational and axial energy losses produced by the propeller. Standard classification of ESDs is by their longitudinal position on the ship stern with respect to the propeller plane on (Carlton, 2012): zone I (near the propeller inflow), zone II (at the propeller plane) and zone III (in the propeller slipstream), Fig. 1.

Current research trend in the field of ESDs is mostly focused on their hydrodynamic performance with the main goal of reducing the delivered power to the propeller. When estimating the benefits of any ESD type, either an experimental or a numerical approach is necessary for hydrodynamic evaluation. Regarding the experimental approach, a well-known Reynolds number inequality is especially pronounced in the case of ESDs since the majority of the analysis is focused on the ship wake which largely differs in model and full-scale (Dang et al., 2012). On the other hand, numerical approach works at equally accurate level regardless of the ship scale with the validation of numerical results and the experimental data necessary, especially for new and non-standard designs (Nowruzi and Najafi, 2019; Paik et al., 2015). In order to simulate the flow near the ESDs, Computational Fluid Dynamics (CFD) is regularly used since both viscosity and turbulence have an important role in forming the wake field near the propeller plane. Substantial research output is found within this field featuring propeller inflow devices such as Pre-Swirl Stator (PSS) (Park et al., 2015), duct type ESD (Shin et al., 2013) or their combination (Kim et al., 2015), devices recovering the energy from propeller slipstream (Shin et al., 2018; Kim et al., 2014), non-standard propeller designs (Min et al., 2009) or boss cap improvements (Lim et al., 2014).

In most of the above mentioned works, the focus is placed upon the thrust efficiency, estimation of fuel reduction or gas emissions
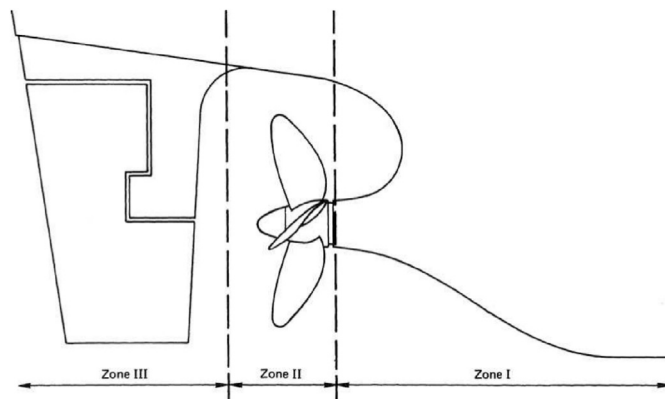
Fig. 1. ESD classification by position with respect to the propeller (Carlton, 2012).

and other performance issues. Although such subjects are of great importance in the design of ESDs, from practical use, they give no insight into the structural integrity of ESDs which are known to suffer from structural problems due to non-standard dynamic loads in a relatively complex flow field influenced by the global ship motion, propeller rotation and wake field. Currently, due to the mentioned complexities related to PSS hydrodynamic loads, a unified approach to its design is not defined in a straightforward manner. Usually, for any type of floating object and its appendices, the classification rules provide a set of guidelines guaranteeing the structural integrity, but in the case of PSS such procedure is not existing. Bearing in mind the PSS slender geometry subjected to various sea conditions and probable issues with the vaguely investigated structure, the topic has become relevant to both the industry and researchers. The Joint Research Project GRIP (Prins et al., 2016) evaluated PSS natural frequencies and compared them with the propeller blade frequencies while approximately calculating the Vortex Induced Vibrations (VIV). Extending the procedure, Paboeuf and Cassez (2017) developed a methodology for the estimation of PSS loads from the ship motion in waves. Different approach with respect to ship motions is proposed by Lee et al. (2016) and extended by Ju et al. (2018) featuring neural networks and regression formulas. Unfortunately, all proposed methodologies neglect the rotational effects from the propeller blades on the flow field near the PSS and more importantly, do not consider the propeller suction effect which can drastically change the pressure distribution on the duct type of ESD (see Bakica et al., 2020b). In order to consider the upstream influence of the propeller, multiple options are possible for the hydrodynamic model in the CFD simulation. Simplest propeller model would be the idealized disk approach (Bakica et al., 2019), which can accurately compute the global flow features with the significant reduction in the computational cost. Another type of simplification is presented by Gaggero et al. (2017) by employing the coupling between CFD and Boundary Element Method (BEM) to avoid the costly viscous propeller computation. Since the pressure forces are dominant in the propeller rotation, such simplification is justified and yields accurate results. Different approach to enhance efficiency of solving the unsteady non-linear periodic flows is by Harmonic Balance (HB) method (Cvijetić et al., 2018) where the variable decomposition is performed using the Fourier series. All these models are made due to significant complexities arising with the direct propeller computations. Nevertheless, if such direct calculations are necessary i.e. when transient phenomena and vortex creation are of high importance, the propeller rotation interface can be modelled in different ways. The first approach uses a rotating mesh region inside the surrounding domain as shown by Gokce et al. (2019) with

proper interpolation of the fields on the interface. The second approach is by employing the overset grid technology (see Carrica et al., 2011; Wang and Wan, 2020)) where the interpolation is calculated between the two overlapping mesh regions. Both approaches can estimate the propeller characteristics in an accurate manner and the final choice of modelling principles mostly depends on the CFD solver capabilities.

Overview of the current state-of-the-art in ESDs reveals an obvious gap regarding the ESD structural response. Structural analysis tends to oversimplify the hydrodynamic loads, while the CFD calculations are mostly focused on the analysis of the ship performance with and without the ESD. Existing design procedures usually neglect the influence of the propeller or fluid viscosity which significantly affects the ship wake and as such definitely has an effect on the pressure distribution, consequently leading to a different structural response. In order to investigate the actual hydrodynamic loads on the ESD structure, a full CFD computation needs to be performed and then the computed surface pressure field per time-step can be exported to the FEM model to properly study the obtained stress distribution and to have a clear correlation with the hydrodynamic conditions. Only with this approach, the actual influence of the propeller rotation or ship motions related to the ESD can be consistently analysed and their importance weighted for future definition of the structural design procedure especially when bearing in mind the current lack of straightforward classification rules with the installation of any ESD.

This paper aims to reveal the effect of propeller modelling on the structural response of a PSS type of ESD. First, the influence of different hydrodynamic models on the stress distribution is studied. Three different flow models are examined: without the propeller (no propeller modelling), with the propeller (direct propeller simulation) and with the Actuator Disk (AD) (simplified propulsion model). The main concern is to clearly distinguish the differences in the pressure distribution between the simpler propeller model and the full propeller computation as well as the stress differences between models. Besides the calm-water conditions, the three flow models are additionally tested in head waves to investigate their contribution on the final stress distribution, thus showing the necessary propulsion complexity needed to properly capture the structural impact on the PSS when the ship is sailing in waves. All of the computations include the free-surface and the dynamic body motion which is coupled with the propeller forces if present in the domain. This paper briefly investigates the PSS performance issues in order to verify the design quality which also proves the PSS effects near the propeller properly resolved. The CFD framework used in this work has already been validated on a full-scale ship trials (Jasak et al., 2019) as well as on model scale tests (Bakica et al., 2019, 2020b) with and without the ESD with sufficiently accurate results on global variables, near the propeller plane local flow field and propulsion coefficients. Hydrodynamic performance is not the main subject of this work, hence the assessment of the grid uncertainty is omitted. Although the changes in the CFD solution have an effect on the final structural response, this study focuses on the relative comparison of different conditions, thus making the small oscillations of the CFD solution irrelevant. Even so, one step of mesh refining is performed in order to verify that the forces on the ESD do not change significantly. All this with the above mentioned references shows the reliability of the solver and the proposed approach. Although the quality of the ESD design (PSS in this case) is examined in terms of efficiency gains, the design itself is more or less irrelevant from the structural point of view and any variations of the PSS geometry which aim to maximize the hydrodynamic gains are not performed. There are numerous works related to the hydrodynamic operation of PSS and the interested reader is referred to Sakamoto et al. (2019) for an extensive CFD study and Dang et al.

(2012) with the mainly experimental approach.

The paper is divided into six sections. The second section briefly explains the theoretical background of the mathematical models, the third section contains all the background necessary to establish hydrodynamic and structural numerical cases, the fourth section is dedicated to the hydrodynamic solution in calm-water and waves while the fifth section deals with the structural response for studied hydrodynamic conditions. Finally, in the sixth section a conclusion is given, outlining the work findings.

2. Theoretical background

In this section the theory behind the computations is given briefly for the hydrodynamic and structural part.

Hydrodynamic model is based on the Finite Volume (FV) discretisation in the arbitrary polyhedra framework of OpenFOAM (Weller et al., 1998) developed in the foam-extend environment. Dedicated in-house library for naval applications NavalHydro Pack (Vukčević et al., 2016a,b; Gatin et al., 2017) is employed in the study. Non-linearity of the solution is achieved through the combination of SIMPLE loop with a nested PISO loop i.e. pressure is solved multiple times for each velocity outer corrector (Jasak and Uroić, 2020). Fluid is assumed incompressible and the following equations are solved:

- continuity equation

$$\nabla \cdot u = 0, \tag{1}$$

- momentum equation

$$\frac{\partial u}{\partial t} + \nabla \cdot (u(u - u_G)) - \nabla(\nu \nabla u) = -\frac{1}{\rho x} \nabla p_d + \nabla \cdot R. \tag{2}$$

where $\rho(\bar{x})$ is the density which depends on the spatial vector $\bar{x}$, p_d is the dynamic pressure, ν is the kinematic viscosity, $\overline{u_G}$ is the grid velocity and $\overline{R}$ is the Reynolds stress tensor. Surface tension is neglected in Eq. (2) since the effects are assumed small for overall flow solution in naval applications. Free surface is considered using the Level Set (LS) formulation, (Sun and Beckermann, 2007), defining the field as the signed distance from the free surface:

$$\phi(\psi) = \tanh\left(\frac{\psi}{\varepsilon\sqrt{2}}\right), \tag{3}$$

where ψ is the signed distance field and ε is the smearing parameter dependent on the mesh resolution near the free surface. Treatment of the discontinuities at the interface is achieved with the Ghost Fluid Method (GFM) (Huang et al., 2007), thus removing the smearing of the density field. Details of the implementation regarding the entire hydrodynamic model can be found in Vukčević (2016). Relaxation zones are introduced at boundary edges to prevent wave reflection in the solution (Jasak et al., 2015). Regarding the turbulence model, a two-equation $k - \omega\ SST$ model is deemed accurate enough for the current analysis due to its proven reliability with ship self-propulsion flows (see Bakica et al., 2019). Near boundary flow is modelled with the use of wall functions sensitive to flow unsteadiness and pressure gradient effects (for details see Popovac and Hanjalic, 2007).

Structural model is based on the FEM formulation with the use of a well-established commercial code NASTRAN and for the details the reader can refer to Siemens (2014). Coupling of the structural and hydrodynamic solutions is performed using an in-house code fully explained in Bakica et al. (2020a), so here only a brief

description is given. Interpolation for partially overlapping meshes is based on the projection method. In order to reduce the error, the hydrodynamic CFD field is interpolated directly on the FEM element integration points. By obtaining these values, the resulting element nodal forces can be easily computed. Since the coupling is performed in a one-way approach, the utility can be run after the CFD simulation is finished on all of the necessary time-steps. After loading conditions are prepared for the FEM model, the structural analysis is performed.

In order to consider the fatigue response, the cumulative damage ratio for a certain stress $\Delta\sigma_{Ni}$ range is obtained by the following expression:

$$D_f = \sum_{i=1}^{n} \frac{n_f}{N_f}, \tag{4}$$

where D_f is the cumulative damage ratio for full load condition, n_f is the number of cycles at stress range $\Delta\sigma_{Ni}$ and N_f is the number of cycles to failure at stress range $\Delta\sigma_{Ni}$. Finally, the fatigue life can be calculated as a ratio of estimated design life and the previously defined cumulative damage D_f ratio.

3. Numerical setup

Ship geometry is a well known benchmark case KRISO Tanker KVLCC2. Geometry is openly available and the ship particulars can be found in CFD Workshop Website (2010). No experimental comparison is given here since the self-propulsion simulations have been validated against CFD results (Jasak et al., 2019; Bakica et al., 2019, 2020b) and in works of other authors (for example Gokce et al., 2019; Carrica et al., 2011). Furthermore, model scale simulations are not performed at all due to differing ship wake at propeller plane compared to the full scale flow and more importantly, due to the fact that the structural model of the PSS exists only in full scale. Ship and propeller particulars with the working condition for calm water and waves are given in Table 1. Main PSS geometry outline and fin numbering is given in Fig. 2. All three fins are created from the same airfoil sections differing only in the span-wise length.

3.1. Flow domain

Since PSS is an asymmetric device with respect to the y axis and the direct propeller modelling is necessary, a full CFD domain is created. The mesh is generated with the open-source tool

Table 1
KVLCC2 ship particulars.

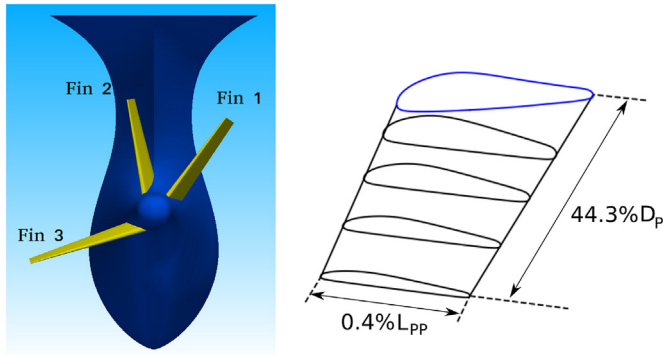| Hull parameters		
Length overall	L_{OA} [m]	325.5
Length between perpendiculars	L_{PP} [m]	320.0
Breadth	B [m]	58.0
Depth	H [m]	30.0
Design draught	T_d [m]	20.8
Ship speed	U [kn]	16.5
Propeller parameters		
Blade number		4
Diameter	D_P [m]	10.6
Ae/A0		0.4288
Hub ratio		0.155
Wave condition		
Wave height	H [m]	4.8
Wave length	λ [m]	384.0
Wave incident angle	β [deg]	0.0

Fig. 2. Fin numbering abbreviation (left) and the outlined geometry and sectional cuts for the Fin 3 (right) with the hull connection in blue (D_P - propeller diameter, L_{PP} ship length between perpendiculars).

snappyHexMesh. The overall CFD domain spans $2 \cdot L_{PP}$ from ship fore to the inlet boundary, $2 \cdot L_{PP}$ to each of the side boundaries and $2.5 \cdot L_{PP}$ to the outlet boundary. Free surface is refined in order to have an approximately 12 cells in the vertical direction per wave height for the coarsest mesh. Five boundary layers are added to the ship and on the PSS surface with the first layer thickness of 0.04 m and 0.005 m, respectively. CFD final generated mesh around the hull is shown in Fig. 3 which is equal for all simulations. Boundary conditions are set for the free-surface flow with relaxation zones on the domain outlet and sides to prevent wave reflection. For the two-phase flow fluid density and viscosity is adjusted to air and sea-water properties.

In the AD case, the disk is simply extracted from the mesh configuration without the propeller. All the details of the AD implementation are more thoroughly explained in Bakica et al. (2019), therefore here are given briefly. It is only important to state that the AD implementation is based on the idealized disk theory featuring pressure and velocity jumps at the selected faces based on open-water test data, inflow speed and rotation rate. Important characteristic of the current implementation is that the jump conditions are set at mesh faces as boundary conditions which does not require re-meshing of the previously developed domain without the AD. Rotation rate is obtained in the calm-water simulation with the AD using a PI controller until the resistance and thrust force reach an equilibrium (see Bakica et al., 2019, for implementation details).

For the most complex case with the inclusion of the propeller geometry, the mesh is generated in a different manner. First of all, the propeller rotation is modelled with a rotating mesh region inside the surrounding hull mesh where the propeller region is given an axis of rotation and rotational speed. For the interface between the two discontinuous meshes General Grid Interface (GGI) (Beaudoin and Jasak, 2008) is used which is readily available in the foam-extend environment. The GGI is based on the face area weight interpolation model at the matching interfaces which enables conservative and consistent solution of the flow variables at the disconnected mesh regions. For example, two geometrically conformal patches without any mesh connectivity between them and with different types of discretisation levels can be merged into a single simulation output without the loss of numerical stability. In the case of ship with the propeller, this approach can enable the proper mesh discretisation size near the hull and near the propeller which can significantly differ. Regarding the solver, GGI is introduced into the solution loop as the boundary condition, meaning it is updated multiple times in each outer corrector, thus providing necessary communication between the outer and inner interface boundary. For additional details regarding the GGI implementation such as face-cut algorithms and flow variable interpolation, the reader is referred to Beaudoin and Jasak (2008). The mesh for the propeller region is created using a detailed body-fitted procedure with the commercial tool Pointwise since any type of unstructured cut-mesh techniques from prior experience tend to create a step-wise pressure profile on the propeller blades due to reduced geometrical smoothness on the surface. The propeller blades are fitted with 10 boundary layers and structured mesh at the blade edges to ensure a high mesh quality where the most complex flow is expected. Although GGI does not set any constraints on the mesh size at the two merging mesh regions, it is clear that the size of interface face areas at both regions should be reasonably close, at best in one-to-one ratio, but this is not mandatory to achieve. Keeping this in mind, generated mesh with the GGI is shown on Fig. 5. Rotation rate for the propeller case is obtained in the same manner as for the AD, using a PI controller until the ship resistance and thrust are equal.

The final mesh with the propeller geometry included counts 3.35 M cells, opposed to 2.25 M cells in the case of the AD or without the propeller, with the propeller rotative region consisting of 1.35 M cells. Stern meshes for different configurations are presented in Fig. 4. All mesh cases have cell non-orthogonality condition satisfied below 70° and the OpenFOAM specific skewness criteria maximum around 4 for only a few mesh cells, which is deemed satisfactory.

When evaluating the PSS efficiency, two cases are run and both with the direct propeller modelling since benefits from the PSS are mainly from reducing the rotational losses which the current AD model cannot accurately predict. When finding the self-propulsion point for the two configurations, the comparison of propeller
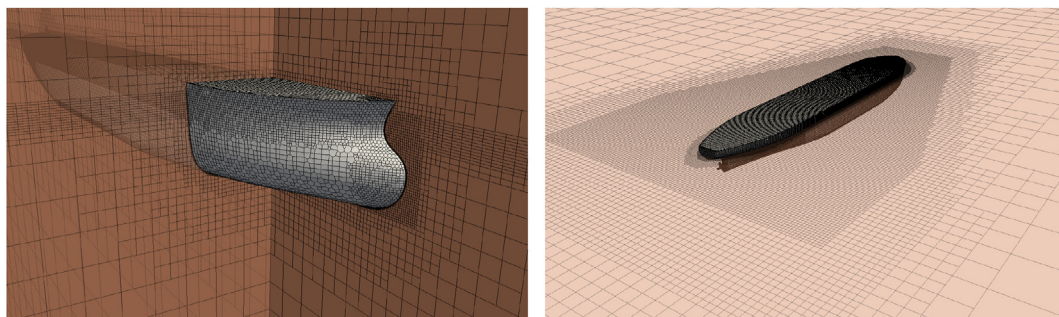

Fig. 3. Mesh around the hull and in the vicinity of the free surface.
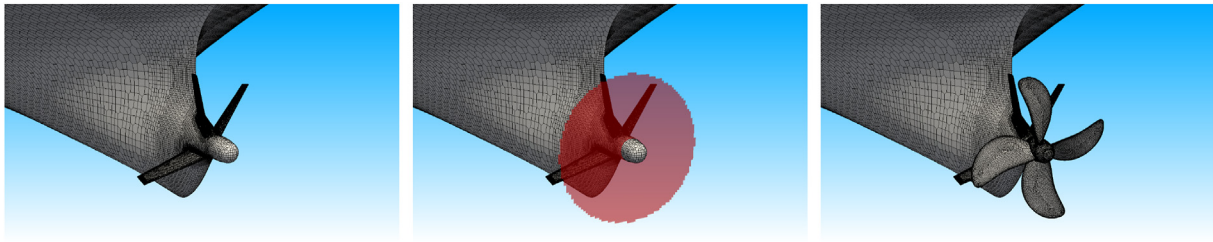
Fig. 4. Stern mesh without the propeller (left), with the AD highlighted in red (center) and with the propeller (right).

efficiency variables can be made, most importantly the shaft delivered power. The CFD solver is run until all of the global and local forces have reached convergence as well as the global ship motions. It should be noted that in all of the hydrodynamic cases ship is allowed only pitch and heave motions. Even small oscillation in the ship motions contribute to the force on the fins so the full domain convergence is necessary before evaluating local effects. The most important region in the flow is the ship aft containing the PSS. Forces on each fin are computed during the entire simulation and the simulation is run until those forces have converged. In order to eliminate the different discretisation step on the solution when comparing the cases i.e. grid size and time step, all three simulations are run in equal conditions. Equal grid size is achieved by keeping the same mesh connectivity on the PSS geometry in all three cases. Recall that without propeller and with AD cases have actually the same mesh, while the case with propeller only differs in the region where the propeller is included. Regarding the discretisation in time, the situation is somewhat different. The major concern is the case with the propeller. In order to achieve convergence, the time step needs to adjust to the propeller rotation for the local flow effects to be correctly captured, thus the time-step is set at 1.5° of propeller rotation. In all of the simulations, the same time step size is used to avoid time discretisation discrepancy between the cases when comparing the results. Although it seems irrational to use such a small time discretisation for the case without the propeller or for the AD case (especially when recalling that the AD implementation is written exactly to avoid the CPU heavy time step reduction), authors find this approach necessary for the relative comparison between the cases to be fully consistent. The three cases are computed on a cluster featuring Intel Xeon CPU E5-2637 v3 3.50 GHz with 40 processor cores employed. Finally, grid or time step uncertainty analysis is not performed and the cases relative comparison is deemed sufficient for further evaluation. It is assumed that the small deviations in the resulting force due to mesh refining are not significantly influencing the PSS forces and stresses. Nonetheless, one step of grid refining is performed to confirm this assumption and the resulting pressure loading in terms of lift and drag coefficients is evaluated in order to verify the

small dependency of the mesh size on the final solution. Mesh is refined to 5.6 M cells and the simulations are performed for the cases without the propeller and with the AD.

3.2. FEM model

Finite element model is created only for the ship aft structure including the PSS. Model mostly consists of the quadrilateral plate elements and triangular plate elements. Near the connection with the hull, solid elements are present. Constraints are imposed on the fore section of the model as necessary boundary conditions. The model is shown in Fig. 6 with relevant fin numbering. Each node of the fore section in the model is constrained for three translations and three rotations. The material on all elements in the model is a regular shipbuilding steel. When transferring the pressure distribution from the CFD flow solution, FEM model is kept stationary i.e. it is not moved corresponding to the ship sinkage and trim motion. Instead, the gravity vector is rotated with respect to the ship rotation, thus representing the same physical condition. In the calm-water condition only gravity is present as external acceleration while the wave simulation contains additional ship translational and rotational accelerations which should be considered.

Loading conditions are exported from the flow solution directly to the NASTRAN solver and are all automatically run using the subcases keywords and chosen loading types in NASTRAN framework. In order to prepare the model for the pressure transfer, elements in contact with water have to be extracted from the full FEM structural model to have an interface surface well defined between the fluid and the structure. Once the wetted surface is created the interpolation can be run on the stored CFD solutions. After generating the FEM load files with the interpolated pressures as nodal forces, these files need to be included in the full FEM model and the analysis can be run for all the subcases selected. It is worth mentioning that the interpolation process holds negligible CPU cost and time compared to the entire CFD analysis. As previously stated, the interpolation is performed following the procedure from Bakica et al. (2020a) where the pressure transfer between partially overlapping meshes is explained in detail.
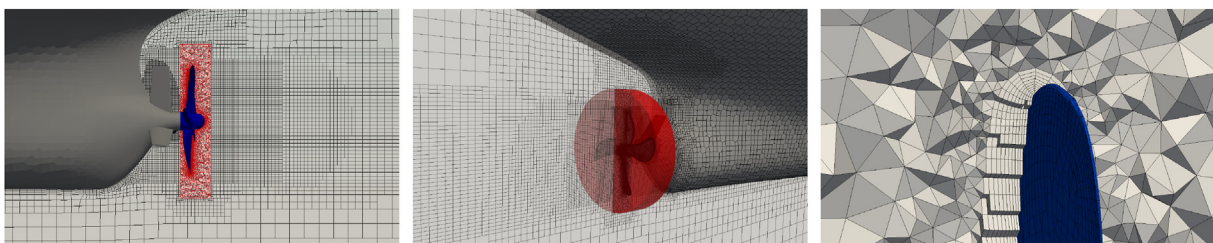

Fig. 5. Propeller mesh (left), GGI overlapping region highlighted in red (center) and close up view on the propeller tip mesh boundary layer (right).
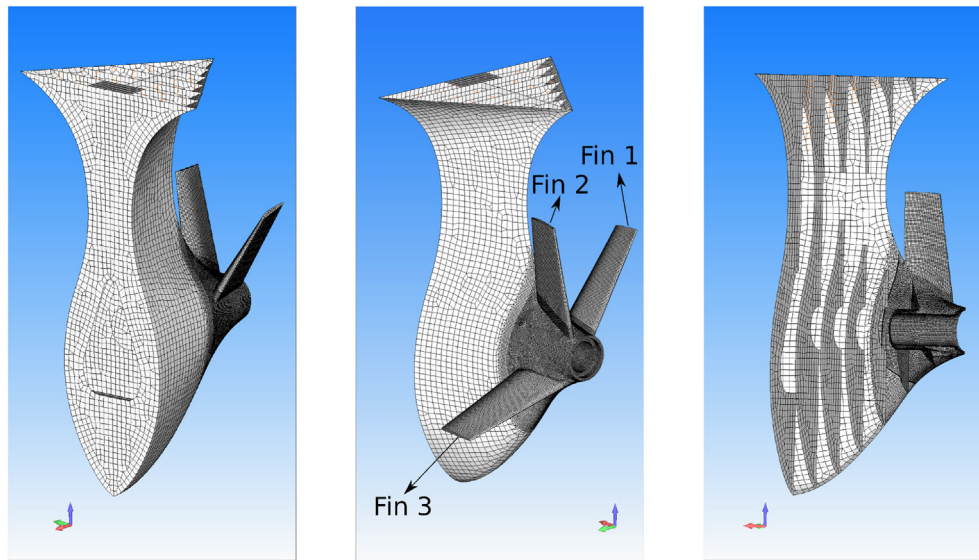
Fig. 6. FEM model of the aft ship structure with the PSS.

Fatigue analysis is performed for the calm-water case with the propeller. Design life is estimated to 25 years while the stress range is obtained from the FEM analysis loaded with the CFD pressure. The S-N curve is chosen according to (Tsou et al., 2019). For the wave simulation fatigue life is not estimated since it would require a more extensive study considering all of the sea-states which is out of scope for the current study.

4. Hydrodynamic results

4.1. PSS design evaluation

For the two cases with and without the PSS, the propulsion characteristics are evaluated and shown in Table 2. As can be observed, in the case with the PSS, torque coefficient is 4.7% higher and the rotation rate is 3.17% lower than without the ESD. This is consistent with the PSS operational characteristics. Each fin creates a rotative velocity component opposite to the propeller rotation which induces higher loads on the propeller blades, thus providing higher torque for lower rotation rate and equal amount of thrust. The most important benefit of the propeller and PSS interaction is the lower amount of the kinetic energy losses in the propeller wake which in turn has a direct effect on lowering the power delivered to the propeller shaft. For this design the estimated savings in delivered power are 4.69%. Amount of power gains due to PSS is similar in quantity as in the extensive study shown by Furcas and Gaggero (2021). The propeller pressure field is visualized on Fig. 7 for both conditions where slightly higher loading can be observed on the two bottom blades with the PSS. This shows the PSS design to be beneficial in terms of ship efficiency while showing the propeller and PSS interaction properly captured. However, the most important issue in the current study is related to the PSS structural response, so further analysis of the hydrodynamic results is omitted in this study.

4.2. Calm water - PSS hydrodynamic loads

The forces on the PSS are analysed in their local coordinate system divided into the drag and lift force. For future analysis, PSS fins are also numbered according to Fig. 2 in counterclockwise direction making the horizontal fin on the port side as Fin 3. Forces are compared in terms of lift and drag coefficients which are calculated using each fin projected area, density and velocity which is taken equal to the ship speed. Force signal is averaged for the last 15 periods of propeller rotation while the same time frame is used for averaging the other two cases. Without the propeller and with the AD are compared with the propeller case since it fully accounts for the propeller rotation, suction effect and blade passage, thus it is considered as the reference to other conditions. Flow domain is run for 450 s simulation time for each numerical model. The CPU time for the without propeller case is 45.2 h compared to 133.4 h for direct propeller simulation. The AD case is run from the last stored solution of the case without the propeller until local flows near the AD and PSS converge so it cannot be explicitly compared, but the overall CPU cost is almost equal to the without the propeller case per time-step. It is important to mention that the AD and without the propeller cases are currently run with a substantially lower time-step than necessary to have the same time discretisation as the propeller case so their CPU cost can be significantly lowered.

Comparison of lift and drag coefficients for each condition is given in Table 3 where the difference between cases is calculated with respect to the direct propeller computation. From the results it is obvious the difference is consistently lower for the AD case in both lift and drag coefficients for all three fins compared to the setup without the propeller. Observing the only AD case, the difference is lower for the drag in the entire PSS, especially when compared to the large difference in the without the propeller drag coefficient. The difference is reduced from 41.80%, 10.06% and 3.81% to only 1.65%, 4.94% and 0.49%. On the other hand, the lift force also features an improvement when the AD is active, but the overall comparison w/propeller can still be relatively large and is maximum for the Fin 3 with value of 23.18%, yet it is still a significant improvement compared to 38.93% without the propeller. It can be concluded that the suction effect from the actuator disk creates a relatively similar flow field upstream of the propeller plane, hence the accuracy in the drag force is sufficient with such
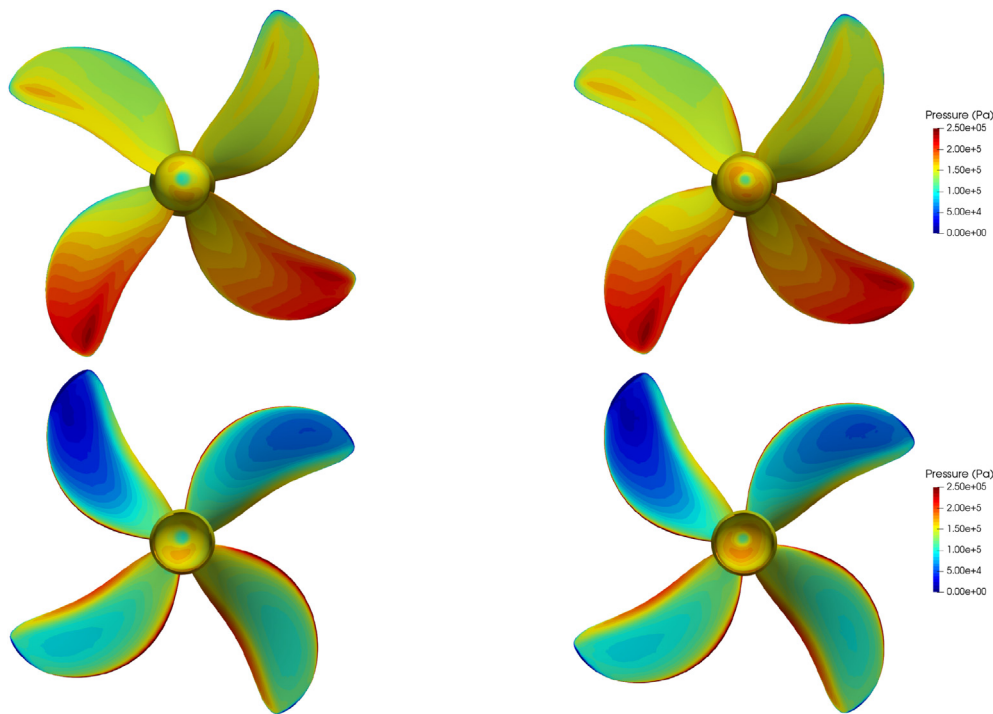
Table 2
Self-propulsion results.

Ship condition	U_s (kn)	n_s (rpm)	K_T	$10K_Q$	P_D (kW)
Without PSS	16.5	70.14	0.1333	0.1638	2258
With PSS	16.5	67.92	0.1428	0.1720	2152

Fig. 7. Pressure contours on the propeller surface, with PSS (right), without PSS (left).

Table 3
PSS - Lift and drag coefficients in calm water.

	w/o propeller			With AD			With propeller		
	Fin 1	Fin 2	Fin 3	Fin 1	Fin 2	Fin 3	Fin 1	Fin 2	Fin 3
C_D	0.0364	0.2111	0.1547	0.0252	0.2013	0.1497	0.0257	0.1918	0.1490
$D^*_{C_D}$ (%)	−41.799	−10.055	−3.806	1.651	−4.944	−0.489	/	/	/
C_L	0.2178	0.2674	0.3599	0.2063	0.3184	0.4527	0.2109	0.3537	0.5893
$D_{C_L}(\%)^*$	−3.249	24.393	38.933	2.185	9.985	23.179	/	/	/

* D_{C_L} and D_{C_D} are calculated as the relative difference compared to the case with the propeller (e.g. $D_{C_L} = 1 - \frac{C_L^{AD}}{C_L^{Propeller}} \cdot 100\%$).

simplified model. This also explains the highest difference in the Fin 2 drag which is located near to the ship centerline where the drag component is least influenced by the propeller suction (drag coefficient only slightly changes in all three cases, see in Table 3) due to close proximity of the hull structure upstream and recirculation from one side to the other at the ship center top wake field. When observing the lift results, the value rises when moving from Fin 1 to Fin 3 where the largest difference is obtained. Besides the change in the axial velocity, this can also be explained by the propeller right-handed direction. As can be observed from Fig. 5, Fin 2 and 3 are on the ship port side meaning that the propeller rotation induced velocity adds with the velocity wake component which occurs from the narrowing of ship waterlines at the stern. From the starboard side the situation is reversed, hence the Fin 1 has the lowest lift coefficient change because the transversal velocities from the propeller rotation and wake subtract.

Overall, simple AD model has shown much better comparison with the direct propeller simulation in terms of forces on the PSS compared to the without the propeller case. Larger differences are found only in the rotational components which is expected due to physically non-existing propeller blades in the AD model. Example of the lift and drag coefficient signal is shown in Fig. 8 for all fins from where the improvement of AD approach is visible. On all three fins, the dominant effect on the force oscillation is carried by the

propeller blade passage. In the case with the propeller the amplitude of the oscillation is much larger, even up to 20% of the lift force, and the oscillation is equal to the frequency of the propeller rotation divided by the number of blades as expected. For this reason, in the propeller simulation the entire period of one blade passage should be considered when evaluating the structural response. Regarding the local flow characteristics, as shown in Fig. 9 from the pressure field on the PSS, it is obvious that the propeller rotation creates the most complex flow field near the PSS. These local effects (e.g. tip separation) can be interested from efficiency perspective, but in terms of PSS structural response their effect on the entire fin is small.

In order to show the reliability of the current solution, the refined mesh results are presented in Table 4 with the computed relative difference to the coarse mesh. Large difference is only present in the C_D coefficient for Fin 1 due to the absolute value being very small. For the other two fins the difference is lower than 4% in both cases. Overall, the relative difference between the without propeller and AD case is similar as in the coarse mesh. Given the results, it can finally be safely assumed that the grid refinement study will not significantly alter the findings when comparing the results depending on the propulsion model for a single grid density. After the evaluation of the calm water simulations, next step is to investigate how all these results will be
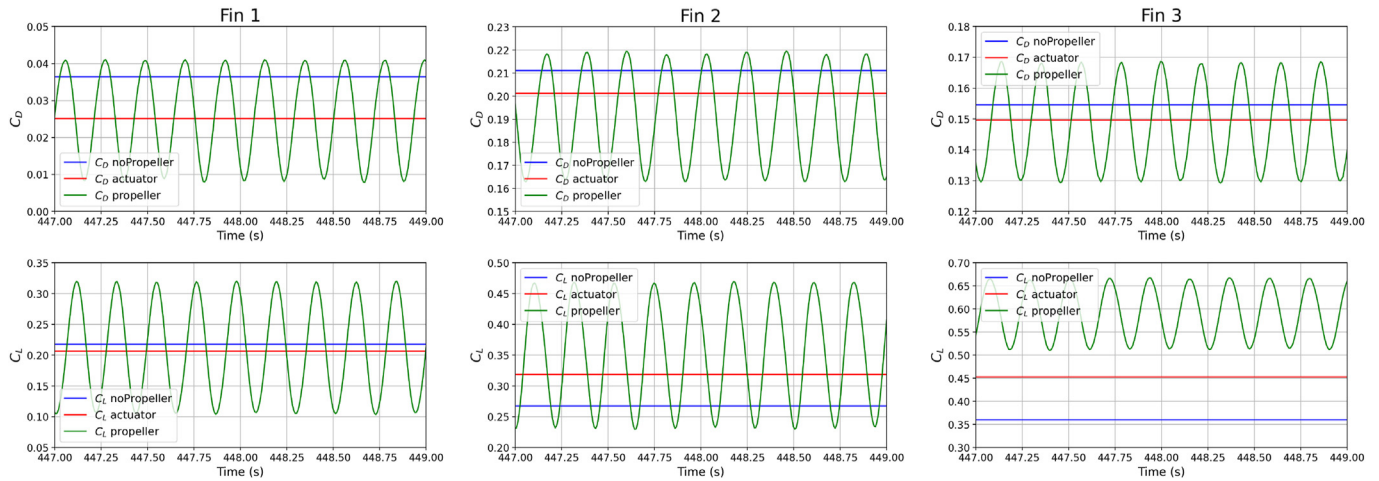
Fig. 8. Drag and lift coefficient signal for PSS (Fin 1 - 1st column, Fin 2 - 2nd column and Fin 3 - 3rd column).
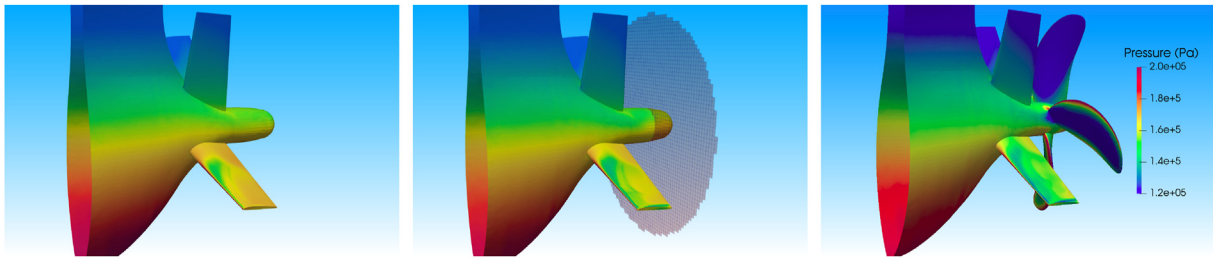

Fig. 9. Pressure distribution on PSS in different conditions. No propeller (left), actuator disk (center), propeller (right) with averaged pressure on PSS surface over one blade passage period.

Table 4
Lift and drag coefficients in calm water for coarse and refined mesh.

		w/o propeller			with AD		
		Fin 1	Fin 2	Fin 3	Fin 1	Fin 2	Fin 3
Coarse	C_D	0.0364	0.2111	0.1547	0.0252	0.2013	0.1497
Fine	C_D	0.0390	0.2096	0.1590	0.0301	0.1994	0.1552
	$E_{C_D}^*(\%)$	−7.032	0.694	−2.763	−19.315	0.923	−3.694
Coarse	C_L	0.2178	0.2674	0.3599	0.2063	0.3184	0.4527
Fine	C_L	0.2031	0.2570	0.3460	0.2125	0.3110	0.4605
	$E_{C_L}^*(\%)$	6.743	3.888	3.867	−2.983	2.331	−1.717

* E_{C_L} and E_{C_D} are calculated as the relative difference compared to the coarse mesh cases (e.g. $E_C = 1 - \frac{C^{fine}}{C^{coarse}} \cdot 100\%$).

affected when the ship is moving in waves.

4.3. Head waves - PSS hydrodynamic loads

After evaluating the calm water results ship is simulated in head waves in all three conditions. Wave length is selected close to 1.2 · L_{PP} to ensure ship excitation in heave and pitch motion, while the wave height is set at around 20% of the ship draft. The exact wave parameters are given in Table 1. More than 20 encounter periods are simulated with each period of 11.64 s and totals to 278 s simulation time. Simulations without the propeller and with the AD required 55.8 h of CPU time, less than half compared to 120.3 h for the same amount of simulation time with the direct propeller model. Similarly to the calm water case, lift and drag coefficients are calculated for each time step during the last 2 periods in the

simulation. This required the recalculation of the transformation matrix from global to the local PSS coordinate system for each fin due to ship motions in waves. Coefficients are given in Table 5. Results suggest the same behaviour in waves as in the calm water case. Lift coefficient increases from Fin 1 to Fin 3, inclusion of the AD improves the results with respect to the propeller case and the overall difference in the AD case is much lower for the drag than for the lift. It is interesting to observe the lift overshoot by 4.574% for the Fin 3 in waves, while in calm water this particular case contained the largest difference comparing to the propeller case. This indicates the reduced influence of propeller rotation on the local flow when combined with the ship motion and wave incident velocity. Differences for the remaining two fins are close to 15% for the lift with the AD which is for Fin 1 a large increase compared to the calm water results where there was only 2.185% discrepancy. Larger

Table 5
PSS - Lift and drag coefficients in waves.

	w/o propeller			With AD			With propeller		
	Fin 1	Fin 2	Fin 3	Fin 1	Fin 2	Fin 3	Fin 1	Fin 2	Fin 3
C_D	0.0458	0.2214	0.1622	0.0352	0.2138	0.1586	0.0319	0.2102	0.1602
$D_{C_D}^*$ (%)	−43.316	−5.355	−1.241	−10.362	−1.728	1.043	/	/	/
C_L	0.1913	0.2985	0.4989	0.2011	0.3641	0.5981	0.2397	0.4264	0.5719
D_{C_L} (%)*	20.210	29.991	12.769	16.105	14.619	−4.574	/	/	/

* see Table 3 for D_{C_L} and D_{C_D} calculation details.

difference is expected since the interaction between the wake, propeller, ship motion and wave incident field is fully non-linear with each component having an effect on the resulting force on the PSS. However, it should be noted that these C_D and C_L values are simply averaged throughout the encounter period and serve only for representative purposes.

Lift and drag coefficients for the wave simulation are presented in Fig. 10 for Fin 3 which is most liable to the ship global motions. Ship motions at the same time frame as those of lift and drag coefficients are shown in Fig. 11. It can be seen that in the overall hydrodynamic loads on the fin, the propeller rotation becomes less significant compared to the ship motion which drastically changes the force distribution. When comparing the pitch in Fig. 11 with the lift coefficient from Fig. 10 it seems that the pitch motion has a leading effect on the hydrodynamic loads. Regarding the local flow on the PSS surface, pressure for the propeller case at different instants during encounter period is shown in Fig. 12. Also, very strong pressure variation can be seen between different time-steps with the great majority of the pressure change observed on the upper part of the Fin 3 surface, hence the lift coefficient is much higher for the bow down position.

Although these effects are clearly visible from the hydrodynamic perspective and can be used to improve the design, it remains to see how much this pressure variation will actually be transmitted to the structural response in terms of stresses and

deformations.

5. Structural analysis

This section contains results for the calm-water and wave simulations performed in the previous section. Structural solution is obtained as a series of linear static analysis which means that there is no mutual interaction between different time-steps and the stiffness matrix is kept constant throughout the structural analysis. There is no mutual interaction between the structural and hydrodynamic solver meaning that the coupling approach can be referred to as one-way coupling.

5.1. Calm water

First step in this type of the structural analysis is the inspection of the hydrodynamic transferred loads to confirm that the imposed pressure forces are indeed valid. The comparison is shown in Fig. 13 from where it can be seen that the transfer process is performed correctly. As previously stated in section 4, for the without the propeller and actuator disk cases, one loading condition is imposed, and for the propeller case one period of blade passage is analysed.

Structural response is expressed in terms of Von Mises Stress (VMS) for each fin separately to investigate the impact of different hydrodynamic condition on a particular fin structure. For each fin
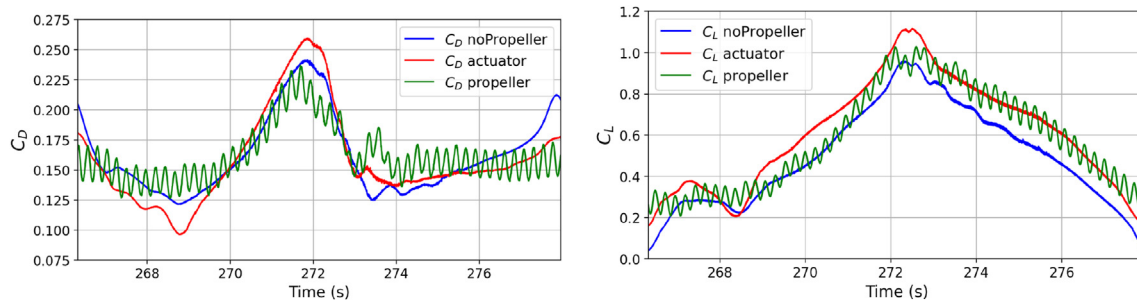
Fig. 10. Drag and lift coefficient signal for Fin 3.
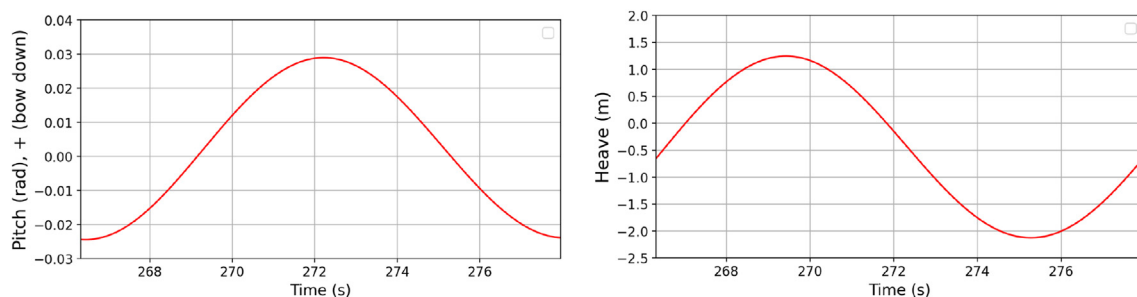
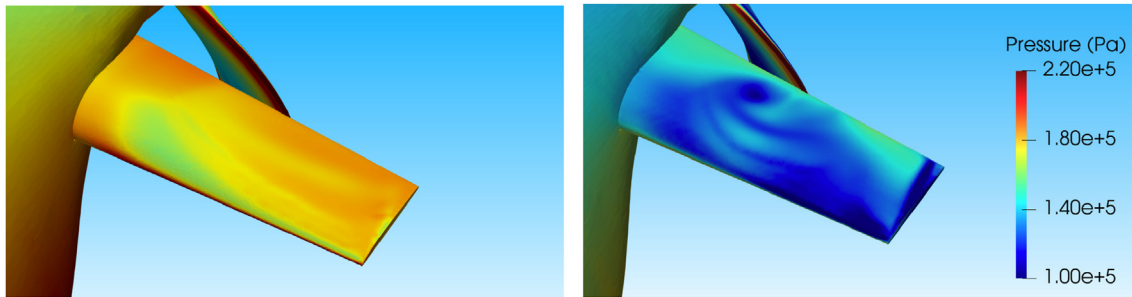**Fig. 11.** Pitch (left) and heave (right) motion during encounter period.

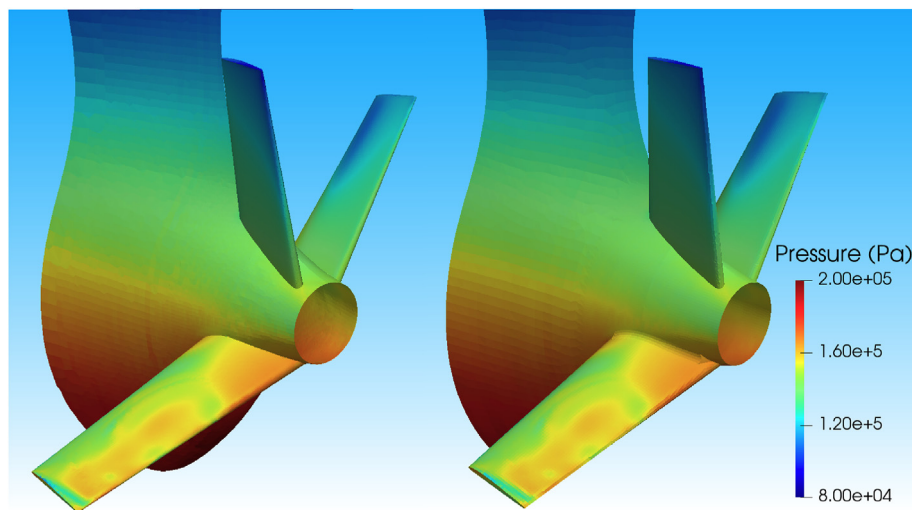**Fig. 12.** Fin 3 pressure distribution at time 266.9 s and at 272.2 s (right).

Fig. 13. Hydrodynamic pressure transfer on the FEM-CFD interface surface. Fluid mesh (left), structural mesh (right).

an element containing the highest stress is selected and compared for the three hydrodynamic cases. Example of stress distribution with the selected element is shown in Fig. 14 for Fin 3. For the other two fins similar stress concentration is found near the fin root. Comparison of three hydrodynamic cases for the part of one propeller period are shown in Fig. 15. As already stated in section 4.2, it seems that the propeller rotation direction not only has an impact on the lift coefficient, but is also clearly correlated to the resulting VMS distribution. Fin 1 which was minimally influenced by propeller rotation in terms of lift coefficient and is mostly protected from the rotational impacts by Fin 2 actually has a highest VMS for the case without the propeller. This reasoning can be further extended when observing that the amplitude of the propeller periodic impact on Fin 2 is largest compared to the other two fins and equals 2.77 MPa compared to the 1.33 MPa in Fin 1 and 1.22 MPa in Fin 3. Although the highest VMS is located in Fin 3, Fin 2 would be most liable to long-term damage induced by the propeller in terms of fatigue (highest amplitude). Furthermore, when assessing the
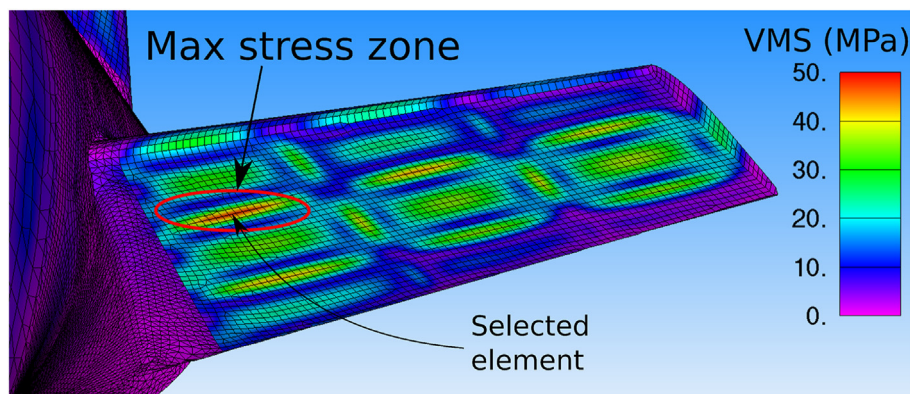

Fig. 14. VMS (MPa) distribution on Fin 3 at particular time-step for propeller case.
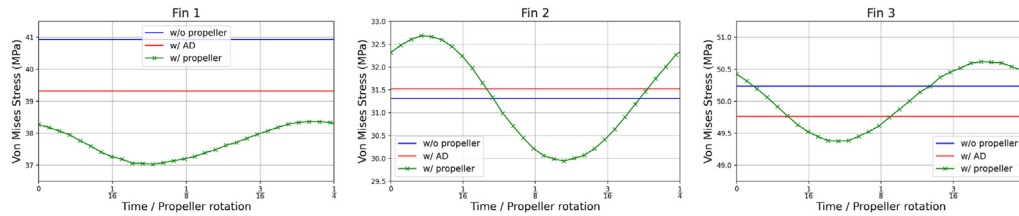
Fig. 15. VMS distribution in calm-water for the maximum loaded element per fin.

design of the PSS, from the results and for this particular PSS, hull lines and propeller combination, there is no structural exposure to ultimate strength failure. However, for the exact loading computations in calm-water, the inclusion of the propeller geometry is deemed necessary to estimate the correct stress distribution and amplitude. Fatigue life for direct the propeller case using the obtained stress ranges is estimated for the three fins and equals 2896 years, 1495 years and 2727 years, respectively. For all of the fin elements the estimated fatigue life is well over necessary 25 years.

5.2. Head waves

For the ship sailing in waves, a total number of 21 time-steps is estimated sufficient for capturing the structural response of the PSS properly. Even for the propeller case, the same number of time-steps is selected which means that in the stress distribution a continuous propeller rotation will not be visible. For the propeller induced oscillation to be fully captured in the structural response during the encounter period, it would require too expensive computations of a large number of hydrodynamic solutions. More precisely, wave encounter period in this case roughly equals to an approximately 10 propeller rotations per period. In order to capture all the flow details, it would require 20 time-steps per blade passage which would (for a 4 bladed propeller) equal to a total of 800 pressure loads and structural solutions. By observing Fig. 10, it seems that the propeller induced oscillation do not influence significantly the lift coefficient, so to perform the comparison more efficiently, it is weighted as best to simply perform 21 time-steps as in the other two cases. If there is a significant difference in the structural response, it should be visible regardless of the time discretisation.

Equivalent stress zones are identified in the PSS structure when analysing the FEM solution, hence the same elements are selected for each fin as in the previous calm-water cases in Section 5.1. Stress distribution in time is presented in Fig. 16. The highest VMS is found for the Fin 3 as in the calm-water condition. The stress peak is enlarged for all three fins due to ship motion effects. When comparing the maximum stress for the propeller case in calm-water and waves, the increase for Fin 1, 2 and 3 is 17.56%, 16.23% and 15.13%, respectively. On the other hand, the amplitude is also

much higher compared to the calm-water, and for the Fin 1, Fin 2 and Fin 3 equals 12.97 MPa, 10.08 MPa and 16.18 MPa, respectively. What is also important to notice is the relative coincidence of VMS for all flow models on every fin. All this implies the reduced effect of the propeller torque and thrust on the PSS when considerable ship motion is occurring. When observing the amplitudes excited by this ship motion a negligible difference is seen between all three hydrodynamic conditions and is much more dependent on the ship motion intensity. Overall, the VMS solution shows that the resulting structural response can be resolved at a minimal CPU cost even without the propeller or with the AD. However, since the AD inclusion itself has a negligible influence on the simulation CPU cost, it is recommended to include it. Although the difference is relatively small compared to the without the propeller case, the AD results resemble more to the propeller case which should be regarded as most accurate. This is shown through lift and drag coefficients comparison in Tables 3 and 5. If for any reason, the actuator disk is not possible to include, the results obtained from the no propeller case are expected to yield the similar long-term response due to ship motions. The authors suggest its inclusion only if the open-water data is readily available and there is no significant CPU overhead in the AD implementation.

6. Conclusion

This study presented different propulsion types when modelling the hydrodynamic loads on a Pre-Swirl Stator (PSS) and their influence on the structural response. Three flow models are performed: without the propeller, with AD and direct propeller calculation. These models are examined in calm-water and in head wave condition which in total corresponds to 6 different conditions. In all the simulations performed, time and space discretisation is kept constant to have a consistent comparison between the cases. Without the propeller and with AD case have completely equal meshes, while with the propeller case only differs in the zone of the propeller geometry where the GGI interface is introduced. Propeller is modelled with the help of a rotating mesh region inside the surrounding hull mesh domain. These hydrodynamic results are used as an input for the structural analysis. This type of coupling would be referred to as a one-way coupling approach. For each
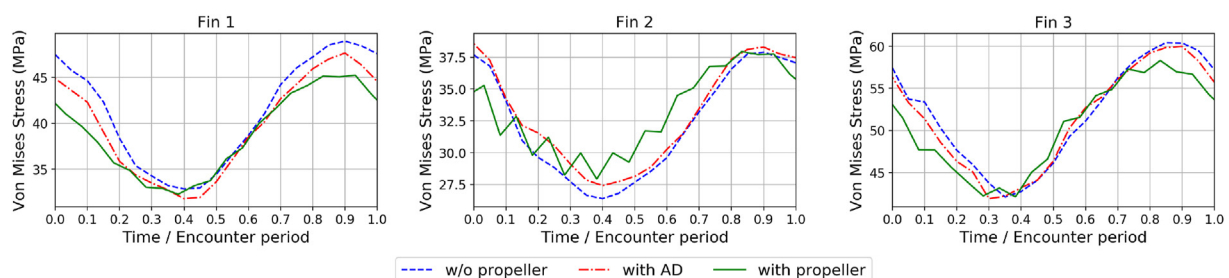

Fig. 16. VMS distribution in an encounter period for the maximum response element per fin.

time-step a linear static analysis is performed meaning there is no mutual interaction between different time-steps or fluid and structural solver.

For the first part of the study, PSS hydrodynamic design is evaluated. PSS has proved to be beneficial to the propeller efficiency with the estimated savings of 4.69%, thus justifying further hydro-structural analysis. Hydrodynamic solution is analysed with respect to the lift and drag coefficients on each fin. In calm-water, the propeller case is regarded as the reference to other conditions since it directly solves the propeller rotation. Larger differences are found between the without propeller and with propeller case, while the AD case decreases the pressure difference substantially compared to the without the propeller case which is especially visible in the drag coefficient. On the other hand, the AD also improves the lift coefficient where the results are somewhat worse compared to the drag coefficient. However, this is expected since the AD does not model the propeller rotation properly. In waves, the propeller rotation effect on the pressure is significantly reduced and most of the force oscillation is excited by the ship motion, in majority by pitching motion for this particular case.

In the second part, the CFD results are imposed on the structural model and VMS is examined on the PSS. For each fin, element containing maximum stress is selected and analysed. In calm-water and in waves same zones of the structural model are found excited the most. In calm-water, there is no structural exposure to ultimate strength failure, however, in terms of fatigue, the propeller modelling is shown as necessary since for the other two models the amplitude of a blade passage cannot be captured which could be important from the design aspect. On the contrary, in waves, the propeller rotation effect does not have a considerable effect on the structural stress. In this case, the ship motion has the strongest impact on the amplitude of the propeller rotation which is for this particular wave about 10 times higher for each fin. It is found that the propeller suction effect either has little or no effect on the resulting VMS in Fins 1, 2 and 3. Stress is substantially increased in waves, but even the case without the propeller properly captures the necessary structural stresses and ship motion induced amplitudes.

From the calculated structural responses, following major conclusions can be summarized. First, in calm-water, the propeller should be included in the simulation to capture properly the force oscillation which is necessary to calculate the long-term fatigue and to properly evaluate the ultimate strength criteria. Second, in waves, the propeller effects hold negligible impact on the resulting structural response and the majority of the important flow characteristics is captured even without the propeller or AD while the dominant parameter governing the force oscillation are the ship motions amplitudes. All said, in the entire ship life-cycle from the perspective of statistical wave analysis, a propeller inclusion for this type of ESD is deemed unnecessary to evaluate the actual loadings. On the other hand, the AD inclusion seems reasonable since it creates a more accurate pressure distribution comparing to the without the propeller case at a negligible CPU expense.

The main intention of this work was to properly identify the dominant effects in the hydrodynamic model influencing the ship structural response in order to have a clear picture for future design procedure definition. Since the PSS straightforward design procedure is still under investigation, within the future work the authors intend to extend the current work to a more rigorous statistical wave approach and a more complex fluid-structure dynamic coupling.

Declaration of competing interest

The authors declare that they have no known competing

financial interests or personal relationships that could have appeared to influence the work reported in this paper.

Acknowledgement

References

Bakica, A., Gatin, I., Vukčević, V., Jasak, H., Vladimir, N., 2019. Accurate assessment of ship-propulsion characteristics using CFD. Ocean Eng 175, 149–162.

Bakica, A., Malenica, Š., Vladimir, N., 2020a. Hydro-structure coupling of CFD and FEM - Quasi-static approach. Ocean Eng 217.

Bakica, A., Vladimir, N., Gatin, I., Jasak, H., 2020b. CFD Simulation of Loadings on Circular Duct in Calm Water and Waves. Ships and Offshore Structures. https://doi.org/10.1080/17445302.2020.1730082 (in press).

Beaudoin, M., Jasak, H., 2008. Development of a generalized grid interface for turbomachinery simulations with OpenFOAM. In: Open Source CFD International Conference, pp. 1–11. URL papers3://publication/uuid/81CCD00D-DF48-4595-B591-C577955CEA06.

Carlton, J., 2012. Marine Propellers and Propulsion, third ed.

Carrica, P.M., Fu, H., Stern, F., 2011. Computations of self-propulsion free to sink and trim and of motions in head waves of the KRISO Container Ship (KCS) model. Appl. Ocean Res. 33, 309–320.

CFD Workshop Website, 2010. Gothenburg 2010: a Workshop on CFD in ship hydrodynamics. \\url. http://www.insean.cnr.it/sites/default/files/gothenburg2010/index.html.

Cvijetić, G., Gatin, I., Vukčević, V., Jasak, H., 2018. Harmonic balance developments in OpenFOAM. Computers and Fluid 172, 632–643.

Dang, J., Dong, G., Chen, H., 2012. An exploratory study on the working principles of energy saving devices (ESDs): PIV, CFD investigations and ESD design guidelines. In: International Conference on Ocean, Offshore and Arctic Engineering, p. 25. URL. http://proceedings.asmedigitalcollection.asme.org/proceeding.aspx?doi=10.1115/OMAE2012-83053.

Furcas, F., Gaggero, S., 2021. Pre-swirl stators design using a coupled BEM-RANSE approach. Ocean Eng 222 (January), 108579. https://doi.org/10.1016/j.oceaneng.2021.108579. URL.

Gaggero, S., Villa, D., Viviani, M., 2017. An extensive analysis of numerical ship self-propulsion prediction via a coupled BEM/RANS approach. Appl. Ocean Res. 66, 55–78. https://doi.org/10.1016/j.apor.2017.05.005. URL.

Gatin, I., Vukčević, V., Jasak, H., Rusche, H., 2017. Enhanced coupling of solid body motion and fluid flow in finite volume framework. Ocean Eng 143 (December 2016), 295–304.

Gokce, M.K., Kinaci, O.K., Alkan, A.D., 2019. Self-propulsion estimations for a bulk carrier. Ships Offshore Struct. 14 (7), 656–663. https://doi.org/10.1080/17445302.2018.1544108. URL.

Huang, J., Carrica, P.M., Stern, F., 2007. Coupled ghost fluid/two–phase level set method for curvilinear body–fitted grids. Int. J. Numer. Methods Fluid. 44, 867–897.

Jasak, H., Uroić, T., 2020. Practical computational fluid dynamics with the finite volume method. In: Modeling in Engineering Using Innovative Numerical Methods for Solids and Fluids. http://link.springer.com/10.1007/978-3-030-37518-8.

Jasak, H., Vukčević, V., Gatin, I., 2015. Numerical simulation of wave loads on static Offshore structures. In: CFD for Wind and Tidal Offshore Turbines. Springer Tracts in Mechanical Engineering, pp. 95–105.

Jasak, H., Vukčević, V., Gatin, I., Lalović, I., 2019. CFD validation and grid sensitivity studies of full scale ship self propulsion. Int. J. Naval Architect. Ocean Eng. 11 (1), 33–43.

Ju, H.B., Jang, B.S., Lee, D.B., Kim, H.J., Park, C.K., 2018. A simplified structural safety assessment of a fin-typed energy saving devices subjected to nonlinear hydrodynamic load. Ocean Eng 149 (June 2017), 245–259. https://doi.org/10.1016/j.oceaneng.2017.12.022. URL.

Kim, J.H., Choi, J.E., Choi, B.J., Chung, S.H., 2014. Twisted rudder for reducing fuel-oil consumption. Int. J. Naval Architect. Ocean Eng. 6 (3), 715–722. https://doi.org/10.2478/IJNAOE-2013-0207. URL.

Kim, J.H., Choi, J.E., Choi, B.J., Chung, S.H., Seo, H.W., 2015. Development of Energy-Saving devices for a full Slow-Speed ship through improving propulsion performance. Int. J. Naval Architect. Ocean Eng. 7 (2), 390–398. https://doi.org/10.1515/ijnaoe-2015-0027. URL.

Lee, D.B., Jang, B.S., Kim, H.J., 2016. Development of procedure for structural safety assessment of energy saving device subjected to nonlinear hydrodynamic load. Ocean Eng 116, 165–183. https://doi.org/10.1016/j.oceaneng.2016.02.038. URL.

Lim, S.S., Kim, T.W., Lee, D.M., Kang, C.G., Kim, S.Y., 2014. Parametric study of propeller boss cap fins for container ships. Int. J. Naval Architect. Ocean Eng. 6 (2), 187–205. https://doi.org/10.2478/IJNAOE-2013-0172. URL.

Min, K.-S., Chang, B.-J., Seo, H.-W., 2009. Study on the Contra-Rotating Propeller system design and full-scale performance prediction method. Int. J. Naval Architect. Ocean Eng. 1 (1), 29–38.

Nowruzi, H., Najafi, A., 2019. An experimental and CFD study on the effects of different pre-swirl ducts on propulsion performance of series 60 ship. Ocean Eng 173 (424), 491–509. https://doi.org/10.1016/j.oceaneng.2019.01.007. URL.

Paboeuf, S., Cassez, A., 2017. ESD structural issue - UPstream device. Int. Shipbuild. Prog. 63 (3–4), 291–314.

Paik, K.J., Hwang, S., Jung, J., Lee, T., Lee, Y.Y., Ahn, H., Van, S.H., 2015. Investigation on the wake evolution of Contra-rotating propeller using RANS computation and SPIV measurement. Int. J. Naval Architect. Ocean Eng. 7 (3), 595–609. https://doi.org/10.1515/ijnaoe-2015-0042. URL.

Park, S., Oh, G., Hyung Rhee, S., Koo, B.Y., Lee, H., 2015. Full scale wake prediction of an energy saving device by using computational fluid dynamics. Ocean Eng 101, 254–263. https://doi.org/10.1016/j.oceaneng.2015.04.005. URL.

Popovac, M., Hanjalic, K., 2007. Compound wall treatment for RANS computation of complex turbulent flows and heat transfer. Flow, Turbul. Combust. 78 (2), 177–202.

Prins, H.J., Flikkema, M.B., Schuiling, B., Xing-Kaeding, Y., Voermans, A.A., Müller, M., Coache, S., Hasselaar, T.W., Paboeuf, S., 2016. Green retrofitting through optimisation of hull-propulsion interaction - GRIP. Transport. Res. Procedia 14, 1591–1600. https://doi.org/10.1016/j.trpro.2016.05.124 (0).

Sakamoto, N., Kume, K., Kawanami, Y., Kamiirisa, H., Mokuo, K., Tamashima, M., 2019. Evaluation of hydrodynamic performance of pre-swirl and post-swirl ESDs for merchant ships by numerical towing tank procedure. Ocean Eng 178

(February), 104–133. https://doi.org/10.1016/j.oceaneng.2019.02.067. URL.

Shin, H.J., Lee, J.S., Lee, K.H., Han, M.R., Hur, E.B., Shin, S.C., 2013. Numerical and experimental investigation of conventional and un-conventional preswirl duct for VLCC. Int. J. Naval Architect. Ocean Eng. 5 (3), 414–430. https://doi.org/10.2478/IJNAOE-2013-0143. URL.

Shin, Y.J., Kim, M.C., Lee, J.H., Song, M.S., 2018. A numerical and experimental study on the performance of a twisted rudder with wavy configuration. Int. J. Naval Architect. Ocean Eng. 1–12. https://doi.org/10.1016/j.ijnaoe.2018.02.014. URL.

Siemens, 2014. NX NASTRAN User's Guide.

Sun, Y., Beckermann, C., 2007. Sharp interface tracking using the phase-field equation. J. Comput. Phys. 220, 626–653.

Tsou, W.H., Guan, P.C., Chang, W.H., Chen, C.J., 2019. Structural design and strength estimation of energy saving Y-fin by using finite element method. In: Proceedings of the 14th International Symposium PRADS 2019, vol. 2, pp. 209–231.

Vukčević, V., 2016. Numerical Modelling of Coupled Potential and Viscous Flow for Marine Applications. Ph.D. thesis. Faculty of Mechanical Engineering and Naval Architecture, University of Zagreb.

Vukčević, V., Jasak, H., Malenica, S., 2016a. Decomposition model for naval hydrodynamic applications, Part I: computational method. Ocean Eng. 121, 37–46.

Vukčević, V., Jasak, H., Malenica, S., 2016b. Decomposition model for naval hydrodynamic applications, Part II: verification and validation. Ocean Eng. 121, 76–88.

Wang, J., Wan, D., 2020. CFD study of ship stopping maneuver by overset grid technique. Ocean Eng 197 (May 2019), 106895. https://doi.org/10.1016/j.oceaneng.2019.106895. URL.

Weller, H.G., Tabor, G., Jasak, H., Fureby, C., 1998. A tensorial approach to computational continuum mechanics using object oriented techniques. Comput. Phys. 12, 620–631.

ARTICLE 5

Preprint of the published journal article.

Hydroelastic analysis of Pre-Swirl Stator

Andro Bakica[a,*], Šime Malenica[b], Nikola Vladimir[a], Ivo Senjanović[a]

[a]*University of Zagreb, Faculty of Mechanical Engineering and Naval Architecture, Ivana Lučića 5, Zagreb, Croatia*
[b]*Bureau Veritas Marine & Offshore, Departement Recherche, Le Triangle de lArche, 8 Cours du Triangle, Paris La Defense, France*

Abstract

This paper presents the investigation of the dynamic effects in the structural response of a Pre-Swirl Stator. The implemented model is based on the modal superposition which improves the efficiency of the hydro-structural coupling. Structural response is decomposed into a set of orthogonal dry modes which are computed in the pre-processing stage. Mode shape displacement vectors are interpolated from the structural nodes onto the fluid mesh on the selected merging interface. This allows the dynamic equation solution directly inside the fluid solver. Compared to the standard hydro-structural interaction which requires additional iterations between the structure and fluid models per time-step, this approach reduces the complexity and computational effort. Model is verified on a simplified PSS simulation setting and computational guidelines are derived. The PSS is further analysed on the realistic cases of propeller and wave loads with the hydroelastic effects included. The results suggest a negligible amount of dynamic amplification in the current PSS design.

Keywords: CFD-FEM, Pre-Swirl Stator, Hydroelasticity, Modal superposition

*Corresponding author.

Email addresses: `andro.bakica@fsb.hr` (Andro Bakica),
`sime.malenica@bureauveritas.com` (Šime Malenica), `nikola.vladimir@fsb.hr`
(Nikola Vladimir), `ivo.senjanovic@fsb.hr` (Ivo Senjanović)

1. Introduction

Environmental problems in shipping represent probably one of the most important research topics in the field, which influenced both by ever stringent regulations set by the International Maritime Organization (IMO) and permanent intention of ship-owners and ship operators to reduce operative costs through the reduction of fuel consumption. In line with this, there is number of recommended technical solutions, operative strategies and market-based measures that lead to reduction of fuel consumption and consequently greenhouse gas (GHG) emissions. In the context of naval hydrodynamics, some typical solutions include hull form optimization, draught and trim optimization, improving the propeller efficiency by its innovative design, and installation of special thrust augmented devices.

These devices are usually referred to as Energy Saving Devices (ESDs). Given the reducing CPU cost in the computational hydrodynamic models which include viscosity and turbulence, Computational Fluid Dynamics (CFD), the flow in the vicinity of the propeller can be examined in-depth, hence improving the operability benefits of the ESDs. CFD solution has been validated with experiments in number of papers [1–5]. Regarding the Pre-Swirl Stator (PSS), Furcas and Gaggero [6] performed an extensive study of the ESD design using optimization algorithm with the peak efficiency increase for the optimal design at even 8%. PSS scale effects are also often studied owing to the unreliable extrapolation of efficiency gains in model to full scale [7].

Although hydrodynamic improvements play a vital role and are a prerequisite for the installation/retrofit of any ESD, their structural evaluation is limited to only several investigations. GRIP project [8, 9] studied both the hydrodynamic and structural issues of the PSS. In hydrodynamic part, the efficiency of the PSS is verified on the full-scale measurements, while for the structural part, the design methodology also accounted for the wave loads on PSS. Lee et al. [10] examined the wave loads and the structural response by replacing the costly CFD simulations with the neural network. This procedure is further extended by Ju et al. [11] to consider the arbitrary PSS shape. Bakica et al. [12] studied the effect of the propeller loads and the wave loads on the PSS structure while using direct interpolation of the CFD pressure to the FEM model instead of approximating the fluid force.

When assessing the structural response, most often terms used in the literature are the so-called one-way (quasi-static) or two-way (dynamic, hy-

droelastic) coupling. In the quasi-static approach, the word "quasi" referrers to the independence of the force from the structural displacement. The major issue in this type of analysis is the interpolation of the loads from the hydro interface to the structural interface. Ji et al. [13] coupled the potential flow hydro solution with the FEM structural model using the projection method to interpolate the pressure value on the FEM wetted surface elements. Bakica et al. [14] presented a CFD-FEM coupling with the interpolated pressure computed at the FEM wetted element integration points, thus enabling the direct computation of nodal forces. The pressure transfer features an important step in the overall structural analysis, but when the dynamic response is important, hydroelastic approach is necessary. This is the case in different practical problems. For example, hydroelastic approach has been increasingly investigated for highly slender floating structures [15, 16], slamming responses [17, 18], LNG membrane-type tanks [19] and floating wind turbines [20]. Takami et al. [21] performed a CFD-FEM coupling with the results correlating well with the experiment. Kim et al. [22] used the full-scale measurements to estimate the fatigue damage and found a 75-80% increase in fatigue damage due to influence from vibrations. Flexible barge case is investigated in [23] where a two-way coupling approach is employed with the commercial software StarCCM+ and Abaqus for CFD and FEM, respectively. Method is based on the mutual interaction between the solvers during each time-step. Also, on the flexible barge experiment, Seng et al. [24] validated a hydroelastic model using modal superposition which significantly reduces the CPU cost. However, in terms of ESDs, particularly PSS, there has been no work related to their direct CFD-FEM coupling while considering the structural dynamics.

Another subject of interest is related to the morphing of the mesh when the flexible body motion occurs. The work by Seng et al. [24] used a Laplace morphing method where the mesh quality is preserved, but with the considerate computational cost. Often used, but different type of morphing, is by using Radial Basis Functions (RBF) inside the CFD framework. This method also offers similar amount of robustness and successful implementation can be found in [25] with comparison to remeshing strategy. However, the scalability of the method and CPU cost are not negligible [26]. Although these approaches are quite robust and perform well with respect to mesh quality preservation, a high CPU cost is not justified for the small structural nodal displacements where a simpler geometrical morphing method can be employed.

3

The main purpose of this work is to present the method for the computation of the stresses on the PSS structure while including the structural dynamics. The authors have already dealt with the pure FEM dynamic analysis [27], pressure hydro-structural transfer i.e. one-way procedure [14] and the evaluation of the propeller loads [12], as well as the entire procedure for the extreme PSS loads analysis [28]. Although there are clear justifications for employing the one-way coupling approach in the previous works (comparison of the excitation and structural natural frequencies reveals no resonance behaviour), this study aims to clarify the amount of dynamic effects acting on the structure and serves as a basis when the dynamic or otherwise called hydroelastic approach is indeed necessary. Although very rarely, it could happen that dynamic amplification should be checked in case of closer values of structural natural frequencies and excitation frequencies. Method implemented in this work is based on the modal superposition first presented in [24] which significantly reduces the CPU time. Model is further extended to the clamped beam case of PSS attached to the moving rigid body of a ship. The procedure for the computation of the stresses including the dynamics is also explained.

Paper is divided into six sections: second section explains the mathematical mode, third section verifies the implemented hydroelastic model, fourth section features the numerical setup of the ship realistic load cases, fifth section presents the results and the sixth section concludes the study.

2. Mathematical model

The mathematical model for the fluid region is based on the finite volume discretisation in the framework of an open-source CFD code OpenFOAM [29]. The multiphase flow i.e. free-surface resolution is implemented in the NavalHydro Pack based on the Ghost Fluid Method (GFM) [30, 31]. The governing equations are as follows:

- continuity equation

$$\nabla \cdot \mathbf{v} = 0, \tag{1}$$

- momentum equation

$$\frac{\partial \mathbf{v}}{\partial t} + \nabla \cdot (\mathbf{v}\mathbf{v}) - \nabla \cdot (\nu \nabla \mathbf{v}) = -\frac{1}{\rho(\mathbf{x})} \nabla p_d + \nabla \cdot \mathbf{R}. \tag{2}$$

4

where $\mathbf{v}$ is the velocity vector, $\rho(\mathbf{x})$ is the density which depends on the spatial vector $\mathbf{x}$, p_d is the dynamic pressure, ν is the kinematic viscosity and $\mathbf{R}$ is the Reynolds stress tensor. Solution of the rigid body is derived as explained and validated in [32].

Structural model is disretised using the Finite Element Method (FEM) where the wetted surface elements are consisting of triangular and quadrilateral plate elements. Software employed in this study is a well-known and validated commercial FEM solver NASTRAN [33]. Coupling between the fluid and structural regions is achieved using both quasi-static and hydroelastic approach, often called one-way and two-way coupling procedures, respectively. Since the goal in the current study is the evaluation of the hydroelastic response meaning that the actual stresses in the structure are considered with the dynamics, both approaches are combined to compute these values consistently. In this type of structural analysis, the relations between the natural frequencies (structural model) and the excitation frequencies (fluid model) govern the Dynamic Amplification Factor (DAF) of the response. A typical DAF is shown in Figure 1 with the applicability of each approach highlighted. When assessing the dynamic response, a number of modes of interest is examined. Although these usually play a critical role in the overall stress response, the contribution of the remaining modes should not be neglected. Consider a linear quasi static analysis of the structure subjected to a slowly varying external loading:

$$\mathbf{K}\mathbf{u} = \mathbf{F} \tag{3}$$

where $\mathbf{u}$ is the vector of nodal displacements, $\mathbf{K}$ is the stiffness matrix and $\mathbf{F}$ is the external loading. In this case, the structural response consists of the infinite amount of modes meaning that the final nodal displacement $\mathbf{u}$ can be represented as the sum of all the mode shapes:

$$\mathbf{u} = \sum_{i=1}^{\infty} \mathbf{u}_i, \qquad \mathbf{u}_i = \mathbf{\Phi}_i q_i, \tag{4}$$

where Φ is the mode shape vector of nodal displacements and q is the modal amplitude for i-th mode. In order to consider both the quasi-static and the dynamic response, the following is obtained:

$$\mathbf{u} = \sum_{i=1}^{m} (\mathbf{u}_i^d - \mathbf{u}_i^{qs}) + \sum_{i=1}^{\infty} \mathbf{u}_i^{qs} \tag{5}$$

5
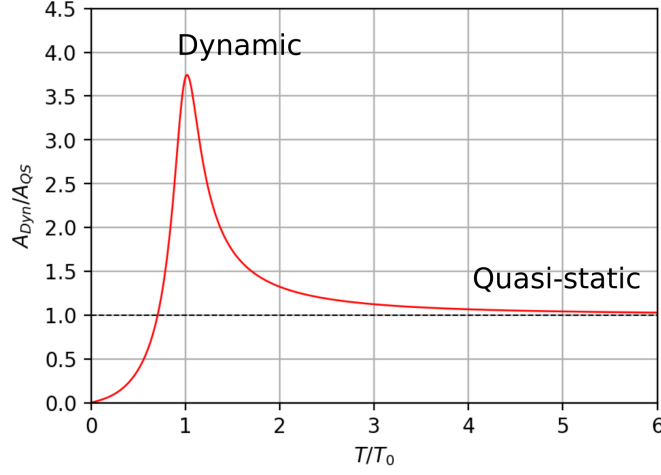
T_0 - structural natural period, T - external excitation period.

Figure 1: Typical DAF for modal response under harmonic loading.

where superscript qs and d denote the quasi-static and dynamic response, respectively, while m refers to the selected number of mode shapes studied dynamically. Each term on the r.h.s. in Equation 5 is a result of a separate computation for the consistent hydro-structural analysis. The first term is computed by hydroelastic analysis fully considering the effect of the structural nodal displacement in the fluid excitation and vice-versa, the second term is the static analysis of the same modes previously analysed dynamically and the third term is the straightforward static analysis where the pressure is interpolated on the structural model and the Equation 3 is solved. The inclusion of the second term is necessary since the response of the quasi-static analysis already contains the stresses contributing from those modes. It remains to further elaborate how these different coupling terms are defined in the FEM-CFD simulation framework.

Hydroelastic response is represented as the superposition of certain number of modes. In this approach the mode shapes are extracted from the structural FEM model in the pre-processing stage. The method is based on the modal projection where fluid and other possible external loads are imposed on the selected number of modes. This requires the interpolation of each mode shape displacement vector from the structural to the fluid matching wetted surface. Interpolation is performed in the same manner as fluid

6

to structure pressure interpolation in [5] with the only difference of reversing the structural mesh as the input and fluid mesh as the output. Hydro points and face centres are projected to the structural mesh from where the value of the displacement vector can be calculated based on the element nodal values.

Method is based on the implementation by Seng et al. [24] where compact mass matrices are computed as part of a pre-processing step. In this work, the similar method is applied to the clamped beam structure fitted on the moving rigid body of a ship. The main dynamical equation solved for is as written:

$$\mathbf{M}\ddot{\mathbf{q}} + \mathbf{C}\dot{\mathbf{q}} + \mathbf{K}\mathbf{q} = \mathbf{F}_e + \mathbf{Q} \tag{6}$$

where $\mathbf{M}$, $\mathbf{C}$ and $\mathbf{K}$ are the modal mass, structural damping and stiffness matrices, respectively, $\mathbf{F}_e$ is the generalized external forcing term and $\mathbf{Q}$ are the quadratic velocity terms. In case of dry modes decomposition, the resulting matrices on the l.h.s. are diagonal with $\mathbf{M}$ equal to identity matrix for the normalized modal mass ($\mathbf{\Phi}^T\mathbf{M}_{fe}\mathbf{\Phi} = 1$ where $\mathbf{M}_{fe}$ is the finite element mass matrix in body fixed coordinate system), $\mathbf{C}$ is defined as percentage fraction of the critical damping and $\mathbf{K}$ is the modal stiffness which due to normalized modal mass contains the squared mode frequencies values on the diagonal (ω_0^2). Size of diagonal matrices $\mathbf{M}$, $\mathbf{C}$, $\mathbf{K}$ is determined by the number of selected dry modes (for m modes the size is $m \times m$). In the case of the PSS attached to the ship, $\mathbf{F}_e$ contains the following: gravity acceleration loads, fluid pressure loads and ship translational/rotational acceleration contribution. The external fluid forcing projected to the mode shapes is defined as:

$$\mathbf{F}_e^{fluid} = \underbrace{\left[(\Phi_1^{tr})^T\mathbf{A}^T \quad \cdots \quad (\Phi_1^{tr})^T\mathbf{A}^T\right]}_{m \times 3n} \underbrace{\begin{bmatrix} f_{e,1}^{fluid} \\ \vdots \\ f_{e,n}^{fluid} \end{bmatrix}}_{3n \times 1} \tag{7}$$

where m is the number of mode shapes, n is the number of elements from which the selected deformable fluid surface is comprised of, $\mathbf{A}$ is the rotation matrix transferring from body fixed to earth-fixed coordinate system and Φ_{tr} are the translational displacements on the fluid faces interpolated from the FEM nodal values. The gravitational acceleration contribution is computed

as follows:

$$
\mathbf{F}_e^{gr} = \underbrace{\begin{bmatrix} \boldsymbol{\Phi}_1^T & \cdots & \boldsymbol{\Phi}_k^T \end{bmatrix}}_{m \times 6k} \mathbf{M}_{fe} \overbrace{\underbrace{\begin{bmatrix} \mathbf{I}_3 \\ \mathbf{O}_3 \\ \vdots \\ \mathbf{I}_3 \\ \mathbf{O}_3 \end{bmatrix}}_{6k \times 3}}^{m_g^c} \mathbf{A}^T \mathbf{g} \tag{8}
$$

where k refers to the number of nodes in the structural model, $\mathbf{g}$ is the gravity vector and m_g^c is the precomputed constant mass matrix. The scheme of the CFD-FEM coupling is shown in Figure 2. For further details on the general derivation of the free flexible body, use of compact mass matrices and quadratic velocity terms, the reader is referred to [24].

Following the elastic motion of the body the mesh requires some type of deformation treatment in order for the fluid mesh to remain valid and also to properly include the normal velocities arising from nodal displacement. In this work, the implemented mesh deformation is achieved using the closest point mesh morphing method. In this method, each point in the vicinity of the deformable body is paired with the closest point on the body surface. The selected points are divided into two parts with two variables: inner and outer distance. The points inside the inner distance move equally as the assigned closest point, while the points between the inner and outer boundary are given a slowly decaying weights, dependent on the distance from the paired surface point, multiplied with the surface point motion. In mathematical terms the morphing for each hydro point can be expressed as:

$$
\mathbf{u}_j^h = w_j \cdot \mathbf{u}_j^s \tag{9}
$$

where superscripts h and s refer to hydrodynamic or structural point, superscript j refers to the hydro point index, u_j^s and w_j is the paired structural node and assigned weight to the j-th hydro point, respectively. In the region inside the inner boundary, the weight is equal to 1 and in the region outside of the outer boundary the weight is equal to 0. Either an exponential or linear function can be used for the transition region. This work employed the linear function as shown in the illustrative example in Figure 3.

It is only left to explain how to practically compute the solution of the Equation 5. First of all, the approach requires two separate CFD simulations.
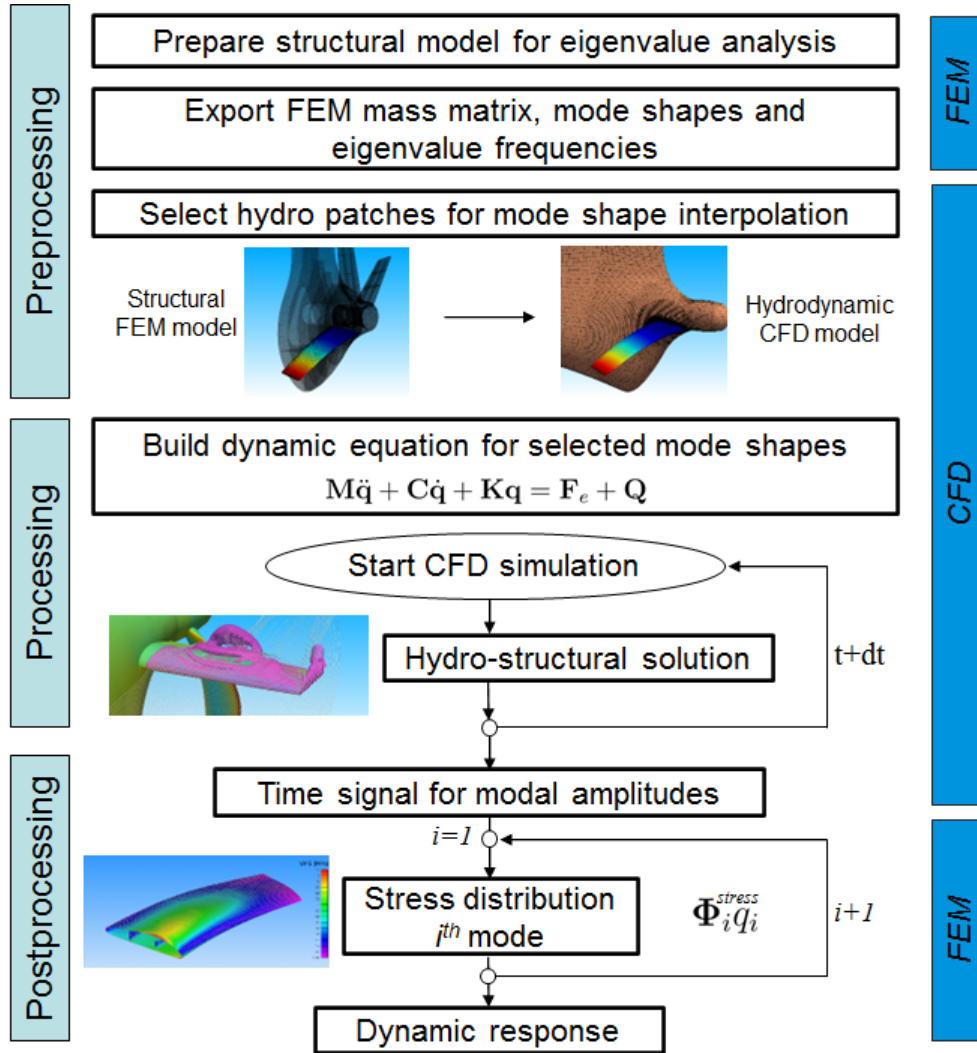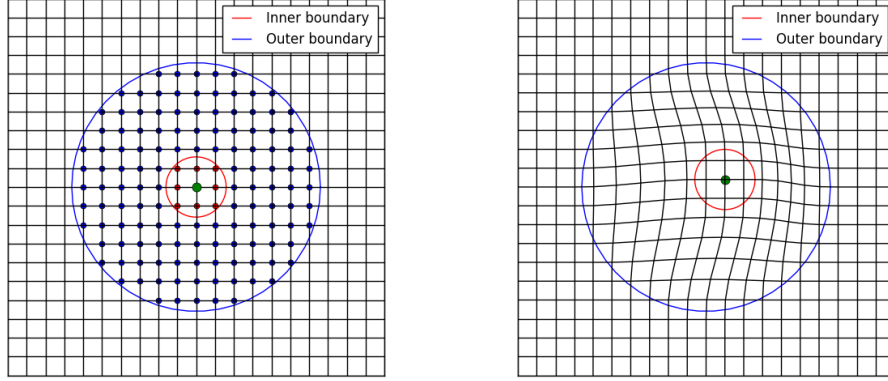
Figure 2: CFD-FEM hydroelastic coupling scheme.

Figure 3: Closest point mesh deformation.

One with the structural nodal displacement included and the other without. Former is employed in the hydroelastic analysis and enables the computation of the dynamic modal responses which correspond to the first term on the r.h.s. of Equation 5. The latter, without the structural displacement, calculates the fluid loads which are used for the static structural analysis. With these loads, two structural responses are computed. First analysis is related only to the previously selected mode shapes and their static response is sought, which means solving the Equation 6 without the acceleration and velocity. This computes the second term in r.h.s. of Equation 5. The second structural analysis computes the quasi-static response by solving Equation 3 which includes infinite number of modes and corresponds to the third term in Equation 5. Quasi-static approach is fully explained and validated in Bakica et al. [5] and is performed as a set of linear static analysis. In summary, to evaluate the stresses and include the structural dynamics, two different fluid solutions are needed and three separate structural responses.

Finally, regarding the solution loop in the CFD code, the deformable clamped appendage motion equation is solved in each time-step after the ship rigid body solution, thus making the ship translational and rotational accelerations readily available in the flexible appendage dynamic equation. The flexible dynamic equation is solved using a standard OpenFOAM library ODE integrator, fifth-order Cash-Karp embedded Runge-Kutta scheme with error

10

control.

3. Model verification

3.1. Wet frequency response

First step in developing the hydro-structural interaction model is the structural pre-processing to obtain mode shapes and their corresponding natural frequencies. The structural model is shown in Figure 4 with the separated fin which is investigated in detail. The coarse mesh features $0.41\,\mathrm{M}$ cells while the fine mesh size is $3.2\,\mathrm{M}$. The fin structure is made of plate elements of standard shipbuilding steel with the internal elements of $18\,\mathrm{mm}$ thickness and outer shell elements of $24\,\mathrm{mm}$ thickness. Analysis of the fin is performed for dry and wet frequencies in order to asses the influence of the added mass. The fin is constrained with fixed boundary condition in its root before computing the dry natural modes. Wet mode is computed using MFLUID option in the NASTRAN solver. First two dry natural frequencies are equal to $29.1\,\mathrm{Hz}$ and $96.2\,\mathrm{Hz}$. With these results, dynamic amplification is only relevant for the 1st mode since the 2nd mode frequency is already too high to meet any kind of dynamical behaviour induced by the fluid loads. Due to the stated reason, the following verification computations in CFD-FEM coupling are only presented for the 1st mode in calm-water and without forward speed.

In this particular case, hydrodynamic mesh is created only in the vicinity of the fin. This enables fast and efficient computation of the modal response. Mesh is shown in Figure 5 and spans roughly 12 PSS fin lengths in each direction, while the top boundary is positioned slightly below the free surface to avoid two-phase modelling which is deemed unnecessary for this type of problem. Interpolated fluid mode shape compared to the structural one can be observed in Figure 6. The structural dynamics are tested with the imposed artificial force acting on the fin. The fin is initially imposed with the impulse force and the damped modal response is computed in time. The frequency and amplitude of the response is investigated with respect to mesh size and time integration schemes. Two integration schemes are used: Euler and backward. Two meshes are employed, coarse with the $0.4 \cdot 10^6$ cells and fine with $3.2 \cdot 10^6$. Time-step is tested for sizes $T_0/dt = 12, 24, 48, 120$ and 600. Performing the Fourier transform of the signal reveals the necessary time-step size to accurately compute the wet frequency as at least $T_0/dt = 24$ for
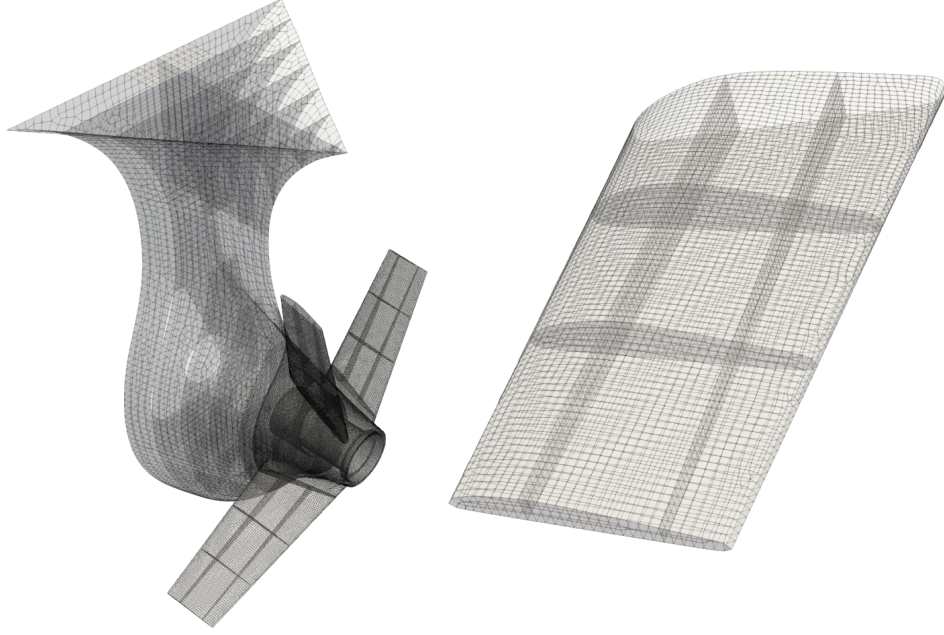
Figure 4: FEM structural model.

which the frequency difference is only at 0.3% for the Euler scheme. When comparing the values, the CFD frequency yields 16.70-16.78 Hz for time-steps above $T_0/dt = 24$, while the FEM MFLUID wet frequency equals 16.79 Hz which is sufficiently correlated. Example of the response for Euler and backward scheme of lowest time-step and coarse mesh is shown in Figure 7. Small additional damping can be seen by using the Euler scheme. Coarse and fine mesh show negligible difference below 0.1% between the results in terms of wet frequency. Given the results for the current test case, the following can be concluded:

- wet frequency is accurately captured in CFD,

- backward scheme is preferred since Euler scheme introduces additional damping,

- coarse mesh is capable of accurately capturing the modal response
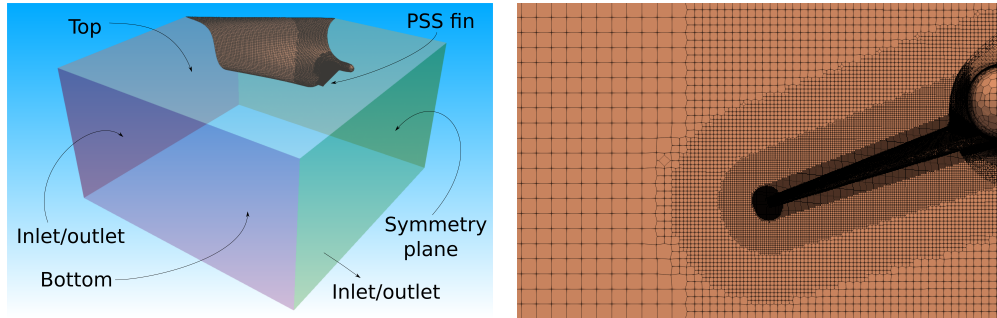
Figure 5: CFD mesh for wet frequency analysis.
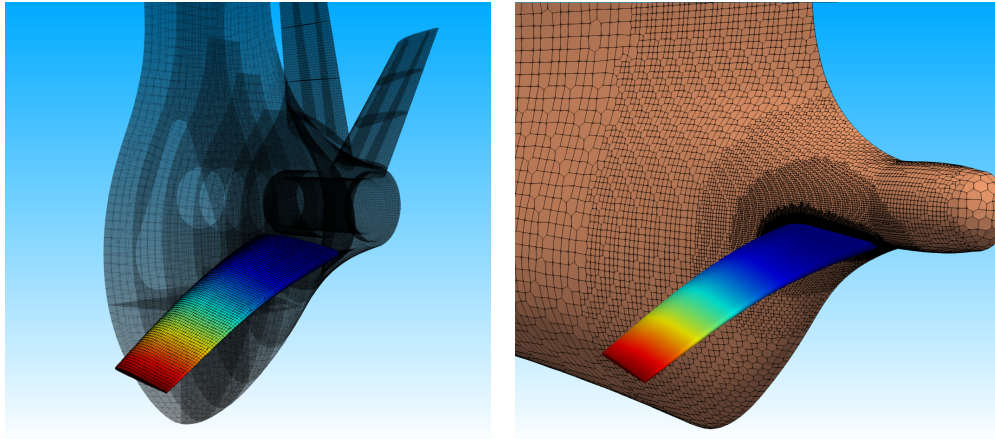
Figure 6: FEM mode shape for PSS fin (left), interpolated mode shape on fluid mesh (right).
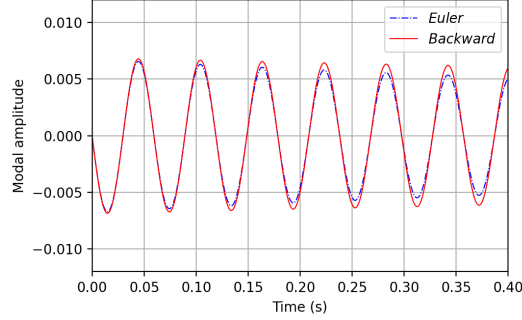
Figure 7: Modal response at Euler and backward schemes for lowest time-step.

3.2. Periodic excitation force

Following the conclusions from the previous subsection, the flexible model of the fin is imposed with the periodic artificial forcing of different frequencies. The main goal is to evaluate if the computed structural response is correlated with the expected theoretical behaviour, hence verifying the flexible model implementation. Only coarse mesh is used for this study with the time-step adjusted to $T_0/dt = 60$ and the second order time scheme which should produce an acceptable level of accuracy. Structural damping is estimated at 0.5%, of critical damping but also different values of structural damping are evaluated. The outcome of this subsection is to calculate the DAF for the fin 1st modal response. Prerequisite for the DAF calculation is the static mode response meaning that a separate CFD simulation is run without the structural nodal displacement considered. Computed force is projected on the selected mode shape with acceleration and velocity set to zero in Equation 6. Dynamic response is normalized by this statical value to obtain the DAF curve.

The results are shown in Figure 8 with the highlighted zones of expected propeller load and wave loads which are well outside of the given figure frame. Approximately 20 response periods were required for each simulation until convergence is achieved. Regarding the necessary time-step for the resolution of the modal response in case of large T/T_0 ratios, for the largest ratio of 10, the simulation is additionally run for lower-time steps of T_0/dt equal to 12, 24 and 48. The response amplitude remains equal for all four cases. However, any further increase in time-step size below $T_0/dt = 12$ starts to

14

exhibit simulation instabilities.

Considering the structural damping which is immensely important for the resonant period, when assessing the values above the $T/T_0 = 1$ its importance is less relevant. This is illustrated by computing the response at $T/T_0 = 2$, where the propeller 2nd harmonic excitation is expected, for different structural damping levels. Compared to the 0.5% damping as the reference, the response differences equal only 0.05% and 0.11% for 2% and 4% damping, respectively. Given the results, 0.5% damping is applied in the forthcoming application cases. The results presented in this section clearly suggests that for the propeller, the quasi static approach is sufficient with the possibility of moderate DAF influence. As for the wave loads, the wave excitation is even larger than the ratio of $T/T_0 = 10$ deeming the hydroelastic analysis unnecessary. Nonetheless, in the forthcoming section, the computations will be performed in order to show the applicability of the implementation as well as presenting the accuracy of the method on the realistic ship structural load case examples. Overall, the following guidelines can be deduced from this section:

- structural damping has a minimal influence on the response at T/T_0 away from resonance,

- wave excitation is suitable for quasi-static response,

- propeller excitation could exhibit moderate DAF values,

- excitation loads with period $T/T_0 > 2$ can be safely run on time-step $T_0/dt = 24$

4. Numerical setup

Two cases are prepared for further analysis, one for wave loads and the other for the propeller loads on the PSS fin. The ship equipped with the PSS is a well-known benchmark model KVLCC2 whose geometry and particulars are readily available in [34]. The propeller and ship particulars are given in Table 1 together with the wave parameters employed in the simulation. Propeller rotation is adjusted according to the previous work, where the PSS efficiency is investigated [12] by running the simulations with and without the PSS. On the contrary, for the wave analysis the parameters can be chosen somewhat arbitrary since all of the wave frequencies are well above any
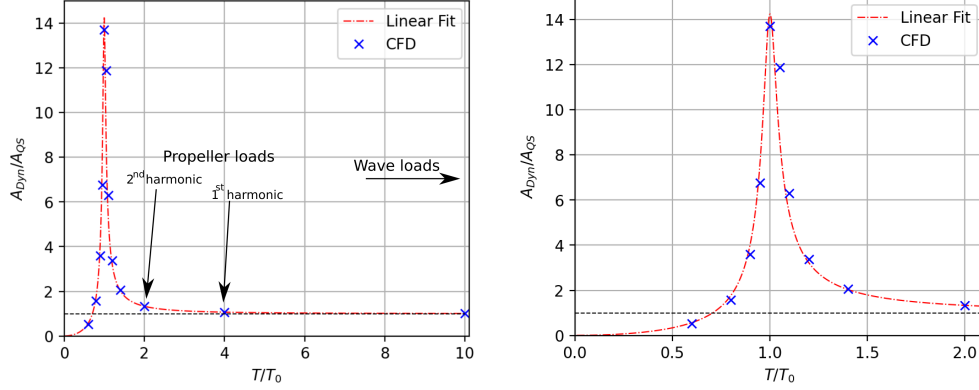
15

Figure 8: Fin DAF computed in CFD (left) and close-up for $T/T_0 < 2$ ratio (right).

possibility of the structural resonance. However, the authors decided to use the head wave direction due to efficiency as it allows the use of symmetry plane.

Wave simulation is prepared so that the wave spatial profile can be properly resolved throughout the simulation domain. Main goal is to achieve proper refinement concerning the wave height H and wavelength λ. Since the currently used wavelength is larger than the ship length, for the longitudinal refinement λ is used as reference. Mesh is prepared in the following manner: $1.5 \cdot \lambda$ from inlet to ship fore, $2 \cdot \lambda$ from outlet to ship aft, $1 \cdot L_{PP}$ from top to freesurface, $1.5 \cdot \lambda$ from bottom to freesurface and $1.5 \cdot \lambda$ from farfield to ship sides. In terms of height near the freesurface, the mesh has 20 cells in the vertical direction per waveheight. On the other hand, for the propeller case, the mesh is prepared in the similar manner, except that the longitudinal refinement is performed featuring L_{PP} instead of λ, and with the smaller height refinement near the interface adjusted to calm-water flow. The propeller simulation also requires the inclusion of the propeller inside the mesh. The coupling is performed using the General Grid Interface (GGI) [35] available in the `foam-extend` version of OpenFoam. Overall fluid domain with the mesh is shown in Figure 9. Both meshes are made with fin refinement ratio as evaluated in the subsection 3.1. The wave case consists of $11.1\,\mathrm{M}$ cells and the propeller mesh counts $7.7\,\mathrm{M}$ cells for the hull region and $5.2\,\mathrm{M}$ cells for the propeller rotative region. Regarding the simulation setup $k - \omega$

Table 1: KVLCC2 ship particulars.

Hull parameters

Length overall	L_{OA} [m]	325.5
Length between perpendiculars	L_{PP} [m]	320.0
Breadth	B [m]	58.0
Depth	H [m]	30.0
Design draught	T_d [m]	20.8
Ship speed	U [kn]	16.5

Propeller parameters

Blade number		4
Diameter	D_P [m]	10.6
Ae/A0		0.4288
Hub ratio		0.155
Rotation	RPM	67.92

Wave condition

Wave height	H [m]	2.0
Wave length	λ [m]	304.4
Wave incident angle	β [deg]	180.0
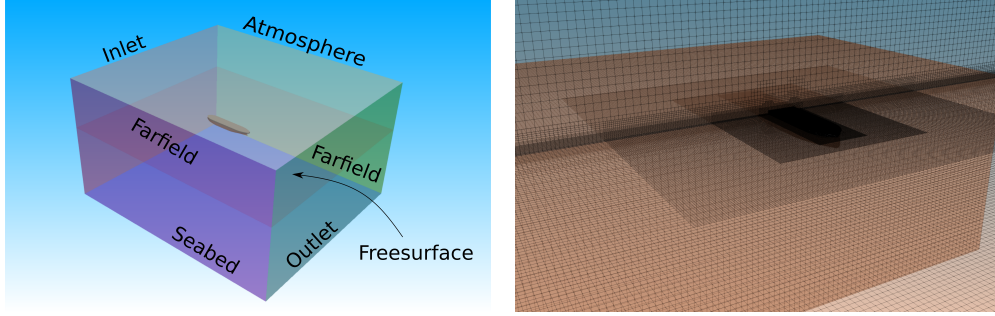
Figure 9: CFD domain (left) and mesh for wave simulation.

SST turbulence model is used in all simulations with second order derivative time scheme. Four outer correctors are employed with two inner correctors meaning that the pressure equation is solved 8 times per each time-step. For the propeller case, time-step is equal to $T_0/dt = 24$ which corresponds to 2.0° of propeller rotation. The wave case time-step is set at same value due to constraints imposed by the structural natural period size. Both simulations are adjusted according to the investigation carried out in section 3.1 to obtain properly resolved structural response. Each of the two cases is run twice, once with the flexible motion of the fin and another with the rigid structure. Although the flexible displacements are small, two simulations are necessary to ensure consistent comparisons between the results. To reduce the necessary computational time, simulations are run until convergence is achieved for all the global and local variables and then the case is re-run with or without the flexible motions by comparing only the last few periods of excitation.

5. Results

5.1. Propeller case

Results are analysed after the last 10 periods of excitation have converged, 2.5 full propeller revolutions for a 4-bladed propeller (each consecutive amplitude difference is lower than 0.5% in this simulation). Snapshot from the CFD simulation is shown in Figure 10. Results for the modal response on the fin are shown in Figure 11 for rigid and flexible case. As can be seen, there is
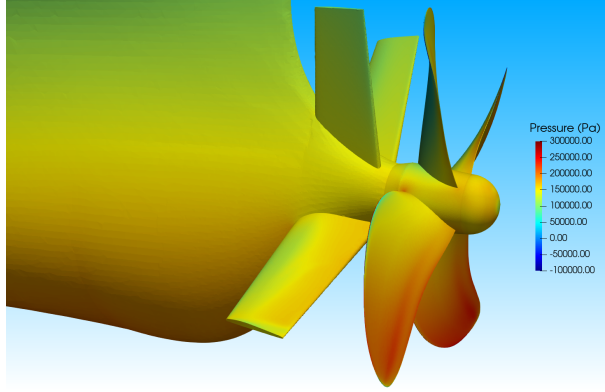
Figure 10: Pressure field on PSS for simulation with propeller.

an amplification of the response in the hydroelastic model. The Fourier analysis of the signal also reveals only the 1st propeller harmonic to be present in the response. DAF for $T/T_0 = 4$ equals 1.197 meaning that the static amplitude is increased by 19.7%. This is consistent with the results from the subsection 3.2 where for the $T/T_0 = 4$ the DAF is also moderately increased. It suffices to say that these motions are quite small and do not influence the propeller thrust, with the maximal nodal displacement amplitude at the fin tip of 3.2 mm per excitation period.

The results should be observed from the perspective of the overall structural response where the studied mode is only a fraction of the entire stresses. In the quasi-static analysis, the response includes implicitly an infinite number of modes of which each mode has a contribution to the final structural stress. The Von Mises Stress (VMS) stress distribution can be computed for any modal amplitude by using the known modal distributions of elemental plane and shear stress. Example of VMS distribution for an arbitrary amplitude is shown in Figure 12. For one period of excitation, a full quasi-static analysis is performed by running a set of linear static analysis per each time-step in the CFD rigid PSS case. This is simply performed by interpolating the pressure distribution [5] and solving Equation 3. To obtain the actual structural response with hydroelastic effects, Equation 5 needs to be solved. Since all of the structural stresses are well-below the standard shipbuilding steel limit (maximum stress around 50 MPa), an element with the highest VMS range for the selected mode is chosen for further analysis to clarify if
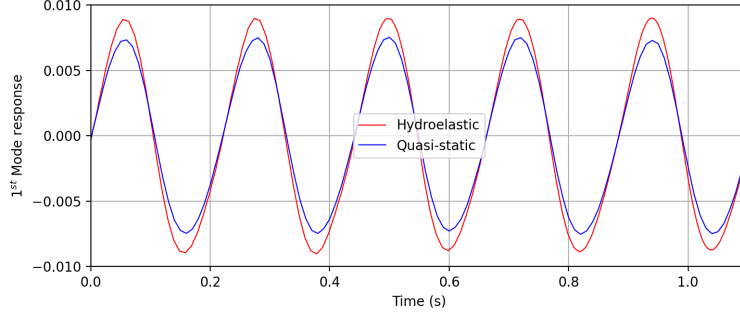
19

Figure 11: Time history of modal response for the hydroelastic and quasi-static model.

there is any serious impact on the structure fatigue. The contribution of the 1st mode amplitude on the overall structural response can be estimated by comparing the static modal response with the linear static analysis results. For this particular element, the 1st mode contribution on the stress range equals 32.1% and it means that the actual stress range considering the structural dynamics will be amplified by only 6.32%. In terms of fatigue this amplification is negligible. Results for this element are shown in Figure 13. This analysis shows that for the propeller loads, quasi-static response can be safely used for the structural computations with the dynamic contribution, featuring complex hydro-structural simulations, carrying negligible effect on the results.

5.2. Wave loads

Wave simulations are run for 30 periods until the convergence of ship motions and PSS fin forces have occurred by comparing the amplitudes of the last 5 periods. Snapshot from the CFD simulation is shown in Figure 14. Results presented here are taken from the last computed encounter period. Signal of heave and pitch for the last few periods is shown in Figure 15. Same approach is taken as in the previous section by performing hydroelastic and static analysis of the fin with two separate simulations. Modal response on the PSS fin is shown in Figure 16 with the hydroelastic and quasi-static approach. As expected, there is no amplification factor present in the results with the dynamic and static analysis being almost exactly equal. When observing the T/T_0 ratio, it is well above 10 where already $DAF = 1$ is
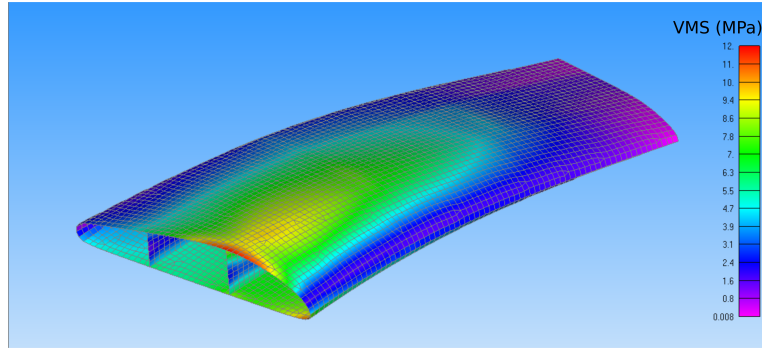
20

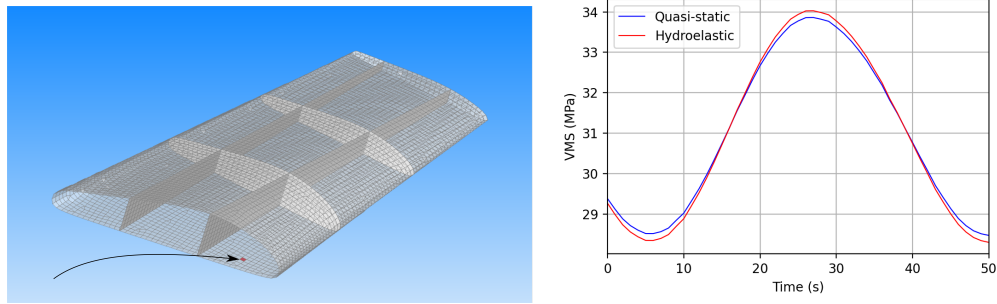Figure 12: Von Mises Stress distribution on 1st mode.

Figure 13: VMS for propeller load cycle (right) on the element with highest stress range (left).
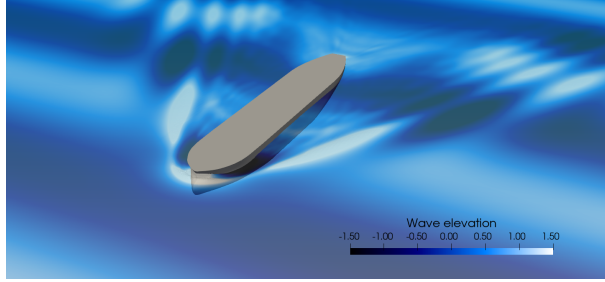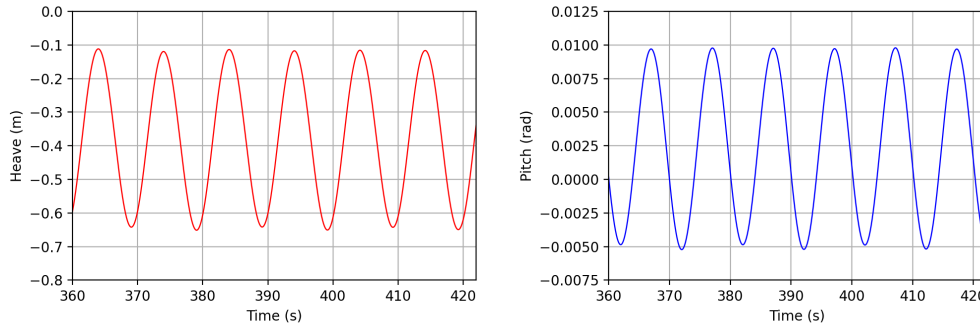
Figure 14: Snapshot from the CFD wave simulation.

Figure 15: Heave (left) and pitch (right) for wave simulation.

expected. Overall, these results do not need additional clarification or computations, since the there is no dynamic influence on the solution. This shows the discussion and results in section 3.2 as consistent and proving the hydroelastic model to be reliable.

6. Conclusion

In this paper a hydroelastic model for the ship appendage of PSS is presented. The model is based on the modal superposition which significantly improves the efficiency of hydro-structural coupling compared to the regular two-way coupled approached where iteration per time-step between the structural and fluid solvers is necessary. The current model requires the precomputed mode-shapes and natural frequencies from the structural solver.
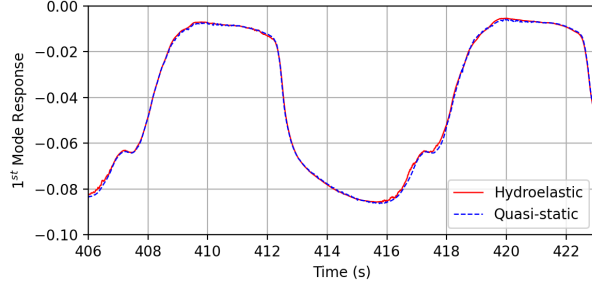
Figure 16: Modal response for the wave simulation.

These mode shapes are appropriately scaled and translated before interpolating the displacement vector to the fluid mesh. Interpolated mode shapes are employed as degrees of freedom for the fluid body and correlated dynamic Equation 6 is solved in the fluid solver. In this manner, the structural displacements are readily available and computed within the fluid domain, thus bearing minimum CPU cost. The computed structural modal response can than be used for the computation of the stresses since each natural mode has a distinctive stress distribution.

Model is verified on a static fluid case with no forward speed. Two types of artificial forces are applied. First, the impulsive force is transmitted to the structure which causes the vibrational response, but since the structural model is submerged, a wet natural frequency response is relevant. Tests are performed with respect to the grid size, time-step and time derivative scheme. The wet frequency is compared to the MFLUID option in NASTRAN and good agreement between the results is found. In the CFD, wet frequency for lowest time-step is 16.78 Hz, while using the MFLUID option the wet frequency equals 16.79 Hz. Grid size effect on the frequency is negligible and response is well resolved with the at least 24 time steps per period. Second case featured a periodic artificial force excitation from which the DAF can be deduced. These results have shown resonance behaviour to be consistent with the theory and have also shown that the time-step can be enlarged in case of higher T/T_0 ratios while still acquiring accurate results. Also, the structural damping is shown to have negligible effect on the results outside the resonance range.

The guidelines obtained from the verification are employed in the two re-

23

alistic ship load cases, PSS under propeller load and under ship motion loads induced by the waves. Results for the propeller case have remained consistent with the verification cases, yielding moderate DAF for the dynamic analysis where $T/T_0 = 4$. However, when assessing this dynamic amplification in the overall stress exhibited by the structure, the entire increase from the hidroelasticity effect is quite small. For the element with the highest stress range, this dynamic effect accounts to only 6.32% amplification which can be neglected in the reasonable fatigue analysis, especially when considering the complexities necessary for the hydro-structural interaction. On the other case, the wave loads are well above the ratio $T/T_0 = 10$ where DAF is equal to 1. From the results, the difference between the quasi-static and hydroelastic cases is negligible as expected and does not require any further analysis.

At last, the study has shown the presented hydroelastic model to obtain reasonable results according to the theoretical background at a practical CPU cost given the efficient modal superposition method. The realistic ship load cases have given consistent results according to the verification study, hence further proving the reliability of the coupling approach. The presented model is implemented in a general manner and can be easily applied to different hydro-structural models without any modifications such as flexible propellers, ship breakwater etc.

References

[1] S. Hai-Long, E. O. Obwogi, S. Yu-Min, Scale effects for rudder bulb and rudder thrust fin on propulsive efficiency based on computational fluid dynamics, Ocean Engineering 117 (2016) 199–209. URL: http://dx.doi.org/10.1016/j.oceaneng.2016.03.046. doi:10.1016/j.oceaneng.2016.03.046.

[2] Y. J. Shin, M. C. Kim, J. H. Lee, M. S. Song, A numerical and experimental study on the performance of a twisted rudder with wavy configuration, International Journal of Naval Architecture and Ocean Engineering (2018) 1–12. URL: `https://doi.org/10.1016/j.ijnaoe.2018.02.014`. doi:10.1016/j.ijnaoe.2018.02.014.

[3] H. Nowruzi, A. Najafi, An experimental and CFD study on the effects of different pre-swirl ducts on propulsion performance of series 60 ship, Ocean Engineering 173 (2019) 491–509. URL: `https://doi.org/10.1016/j.oceaneng.2019.01.007`. doi:10.1016/j.oceaneng.2019.01.007.

[4] N. Sakamoto, K. Kume, Y. Kawanami, H. Kamiirisa, K. Mokuo, M. Tamashima, Evaluation of hydrodynamic performance of pre-swirl and post-swirl ESDs for merchant ships by numerical towing tank procedure, Ocean Engineering 178 (2019) 104–133. URL: `https://doi.org/10.1016/j.oceaneng.2019.02.067`. doi:10.1016/j.oceaneng.2019.02.067.

[5] A. Bakica, N. Vladimir, I. Gatin, H. Jasak, CFD simulation of loadings on circular duct in calm water and waves, Ships and Offshore Structures 15 (2020) 100–112. URL: `https://doi.org/10.1080/17445302.2020.1730082`. doi:10.1080/17445302.2020.1730082.

[6] F. Furcas, S. Gaggero, Pre-swirl stators design using a coupled BEM-RANSE approach, Ocean Engineering 222 (2021) 108579. URL: `https://doi.org/10.1016/j.oceaneng.2021.108579`. doi:10.1016/j.oceaneng.2021.108579.

[7] S. Park, G. Oh, S. Hyung Rhee, B. Y. Koo, H. Lee, Full scale wake prediction of an energy saving device by using computational fluid dynamics, Ocean Engineering 101 (2015) 254–263. URL: `http://dx.doi.org/10.1016/j.oceaneng.2015.04.005`. doi:10.1016/j.oceaneng.2015.04.005.

[8] S. Paboeuf, A. Cassez, ESD structural issue - UPstream device, International Shipbuilding Progress 63 (2017) 291–314. doi:10.3233/ISP-170135.

[9] H. J. Prins, M. B. Flikkema, B. Schuiling, Y. Xing-Kaeding, A. A. Voermans, M. Müller, S. Coache, T. W. Hasselaar, S. Paboeuf, Green Retrofitting through Optimisation of Hull-propulsion Interaction - GRIP, Transportation Research Procedia 14 (2016) 1591–1600. URL: `http://dx.doi.org/10.1016/j.trpro.2016.05.124`. doi:`10.1016/j.trpro.2016.05.124`.

[10] D. B. Lee, B. S. Jang, H. J. Kim, Development of procedure for structural safety assessment of energy saving device subjected to nonlinear hydrodynamic load, Ocean Engineering 116 (2016) 165–183. URL: `http://dx.doi.org/10.1016/j.oceaneng.2016.02.038`. doi:`10.1016/j.oceaneng.2016.02.038`.

[11] H. B. Ju, B. S. Jang, D. B. Lee, H. J. Kim, C. K. Park, A simplified structural safety assessment of a fin-typed energy saving devices subjected to nonlinear hydrodynamic load, Ocean Engineering 149 (2018) 245–259. URL: `https://doi.org/10.1016/j.oceaneng.2017.12.022`. doi:`10.1016/j.oceaneng.2017.12.022`.

[12] A. Bakica, N. Vladimir, H. Jasak, E. S. Kim, Numerical simulations of hydrodynamic loads and structural responses of a Pre-Swirl Stator, International Journal of Naval Architecture and Ocean Engineering 13 (2021) 804–816. URL: `https://doi.org/10.1016/j.ijnaoe.2021.09.002`. doi:`10.1016/j.ijnaoe.2021.09.002`.

[13] J. Ji, K. Kim, M. Seo, T. Kim, D. Park, Y. Kim, K. H. Ko, Load mapping for seamless interface between hydrodynamics and structural analyses, Advances in Engineering Software 71 (2014) 9–18. URL: `http://dx.doi.org/10.1016/j.advengsoft.2014.01.015`. doi:`10.1016/j.advengsoft.2014.01.015`.

[14] A. Bakica, Š. Malenica, N. Vladimir, Hydro-structure coupling of CFD and FEM - Quasi-static approach, Ocean Engineering 217 (2020). doi:`10.1016/j.oceaneng.2020.108118`.

[15] W. Wei, S. Fu, T. Moan, C. Song, T. Ren, A time-domain method for hydroelasticity of very large floating structures in inhomogeneous sea conditions, Marine Structures 57 (2018) 180–192. URL: `http://dx.doi.org/10.1016/j.marstruc.2017.10.008`. doi:`10.1016/j.marstruc.2017.10.008`.

26

[16] Y. Cheng, C. Ji, G. Zhai, O. Gaidai, Hydroelastic analysis of oblique irregular waves with a pontoon-type VLFS edged with dual inclined perforated plates, Marine Structures 49 (2016) 31–57. URL: `http://dx.doi.org/10.1016/j.marstruc.2016.05.008`. doi:10.1016/j.marstruc.2016.05.008.

[17] Z. Sun, Y. chen Jiang, G. yong Zhang, Z. Zong, J. T. Xing, K. Djidjeli, Slamming load on trimaran cross section with rigid and flexible arches, Marine Structures 66 (2019) 227–241. URL: `https://doi.org/10.1016/j.marstruc.2019.04.010`. doi:10.1016/j.marstruc.2019.04.010.

[18] H. Xie, F. Liu, H. Tang, X. Liu, Numerical study on the dynamic response of a truncated ship-hull structure under asymmetrical slamming, Marine Structures 72 (2020) 102767. URL: `https://doi.org/10.1016/j.marstruc.2020.102767`. doi:10.1016/j.marstruc.2020.102767.

[19] H. B. Ju, B. S. Jang, J. Choi, K. H. Yim, Y. J. Yang, S. Han, Structural safety assessment procedure for membrane-type LNG CCS considering hydroelasticity effect, Marine Structures 78 (2021) 102962. URL: `https://doi.org/10.1016/j.marstruc.2021.102962`. doi:10.1016/j.marstruc.2021.102962.

[20] B. Wiegard, M. König, J. Lund, L. Radtke, S. Netzband, M. Abdel-Maksoud, A. Düster, Fluid-structure interaction and stress analysis of a floating wind turbine, Marine Structures 78 (2021). doi:10.1016/j.marstruc.2021.102970.

[21] T. Takami, S. Matsui, M. Oka, K. Iijima, A numerical simulation method for predicting global and local hydroelastic response of a ship based on CFD and FEA coupling, Marine Structures 59 (2018) 368–386. URL: `https://doi.org/10.1016/j.marstruc.2018.02.009`. doi:10.1016/j.marstruc.2018.02.009.

[22] Y. Kim, B. H. Kim, B. K. Choi, S. G. Park, S. Malenica, Analysis on the full scale measurement data of 9400TEU container Carrier with hydroelastic response, Marine Structures 61 (2018) 25–45. URL: `https://doi.org/10.1016/j.marstruc.2018.04.009`. doi:10.1016/j.marstruc.2018.04.009.

[23] P. A. Lakshmynarayanana, P. Temarel, Application of CFD and FEA coupling to predict dynamic behaviour of a flexible barge in regular head waves, Marine Structures 65 (2019) 308–325. URL: `https://doi.org/10.1016/j.marstruc.2019.02.006`. doi:`10.1016/j.marstruc.2019.02.006`.

[24] S. Seng, J. J. Jensen, Š. Malenica, Global hydroelastic model for springing and whipping based on a free-surface CFD code (OpenFOAM), International Journal of Naval Architecture and Ocean Engineering 6 (2014) 1024–1040. doi:`10.2478/IJNAOE-2013-0229`.

[25] M. E. Biancolini, I. M. Viola, M. Riotte, Sails trim optimisation using CFD and RBF mesh morphing, Computers and Fluids 93 (2014) 46–60. URL: `http://dx.doi.org/10.1016/j.compfluid.2014.01.007`. doi:`10.1016/j.compfluid.2014.01.007`.

[26] F. Gagliardi, K. C. Giannakoglou, A twostep radial basis function-based CFD mesh displacement tool, Advances in Engineering Software 128 (2019) 86–97. URL: `https://doi.org/10.1016/j.advengsoft.2018.11.011`. doi:`10.1016/j.advengsoft.2018.11.011`.

[27] N. Vladimir, A. Bakica, Š. Malenica, H. Im, I. Senjanović, D. S. Cho, Numerical method for the vibration analysis of pre-swirl stator, Ships and Offshore Structures 16 (2021) 256–265. doi:`10.1080/17445302.2021.1907072`.

[28] A. Bakica, N. Vladimir, Š. Malenica, H. Im, Numerical procedure for Pre-Swirl Stator structural integrity evaluation, Ocean Engineering 258 (2022) 111698. URL: `https://doi.org/10.1016/j.oceaneng.2022.111698`. doi:`10.1016/j.oceaneng.2022.111698`.

[29] H. G. Weller, G. Tabor, H. Jasak, C. Fureby, A tensorial approach to computational continuum mechanics using object oriented techniques, Computers in Physics 12 (1998) 620–631.

[30] V. Vukčević, H. Jasak, S. Malenica, Decomposition model for naval hydrodynamic applications, Part I: Computational method, Ocean Eng. 121 (2016) 37–46. doi:`10.1016/j.oceaneng.2016.05.022`.

[31] V. Vukčević, H. Jasak, S. Malenica, Decomposition model for naval hydrodynamic applications, Part II: Verification and validation, Ocean Eng. 121 (2016) 76–88. doi:`10.1016/j.oceaneng.2016.05.021`.

[32] I. Gatin, V. Vukčević, H. Jasak, H. Rusche, Enhanced coupling of solid body motion and fluid flow in finite volume framework, Ocean Engineering 143 (2017) 295–304. doi:`10.1016/j.oceaneng.2017.08.009`.

[33] Siemens, NX NASTRAN User's Guide, 2014.

[34] CFD Workshop Website, Gothenburg 2010: A Workshop on CFD in Ship Hydrodynamics, \url{http://www.insean.cnr.it/sites/default/files/gothenburg2010/index.html}, 2010.

[35] M. Beaudoin, H. Jasak, Development of a Generalized Grid Interface for Turbomachinery simulations with OpenFOAM, in: Open Source CFD International Conference, 2008, pp. 1–11. URL: `papers3://publication/uuid/81CCD00D-DF48-4595-B591-C577955CEA06`.

ARTICLE 6

Preprint of the published journal article.

Numerical Procedure for Pre-Swirl Stator Structural Integrity Evaluation

Andro Bakica[a,*], Nikola Vladimir[a], Šime Malenica[b], Hongil Im[c]

[a]*University of Zagreb, Faculty of Mechanical Engineering and Naval Architecture, Ivana Lučića 5, Zagreb, Croatia*
[b]*Bureau Veritas Marine & Offshore, Departement Recherche, Le Triangle de lArche, 8 Cours du Triangle, Paris La Defense, France*
[c]*Hyundai Heavy Industries Co. Ltd., 1000, Bangeojinsunhwan-doro, Dong-gu, Ulsan, 44032, Korea*

Abstract

This paper presents the numerical procedure for Pre-Swirl Stator (PSS) structural design with emphasis on wave induced hydrodynamic loads. The procedure consists of three main steps: definition of Dominant Loading Parameter (DLP), long-term wave statistical analysis leading to Equivalent Design Waves (EDWs) and non-linear simulations of defined EDWs. DLP is defined using simplified lift force approximation for airfoil profile. Non-linearity in the DLP definition requires the time development of each contributing sea-state from the scatter diagram and analysis of the signal to obtain proper statistical parameters for further long-term estimations. In the long-term wave analysis, potential flow is used due to its efficiency compared to more complex CFD method. Non-linear EDW simulations are performed with the CFD/FEM coupling model for a more realistic estimation of the loads and stresses. Extreme response and fatigue are assessed in this work with detail verification and explanation of each step in the entire procedure. Potential flow is solved by means of HydroStar, CFD solution is obtained using open-source tool OpenFOAM and FEM solution is obtained by means of NASTRAN. Overall, the results show that the proposed method can reliably predict the maximum expected wave loads and proves the current design of

---

[*]Corresponding author.

Email addresses: `andro.bakica@fsb.hr` (Andro Bakica), `nikola.vladimir@fsb.hr` (Nikola Vladimir), `sime.malenica@bureauveritas.com` (Šime Malenica), `okil@hhi.co.kr` (Hongil Im)

analysed PSS to satisfy the extreme response and fatigue criteria.

1. Introduction

Recent developments in the accuracy and accessibility of the computationally complex flow models have influenced the hydrodynamic improvements in the modern ship propulsion prediction. Adding the impact from the new IMO regulations related to the ship efficiency, it is expected from the ship industry to turn more intensively to the non-standard and innovative propulsion solutions.

Lately, the new trend in the field of the efficient ship propulsion are the Energy Saving Devices (ESDs). ESDs are placed near the propeller plane in order to improve the flow near the propeller and reduce the energy losses. As a consequence, ship fuel consumption is decreased, thus improving the overall ship efficiency. For the newly built vessels, this means lower Energy Efficiency Design Index (EEDI) (IMO, 2011), but for the existing ships retrofit with ESDs could enable the fulfilment of the upcoming Energy Efficiency Existing Ship Index (EEXI) (IMO, 2021) requirement that enter in force in 2023. There is a number of devices currently under development with the most promising and commercially available ESDs placed in front of the propeller. Sakamoto et al. (2019) performed an extensive research of different hull forms and ESDs by experimental and numerical approach employing Computational Fluid Dynamics (CFD) solver. Most of the research related to ESDs in terms of numerical tools applied is by means of CFD due to their complex flow field in operation (propeller influence, flow separation at the ship stern etc.). Validation of CFD results has been reported for duct type ESD (Bakica et al., 2020b), Pre-Swirl Stator (PSS) (Kim et al., 2015) or the combination of both i.e. duct with the supporting fins inside (Shin et al., 2013). Additionally, lot of work has been performed in the field of hydrodynamic design and optimization of ESDs, as for example, Furcas and Gaggero (2021) combined the RANS-BEM solver for the PSS optimization with reported savings of even up to 8%. There are many papers dealing with ESDs from a hydrodynamic perspective (Nouri et al., 2018; Zhao et al., 2015; Nowruzi and Najafi, 2019; Shin et al., 2018; Lee et al., 2014).

On the contrary, when assessing the structural integrity of ESDs, there is no direct methodology for the design of these thrust improving devices. Lack

of a such procedure served as a research background for GRIP project (Prins et al., 2016; Paboeuf and Cassez, 2017) in order to inspect the PSS structural issues by using potential flow solutions. Lee et al. (2016) developed a procedure for PSS structural evaluation using neural networks in order to reduce the portion of the CPU heavy CFD simulations. The procedure is further extended by Ju et al. (2018) to account for the variable PSS shape. However, in all of the above work, direct hydro-structural coupling is either performed in a simplified manner or by using potential flow models. Mapping between partially overlapping meshes presents a separate field of research where the consistency of pressure transfer from fluid to structural interface represents a major subject of interest. Ji et al. (2014) presented a potential to FEM coupling procedure with the entire panel being projected to the FEM surface mesh. Projection method is used by Bakica et al. (2020a) where the integration points per structural element are projected onto the fluid mesh and the interpolated pressure value is imposed on the FEM wetted element.

Even if the hydro-structural coupling is done at sufficient level of accuracy, it still remains unknown on which wave parameters should the simulation be run. It is not practical to perform a large series of CFD simulations. For this type of design procedure, usually called the Equivalent Design Wave (EDW) approach, a potential wave statistical analysis is carried out singling out the critical case for which further non-linear analysis is made. Efficiency of the potential analysis is high due to the fact that the flow equations are solved in frequency domain. In this statistical process, the crucial step is to properly choose the Dominant Loading Parameter (DLP) which will maximize the observed stresses in the analysed floating structure. Jensen (2009) elaborated different stochastic approaches for marine structures where the estimation of the wave-induced bending moment extreme value is sought. For the green sea loads extreme, Gatin et al. (2019) illustrated a procedure where the DLP is set as a relative wave elevation (water height at bow considering the ship pitch and heave) which is a linear indicator, thus enabling all of the stochastic properties to be analytically calculated. Statistical procedure is performed by potential flow, while the non-linear analysis is run only for the estimated EDW by using CFD solver OpenFOAM.

This paper proposes the design wave approach for the PSS type of ESD. With the large unsupported span, the PSS fins act as clamped beams which are specifically subjected to the wave-induced ship motions. This paper present an EDW procedure where the DLP for a particular fin is the vertical bending force computed in a simplified form. However, the force is

3

not linearly proportional to the wave height, thus demanding a development of each particular sea-state in time and consequently computing the bending force time-signal which can be converted to statistical parameters mandatory for the stochastic procedure. Each step of the statistical procedure is thoroughly verified and explained. With the obtained EDW parameters (wave height and frequency) the non-linear CFD-FEM computation is performed. The response is calculated with the appropriate fluid-structure regime (quasi-static) after evaluating the structural and loading frequencies. Work has been done related to the preliminary computations regarding the PSS structural dynamics (Vladimir et al., 2021) using the analytical and numerical procedures. Additionally, the authors have previously dealt with the quasi-static pressure transfer from the fluid mesh to the structural model with the appropriate validation (Bakica et al., 2020a). EDW is used for the extreme response computation and also for different probabilities of occurrence needed for fatigue life estimation. The non-linear loadings are transferred to the structure and stress ranges are used for further analysis.

Paper is structured in the following way: second section explains the theory behind the design procedure, third section describes the numerical setup, fourth section contains the verification of the procedure steps, fifth section presents the results for the current PSS example design and sixth section briefly outlines the study findings.

2. Methodology

The procedure for the evaluation of the PSS structural integrity is shown schematically in Figure 1. The method for vibration analysis of the PSS has been illustrated in (Vladimir et al., 2021), fluid-structural interface definition and interpolation of the loads has been thoroughly verified in (Bakica et al., 2020a) and the influence of the propeller on the PSS structural response is examined in (Bakica et al., 2021) where it is concluded that the propeller can be neglected in the wave analysis due to its limited impact on the stress range.

This paper deals with the following subjects in the scope of the entire procedure:

- definition of the dominant loading parameter,

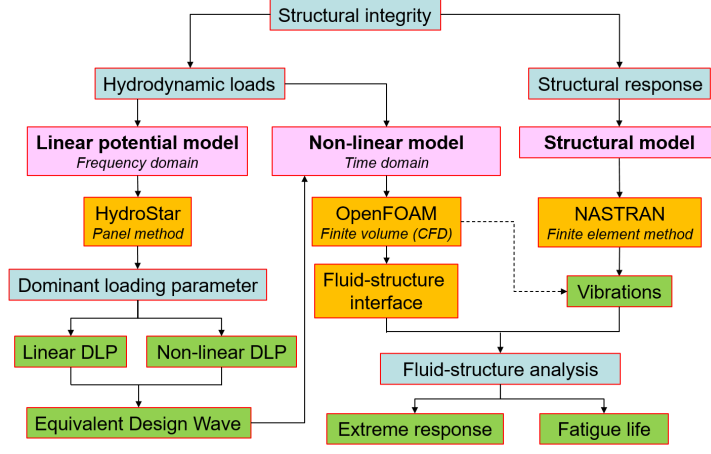- statistical wave analysis leading to EDWs,

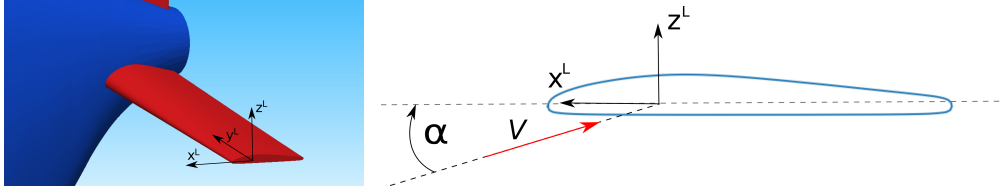Figure 1: Numerical method for PSS structural integrity evaluation.

Figure 2: PSS fin with the dedicated local coordinate system in black.

- extreme response and fatigue evaluation on defined EDWs.

2.1. Dominant loading parameter

Base assumption for the DLP definition is the proportionality of the force and the squared velocity at the point on PSS fin tip. When decomposing the force on the fin using drag and lift components, the majority of the bending moment on the fin is contributed by the lift force i.e. the vertical axis (z^L) in the PSS fin local coordinate system as shown in Figure 2. The lifting force on each fin can be estimated with the following expression:

$$F_L = \frac{1}{2}\rho A C_L(\alpha) V^2, \tag{1}$$

where A is the reference surface of the particular fin, ρ is the fluid density, V is the fluid velocity, C_L is the lift coefficient which depends on the airfoil

5

geometrical profile and is expressed as a function of the angle of attack abbreviated as α. From the Equation 1 the referent surface A is defined by the PSS geometry and the fluid density ρ is a known constant. The lift coefficient function and the velocity magnitude V remain as the unknowns. It is important to notice that for the accurate decomposition and calculation of forces, the velocity needs to be transformed to the local coordinate system of each fin, otherwise α cannot be properly computed. Regarding the lift coefficient, the computation requires the use of CFD to consider properly the flow at the airfoil profile bearing in mind the separation occurring at higher angles. These coefficients depend on the geometry of the body profile and the angle of the incoming fluid flow. Simulations are performed only for the 2D airfoil profile. While three dimensional simulations seem to offer a higher accuracy, due to highly non-uniform flow pattern near the PSS at ship stern, such computations of a uniform flow would not bring any additional accuracy to the coefficients estimation in this case. The relative difference between the potential flow responses for each sea-state is likely to remain consistent and by performing direct non-linear CFD analysis on those critical cases the realistic value can be obtained and later used in the structural assessment.

To compute the velocity magnitude in the potential flow, as briefly stated in the introduction, the velocity decomposition is performed in the following manner:

$$V = V^c + V^w, \tag{2}$$

where V^c is the calm-water velocity computed in the separated calm-water CFD simulation, while the V^w is the relative velocity induced by waves on the fin calculated in the linear potential flow model. The V^c contains all the non-linearities, turbulence and viscosity effects which CFD is capable to capture on top of which the linear wave perturbation is added. Obviously, this neglects their mutual interaction, but provides a better estimation than by using only potential solution to estimate the flow variables at a given point.

2.2. Statistical wave analysis

Potential flow solution theory is based on the well known panel method. Hull wetted surface is geometrically discretised before solving the Laplace equation in the entire domain while the fluid viscosity and rotation is neglected. Most importantly, the linearity of the solution allows the model to be computed in the frequency domain which significantly increases the efficiency of the method. Final solution is obtained in the form of Response

Amplitude Operators (RAOs) in terms of wave frequency (ω), heading (β) and unit amplitude ($A = 1m$). Solution can be easily scaled for any amplitude due to assumed linearity. The RAOs are computed by means of linear potential flow code HydroStar (Bureau Veritas, 2016a).

The long-term statistics in this study is based on the guidances in (Bureau Veritas, 2019). The long-term extreme response is based on the accumulation of the short-term sea-states i.e. counting cycles method (Bureau Veritas, 2016b):

$$n_{ex} = \sum_{1}^{N_{ss}} n_{ss}(1 - P(x)), \tag{3}$$

where n_{SS} is the number of response cycles for a particular sea-state, $P(X)$ is the maxima distribution for the particular sea-state, N_{SS} is the total number of sea states and n_{ex} is the expected number of exceedance of a response level X.

The long-term value definition i.e. most probable maximum DLP, is crucial for the assessment of the overall structural wave loads. If the DLP is linear, the maxima distribution in the Equation 3 is analytically defined and follows the Rayleigh distribution. Furthermore, since all of the potential solutions are available in the frequency domain, the response spectrum and all the necessary characteristics are easily computed, thus defining the long-term DLP. When recalling the Equation 1, it is obvious the DLP defined in this work is not linear due to squared velocity term and the C_L function. When the DLP is non-linear, meaning that the proportionality of the wave height and response is lost, the procedure for defining the short-term contributions in the long-term response significantly gains in complexity. First of all, the problem has to be solved in the time-domain which requires developing the sea-state time-signal corresponding to its frequency domain counterpart. This procedure is performed for each significant height H_S and peak period T_P in the scatter diagram. The generic method of reconstructing the time signal from the frequency domain consists of the following steps:

- select the parameters defining the sea-spectrum $\rightarrow H_S, T_p$

- discretise the selected sea spectrum with $\Delta\omega \rightarrow \omega_i, A_i$

- generate random phase ϕ_i^r for each wave component

- interpolate RAO with ω_i for appropriate heading $\beta \rightarrow RAO(\omega_i, \beta)$

- compute the time-domain response for the selected sea-state:

$$R(t) = \sum_i^n A_i |RAO(\omega_i, \beta)| \cos(\omega_i t + \phi_{RAO}(\omega_i, \beta) + \phi_i^r) \qquad (4)$$

where R is the response, n is the number of discretisation steps in the sea-spectrum, β is the ship heading angle, A_i is the wave amplitude, ω_i is the wave frequency, ϕ_{RAO} is the response phase, ϕ_i^r is the random generated wave phase and t is time.

According to the Bureau Veritas (2019), the short term sea-state should be developed for 3 hours and the long term evolution of waves is modelled as a succession of these short-term stationary states. In this study, the results are interpreted with the up-crossing analysis from which specific statistical parameters can be derived such as the mean up-crossing period (T_Z) or the number of cycles (N). Probability of exceedance for each cycle is obtained by sorting the extremes in descending order and assigning each with the probability of $1 - i/(N+1)$, where $i = 1, 2.., N$ with the lowest probability $i = 1$ given to the maximum occurring extreme. Finally, the obtained empirical distribution is fitted with the appropriate analytical distribution, thus obtaining all the necessary statistical parameters for the long-term estimation.

Before proceeding to the non-linear setup, it remains to clarify how the EDWs are chosen. In this study, EDW is composed from a single frequency (regular wave) which requires the determination of the heading angle and amplitude. Heading is selected by computing the most contributing wave direction to the long-term value and the frequency is chosen where the RAO for this particular heading is maximal. The only variable left to set is amplitude, which is adjusted to the computed long-term response. Extreme response is calculated for the maximum probable response the ship could encounter during its life-time which corresponds to probability of 10^{-8}. Fatigue is evaluated following the guidelines (Bureau Veritas, 2020) where different levels of probability are considered (from 10^{-6} to 10^{-1}). Either fitting of the Weibull distribution or interpolation on the data points (stress range and probability) enables the computation of the long-term fatigue damage from which the design life can be estimated. Regarding the rules coefficients, F2 basic design S-N curve is chosen for welded steel plate joints with cathodic protection in sea-water.

2.3. Design wave non-linear simulation

Non-linear model is performed using CFD simulation with the Finite Volume (FV) spatial discretisation in the framework of OpenFOAM (Weller et al., 1998). In-house library for naval applications NavalHydro Pack (Vukčević et al., 2016a,b; Gatin et al., 2017) developed in the `foam-extend` environment is employed in the study. Incompressible flow is solved using the following equations:

- continuity equation

$$\nabla \bullet \mathbf{u} = 0, \tag{5}$$

- momentum equation

$$\frac{\partial \mathbf{u}}{\partial t} + \nabla \bullet (\mathbf{u}(\mathbf{u})) - \nabla \bullet (\nu \nabla \mathbf{u}) = -\frac{1}{\rho(\mathbf{x})} \nabla p_d + \nabla \bullet \mathbf{R}. \tag{6}$$

where $\rho(\mathbf{x})$ is the density which depends on the spatial vector $\mathbf{x}$, p_d is the dynamic pressure, ν is the kinematic viscosity and $\mathbf{R}$ is the Reynolds stress tensor. Details on the hydrodynamic model can be found in Vukčević (2016). Relaxation zones are introduced at boundary edges to prevent wave reflection in the solution (Jasak et al., 2015). For turbulence, a two-equation $k - \omega$ SST is used for proven accuracy in free-surface naval applications (see Bakica et al., 2019).

The non-linear simulation also requires the structural model to be coupled with the hydrodynamic solution. The PSS model is disretised with the Finite Element Method (FEM) by means of NASTRAN (Siemens, 2014). For the coupling of the hydro-structural interface surface an in-house code is used and the reader can find the full explanations in Bakica et al. (2020a). Since the coupling is performed in a one-way approach, the utility can be run after the CFD simulation is finished on all of the necessary time-steps. After loading conditions are prepared for the FEM model, the structural analysis is performed which enables computation of the appropriate stress peak values and ranges per each probability level.

3. Numerical setup

3.1. Dominant loading parameter

For the 2D airfoil profile, a set of simulations needs to be performed in order to capture all possible angles of attack which the ship could encounter
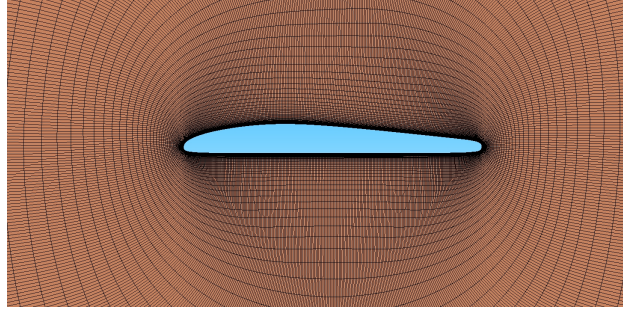
Figure 3: 2D airfoil mesh.

during its service. A reasonable estimation which should cover the entire range is set from $-70\,^\circ$ to $70\,^\circ$ with the increment of $2.5\,^\circ$ per simulation. Turbulence $k - \omega\ SST$ model is used with y^+ value below 1 on the entire airfoil section. Mesh is shown in Figure 3. Input velocity magnitude is set equal to ship design speed. It is important to note that the lift coefficient is not calculated as in the conventional aerodynamic theory i.e. for Equation 1 referent surface A does not depend on the α and is kept constant. It means that irrespective of the velocity direction the lift force is always normal to the airfoil profile always corresponding to the bending force direction on a 3D fin.

3.2. Linear potential flow

For the linear model, only the surface mesh requires discretisation to obtain a flow solution in the entire domain. Ship particulars are given in Table 1. Surface mesh is shown in Figure 4 with a considerable detail on the stern mesh. This is usually not necessary since it does not affect the ship motion results, but in this study the velocity at the PSS point is important, which is located near the hub. This requires a more refined mesh at the stern region for an accurate computation. Half mesh consists of 4015 panels which is relatively fine for the potential computation. For the long-term analysis North-Atlantic scatter diagram (IACS recommendation 34) is used with each sea-state modelled as a Pierson-Moskowitz wave spectrum.

When developing the sea-state in time, the RAO for the velocity at the fin tip needs to be transformed to the PSS fin local coordinate system. Since the solution obtained from HydroStar is given in a separate RAO for each

Table 1: KVLCC2 ship particulars.

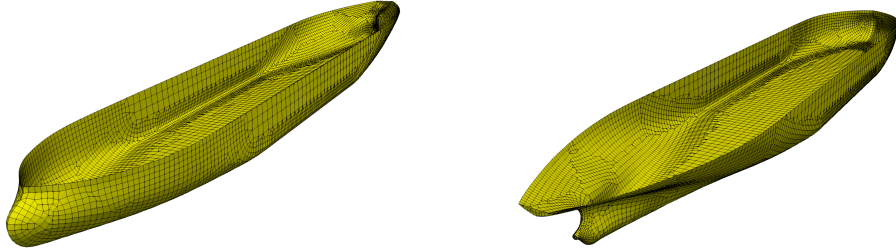|		
Length overall	L_{OA} [m]	325.5
Length between perpendiculars	L_{PP} [m]	320.0
Breadth	B [m]	58.0
Depth	H [m]	30.0
Design draught	T_d [m]	20.8
Ship speed	U [kn]	16.5
Design life	T_{DF} [years]	25.0

Figure 4: HydroStar surface mesh fore and aft.

direction x, y and z, the RAO amplitude can be directly transformed to the local coordinate system by the following expression (see Appendix A for details):

$$RAO_i^L = \sqrt{a_i^2 + b_i^2},$$

$$a_i = \sum_{j=1}^{3} R_{ij} RAO_j \cos(\phi_j),$$

$$b_i = \sum_{j=1}^{3} R_{ij} RAO_j \sin(\phi_j),$$

$$\phi_i = \tan \frac{b_i}{a_i}, \quad \text{for } i = 1, 2, 3$$

(7)

where R is a 3x3 orthogonal transformation matrix from global to local coordinate system, the superscript L denotes the local coordinate system, ϕ is the phase of each response, i and j refer to the three directions of the local or global coordinate system, respectively. It is important to keep the phase between $V_{x^L}^w$ and $V_{z^L}^w$ fixed when developing the time signal to accurately compute the angle α at each time instance. This is achieved by using the same discretised spectrum parameters per each wavelength for both local velocity $RAOs$. Assuming the velocities are developed in time and transformed to local coordinate system, α can be computed as written:

$$\alpha = \arctan \left(\frac{V_{z^L}^c + V_{z^L}^w}{V_{x^L}^c + V_{x^L}^w} \right)$$

(8)

Lastly, the procedure is shown schematically in Figure 5. The input parameters are the airfoil 2D computations, calm-water speed at PSS point in CFD, HydroStar RAO file for the water velocity at the same point and scatter diagram for North Atlantic. RAO for V_x^w, V_y^w and V_z^w is transformed to the local coordinate system (Equation 7) and the sea-state is discretised to establish the 3h response signal of the local coordinate velocities following the steps in subsection 2.1. Using $V_{x^L}^w$ and $V_{z^L}^w$ time signals and adding the appropriate calm-water component ($V_{x^L}^c$, $V_{z^L}^c$) to each, the signal of α is constructed. This allows easy interpolation of the C_L which leads to the final expression in Equation 1 and the assembly of the force time signal. Upcrossing analysis of the force signal gives the empirical distribution on which a proper distribution is fitted using Maximum Likelihood Estimate (MLE). The outputs are the MLE fits to each short-term sea-state which
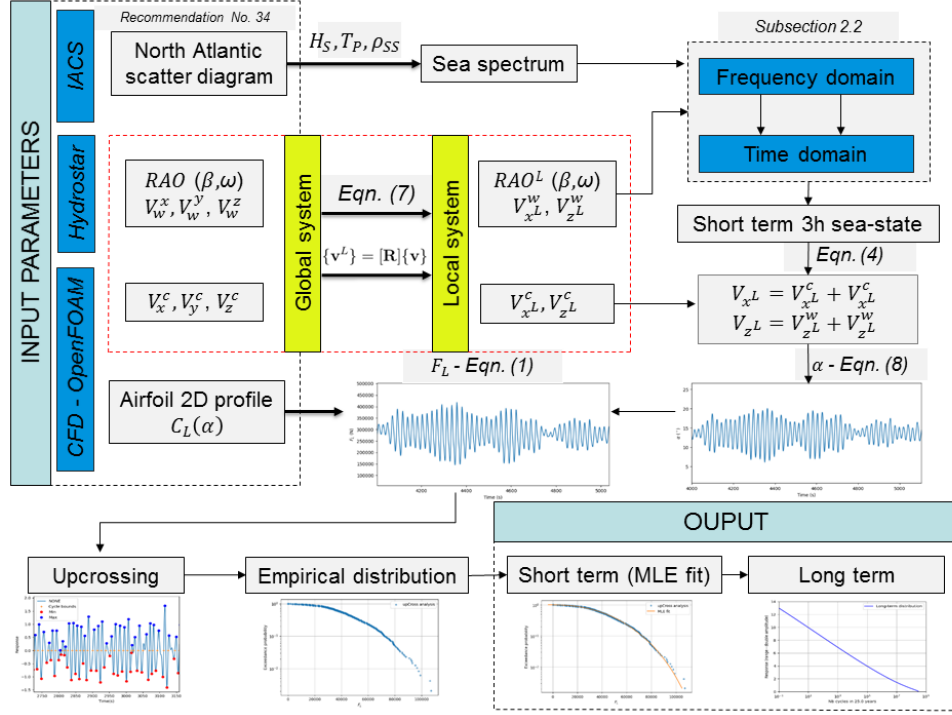
Figure 5: Schematic illustration of the procedure for obtaining the short-term distribution for each H_S, T_P and heading (β).

contribute to the long-term value. In this procedure Johnson SB distribution, first introduced by Johnson (1949), is used for the fit which provides high amount of flexibility given the 4 parameters defining the distribution and is particularly good at fitting the tails.

3.3. Non-linear simulation

First part of the non-linear simulation is the CFD fluid domain setup. Each domain is arranged according to the wave input parameters (wave height H and wavelength λ). At the inlet at least $1.5 \cdot \lambda$ length to the ship fore is set, while behind the ship there is a slightly larger length of $2 \cdot \lambda$ from the ship stern to the domain outlet because of the ship forward speed, and the sides are also dimensioned to account $1.5 \cdot \lambda$ from farfield boundary to ship sides. The fluid domain limit for shorter wavelengths is $2 \cdot L_{PP}$ to the outlet, $1.5 \cdot L_{PP}$ to the sides and inlet with the sea-bottom $1.5 \cdot L_{PP}$ in
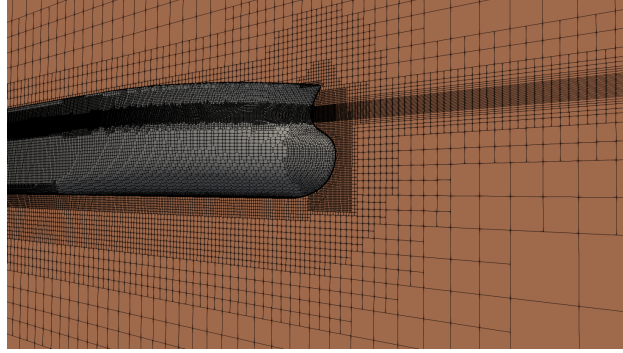
Figure 6: CFD computational mesh.

length. Depending on the flow conditions, vertically there is at least 18 cells per H near the free-surface with the sea-bed being distanced $1 \cdot \lambda$ from the ship bottom to avoid shallow water effects. Mesh size is equal to $11\,\mathrm{M}$ for the full domain. Ship domain is shown in Figure 6 for the condition where $H=2\,\mathrm{m}$. For each case, 20 periods is run. Body motion is solved following the practice explained by Gatin et al. (2017). Relaxation zones are set on four sides of the fluid domain and the length is equal to the wavelength in each case.

Structural model is created only for the ship aft structure. The entire model is shown in Figure 7 with the fin abbreviation. The analysis shown in this work is illustrated only on Fin 3. Fore section of the model is fully fixed imposing necessary boundary conditions. Fin thickness of the outer shell and internal structure is equal to $24\,\mathrm{mm}$ and $18\,\mathrm{mm}$, respectively. Model of the fin structure is made from plate elements with the standard shipbuilding steel as material.

Hydrodynamic pressure is transferred through the developed in-house hydro-structural interface described and validated in (Bakica et al., 2020a) as previously mentioned. Regardless of the coupling type, the overlapping i.e. wetted elements on hydrodynamic and structural side need to be extracted for the strict definition of the interface surface. By comparing the structural natural frequencies to the wave frequencies, appropriate fluid-structure regime can be chosen. First natural frequency is equal to $29.2\,\mathrm{Hz}$ as shown in Bakica et al. (2020b) and already for this lowest mode, the structural frequency is 10 times higher than all the probable wave frequencies encountered
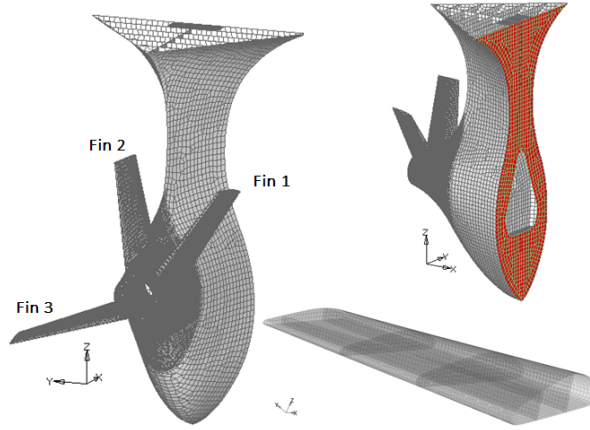
Figure 7: Structural model with fin numbering and internal structure of Fin 3 (fixed elements are shown in red).

by the ship. This implies that in the current work, where the wave loads on the PSS are studied, for the hydro-structural problem the quasi-static approach is applicable.

4. Verification

The following steps of the procedure need verification before the entire procedure can be run on the real PSS case. First is the verification of the dominant loading parameter assumptions in subsection 2.1 and Equation 2, and second is the verification of the long-term statistical analysis along with the developed short term sea-states in time domain.

4.1. Dominant loading parameter comparison

Three types of computations are performed: calm-water CFD simulation at design speed, potential flow and CFD response comparison at zero speed and at ship design speed both at head wave condition. Calm-water CFD solution is necessary to compute the average velocity at the tip of the Fin 3 (V^c in Equation 2) which is later compared to the average velocity at the same point in wave simulations with forward speed. Besides comparing the average velocity, the peturbed component (V^w in Equation 2)

is compared to HydroStar potential solution and for this reason zero speed simulations are performed. Since the forward speed effect in HydroStar is included through the encounter frequency approximation such results cannot be reliably compared to the CFD, hence a priori comparison in zero speed condition verifies the CFD solution against the HydroStar and the possible differences when comparing the forward speed results can be attributed to the potential flow approximated forward speed effect. Head wave conditions is chosen for efficiency reasons in the verification study since it enables the use of the symmetry plane, thus halving the number of mesh cells. Besides the fine mesh of $5.5\,\mathrm{M}$ cells for half-domain, also coarser mesh of $2.1\,\mathrm{M}$ is made so that the consistency of results regarding to the mesh size can be addressed.

CFD results are run only for the wave frequencies in the range of 0.3-$0.9\,\mathrm{rad/s}$ where the majority of the response is contained. Time step for each simulations is adjusted to 0.25% of the encounter period. First comparison is related to the ship motions which has a significant effect on the wave induced loads on the PSS. Zero speed condition comparison is shown in Figure 8. The results show very good correlation between HydroStar and CFD with the largest difference of 5% in the pitch at $0.35\,\mathrm{rad/s}$. Furthermore, for the ship design speed the comparison is presented in Figure 9. There are larger differences in this case, particularly for the heave motion. However, the results are still relatively similar with only the peak in the heave motion being exaggerated in HS. Finally, the flow at the tip of the Fin 3 is also compared at forward speed for the average velocity and perturbed component. This potential flow RAO is used for the construction of the force signal. The results are shown in Figure 10. The perturbed component has a similar results for the lower frequencies, while the higher frequencies are overestimated by potential model. This will yield somewhat higher forces on the long-term analysis in the larger wave frequencies which is deemed acceptable. The base assumption in the entire procedure is that the potential solution can accurately predict the critical conditions on which non-linear analysis is performed. Similar trends in the curves justify this assumption and when comparing the average velocity change in waves where the largest difference is about 2%, the approach proposed in subsection 2.1 can be assessed as reasonable.

Time-step and grid dependency is studied on a case of $\omega = 0.4$ where the peak of the lift velocity is located. Results are presented in Table 2. The results show the grid size to exhibit similar results with the difference below 1%
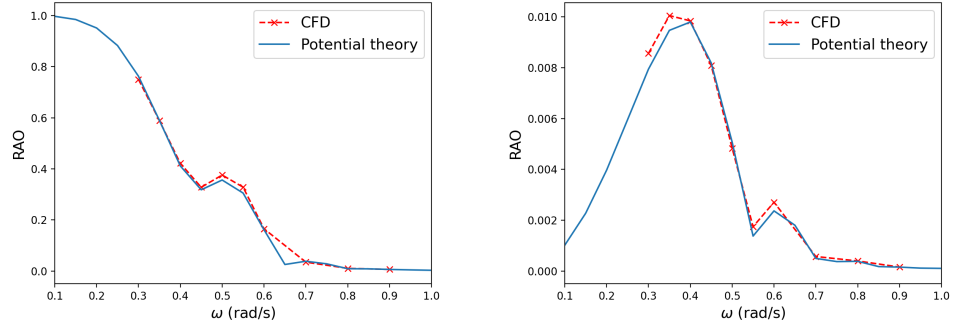
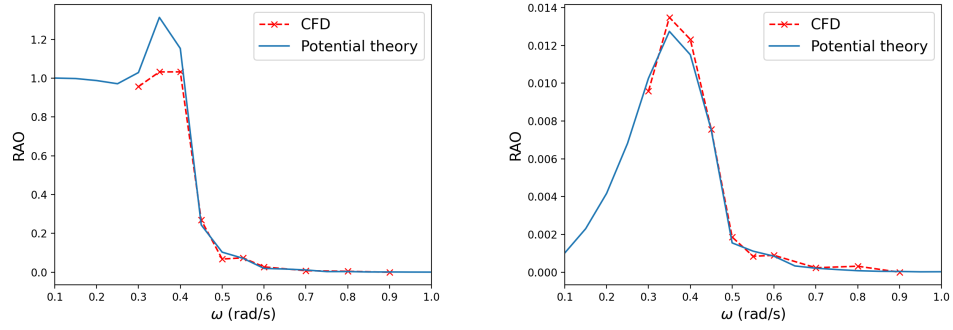Figure 8: Heave (left) and pitch (right) comparison at zero speed.

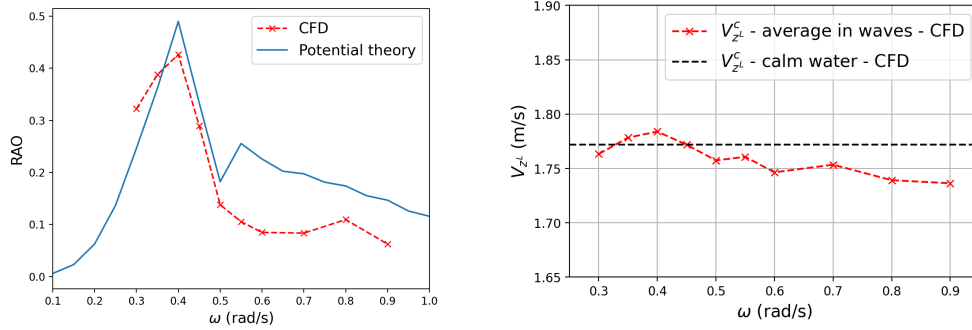Figure 9: Heave (left) and pitch (right) comparison at design speed.

Figure 10: Lift velocity (V_{z^L}) at Fin 3 tip, comparison of perturbed V^w (left) between CFD and potential flow, and average velocity V^c difference for CFD in calm-water and waves (right).

for ship motion. The time-step variation shows reliability and convergence of the results even as the time-step is drastically reduced. This is important for future cases because the inclusion of the PSS in the CFD simulation requires a very low time-step (0.0625% of encounter period) to properly resolve the flow at local scale. This is also observable with the larger dependency of the lift velocity on time-step than grid refinement. Additionally, the same case is run at different amplitudes to demonstrate the effect of wave steepness H/λ on the RAO solution when the wave parameters are outside the fully linear theory. For the stated reason, besides the case with $A = 1$ m, three more simulations are run for amplitudes of 2 m, 4 m and 8 m. Results are given in Table 3 for the normalized response. Ship motions amplitude deteriorates as the wave height is increased and this is expected due to effects of bow flare, wave breaking and green water. On the other hand, the local velocity at the PSS does not have a straightforward correlation with the wave steepness. The local lift velocity signals are shown in Figure 11 where the 2nd order effects are already visible on $H/\lambda = 0.02$. This non-linear effect between the wave incident field, ship motions and wake velocities is not practical to deterministically quantify. When considering that this should be performed for all wave frequencies, wave heights and headings, the full CFD approach would not be possible in a reasonable amount of time. In order to make the procedure useful and efficient, the design procedure features a two-step approach with potential long-term wave analysis followed by a non-linear

18

Table 2: Error (%) for $\omega = 0.4$ and forward speed.

Mesh type	Coarse	Fine			
dt (% of ω_e)	0.5	0.5	0.25	0.125	0.0625
Heave	0.2	-2.94	-0.23	-0.036	/
Pitch	-0.36	-0.91	-0.16	-0.062	/
Lift velocity	-5.91	-5.31	-3.59	-1.84	/

* Fine mesh with $dt = 0.0625\%\omega_e$ is considered as reference for error calculation.

Table 3: Wave steepness effect on ship response.

H/λ	0.005	0.010	0.021	0.042
Heave (m/m)	1.004	0.870	0.727	0.492
Pitch (rad/m)	0.012	0.011	0.010	0.008
Lift velocity (m/s /m)	0.428	0.424	0.503	0.369

* Results are normalized by wave amplitude (A).

CFD/FEM simulation as mentioned previously.

4.2. Wave statistical analysis

First part of the long-term analysis is the development of the time-domain signal. Goal is to verify that the time signal stochastic properties correspond to the frequency domain parameters given by the response spectrum. According to the linear wave statistics, the wave amplitudes with a narrow-band random process assumption follow the Rayleigh distribution, hence the parameters linearly dependant on the wave amplitudes also follow that distribution. This means that the computed probability of exceedance for a linear variable should comply to specific analytical theories. For this purpose, a linear response spectrum is developed in time-domain and compared to the analytical theory. Verification is performed in a straightforward manner. The 3h time-domain signal is analyzed by upcrossing analysis and the empirical distribution is fitted with the Rayleigh distribution using MLE. This fitted distribution is compared to the analytical Rayleigh distribution. However, the 3h sea-state is a finite sample, thus the fitted Rayleigh distribution will not exactly match the analytical assumptions on each run. The time response is developed 500 times and each run is fitted with the Rayleigh distribution. The results are shown in Figure 12. The generated time signal properties do not exceed the standard deviation approximated analytically for this number
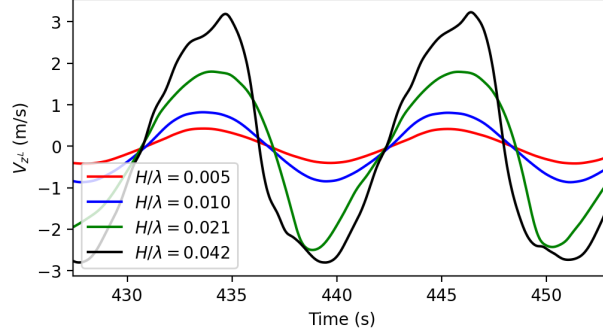
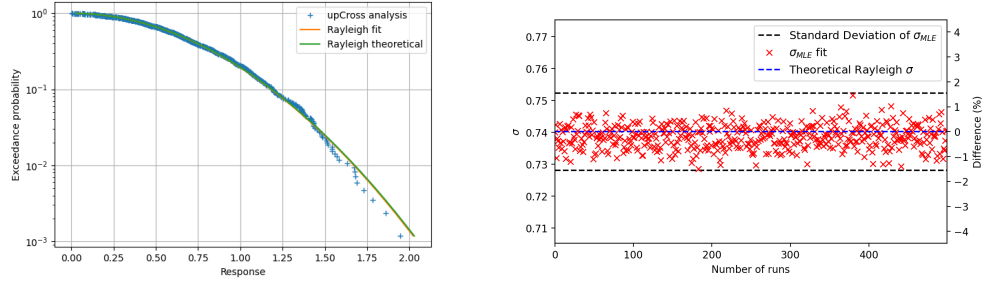Figure 11: Lift perturbed velocity $(V_{z^L}^w)$ at different H/λ for $\omega = 0.4$.

Figure 12: Example of a Rayleigh fit and theoretical distribution on a particular time-signal (left), multiple Rayleigh σ_{MLE} fits windowed by standard deviation (right).

of samples (3h sea-state). Difference between the theoretical σ and average of all the computed σ_{MLE} is at 0.23%, meaning that the maximum short-term response will be on average lowered by this percentage fraction. From the perspective of the entire analysis this is sufficiently correct.

After proving the time developed signal to be suitable, the entire long-term analysis is verified against the commercial Bureau Veritas StarSpec software (Bureau Veritas, 2016b). For the test case, a typical RAO is selected and analyzed for the North Atlantic scatter diagram and equiprobable headings from 0° to 360°. Each sea-state is modelled as Pierson-Moskowitz spectrum. The comparison with the error bars is shown in Figure 13. The
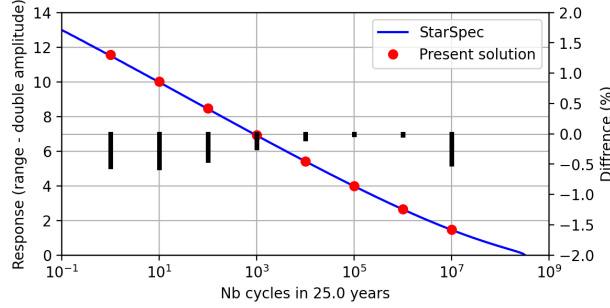
Figure 13: Comparison with StarSpec results for long-term analysis (black bars on right axis represent relative error).

difference is below 0.5% for all probabilities. The differences between the solution may arise due to different discretisation step when integrating the response spectrum or different interpolation procedures used inside the Star-Spec code. Overall, the results are shown to be acceptable. After verifying the short term sea-states and the long-term analysis, the methods explained can safely be applied to the PSS design evaluation.

5. Results

5.1. Long-term wave statistics

First set of results are the input parameters for the long-term procedure as shown in Figure 5. Input results from CFD and linear flow are shown as follows:

- Airfoil 2D profile (CFD)
  Each simulation is run until the lift force converges and the average value is taken from the last 100 iterations. Example of computation and the lift coefficient curve is shown in Figure 14. This step provides the necessary $C_L(\alpha)$ function.

- Calm water velocity (CFD)
  Velocity measuring probes are set at the selected point until the magnitude of each component converges. Results are shown in Figure 15.
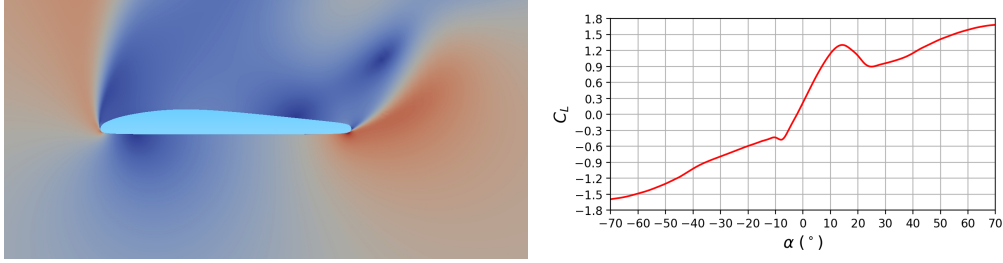
21

Figure 14: Example of an airfoil simulation at $\alpha = 55°$ (left), lift (i.e. bending) coefficient curve (right) from $-70°$ to $70°$.
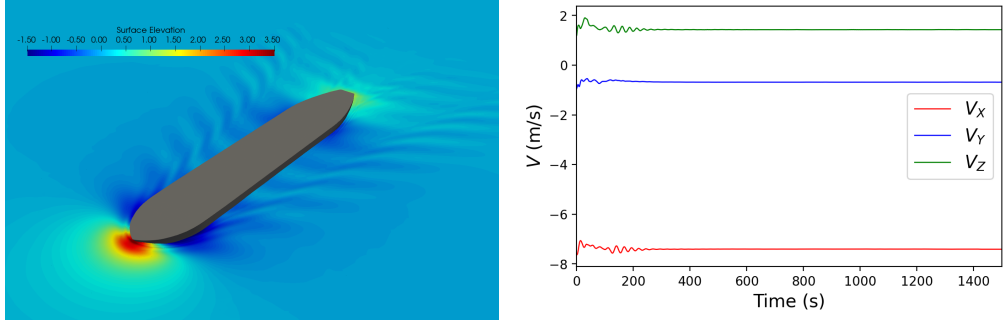

Figure 15: Free-surface snapshot (left) and convergence of the velocities (right) at Fin 3 point from CFD simulation.

- RAOs (Potential theory)
  For each β=0-360° with an increment of 10° RAOs are computed with a range of frequency from $0.05\,\mathrm{rad/s}$ to $2.00\,\mathrm{rad/s}$. Each RAO is transformed to PSS fin local coordinate system following Equation 7 and an example of local velocities RAOs is shown in Figure 16

Since the scatter diagram for North Atlantic is available, the long term analysis can be performed. For each short-term sea-state, local perturbed velocity time signal is developed which is transformed to the local lift force signal. After the upcross analysis, the short term distribution is fitted with the MLE method which enables the computation for all the necessary variables of the long-term analysis. Recalling the Figure 1, EDWs are needed for the fatigue and extreme response. Extreme response is computed for the maximal
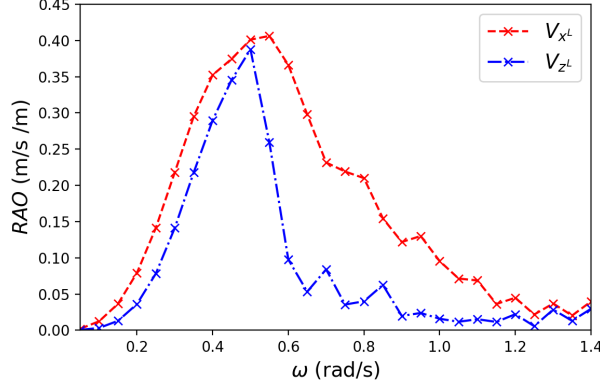
Figure 16: Example results for local velocities RAO at $\beta = 40°$.

probable value at probability of 10^{-8} while the fatigue is computed taking the lower probabilities and computing the stress ranges. For the currently studied PSS structure and Fin 3, the most contributing heading direction is $40°$. For RAO at this direction, the maximum response is at $0.5\,\text{rad/s}$. Given this (β, ω), the amplitude can be computed for each probability level. Long-term results for are shown in Figure 17 with appropriate wave amplitudes. Wave steepness for the highest design wave equals 0.078, while for the lowest the value is 0.018. Comparing to the Table 3 this means that even the smallest wave height will exhibit some non-linearities in the signal. However, at probabilities of 10^{-4} and 10^{-5} where the steepness equals 0.41 and 0.49, respectively, is where larger non-linearities are expected to occur.

5.2. Non-linear EDW simulation

Non-linear simulations are performed for the amplitudes given in Figure 17 which correspond to different EDW probabilities. Ship is allowed three degrees of freedom (heave, pitch and roll). For each probability computed in the CFD, the results are compared to the potential flow analysis expected maximum values and force ranges. Keeping in mind the amount of simplifications considered in the long-term analysis the force peaks and force ranges show a very good agreement to the non-linear computed force ranges as shown in Figure 18. As expected, due to effects which cannot be properly considered in the potential flow model, the non-linear force is underestimated
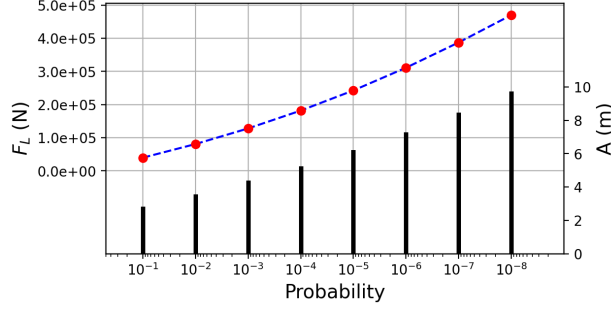
Figure 17: Long term lift force values (blue curve, left axis) and corresponding wave amplitudes (black bars, right axis).

the most for the extreme response wave due to large non-linearities occurring in the CFD model that consequently lower the ship global motions (influence of bow flare, wave breaking etc.). Nonetheless, force ranges necessary for fatigue computations are quite similar in non-linear simulation and linear long-term analysis. However, it should be stressed that the value of the lift force in the linear long-term estimation gives no information about the distribution of the pressure along the fin wetted surface which is mandatory for realistic structural analysis. Overall the comparison shows reasonable agreement for the larger amplitudes and very good corellation for lower amplitudes between the linear statistical analysis with the DLP force approximation and the non-linear simulation, thus justifying the overall approach.

Per each simulation, pressure field on the Fin 3 is exported for the last computed period with a total of 21 points per period selected for further analysis. Pressure is interpolated to the structural model following the method explained in Bakica et al. (2020a). Pressure field on the Fin 3 at time instance for the extreme response is shown in Figure 21 with the interpolated pressure on FEM model. After transferring the hydrodynamic loads, the stress can be computed in the structural solver. Peak stress for extreme response is far below the 235 MPa yielding limit and equals 67.691 MPa. Stress signal is shown in Figure 19 for the selected maximum loaded element on the Fin 3 structure with the highlighted position of the maximum loaded element. Concerning fatigue, all of the structural elements on the Fin 3 are evaluated and the element with the maximum stress ranges for different probabilities is located and further investigated. Location of the element with the stress
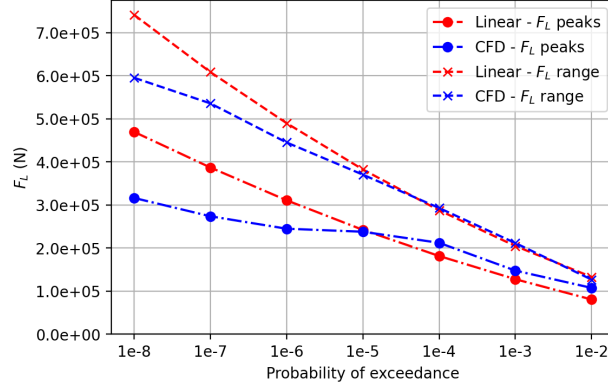
Figure 18: Comparison of linear long-term estimated values and non-linear (CFD).

distribution for multiple probability levels is shown in Figure 20. The element is located at the connection of the fin and the hull as expected. The obtained stress range values are assigned with their probabilities and the statistical distribution is fitted which enables the calculation of the long-term damage using the appropriate S-N curve chosen in subsection 2.2. There are two options possible for the estimation of the long-term damage. Either the Weibull distribution fit on the points can be made, or the simple linear interpolation in log-scale can be performed. Here both methods are compared as shown in Figure 22. The long-term damage, given the design life of 25 years, estimates the fatigue life to be 536 years for the distribution interpolation and 698 years for Weibull distribution fit. For both methods the fatigue life for Fin 3 structural design is well above the necessary design life limit meaning that the structural integrity from the wave induced loads is satisfied for fatigue and extreme response.

6. Conclusion

This paper presented an approach for the evaluation of the Pre-Swirl Stator structural integrity using the potential flow model for the long-term response estimation and definition of the EDWs with the CFD/FEM coupling for the non-linear load computation. The dominant loading parameter is estimated using a simplified lift force approximation. Non-linearities in
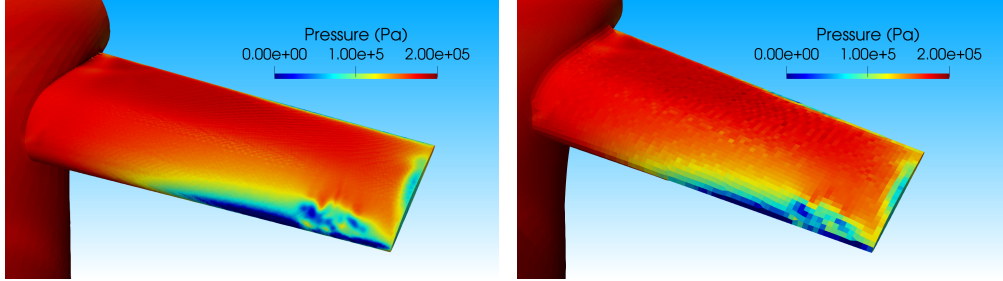
25

Figure 19: CFD pressure on Fin 3 (left) and averaged pressure per panel on FEM model (right) at time instance.
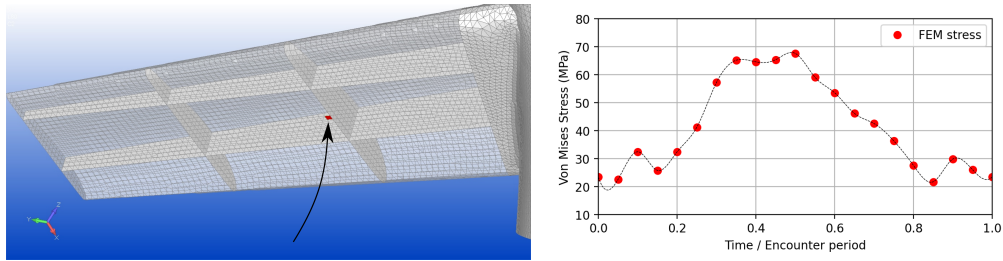

Figure 20: Highlighted element with peak stress value and stress signal per encounter period.
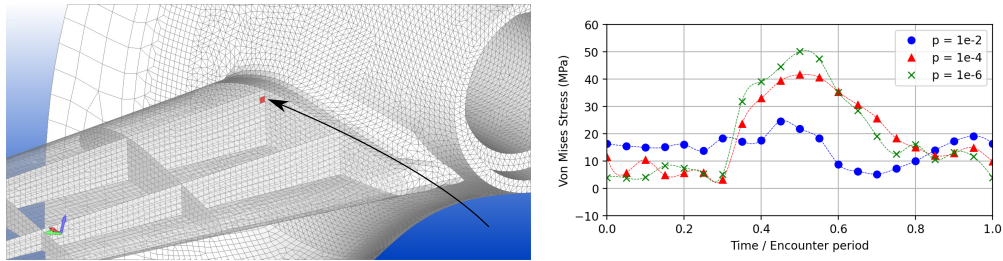

Figure 21: Highlighted element with highest long-term fatigue damage and stress signal at different probabilities.
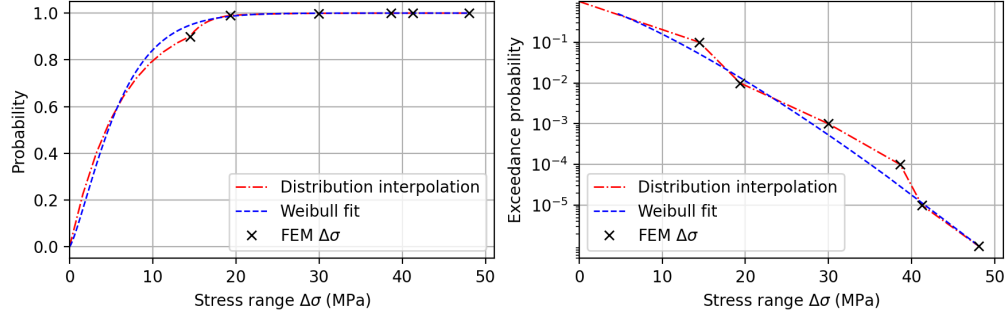
Figure 22: Cumulative distribution function fit (left) and log-scale exceedance probability (right).

the DLP formulation required each H_S, T_P input in the scatter diagram to be developed in time. The upcrossing analysis of each short-term time-signal enabled the estimation of the statistical parameters necessary for the long-term calculation. Long-term maximal values are then used to compute the EDW amplitudes which are further analyzed in the CFD hydrodynamic environment. In CFD, the ship is coupled with the FEM structural model where the pressure is directly interpolated onto the wetted structural elements. In this manner, the expensive non-linear computations are performed for only the selected set of EDWs since the overall non-linear computations for all the sea-states would not be feasible given the enormous CPU time.

Each step of the procedure is carefully verified in section 4 which justifies the proposed approach. Additionally, the computed non-linear responses for each EDW are compared to the potential flow estimation where a very good agreement between the data is found. Difference between the potential and CFD model are highest for the large wave amplitudes as expected since the potential flow model cannot properly consider the various non-linear phenomena occurring during larger wave impact. Overall, for the extreme response wave (probaiblity of 10^{-8}), the structural stresses are well below the steel yielding strength. Regarding the fatigue, multiple probability waves are simulated (from 10^{-6} to 10^{-1}) and given the stress ranges on the element with maximum oscillation, the Weibull distribution is fitted which enables the computation of the long-term fatigue damage using the appropriate S-N curve. Following the analysis for the current Fin 3 structural model, fatigue life is ensured for the necessary design life of 25 years.

Overall, the current study has shown that the proposed approach is reliable in estimating the long-term wave loads on the PSS structure with the simplified non-linear DLP approach giving reasonable estimations.

Appendix A. Coordinate system transformation for Response Amplitude Operator

Velocities in the global and local frame are defined as follows:

$$\mathbf{v} = \left\{ \begin{array}{c} v_x \\ v_y \\ v_z \end{array} \right\}, \qquad \mathbf{v}^L = \left\{ \begin{array}{c} v_x^L \\ v_y^L \\ v_z^L \end{array} \right\}. \tag{A.1}$$

Transformation between coordinate systems for this velocity vector is given as:

$$\mathbf{v} = \mathbf{R}^T \mathbf{v}^L, \qquad \mathbf{v}^L = \mathbf{R} \mathbf{v}, \tag{A.2}$$

Since each component of the velocity vector v in global system has a separate RAO (abbreviated as RAO^{v_i}), the entire velocity vector can be developed in time with careful consideration of phases for each component. For unit amplitude, the time signal for some arbitrary frequency ω can be written as:

$$\begin{aligned} v_x(t) &= RAO^{v_x} \cos(\omega t + \phi_x) \\ v_y(t) &= RAO^{v_y} \cos(\omega t + \phi_y) \\ v_z(t) &= RAO^{v_z} \cos(\omega t + \phi_z) \end{aligned} \tag{A.3}$$

where ϕ denotes the phase for each component. Recalling the expression for the coordinate transformation Equation A.2 the multiplication is as follows:

$$\mathbf{v}^L = \begin{bmatrix} R_{11} & R_{12} & R_{13} \\ R_{21} & R_{22} & R_{23} \\ R_{31} & R_{23} & R_{33} \end{bmatrix} \left\{ \begin{array}{c} v_x \\ v_y \\ v_z \end{array} \right\} = \begin{bmatrix} R_{11}v_x + R_{12}v_y + R_{13}v_z \\ \vdots \\ \vdots \end{bmatrix} \tag{A.4}$$

where the components R_{ij} of the transformation matrix are constructed from Euler angles following the chosen convention (ZYX). Considering only the first row for illustration, the expression can be further expanded using Equation A.3 as written:

$$\begin{aligned} R_{11}v_x + R_{12}v_y + R_{13}v_z = & R_{11}RAO^{v_x} \cos(\omega t + \phi_x) + \\ & R_{12}RAO^{v_y} \cos(\omega t + \phi_y) + \\ & R_{13}RAO^{v_z} \cos(\omega t + \phi_z) \end{aligned} \tag{A.5}$$

With the help of the trigonometric identity this leads to:

$$\underbrace{[R_{11}RAO^{v_x}\cos(\phi_x) + R_{12}RAO^{v_y}\cos(\phi_y) + R_{13}RAO^{v_z}\cos(\phi_z)]}_{a}\cos(\omega t)$$

$$\underbrace{-[R_{11}RAO^{v_x}\sin(\phi_x) + R_{12}RAO^{v_y}\sin(\phi_y) + R_{13}RAO^{v_z}\sin(\phi_z)]}_{b}\sin(\omega t)$$

(A.6)

Bearing in mind the HydroStar convention, the final expression can be written more concisely as shown in Equation 7.

Acknowledgement

References

Bakica, A., Gatin, I., Vukčević, V., Jasak, H., Vladimir, N., 2019. Accurate assessment of ship-propulsion characteristics using CFD. Ocean Engineering 175, 149–162.

Bakica, A., Malenica, Š., Vladimir, N., 2020a. Hydro-structure coupling of CFD and FEM - Quasi-static approach. Ocean Engineering 217.

Bakica, A., Vladimir, N., Gatin, I., Jasak, H., 2020b. CFD simulation of loadings on circular duct in calm water and waves. Ships and Offshore Structures 15, 100–112.
URL https://doi.org/10.1080/17445302.2020.1730082

Bakica, A., Vladimir, N., Jasak, H., Kim, E. S., 2021. Numerical simulations of hydrodynamic loads and structural responses of a Pre-Swirl Stator. International Journal of Naval Architecture and Ocean Engineering 13, 804–816.
URL https://doi.org/10.1016/j.ijnaoe.2021.09.002

Bureau Veritas, 2016a. HYDROSTAR for Experts - User Manual.

Bureau Veritas, 2016b. Starspec - User guide.

Bureau Veritas, 2019. Guidance for Long-term Hydro-structure Calculations NI 638 DT R00 E 33 (February).

Bureau Veritas, 2020. Guidelines for Fatigue Assessment of Ships and Offshore Units 33 (November).

Furcas, F., Gaggero, S., 2021. Pre-swirl stators design using a coupled BEM-RANSE approach. Ocean Engineering 222 (January), 108579.
URL https://doi.org/10.1016/j.oceaneng.2021.108579

Gatin, I., Vladimir, N., Malenica, Š., Jasak, H., 2019. Green sea loads in irregular waves with Finite Volume method. Ocean Engineering 171, 554–564.

Gatin, I., Vukčević, V., Jasak, H., Rusche, H., 2017. Enhanced coupling of solid body motion and fluid flow in finite volume framework. Ocean Engineering 143 (December 2016), 295–304.

IMO, 2011. Resolution MEPC.203(62) Inclusion of regulations on energy efficiency for ships in MARPOL Annex VI. Tech. rep.

IMO, 2021. MEPC 67 Further shipping GHG emission reduction measures adopted in MARPOL Annex VI. Tech. rep.

Jasak, H., Vukčević, V., Gatin, I., 2015. Numerical Simulation of Wave Loads on Static Offshore Structures. In: CFD for Wind and Tidal Offshore Turbines. Springer Tracts in Mechanical Engineering, pp. 95–105.

Jensen, J. J., 2009. Stochastic procedures for extreme wave load predictions - Wave bending moment in ships. Marine Structures 22 (2), 194–208.
URL http://dx.doi.org/10.1016/j.marstruc.2008.08.001

Ji, J., Kim, K., Seo, M., Kim, T., Park, D., Kim, Y., Ko, K. H., 2014. Load mapping for seamless interface between hydrodynamics and structural analyses. Advances in Engineering Software 71, 9–18.
URL http://dx.doi.org/10.1016/j.advengsoft.2014.01.015

Johnson, N. L., 1949. Systems of frequency curves generated by methods of translation. Biometrika 36 (Pt. 1-2), 149–176.

Ju, H. B., Jang, B. S., Lee, D. B., Kim, H. J., Park, C. K., 2018. A simplified structural safety assessment of a fin-typed energy saving devices subjected to nonlinear hydrodynamic load. Ocean Engineering 149 (June 2017), 245–259.
URL https://doi.org/10.1016/j.oceaneng.2017.12.022

Kim, J. H., Choi, J. E., Choi, B. J., Chung, S. H., Seo, H. W., 2015. Development of Energy-Saving devices for a full Slow-Speed ship through improving propulsion performance. International Journal of Naval Architecture and Ocean Engineering 7 (2), 390–398.
URL http://dx.doi.org/10.1515/ijnaoe-2015-0027

Lee, D. B., Jang, B. S., Kim, H. J., 2016. Development of procedure for structural safety assessment of energy saving device subjected to nonlinear hydrodynamic load. Ocean Engineering 116, 165–183.
URL http://dx.doi.org/10.1016/j.oceaneng.2016.02.038

Lee, K. J., Bae, J. H., Kim, H. T., Hoshino, T., 2014. A performance study on the energy recovering turbine behind a marine propeller. Ocean Engineering 91, 152–158.
URL http://dx.doi.org/10.1016/j.oceaneng.2014.09.004

Nouri, N. M., Mohammadi, S., Zarezadeh, M., 2018. Optimization of a marine contra-rotating propellers set. Ocean Engineering 167 (April), 397–404.
URL https://doi.org/10.1016/j.oceaneng.2018.05.067

Nowruzi, H., Najafi, A., 2019. An experimental and CFD study on the effects of different pre-swirl ducts on propulsion performance of series 60 ship. Ocean Engineering 173 (424), 491–509.
URL https://doi.org/10.1016/j.oceaneng.2019.01.007

Paboeuf, S., Cassez, A., 2017. ESD structural issue - UPstream device. International Shipbuilding Progress 63 (3-4), 291–314.

Prins, H. J., Flikkema, M. B., Schuiling, B., Xing-Kaeding, Y., Voermans, A. A., Müller, M., Coache, S., Hasselaar, T. W., Paboeuf, S., 2016. Green Retrofitting through Optimisation of Hull-propulsion Interaction - GRIP. Transportation Research Procedia 14 (0), 1591–1600.
URL http://dx.doi.org/10.1016/j.trpro.2016.05.124

Sakamoto, N., Kume, K., Kawanami, Y., Kamiirisa, H., Mokuo, K., Tamashima, M., 2019. Evaluation of hydrodynamic performance of pre-swirl and post-swirl ESDs for merchant ships by numerical towing tank procedure. Ocean Engineering 178 (February), 104–133.
URL https://doi.org/10.1016/j.oceaneng.2019.02.067

Shin, H. J., Lee, J. S., Lee, K. H., Han, M. R., Hur, E. B., Shin, S. C., 2013. Numerical and experimental investigation of conventional and unconventional preswirl duct for VLCC. International Journal of Naval Architecture and Ocean Engineering 5 (3), 414–430.
URL http://dx.doi.org/10.2478/IJNAOE-2013-0143

Shin, Y. J., Kim, M. C., Lee, J. H., Song, M. S., 2018. A numerical and experimental study on the performance of a twisted rudder with wavy configuration. International Journal of Naval Architecture and Ocean Engineering, 1–12.
URL https://doi.org/10.1016/j.ijnaoe.2018.02.014

Siemens, 2014. NX NASTRAN User's Guide.

Vladimir, N., Bakica, A., Malenica, Š., Im, H., Senjanović, I., Cho, D. S., 2021. Numerical method for the vibration analysis of pre-swirl stator. Ships and Offshore Structures 16, 256–265.

Vukčević, V., 2016. Numerical modelling of coupled potential and viscous flow for marine applications. Ph.D. thesis, Faculty of Mechanical Engineering and Naval Architecture, University of Zagreb.

Vukčević, V., Jasak, H., Malenica, S., 2016a. Decomposition model for naval hydrodynamic applications, Part I: Computational method. Ocean Eng. 121, 37–46.

Vukčević, V., Jasak, H., Malenica, S., 2016b. Decomposition model for naval hydrodynamic applications, Part II: Verification and validation. Ocean Eng. 121, 76–88.

Weller, H. G., Tabor, G., Jasak, H., Fureby, C., 1998. A tensorial approach to computational continuum mechanics using object oriented techniques. Computers in Physics 12, 620–631.

Zhao, Q. X., Guo, C. Y., Zhao, D. G., 2015. Study on self-propulsion experiment of ship model with energy-saving devices based on numerical simulation methods. Ships and Offshore Structures 10 (6), 669–677.
URL `http://dx.doi.org/10.1080/17445302.2014.945765`